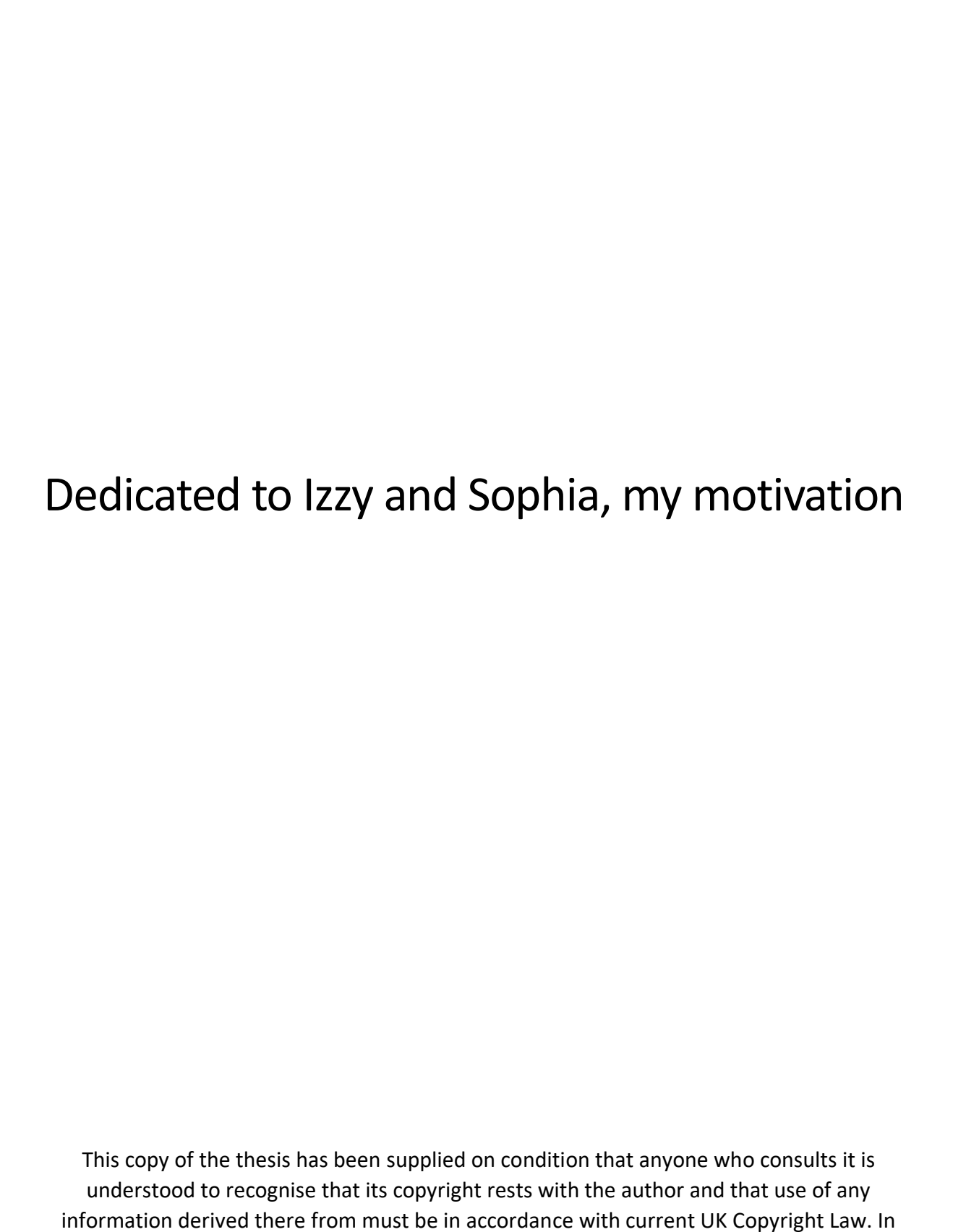
# Investigating Intermolecular Interactions in Multi-Component Pharmaceuticals



# Joseph Tettey Adjimani

University of East Anglia
School of Chemistry, Pharmacy and Pharmacology
December 2024

Thesis submitted to the School of Pharmacy, University of East Anglia in fulfilment of the requirement for the degree of Doctor of Philosophy.



addition, any quotation or extract must include the full attribution.

# **Acknowledgments**

#### 2 Corinthians 2:14 KJVS

"Now thanks be unto God, which always causeth us to triumph in Christ..."

I cannot believe that I am here today, writing MY PhD acknowledgements.

First things first, I want to thank my supervisors, Professor Yaroslav Khimyak and Dr László Fábián, for taking me under their wings and giving me the opportunity to continue this research, on the great work they started. From cold nights in the 850MHz lab at Warwick university, to canapés on the Seine, you've guided me from the MPharm graduate I was to the early-career researcher I am today, and for that I say thank you. I also want to thank you both for caring about me, beyond academia. You always checked how I was faring, you cared about my family and personal life. No time was inconvenient, no question was too daft, no issue was too small. I am very fortunate to have been supervised by you. Dear Karol, gone but never forgotten. You would be proud of me today. You'll never read this, but the world needs to know how grateful I am for your help.

I would like to thank the University of East Anglia for giving me place to undertake this project, the EPSRC for funding my research, and the team at the University of Warwick for the spectrometer time and hospitality.

A special shout out to the NMR basement squad. 4 years in a windowless room (where I sit as I write this), constantly arguing about Spanish cuisine vs English cuisine really has a way of bringing you together. Thanks, Trey, for all your help with the spectrometer (and for letting me borrow your USB memory stick countless times ((until you forced me to get my own)). I will miss your stories (I most definitely will not).

I wouldn't have made it this far without my support system. Thank you Emmarlin, for all the hours of facetime keeping me company whilst I did my "extended BTEC" and "found a cure for covid". Thanks, Ty, for sporadically checking up on me. Thank you Fuad and Dami, for encouraging me, even though you were deep in the trenches too. You understood my struggle

more than anyone else. Thanks Rev Dr Joel Frimpong for constantly telling me I'll make it through and thank you Bishop Richard Aryee for encouraging me to do a PhD in the first place.

Thanks to my father and mother for praying for me, I hope I made you proud. Thanks to my sister and brothers for generally being around.

Lastly, thank you to my wife, my backbone, my best friend. Thank you for supporting me through this journey. After 4 years, all you've learned is that I do research on a 'machine that shakes things really fast', trust me I barely understand it too. I could not have done this without you by my side.

Lastly lastly, to Sophia, my baby girl. You have no idea what's going on right now, but I want you to see this one day and be proud of your old man. Daddy loves you.

I remember this time about 5 years ago, applying for a PhD. One of my reasons was for representation. Not many young, black boys from southeast London get the opportunity to do a PhD. I hope I have inspired some people I met along this journey that if I can, anyone can.

We did it Joe.

#### Jeremiah 29:11 TPT

Here's what YAHWEH says to you: "I know all about the marvellous destiny I have in store for you, a future planned out in detail. My intention is not to harm you but to surround you with peace and prosperity and to give you a beautiful future, glistening with hope...

# **Abstract**

For many years, the question of how to improve the physical properties of Active Pharmaceutical Ingredients (APIs) without changing their covalent structure has challenged the pharmaceutical industry. The development of multicomponent crystal forms has emerged as a significant strategy for improving key properties such as solubility, stability, and bioavailability, while also providing additional avenues for addressing patent-related challenges. To facilitate the discovery of novel multicomponent forms, a deeper understanding of intermolecular interactions is crucial.

We present a systematic study of the intermolecular interactions of two common pharmaceutical cocrystal coformers: isonicotinamide (INA) and nicotinamide (NA). Despite their structural similarity, these compounds exhibit markedly different intermolecular interactions and, consequently, distinct cocrystal formation behaviours. This thesis encompasses database analysis and extensive experimental screening. We characterize new cocrystals, hydrates and solvates of INA and NA using solid-state techniques including Thermogravimetric Analysis (TGA), Differential Scanning Calorimetry (DSC), Powder X-ray Diffraction (PXRD), and solid-state Nuclear Magnetic Resonance (NMR). Solution-state intermolecular interactions are investigated through NMR titrations, Insensitive Nuclei Enhanced by Polarization Transfer (INEPT), Correlation Spectroscopy (COSY), and Nuclear Overhauser Effect Spectroscopy (NOESY).

Additionally, herein is the effective combination of time resolved PXRD and CLASSIC NMR to observe *in-situ* solid-state transformation between different stoichiometric ratios of hydroxybenzoic acid: cyclic amide cocrystal forms. We report the discovery of three new cocrystal forms: 2-HBA<sub>1</sub>:INA<sub>3</sub>, 3-HBA<sub>1</sub>:NA<sub>3</sub>, and 2,3-DHBA<sub>2</sub>:NA<sub>1</sub> and successfully show the stepwise mechanism of formation of all three cocrystals. The necessary experimental conditions have been optimised to observe *in-situ* conversion from the 3-HBA<sub>1</sub>:NA<sub>1</sub> cocrystal to this novel 3-HBA<sub>1</sub>:NA<sub>3</sub> form, and from the 1:3 form back to the 1:1 in a time-resolved experimental set up. These *in-situ* NMR conditions are tested and verified by the conversion of 2,3-DHBA<sub>1</sub>:NA<sub>1</sub> to 2,3-DHBA<sub>2</sub>:NA<sub>1</sub>. This comprehensive study provides important insights into the intermolecular interactions governing multicomponent crystal forms.

#### **Access Condition and Agreement**

Each deposit in UEA Digital Repository is protected by copyright and other intellectual property rights, and duplication or sale of all or part of any of the Data Collections is not permitted, except that material may be duplicated by you for your research use or for educational purposes in electronic or print form. You must obtain permission from the copyright holder, usually the author, for any other use. Exceptions only apply where a deposit may be explicitly provided under a stated licence, such as a Creative Commons licence or Open Government licence.

Electronic or print copies may not be offered, whether for sale or otherwise to anyone, unless explicitly stated under a Creative Commons or Open Government license. Unauthorised reproduction, editing or reformatting for resale purposes is explicitly prohibited (except where approved by the copyright holder themselves) and UEA reserves the right to take immediate 'take down' action on behalf of the copyright and/or rights holder if this Access condition of the UEA Digital Repository is breached. Any material in this database has been supplied on the understanding that it is copyright material and that no quotation from the material may be published without proper acknowledgement.

# **Table of Contents**

Chapte	er 1 - Introduction	14
1.1	The Cambridge Structural Database	14
1.2	Multi-component pharmaceutical forms	15
1.	2.1 Salts	16
1.	2.2 Hydrates and solvates	17
1.	2.2 Cocrystals	18
1.3	Cocrystal screening techniques	
	3.1 Solid state methods	
	3.2 Solution cocrystallisation	
1.	3.3 Computational screening	22
1.4	Intermolecular interactions in cocrystals	
	4.1 Hydrogen bonding	
1.	4.2 The supramolecular synthon	28
1.5 I	n-situ NMR for observing crystallisation	29
1.6 F	Project overview and aims	30
Chapte	er 2 - Main principles of characterisation methods	32
2.1 T	Thermal analysis	32
	1.1 Thermogravimetric analysis (TGA)	
	1.2 Differential scanning calorimetry (DSC)	
2.2 F	Powder X-ray Diffraction (PXRD)	35
2.3 /	Nuclear Magnetic Resonance spectroscopy	37
	3.1 Basic NMR principles <sup>118, 140-144</sup>	
	3.2 Cross Polarisation Magic Angle Spinning (CP/MAS) <sup>145-151</sup>	
	3.3 Combined Liquid and Solid State In-situ Crystallisation NMR (CLASSIC) <sup>119, 123-12</sup>	
2.	3.4 Solution state NMR <sup>153-156</sup>	44
Chapte	er 3 – Experimental methods	48
3.1 L	iquid-Assisted Grinding (LAG)	48
3.2 T	hermogravimetric Analysis (TGA)	49
3.3 E	Differential Scanning Calorimetry	49
3.4 F	Powder X-ray Diffraction (PXRD)	50
3.5 S	Solid-State NMR	51
3.6 S	Solution State NMR	52
Chapte	er 4 Computational studies	54
4.1 S	Statistical analysis, screening and characterisation of nicotinamide and isonicotina	mide
	ystals	
4.2 C	CSD analysis of supramolecular synthon hierarchy in NA and INA cocrystals	56
	2.1 Carboxylic acid - amide	
4.	2.2 Amide - amide	58
4.	2.3 Alcohol – amide	59
4.	2.4 Carboxylic acid – pyridine	60

4.2.5 Phenol – pyridine	61
4.2.6 Phenol – amide carbonyl	61
4.2.7 Summary of findings	62
4.3 Machine learning towards the prediction of NA and INA cocrystals	63
4.3.1 Preprocessing of data for machine learning	
4.3.2 Selection, training and comparison of machine learning algorithms	
4.0.2 Golden, training and companion of machine tearning algorithms	
Chapter 5 – Studying stoichiometry in cocrystals	71
5.1 Solid State	71
5.1.1 Vitamin C <sub>2</sub> :Nicotinamide <sub>1</sub>	
5.1.2 Vanillic Acid <sub>1</sub> :Isonicotinamide <sub>2</sub>	
5.1.3 Vanillic Acid <sub>1</sub> :Nicotinamide <sub>2</sub>	
5.1.4 Sulfasalazine <sub>1</sub> :Isonicotinamide <sub>1</sub>	
5.1.5 Sulfasalazine₁:Nicotinamide₁	
5.1.6 Discussion and conclusions	
5.2 Solution state investigation of cocrystal aggregation dynamics	
5.2.1 Introduction	
5.2.2 <sup>1</sup> H analysis of pure coformers	
5.2.3 Concentration-dependent solution-state interactions of cocrystal coformers	
5.2.3 Correlating solid-state and solution-state interactions	
5.2.4 NMR Titrations	
5.2.5 Insensitive Nuclei Enhanced by Polarization Transfer (INEPT) NMR spectroscopy	
5.2.6 Nuclear Overhauser Effect NMR Spectroscopy	
5.2.7 Variable temperature <sup>1</sup> H NMR measurements	
5.2.8 Summary of findings	123
Chapter 6 - Investigating cocrystal transformations by PXRD and CLASSIC NMR	124
6.1 Introduction	124
6.2 Cocrystal screening by LAG with solvents of varying polarity	128
6.2.1 Analysis of screening results	131
6.2.2 Summary of findings	147
6.3 Observing cocrystal formation via time-resolved PXRD	1/0
6.3.1 3-HBA <sub>1</sub> :NA <sub>1</sub>	
6.3.2 3-HBA <sub>1</sub> :NA <sub>3</sub>	
6.3.3 2-HBA <sub>1</sub> :INA <sub>3</sub>	
6.3.4 2,3DHBA <sub>2</sub> :INA <sub>1</sub>	
6.3.5 Summary of findings	
6.4 Observing cocrystal transformation by Combined Liquid and Solid-State NMR in situ Crys	
(CLASSIC)	
6.4.1 Selection of characteristic peaks for transformation confirmation	
6.4.2 2-HBA <sub>1</sub> :INA <sub>3</sub>	
6.4.3 3-HBA <sub>1</sub> :NA <sub>3</sub>	
6.4.4 2,3-DHBA <sub>2</sub> :INA <sub>1</sub>	180
6.5 Discussion and conclusions	183
Chapter 7 General conclusions and recommendations for future work	186
References	

# List of figures

FIGL	JRE 1-1 - THE DIFFERENT SOLID-STATE FORMS OF APIS15
FIGU	JRE 1-2 - CHEMICAL STRUCTURE OF NAPROXEN SODIUM - POPULAR NSAID PHARMACEUTICAL SALT16
FIGU	JRE 1-3 - COMMON APPLICATIONS OF COCRYSTALS IN MATERIALS AND PHARMACEUTICALS INDUSTRIES19
	JRE 1-4 SCHEMATIC SHOWING PRINCIPLE BEHIND SUPERVISED MACHINE LEARNING24  JRE 1-5 – EXAMPLES OF COMMON GRAPH SET NOTATIONS
FIGU	JRE 1-6 - SCHEMATIC REPRESENTATION OF CLASSIC NMR SEQUENCE USED IN THIS STUDY. ONE ACQUISITION OF <sup>1</sup> H DIRECT DETECTION, <sup>13</sup> C { <sup>1</sup> H} HIGH POWER DECOUPLING AND <sup>13</sup> C CP/MAS
FIGU	SOLID STATE MAKES ONE CLASSIC CYCLE30  JRE 2-1 SCHEMATIC CROSS SECTION OF TGA INSTRUMENT SAMPLE AREA. ADAPTED FROM TA
	INSTRUMENTS 132
FIGU	JRE 2-2 SCHEMATIC REPRESENTATION OF DSC OVEN SHOWING SENSOR BASE, SAMPLE AND
	REFERENCE PANS AND PLATFORMS
	JRE 2-3 SCHEMATIC REPRESENTATION OF X-RAY DIFFRACTOMETER COMPONENTS36
FIGU	JRE 2-4 SCHEMATIC REPRESENTATION OF MAGNETIC SPIN STATES OF SPIN 1/2 NUCLEUS WHERE H IS THE REDUCED PLANCK CONSTANT, $\Gamma$ IS THE GYROMAGNETIC RATIO, AND B <sub>0</sub> IS THE
	MAGNETIC FIELD STRENGTH38
FIGU	JRE 2-5 SCHEMATIC REPRESENTATION OF CHANGE IN BULK MAGNETISATION AROUND FLIP
	ANGLE AS A RESULT OF RF PULSE. 90° PULSE SHOWN HERE40
FIGU	JRE 2-6 SCHEMATIC REPRESENTATION OF THE CROSS-POLARISATION PULSE SEQUENCE. FIRST, A
	90° PULSE IS APPLIED TO THE <sup>1</sup> H NUCLEI, ROTATING THEIR MAGNETISATION INTO THE
	TRANSVERSE PLANE. IMMEDIATELY AFTER THE 90°, A RAMPED RF FIELD IS APPLIED TO THE <sup>1</sup> H
	CHANNEL. SIMULTANEOUSLY, A CONSTANT RF FIELD IS APPLIED TO THE <sup>13</sup> C CHANNEL. RAMPED
	PULSE HELPS BROADEN THE HARTMANN-HAHN MATCHING CONDITIONS, IMPROVING
	EFFICIENCY OF MAGNETIZATION TRANSFER. FOLLOWING CONTACT TIME, THE <sup>13</sup> C FID IS
	RECORDED. DURING THIS ACQUISITION PERIOD, SPINAL-64 DECOUPLING IS APPLIED ON THE 1H
	CHANNEL. SPINAL-64 IS AN ADVANCED DECOUPLING SCHEME THAT PROVIDES IMPROVED
	HETERONUCLEAR DECOUPLING COMPARED TO TRADITIONAL CONTINUOUS WAVE (CW)
	DECOUPLING. AFTER ACQUISITION, A DELAY PERIOD ALLOWS FOR RELAXATION BEFORE NEXT
	SCAN
FIGU	JRE 2-7 <sup>13</sup> C{ <sup>1</sup> H} HIGH POWER DECOUPLING PULSE SEQUENCE. DIRECTLY APPLY 90° PULSE ON <sup>13</sup> C
	FOLLOWED BY FID ACQUISITION AND SIMULTANEOUS HETERONUCLEAR DECOUPLING44
FIGU	JRE 2-8 INEPT PULSE SEQUENCE. 90° PULSE IS FIRST APPLIED TO THE 1H NUCLEI TO ROTATE
	MAGNETISATION PLANE, FOLLOWED BY A DELAY FOR J-COUPLING EVOLUTION. SIMULTANEOUS
	180° PULSES ARE APPLIED TO THE <sup>15</sup> N AND <sup>1</sup> H NUCLEI TO REFOCUS CHEMICAL SHIFT
	EVOLUTION. A FINAL 90° PULSE TO TRANSFER MAGNETISATION TO 15N NUCLEUS AND SIGNAL IS
	ACQUIRED45
FIGI	JRE 2-9 – 2D NOESY PULSE PROGRAM. THREE 90° PULSES ARE APPLIED. THE FIRST PULSE IS
	APPLIED TO CREATE TRANSVERSE MAGNETISATION TO XY PLANE. TIME T1 ALLOWS FOR
	CHEMICAL SHIFT EVOLUTION, WITH DURATION INCREMENTALLY INCREASED TO CREATE THE
	2ND DIMENSION OF THE SPECTRUM. THE SECOND PULSE RETURNS MAGNETISATION TO Z-AXIS
	AND BEINGS MIXING TIME. MIXING TIME IS THE KEY PARAMETER IN NOESY EXPERIMENTS,
	ALLOWING FOR CROSS RELAXATION BETWEEN PROXIMAL NUCLEI. SHORTER MIXING TIMES
	FAVOUR STRONGER NOES FROM SMALLER MOLECULES OR CLOSELY SITUATED NUCLEI,
	LONGER MIXING TIMES ALLOW DETECTION OF WEAKER NOES FROM LARGER MOLECULES OR
	THOSE FURTHER APART. THE THIRD PULSE RETURNS MAGNETISATION TO TRANSVERSE PLANE
	FOR DETECTION. T2 IS THE ACQUISITION PERIOD46
EICI	JRE 4-1- CHEMICAL STRUCTURE OF NICOTINAMIDE (LEFT) AND ISONICOTINAMIDE (RIGHT)54
יוטו	JAL 4-1- OHLIMOAL JIROOTORE OF NICOHNAMIDE (LEFT) AND IJONICOHNAMIDE ( <b>KIGAT)</b> 34

FIGURE 4-2. HYDROGEN BONDING PATTERNS BETWEEN AMIDE-AMIDE CENTROSYMMETRIC DIMER	
( <b>LEFT</b> ) AND CATEMER ( <b>RIGHT</b> )	
FIGURE 4-3 - CARBOXYLIC ACID – PYRIDINE SYNTHON	
FIGURE 4-4 - GRAPH SHOWING PREVALENCE OF SYNTHON OCCURRENCE AS A PERCENTAGE, WH	ERE
100% MEANS THIS SYNTHON IS PRESENT IN ALL COCRYSTALS.	
FIGURE 4-5 - A) AMIDE - CARBOXYLIC ACID HETEROSYNTHON, B) AMIDE – AMIDE HOMODIMER, C)	
AMIDE – ALCOHOL HETEROSYNTHON, D) CARBOXYLIC ACID – PYRIDINE HETEROSYNTHON, E	•
PHENOL – PYRIDINE HETEROSYNTHON, F) PHENOL – AMIDE HETEROSYNTHON	57
FIGURE 4-6. AMIDE-AMIDE DIMER AND CATEMER OBSERVED IN COCRYSTALS OF INA AND NA	59
FIGURE 4-7. HYDROGEN BONDING IN COCRYSTAL OF 1-((2,4-DICHLOROPHENYL)METHYL)-1H-	
INDAZOLE-3-CARBOXYLIC ACID AND NICOTINAMIDE DAQZUT	
FIGURE 4-8 SCHEMATIC SHOWING SUPPORT VECTOR MACHINE SCHEMATIC	
FIGURE 5-1 SIX COFORMERS OF INTEREST. 3-HYDROXYBENZOIC ACID, 2-HYDROXYBENZOIC ACID,	
VANILLIN, VANILLIC ACID, VITAMIN C AND SULFASALAZINE	71
FIGURE 5-2 – HYDROGEN BONDING PATTERNS IN - A. VIT $C_1$ :NA <sub>1</sub> UNIT CELL, B. VIT $C_1$ :NA <sub>1</sub>	
INTERMOLECULAR INTERACTIONS, C. VIT C₁:NA₃ UNIT CELL, D. VIT C₁:NA₃ INTERMOLECULAR	
INTERACTIONS.	
FIGURE 5-3 - DSC THERMOGRAMS OF VITAMIN C, NA, 1:1 AND SUSPECTED 2:1 COCRYSTAL	77
FIGURE 5-4 – <sup>1</sup> H- <sup>13</sup> C CP/MAS NMR SPECTRA OF VITAMIN C, NA, 1:1 (OXOHEQ) AND SUSPECTED 2:1	
COCRYSTAL	
FIGURE 5-5 PXRD PATTERNS OF VC2:NA1 (RIGAKU SMARTLAB SE) AND VC1:NA1 (RIGAKU BENCHTOP	1
DIFFRACTOMETER). KEY DIFFERENCES HIGHLIGHTED IN RED. DIFFERING INSTRUMENT	
RESOLUTIONS LIMIT DIRECT PEAK COMPARISONS.	
FIGURE 5-6 - PXRD PATTERN OF $VA_1$ : INA $_2$ OBTAINED BY LAG (ORANGE) COMPARED WITH COCRYSTA	
OBTAINED FROM SOLUTION CSD – NOA ET AL <sup>190</sup>	
FIGURE 5-7 – A) DSC PLOT OF VA, INA, 1:1 LAG PRODUCT AND 1:2 LAG PRODUCT. B) PXRD PATTERN	
VA, INA AND 1:2	
FIGURE 5-8 A) <sup>1</sup> H- <sup>13</sup> C CP/MAS 1:2 LAG PRODUCT COMPARED TO PURE VA AND /NA	
FIGURE 5-9 – B) <sup>1</sup> H- <sup>13</sup> C CP/MAS 1:2 LAG PRODUCT COMPARED TO PURE VA AND INA, ZOOMED IN OI	
THE ALDEHYDE REGION. C) <sup>1</sup> H- <sup>13</sup> C CP/MAS COMPARING 1:2 LAG PRODUCT, 1:1 LAG PRODUC	
AND VANILLIC ACID	
FIGURE 5-10. HYDROGEN BONDING PATTERN IN VA <sub>1</sub> :NA <sub>1</sub>	
FIGURE 5-11. DSC THERMOGRAMS OF VA, NA, VA <sub>1</sub> :NA <sub>1</sub> AND VA <sub>1</sub> :NA <sub>2</sub> .	
FIGURE 5-12. PXRD PATTERN OF VA <sub>1</sub> :NA <sub>2</sub> COMPARED TO THOSE OF VA <sub>1</sub> :NA <sub>1</sub> AND PURE NA	86
FIGURE 5-13. <sup>1</sup> H- <sup>13</sup> C CP/MAS NMR SPECTRA, COMPARING PEAKS OF PURE VA, NA, 1:1 COCRYSTAL	
AND 1:2 LAG PRODUCT	
FIGURE 5-14. SULPHONAMIDE AMIDE FORM (LEFT) AND CRYSTAL PACKING STRUCTURE (RIGHT). C	
REFCODE: QIZJOYFIGURE 5-15. IMIDE TAUTOMER (LEFT) AND CRYSTAL PACKING STRUCTURE (RIGHT). CSD REFCODE	
KIJBOXKIJBOX	
FIGURE 5-16 PXRD PATTERNS OF SSZ, INA AND 1:1 LAG PRODUCT	
FIGURE 5-16 PXRD PATTERNS OF SS2, INA AND 1:1 LAG PRODUCT FIGURE 5-17. DSC THERMOGRAMS SHOWING MELTING POINTS OF SSZ, INA AND 1:1 LAG PRODUC	
FIGURE 5-18. <sup>1</sup> H- <sup>13</sup> C CP/MAS NMR SPECTRA OF SSZ, INA AND 1:2 LAG PRODUCT	
FIGURE 5-19. – DSC THERMOGRAMS OF SSZ₁:NA₁ AND PURE COFORMERS	
FIGURE 5-21. <sup>1</sup> H- <sup>13</sup> C CP/MAS NMR SPECTRA OF SSZ, NA AND SSZ <sub>1</sub> :NA <sub>1</sub>	92
INTERMOLECULAR BONDING IN 3-HBA. REFCODE: BIDLOP02	00
FIGURE 5-23 - <sup>1</sup> H NMR SPECTRA OF PURE COFORMERS DISSOLVED IN ETHANOL. A) 2-HBA, B) 3-HBA	
C) NA, D) INA	
FIGURE 5-24 – (ABOVE) <sup>1</sup> H NMR SPECTRA OF INA AT CONCENTRATIONS 0.05 TO 0.5 M, (BELOW)	ອອ
CHANGES IN INA 1H CHEMICAL SHIFTS VS CONCENTRATIONS 0.05 TO 0.5 M, (BELOW)	100
OTANOLO IN INA TI OTILITICAL SHIFTS VS CONCENTRATION OF BUTTIN-TI FNUTUNS	. 100

FIGURE 5-25 - ROTATIONAL PATHWAYS FOR PYRIDINE CARBOXAMIDES: ISONICOTINAMIDE (SH	OWN)
AND NICOTINAMIDE (N-PYRIDINE POSITION CHANGES) FOR THE GROUND STATE, TRANSIT	
STATE 1 AND TRANSITION STATE 2. <sup>230</sup>	101
FIGURE 5-26 - <sup>1</sup> H NMR OF NA IN ETHANOL 0.05M TO 0.5M	102
$\textbf{FIGURE 5-27} - {}^{1}\text{H} - {}^{1}\text{H COSY NMR SPECTRUM OF } 0.5 \text{ M INA IN ETHANOL (ABOVE) AND } 0.5 \text{ M NA IN } 0.5 \text$	
ETHANOL (BELOW) IDENTIFYING N-H PEAKS BY THROUGH BOND CORRELATIONS	103
FIGURE 5-28 - <sup>1</sup> H SOLUTION NMR SPECTRA OF 3-HBA, INA AND 3-HBA <sub>1</sub> :INA <sub>1</sub> AT A) 0.05M AND B)	
FIGURE 5-29 - 3-HBA <sub>1</sub> :INA <sub>1</sub> (LUNMEM) SUPRAMOLECULAR SYNTHONS	
FIGURE 5-30 – CHANGES IN <sup>1</sup> H PEAK CHEMICAL SHIFTS OF ET-OH AT DIFFERENT CONCENTRATI	
OF 3-HBA AND INA.	
FIGURE 5-31 - NA (LEFT, CSD:NICOAM) AND 2-HBA1:NA1 (RIGHT, CSD:SODDOF) SOLID STATE CF	
PACKING ARRANGEMENT.	
FIGURE 5-32 - 1H NMR TITRATION SPECTRA OF SOLUTION OF 2-HBA:NA WITH DIFFERENT RATIOS	S FROM
0.1:1 TO 3:1 ACID:AMIDE	114
FIGURE 5-33 - PULSE PROGRAM FOR INEPT INSENSITIVE NUCLEI ENHANCED BY POLARIZATION TRANSFER <sup>153</sup>	
FIGURE 5-34 - 1H-15N INEPT NMR PEAKS	
FIGURE 5-35 - 1H - 1H NOESY SPECTRUM OF 2-HBA AND NA	
FIGURE 5-36 - VARIABLE TEMPERATURE <sup>1</sup> H NMR SPECTRA OF 2HBA-NA IN ETOH SOLUTION, FRO	
TO 328K, BACK DOWN TO 298K	
FIGURE 6-1 – COCRYSTAL COFORMERS ANALYSED IN THIS STUDY	
FIGURE 6-2 - DSC PROFILES OF PURE COFORMERS AND 3-HBA <sub>1</sub> :NA <sub>3</sub> COCRYSTAL	
FIGURE 6-3 - AMIDE-AMIDE CENTROSYMMETRIC DIMER [LEFT] AND CATEMER [RIGHT]	
FIGURE 6-4 - SUPRAMOLECULAR SYNTHONS OF SELECTED COCRYSTALS IN THIS STUDY	
FIGURE 6-5 - DSC PLOT COMPARING MELTING POINTS OF 2-HBA:INA 1:1, 1:2, AND 1:3 COMBINA	
	134
FIGURE 6-6 TGA PLOT OF 2HBA1:INA2 LAG PRODUCT WITH ETHYLENE GLYCOL AS THE SOLVEN	T135
FIGURE 6-7 - PXRD PATTERN AND DSC THERMOGRAMS OF 2-HBA1:INA2 WITH ETG. MULTICOMP	ONENT
SOLID FORM 'PRODUCT B'	136
FIGURE 6-8 DSC THERMOGRAM OF 2HBA1: INA2 LAG PRODUCT WITH ETHYLENE GLYCOL AT DIFF	
HEATING RATES.	137
FIGURE 6-9 - $^{1}$ H- $^{13}$ C CP/MAS NMR SPECTRA OF 2-HBA $_{1}$ :INA $_{2}$ WITH ETG, ETG PEAK SEEN AT 62 PPI	М.
RIGHT – $^{1}$ H- $^{13}$ C CP/MAS NMR SPECTRA OF 2-HBA $_{1}$ :INA $_{2}$ COMPARING REGIONS SUSPECTED	TO BE
INVOLVED IN HYDROGEN BONDING.	
FIGURE 6-10 - A) PXRD PATTERN, B) DSC THERMOGRAM AND C) TGA PLOTS OF 2-HBA $_1$ :INA $_2$ PRO	
BY LAG WITH WATER	
FIGURE 6-11 COMPARISON OF 3HBA1:NA1 COCRYSTAL REPORTED IN CSD VS 'PRODUCT D' LAG	
PRODUCT WITH TOLUENE. A) PXRD, B) DSC AND C) 13C MAS NMR	
FIGURE 6-12 - 3HBA₁:NA₂ – NEW SOLID FORM COMPARED TO STARTING MATERIALS. A) PXRD, B)	
AND C) <sup>13</sup> C MAS NMR	
FIGURE 6-13 - 3HBA₁:NA₂ LAG WITH ETHYLENE GLYCOL 'PRODUCT F' – NEW SOLID FORM COMP	
TO SOLID FORM PRODUCED IN ETHANOL. A) PXRD PATTERNS, B) DSC THERMOGRAM, C) T	
AND D) TGA MAGNIFIED, E) AND F) 13C CP/MAS SPECTRA RECORDED AT 298 K, RECORDED	
400 MHZ SPECTROMETER AT AN MAS RATE OF 12KHZ	
FIGURE 6-14 - PXRD PATTERN OF 3HBA <sub>1</sub> :NA <sub>2</sub> LAG PRODUCT WITH WATER, COMPARED TO ETHAN	
FIGURE 6-15 PXRD PATTERN OF 3HBA <sub>1</sub> :NA <sub>1</sub> . A) AT DIFFERENT TIME POINTS, B) VARYING FREQUE	
C) VARYING ETHANOL VOLUME	
FIGURE 6-16 - 3HBA <sub>1</sub> :NA <sub>2</sub> . A) DSC AT DIFFERENT TIME POINTS, B) PXRD SHOWING TRANSFORMA	
FROM 1:1 COCRYSTAL TO NEW FORM. C) PXRD SHOWING INTERMEDIATE PRODUCES IS 1:	
COCRYSTAL AND EXCESS NA. D) DSC SHOWING SINGLE PEAK FOR PHASE PURE 3HBA <sub>1</sub> :NA	
FIGURE 6-17 <sup>1</sup> H- <sup>13</sup> C CP/MAS NMR SPECTRA OF 3HBA <sub>1</sub> :NA <sub>1</sub> , 3HBA <sub>1</sub> :NA <sub>2</sub> AND 3HBA <sub>1</sub> :NA <sub>3</sub> RECORD	
298 K, RECORDED ON A 400 MHZ SPECTROMETER AT 12KHZ MAS SPEED	15/

FIGURE	<b>6-18</b> - PXRD PATTERNS OF 2HBA <sub>1</sub> :INA <sub>3</sub> AT DIFFERENT TIME POINTS. OVERLAPPING PEAKS	
BE	TWEEN 1:1 COCRYSTAL, 1:3 COCRYSTAL AND EXCESS INA ARE HIGHLIGHTED159	Э
<b>FIGURE</b>	<b>6-19</b> - PXRD PATTERN OF 2,3-DHBA <sub>2</sub> :INA <sub>1</sub> , COMPARED TO 2,3-DHBA <sub>1</sub> :INA <sub>1</sub> AND AT DIFFERENT	
TII	IE POINTS. NO CHANGE OBSERVED BETWEEN 30 SECONDS AND 30 MINUTES OF GRINDING.	
	16	1
FIGURE	<b>6-20</b> <sup>13</sup> C CP/MAS NMR SPECTRA OF 2-HBA, INA, 2-HBA <sub>1</sub> :INA <sub>1</sub> , 2-HBA <sub>1</sub> :INA <sub>3</sub> RECORDED AT 298 K	
	A 400 MHZ SPECTROMETER AT 12 KHZ MAS SPEED. CHARACTERISTIC PEAK OF THE NEW 1:3	
FC	RM IS HIGHLIGHTED IN RED BOX165	5
	<b>6-21</b> - <sup>13</sup> C CP/MAS NMR SPECTRA OF 3-HBA, NA, 3-HBA <sub>1</sub> :NA <sub>1</sub> , 3-HBA <sub>1</sub> :NA <sub>3</sub> RECORDED AT 298K	
	ING A 400MHZ SPECTROMETER AT 12KHZ SPINNING SPEED. CHARACTERISTIC PEAK OF THE	
	W 1:3 FORM IS HIGHLIGHTED IN RED BOX	a
	<b>6-22</b> <sup>13</sup> C CP/MAS NMR SPECTRA OF PURE 2,3-DHBA, PURE INA, 2,3-DHBA <sub>1</sub> :INA <sub>1</sub> AND 2,3-	•
	BA <sub>2</sub> :INA <sub>1</sub> RECORDED ON A 400 MHZ SPECTROMETER AT 298 K AND 12 KHZ MAS RATE.	
	ARACTERISTIC PEAK OF THE NEW 2:1 FORM IS HIGHLIGHTED IN RED BOX16:	7
	6-23 - STEPWISE DEPICTION OF 1:1 AND 1:3 COCRYSTAL FORMATION VIA LAG	
	<b>6-24</b> $^{1}$ H MAS NMR SPECTRA OF 3HBA <sub>1</sub> :NA <sub>1</sub> WITH EXCESS NA AND 10 $\mu$ L ETOH 3HBA <sub>1</sub> :NA <sub>1</sub> AT	J
	FERENT TIME POINTS DURING IN-SITU SOLID-STATE NMR EXPERIMENT. RECORDED AT 298 K,	
	I A 400 MHZ SPECTROMETER AT 12 KHZ MAS RATE17	1
	<b>6-25</b> $^{1}$ H- $^{13}$ C CP/MAS NMR SPECTRA OF 3HBA $_{1}$ :NA $_{1}$ WITH EXCESS NA AND <b>10</b> $\mu$ L ETOH, AFTER 1,	
	AND 70 HOURS OF IN-SITU EXPERIMENT. RECORDED AT 298 K, ON A 400 MHZ SPECTROMETER	
	12 KHZ SPINNING SPEED	I
	6-26 <sup>1</sup> H NMR SPECTRA COMPARING 0.5M NA IN ETOH SOLUTION AS SOLVENT VS PURE ETOH	
Al	TER 2 MINS OF ACQUISITION. RECORDED ON 400 MHZ SPECTROMETER AT 12 KHZ MAS RATE.	_
		_
	6-27. A) - 1H NMR SPECTRA WITH SATURATED 0.5 M NA SOLUTION AS SOLVENT AFTER	
	HOURS UNDER MAS CONDITIONS. <b>B)</b> – <sup>1</sup> H SPECTRA COMPARING PEAK POSITIONS IN THE	
	ECTRA RECORDED AFTER 24 HOURS WITH SATURATED SOLUTION COMPARED TO THE	
	ECTRUM RECORDED FOR 2 MINUTES WITH PURE ETHANOL. RECORDED AT 298 K, ON A D MHZ SPECTROMETER AT 12 KHZ MAS RATE173	2
	6-28 <sup>13</sup> C{ <sup>1</sup> H} HIGH POLAR DECOUPLING SPECTRA AFTER 20 MINUTES OF ACQUISITION IN IN-	2
	U NMR SEQUENCE. 1:3 CHARACTERISTIC PEAK STARRED174	1
		+
	6-29 - RESULTS FROM THE IN-SITU CONVERSION OF 3HBA1:NA3 IN CLASSIC NMR SEQUENCE.	,
	AND <b>C)</b> CHARACTERISTIC PEAK OF 1:3 COCRYSTAL (118PPM) AT DIFFERENT TIME POINTS. PEAK	•
	RRESPONDING TO AROMATIC CARBONS 6A AND 6B (FIGURE 9) 1:1 COCRYSTAL AT 122 PPM CREASES SIMULTANEOUSLY. <b>B)</b> FRACTION OF PHASES AS A FUNCTION OF TIME, EXTRACTED	
	•	_
	OM INTEGRALS OF CHARACTERISTIC PEAKS	
	<b>6-30 -</b> ¹H MAS NMR SPECTRA OF 3HBA₁:NA₃ COCRYSTAL WITH SATURATED 1M 3HBA SOLUTION R 9 HOURS UNDER MAS CONDITIONS178	
	<b>6-31</b> <sup>1</sup> H- <sup>13</sup> C CP/MAS NMR SPECTRA SHOWING CONVERSION OF 1:3 COCRYSTAL TO 1:1. BLACK	•
	GHLIGHTED REGIONS CONTAIN PEAKS UNIQUE TO 1:3 COCRYSTAL REDUCING IN RELATIVE	
IIN	ENSITY. RED HIGHLIGHTED REGIONS CONTAIN PEAKS CORRESPONDING TO EXCESS 3HBA.	_
	180	J
	6-32 – <sup>1</sup> H PROTON NMR SHOWING CHEMICAL SHIFTS AT AFTER 1 HOUR AT MAS CONDITIONS	4
	24 HOURS AT MAS CONDITIONS FOR 2,3-DHBA <sub>1</sub> :INA <sub>1</sub> TO 2,3-DHBA <sub>2</sub> :INA <sub>1</sub> CONVERSION 18 <sup>-</sup>	1
	6-33 <sup>13</sup> C CP/MAS SHOWING CONVERSION OF 2,3-DHBA <sub>1</sub> :INA <sub>1</sub> TO 2,3-DHBA <sub>2</sub> :INA <sub>1</sub> .	
	GHLIGHTED REGIONS CONTAIN PEAKS UNIQUE TO 1:1 COCRYSTAL REDUCING IN INTENSITY,	
	D PEAKS UNIQUE TO 2:1 INCREASING. AT 5 HOURS, WE SEE SIMILAR INTENSITIES, SHOWING	_
I F	AT IS CLOSE TO THE MIDPOINT182	4

# List of tables

<b>TABLE 1-1</b> - GUIDANCE ON PROPERTIES OF WEAK, NORMAL AND STRONG HBS AS CLASS	SIFIED BY
JEFFREY. 101 ADAPTED FROM 102	28
TABLE 4-1. COMPETITION FOR HB DONORS BETWEEN SYNTHONS, WHERE 100% MEANS	THAT WHEN
THIS HB D/A PAIR IS PRESENT IT WILL ALWAYS FORM, 0% MEANS WHEN THIS HB D/A	A IS PRESENT,
IT WILL NEVER FORM.	62
TABLE 4-2. ACCURACY <sub>ALL</sub> VS ACCURACY <sub>NUM</sub> OF EACH MODEL BASED ON THEIR CONFUSI	
, OVERALL ACCURACY, AND COHENS KAPPA	
TABLE 5-1 COCRYSTAL SCREENING RESULTS SHOWING PRODUCTS FORMED FROM LAG	
TABLE 5-2 <sup>1</sup> H TITRATION REGIME FOR 3-HBA, 2-HBA, NA AND INA	
TABLE 5-3 - 3-HBA1:INA1 (LUNMEM) COCRYSTAL BOND LENGTHS	
TABLE 5-4 - CHEMICAL SHIFTS (PPM) OF KEY PROTONS AT DIFFERENT TEMPERATURES	
TABLE 6-1 LAG SCREENING EXPERIMENTS CONDUCTED IN THIS STUDY - * STAR DENOTE	
COCRYSTALS REPORTED IN CSD	129
TABLE 6-2 3-HBA1: NA1 FREQUENCIES, SOLVENT VOLUMES AND TIMEPOINTS FOR TIME RE	SOLVED LAG.
TABLE 6-3 3-HBA1:NA2 FREQUENCIES, SOLVENT VOLUMES AND TIMEPOINTS FOR TIME RE	SOLVED LAG.
	150
TABLE 6-4 2-HBA1:INA2 FREQUENCIES, SOLVENT VOLUMES AND TIMEPOINTS FOR TIME R	ESOLVED
LAG	151
TABLE 6-5 2,3-DHBA2:INA1 FREQUENCIES, SOLVENT VOLUMES AND TIMEPOINTS FOR TIM	
LAG. THE SAME NEW SOLID FORM IS PRODUCED DESPITE VARIED CONDITIONS	159
TABLE 6-6 NMR EXPERIMENTAL CONDITIONS FOR 2-HBA1: INA3 IN-SITU MEASUREMENTS.	. <sup>1</sup> H MAS (D1 =
$5 \text{ S}$ , NS = 8), $^{13}\text{C}\{^1\text{H}\}$ HIGH-POWER DIPOLAR DECOUPLING (D1 = 10 S, 128 TRANSIEN	ITS WERE
ACCUMULATED), AND 1H-13C CP/MAS (D1 = 120 S, NS=64). EACH CYCLE DURATION	WAS 2HOURS
42MINUTES	169
TABLE 6-7. 3-HBA <sub>1</sub> :NA <sub>3</sub> IN-SITU NMR EXPERIMENTAL CONDITIONS. <sup>1</sup> H MAS (D1 = 5 S, NS =	= 16) <sup>1</sup> H{ <sup>13</sup> C}
HIGH POLAR DECOUPLING (D1= $5 S$ , NS= $256$ ), AND $^1H$ - $^{13}C$ CP/MAS (D1 = $60 S$ , NS= $^2$	10). EACH
CYCLE DURATION IS 62 MIN	179
TABLE 6-8 2,3-DHBA <sub>2</sub> :INA <sub>1</sub> IN-SITU NMR EXPERIMENTAL CONDITIONS. <sup>1</sup> H MAS (D1 = 5 S, N	IS = 32) , AND
<sup>1</sup> H- <sup>13</sup> C CP/MAS (D1 = 60 S, NS=40). EACH CYCLE DURATION IS 42 MIN	181

# Chapter 1 - Introduction

# 1.1 The Cambridge Structural Database

The Cambridge Structural Database (CSD)<sup>1</sup> is a repository of small-molecule organic and metal-organic structures, containing over 1 million chemical structures.<sup>2, 3</sup> However, only a small fraction of this number are approved drug molecules.<sup>4</sup> Many potential drug molecules fall by the wayside during the various processes involved in getting a candidate from discovery to approval, which is seen by the 96% overall failure rate in drug development. <sup>5</sup> There are many reasons for this, such as tighter regulations by the authorising bodies <sup>6</sup> and increasing cost of clinical development, but also the fact that there is not enough human resource to screen and trial all the possible candidates. In an attempt to combat this, there has been a switch from the traditional 'trial and error' to a more rationalised and strategic knowledge-based approach. <sup>7</sup>

Successful drug molecules tend to be formulated as oral solid dosage forms including tablets, capsules, and powders. Patients prefer this route of administration because it is convenient, non-invasive, and easy to transport. Pharmaceutical industries and health regulators prefer this formulation because of the cost efficiency of their production. Despite these advantages, the main downside of the active pharmaceutical ingredients (APIs) is often their poor physiochemical properties e.g. bioavailability, solubility, shelf life and taste-masking to name a few. <sup>8</sup>

Considering the complexity of developing a new molecular entity [NME], improving the characteristics of existing molecules may be a viable option. Whilst this had led to many 'me too' drugs, it has also led to many novel methods of combining APIs and coformers to improve characteristics without changing their covalent chemistry.

# 1.2 Multi-component pharmaceutical forms

Solid state APIs are categorised into two systems: amorphous and crystalline.<sup>9</sup> Amorphous solids have no 'long range order' to their organisation.<sup>10</sup> Whilst this can be advantageous and can produce some desirable properties, for example, faster dissolution rate,<sup>11</sup> this also usually results in variable chemical stability and physical properties of these solids.<sup>12</sup> Meanwhile crystalline forms,<sup>13</sup> unlike amorphous solids, have ordered structures made of consistent repeating units. The same chemical compound can exist in different crystalline forms, known as polymorphs.<sup>14</sup> Crystalline forms are more thermodynamically stable than amorphous solids and hence more than 80% of marketed drugs are formulated in the most stable polymorphic crystalline form.<sup>15</sup> Crystalline forms can be classed as single component, as in the case of polymorphs, or multi-component. Multicomponent compounds consist of at least two different molecules in their unit cell. Examples include solvates, salts and cocrystals.

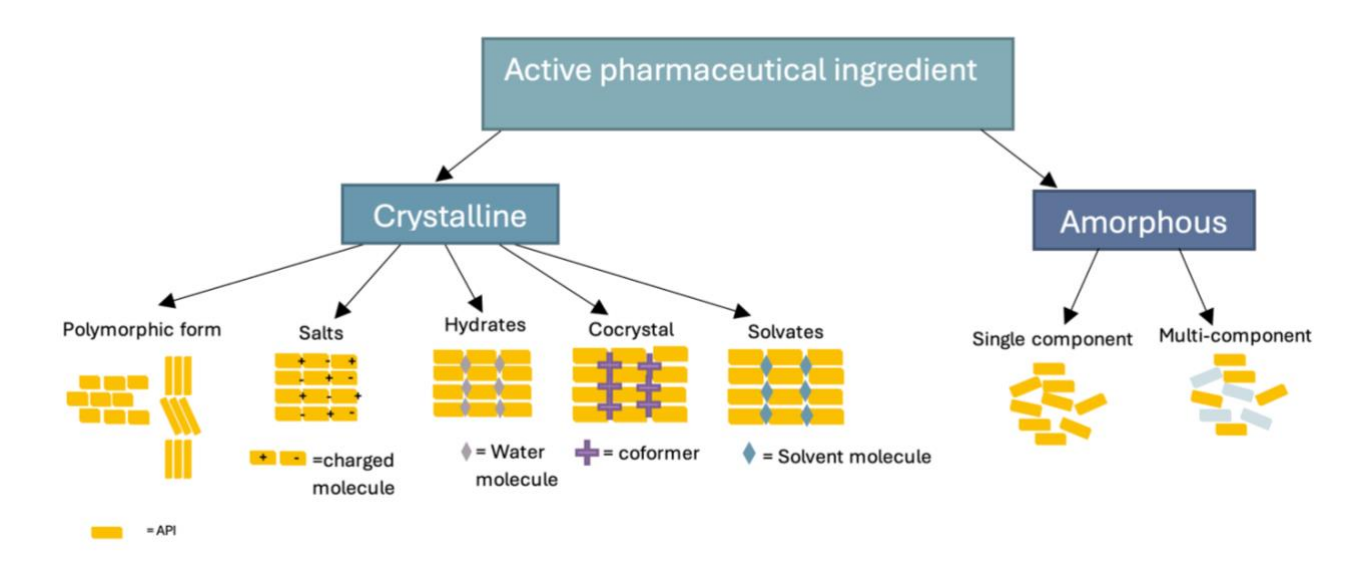


Figure 1-1 - The different solid-state forms of APIs

#### 1.2.1 Salts

The International Union of Pure and Applied Chemistry defines a salt as a "chemical compound comprising an assembly of cations and anions." 16 In the context of pharmaceuticals, a salt is a multicomponent system that consists of an ionizable active pharmaceutical ingredient (API) and a counterion, arranged in a specific stoichiometry to achieve charge balance. Pharmaceutical salts account for at least half the drugs currently on the market. This prevalence is due to several advantages, including the ease of production, the broad selection of anions and cations available for salification, and the ability to modify physicochemical properties such as solubility and dissolution rate. Enhanced solubility and dissolution rates are particularly important as they can lead to increased drug bioavailability. 17-20 The production of pharmaceutical salts is favoured for its reliability and simplicity.<sup>21</sup> By altering the counterion, it is possible to generate a variety of compounds with distinct properties, which can be tailored to meet specific therapeutic needs. The propensity of a drug to form a salt primarily depends on the presence of functional groups within its structure.<sup>22</sup> Most APIs contain either weakly acidic or weakly basic functional groups, or sometimes both. For acidic drugs, sodium is the most commonly used cation, while basic drugs typically utilize chloride ions derived from hydrochloric acid. <sup>23</sup> A classic example is naproxen, a widely used non-steroidal anti-inflammatory drug (NSAID) known for its painrelieving properties. Naproxen contains a carboxylic acid functional group, enabling it to form salts such as naproxen sodium. This transformation into a salt form results in significantly faster absorption, as evidenced by a reduced time to reach maximum plasma concentration T<sub>max</sub> compared to its free acid form. <sup>24</sup>

Figure 1-2 - Chemical structure of Naproxen sodium - popular NSAID pharmaceutical salt.

In recent years, there has been an increasing trend towards formulating APIs into salts with L- $\alpha$ -amino acids like aspartic acid, glutamic acid, arginine, and lysine. <sup>25</sup> These amino acid salts offer additional benefits in terms of solubility and absorption rates. For instance, ibuprofen, another commonly used NSAID available over the counter, is formulated as ibuprofen lysine. This formulation has demonstrated more rapid absorption compared to its traditional form. <sup>26</sup>

#### 1.2.2 Hydrates and solvates

A solvate is a multicomponent crystalline solid, containing both an API/excipient and a solvent molecule in its unit cell. <sup>27</sup> When this solvent is water, the multicomponent crystal is called a hydrate <sup>28</sup>. Depending on the number of water molecules in the unit cell, these structures are categorised as monohydrate, dihydrate etc. Solvates and hydrates are a frequently observed phenomenon <sup>29</sup> with roughly one-third of all organic molecules possessing the ability to form hydrates.<sup>30</sup> What makes these so common? Firstly, the water molecule is one of the most abundant molecules on earth,<sup>31</sup> and the size and flexibility of a water molecule makes it easy for most smaller APIs and excipients to form hydrates and solvates willingly.<sup>28</sup> Next, the ability of water to act as a hydrogen bond donor and acceptor, makes it suitable for intermolecular bonding with its 'host' molecules and presence of its two positively charged and two negatively charged regions make is distinctive, compared to other organic solvents. A study of organic solvents in the CSD showed that water [20,850] is the most common solvate in the repository, followed by methanol [5007] and dichloromethane [4349].<sup>32</sup>

Solvates demonstrate distinct physiochemical differences to their respective unsolvated counterparts, including chemical stability, solubility, mechanical properties, and melting point.<sup>33</sup> However, solvates are hardly viable pharmaceuticals since traces of organic solvent could potentially be harmful. Interestingly, hydrates generally exhibit increased stability compared to their respective anhydrites, yet they display reduced aqueous solubility and rather precipitate in water compared to its anhydrous form. It is therefore crucial to determine if an API forms hydrates; to maintain bioavailability and reduce manufacturing disturbances. <sup>34</sup>

#### 1.2.2 Cocrystals

Cocrystals have been a hot topic in crystal engineering for many years. In 1844, Friedrich Wohler claimed he discovered quinhydrone combining quinone, and colourless hydroquinone resulting in green crystalline product. After some chemical analysis, he concluded that this product was 1:1 stoichiometry of 'green hydroquinone'. <sup>35, 36</sup> This caused some dispute in the crystallography community about the chemical composition of quinhydrone until Matsuda and colleagues irrefutably verified its structure using single crystal XRD. <sup>37</sup> There are records of hundreds of what we now know as cocrystals, however we have the problem of numerous names used to describe the same thing: co-molecular complex, multi-component crystals <sup>38</sup> and co-crystal. <sup>39</sup> In the past three decades, there has been revolutionary work towards the understanding hydrogen bonding and cocrystals, owing to pioneers including Margaret C Etter <sup>40-42</sup> and Gautam R Desiraju on crystal engineering of cocrystals. <sup>43, 44</sup>

The United States Food and Drug Administration (FDA) defined cocrystals in a draft document as "dissociable API-excipient molecular complexes wherein both API and excipients are present in the same crystal lattice". <sup>45</sup> However, this definition caused some unrest amongst academics and industry experts, as it is not concise and does not differentiate cocrystals from other multicomponent solid forms. The 2018 updated FDA definition is "crystalline materials composed of two or more different molecules, typically API and cocrystal formers (coformers), in the same crystal lattice. <sup>46</sup> The European Medicines Association conversely adopted a definition similar to one proposed by a group of 46 scientists: "cocrystals are solids that are crystalline single-phase materials composed of two or more different molecular and/or ionic compounds generally in a stoichiometric ratio, which are neither solvates nor simple salts". <sup>9,47</sup>

Pharmaceutical cocrystals are a sub-division of cocrystals. They contain the most favourable polymorph of an active pharmaceutical ingredient (API) and at least one food or drug grade generally regarded as safe, (GRAS) coformer, bonded non-covalently in a fixed stoichiometric ratio in the unit cell of a crystal lattice. Pharmaceutical cocrystals offer a great way to adjust the physiochemical properties of drug molecules depicted in Figure 1-3. Numerous studies have been successfully conducted of authorised medicines to determine if cocrystallisation can improve their less desirable properties e.g. Lamotrigine - compressibility, <sup>48</sup>

hydrochlorothiazide – permeability,<sup>49</sup> danazol-vanillin - 10-fold higher bioavailability compared to danazol.

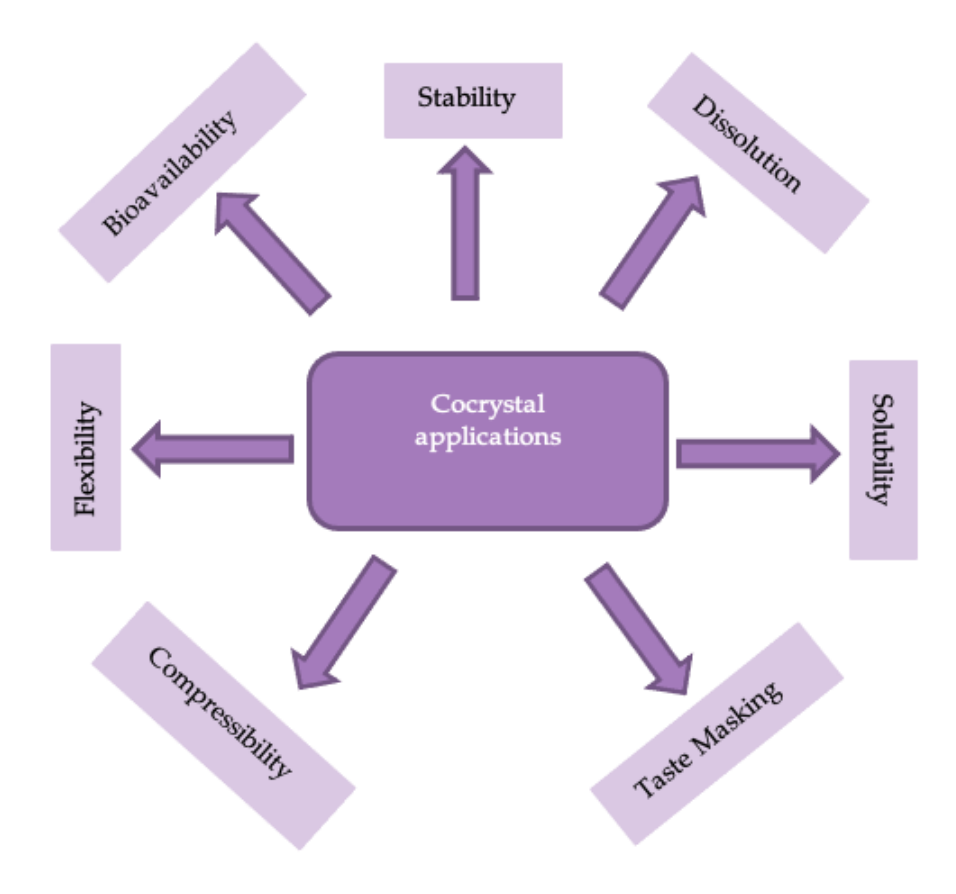


Figure 1-3 - Common applications of cocrystals in materials and pharmaceuticals industries.

## 1.3 Cocrystal screening techniques

Cocrystals can be synthesized using either solid-state or solution-state methods, each offering distinct advantages and limitations. Solid-state techniques for cocrystal screening are particularly advantageous because they produce cocrystals with little to no solvent involvement. Solid state techniques typically rely on mechanochemical force, whereas solution cocrystal screening relies on supersaturation.<sup>50</sup> Below are discussed a few common screening techniques.

#### 1.3.1 Solid state methods

#### **Neat Grinding**

Neat grinding, also known as dry grinding, is a widely used mechanochemical method for the synthesis of pharmaceutical cocrystals. It involves mechanically grinding an active pharmaceutical ingredient (API) and a coformer together without the use of solvents. This process relies on mechanical energy to induce molecular interactions, which are necessary for cocrystallisation. While simple and environmentally friendly, dry grinding requires careful optimization of parameters such as grinding time, force, and equipment to achieve efficient and reproducible cocrystal formation. The use of ball mills surmount the issues of reproducibility and scalability. Sa

#### **Liquid Assisted Grinding**

Liquid-Assisted Grinding (LAG), sometimes referred to as solvent drop grinding, is a mechanochemical technique that enhances the efficiency of dry grinding by incorporating a small amount of solvent into the grinding process. LAG has proven to be more effective than neat grinding, 55 with a greater propensity for polymorph discovery. 56-58 This method leverages the mechanical forces of grinding, while the added solvent is thought to act as a lubricant or a catalyst, facilitating molecular mobility and interaction between the active pharmaceutical ingredient (API) and the coformer. 50 The presence of a solvent can also lower the energy barrier for nucleation, leading to faster cocrystal formation compared to neat grinding. 56, 59

#### Hot melt extrusion

Hot melt extrusion (HME) is a popular technique, which has long been used in the food industry, <sup>60</sup> before being used as a cocrystallisation technique. Extrusion refers to a method of squeezing a material, in our case cocrystal coformers, under high pressure and temperature through a cavity. This process melts the coformers, allowing them to mix at a molecular level. The cocrystal forms in the melt and is fed through the die. <sup>61</sup> Upon cooling, the mixture solidifies into a homogenous product, often in the form of an amorphous solid dispersion or a crystalline structure, depending on the formulation and processing conditions. This method is advantageous due to its fast operating time and reduced waste<sup>50</sup>. It is also known to produce high purity cocrystals, however they are only usually the same polymorph. The absence of solvents makes it environmentally friendly, and its high throughput nature make it a popular cocrystal screening technique. <sup>62, 63</sup>

## 1.3.2 Solution cocrystallisation

Solution cocrystallisation leverages the principles of single-component crystallization, adapting them to accommodate multicomponent systems involving cocrystal coformers. The choice of solvent is critical and depends on the solubility of coformers. As mentioned above, the process is driven by supersaturation, however in a binary cocrystal system, the concentrations of both components must be considered. Solution cocrystallisation offers distinct advantages over solid-state methods, such as precise control over the purity, size distribution, and morphology of the resulting cocrystals.<sup>64</sup> The main techniques are cooling cocrystallisation and solvent evaporation. In the cooling cocrystallisation approach, both coformers are dissolved in a solvent at raised temperatures, followed by a controlled cooling. As the solution is gradually cooled, the solubility of the components decreases, leading to supersaturation, which induces nucleation and crystal growth.<sup>65</sup> Solvent evaporation method involves dissolving both coformers in a suitable solvent, which is then evaporated to achieve supersaturation. This supersaturation facilitates nucleation and growth of cocrystals. Solvent evaporation is particularly effective for producing single crystals that are suitable for structural analysis due to its ability to yield well-defined crystal structures.<sup>66,67</sup>

#### 1.3.3 Computational screening

The use of computational tools has revolutionized cocrystal screening, enabling the prediction of suitable cocrystal coformers before experimental validation. These techniques utilise advanced modelling and simulation methods to predict molecular interactions, stability, and the likelihood of cocrystal formation. The main advantages of computational screening are the time efficiency and resource conservation they offer. These methods also increase the ability of researchers to explore the chemical space.<sup>68</sup>

#### Crystal structure prediction (CSP)

Crystal structure prediction is one of the most prevalent computational approaches for cocrystal screening. CSP models simulate potential crystal structures based on, lattice energies, intermolecular interactions and molecular properties. By predicting the probability of lattice energies combining, based on size and inter/intramolecular forces of attraction we are able to theoretically predict cocrystal formation.<sup>69, 70</sup> CSP was recently used to rank potential coformers for antiviral drug candidate. Maleic acid was ranked highest, and this was confirmed experimentally.<sup>71</sup>

#### Molecular complementarity (MC) analysis

Molecular complementarity involves the use of polarity and shape descriptors to predict possible cocrystal coformers. CSD analysis was carried out on organic crystal structures and 131 molecular descriptors were calculated for each molecule using a range of programs. The descriptor 'fractional polar volumes', the fraction of nitrogen and oxygen atoms, indicated the highest relevance in cocrystal formation, suggesting that if coformers have similar polarity, they are more likely to form. <sup>72 73</sup>

#### Hydrogen bond propensity (HBP)

This method was first introduced by Etter in 1991, by analysing the patterns functional groups exhibit in crystal structures in the CSD.<sup>42</sup> There is now a tool available within Mercury software that can predict if a cocrystal would form on not, based on the functional groups and the occurrence of intermolecular interactions between those functional groups in the CSD. This method quantifies and ranks the likelihood of coformers forming hydrogen bonds, based on their functional groups.<sup>74, 75</sup> If the most likely pairwise hydrogen bonds are present, then the probability of forming a hydrogen bond is high. This method is also useful for differentiating

between coformers more likely to interact with each other, rather than an API. Studies have demonstrated that combining hydrogen-bond propensity (HBP) with other computational tools such as molecular complementarity significantly improves the accuracy of cocrystal predictions. <sup>76</sup> For example, a computational screening study based on MC and HBP identified 17 potential coformers from a library of GRAS compounds. Experimental validation lead to the discovery of a new cocrystal form with improved dissolution rates compared to the pure drug.<sup>77</sup> Another virtual screening study employed HBP and MC, combined with CSP and Molecular electrostatic potential mapping to explore cocrystallisation between dapsone and bipyridine derivatives 2,2' and 4,4'bipyridine. The HBP screen analysed 116 potential coformers for DDS and ranked them based on their likelihood to form cocrystals. From this set, the top 20 coformers with the highest HBP scores were further analysed using molecular complementarity. Interestingly, the MC analysis predicted that 4,4'-bipyridine was a suitable coformer for DDS but suggested no cocrystallisation for DDS with 2,2'-bipyridine due to differences in molecular geometry and polarity. These predictions were validated experimentally through mechanochemical grinding, slurry experiments, and contact preparation methods.<sup>78</sup>

#### Machine learning (ML)

Machine learning methods fall into two categories: supervised and unsupervised. In this thesis, we use supervised machine learning. Supervised ML has labelled input variables [x] and output variables [y]. An algorithm is used to learn the mapping function from x to y.

$$Y = f[x]$$
 Equation 1-1

In supervised learning, the goal is to train the algorithm to understand the patterns in the data so that when the input is new, unseen data, it will correctly predict the outcome based on what the algorithm has learnt. However, when the ML model is fitted too tightly [defined as overfitting], it learns the fluctuations and noise in the training data and is unable to predict from unseen inputs accurately, rendering the model inaccurate. This is a common pitfall in ML and impacts the model's ability to generalise. Conversely, if a model is underfitted, the

model can neither model training data nor new data, rendering the model useless. A good, supervised model ignores the noise and spurious correlations in the data.

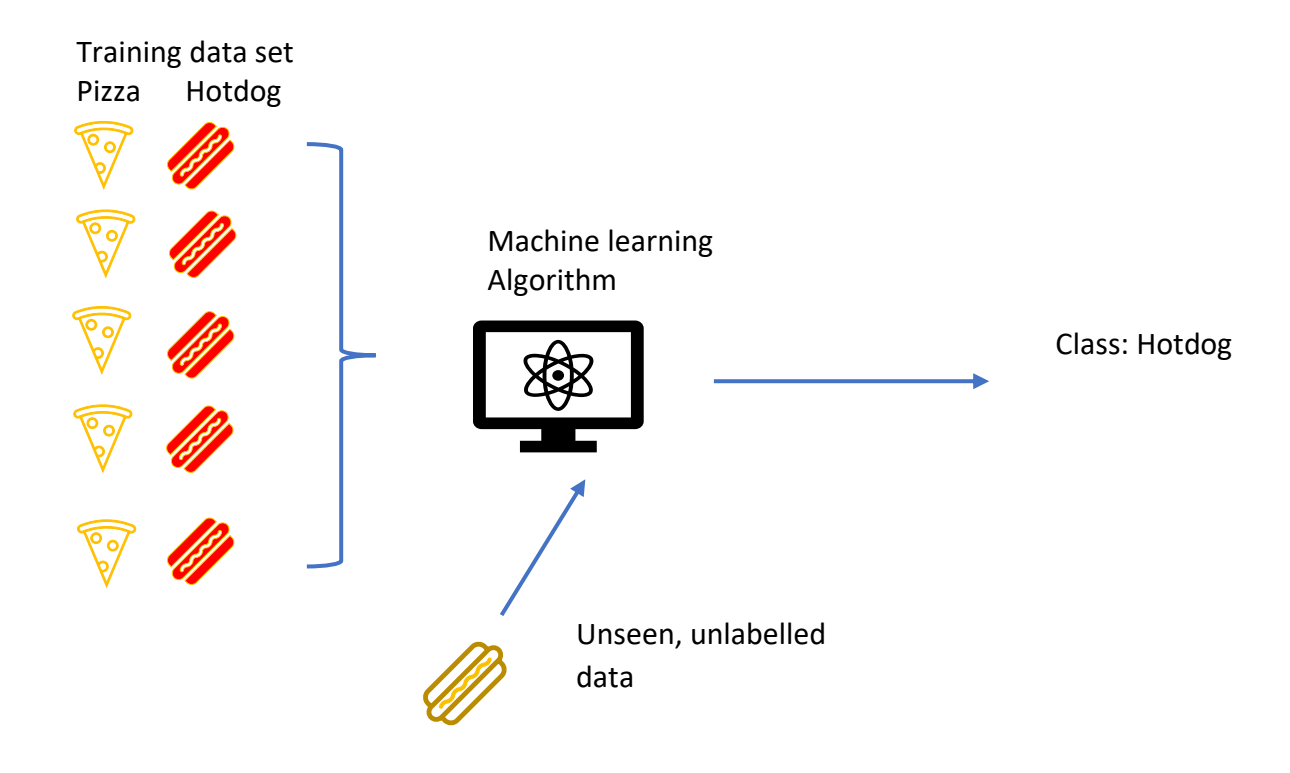


Figure 1-4 Schematic showing principle behind supervised machine learning

Machine learning has recently been employed as a cocrystal screening tool due to the availability of large datasets of known cocrystals, gathered from experimental data. Sophisticated algorithms utilize a range of features, including molecular descriptors, hydrogen bond propensity (HBP), and lattice energies, to train predictive models that can accelerate the discovery of novel cocrystal forms.

The application of ML in cocrystal screening has seen the implementation of various techniques, each with its own strengths. Artificial neural networks (ANN) are the most advanced ML algorithms due to their versatility and extreme level of model complexity. ANN's were inspired by the operations of the neurons in the mammalian brain in 1958 by Frank Rosenblatt. Artificial neurons are organised into multiple interconnected layers, comprising of input, output, and hidden layers. The connections between neurons are assigned weights; the value which represents the knowledge of that network and bias is

applied. The data are then transmitted to the subsequent layers until it reaches an output layer. At the output layer, the probability of which class the input data belongs to is derived. If the prediction is wrong, these data can be back propagated to readjust weights. ANN have shown particularly promising results in predicting cocrystal coformer complementarity, <sup>81,82</sup> as well as physiochemical properties such as lattice energy, crystal density and melting point. <sup>83,84</sup>

Other algorithms such as support vector machines (SVM), which works by finding an optimal hyperplane that separates data points into different classes, has also been shown to effectively rank cocrystal coformer complementarity. <sup>85</sup> Random forests (RF) are built from multiple decision trees during training. Each tree is trained on a random subset of the data and features, reducing overfitting and improving generalization. <sup>86</sup> The final prediction is made by averaging (regression) or majority voting (classification) across all trees. <sup>87</sup> This technique has also proven useful in cocrystal prediction. <sup>88</sup>

The choice of molecular representation and feature selection plays a crucial role in the performance of these ML models. Researchers have employed 1D and 2D descriptors, Extended-connectivity fingerprints (ECFP), and simplified molecular-input line-entry system (SMILES) to extract relevant information from drug molecules and their potential coformers. Feature selection algorithms have been utilized to optimize the number of descriptors, balancing computational efficiency with model performance. Despite its many advantages, the main pitfall of machine learning is that it cannot currently be relied on as an independent method of screening. We discuss the details of machine learning algorithms used in this study in chapter 4.

## 1.4 Intermolecular interactions in cocrystals

#### 1.4.1 Hydrogen bonding

The hydrogen bonding is as an intermediate range attractive interaction between an electron deficient hydrogen and an atom or a group of atoms in the same or a different molecule. Hydrogen bonds (HBs) are usually denoted by X-H...Y-Z, (donor...acceptor). Here, X is an electronegative atom or group, that is more electron dense than hydrogen, for example oxygen, nitrogen, fluorine, double and triple bonds. Y, the hydrogen bond acceptor, is an electron dense region. This usually means it has a lone pair of electrons, and the three dots represent the hydrogen bond. <sup>91, 92</sup> Margaret Etter studied hydrogen bonding in co-crystals and produced a set of rules which forms the basis of a lot of work done today.

#### Etter's rules state that;

- 1. All good proton donors and acceptors are used in hydrogen bonding.
- 2. Six-membered-ring intramolecular hydrogen bonds form in preference to intermolecular hydrogen bonds.
- 3. The best proton donors and acceptors remaining after intramolecular hydrogen bond formation form intermolecular hydrogen bonds.

Etter and co-workers also introduced graph set notation for describing and distinguishing hydrogen bonding motifs, based on the number of donors and acceptors. It is portrayed as  $G^{a}_{d}(n)$ , where G is one of the observed patterns; Self (S) for intramolecular hydrogen bonds, Chain (C) for infinite chains, Ring (R) for intermolecular rings, and Discrete (D) for finite structures as seen in Figure 1-5. Number of atoms in motif is (n) and the number of acceptors and donors is a and d. The variables a and d are not included when a = d = 1.  $^{40, 93, 94}$ 

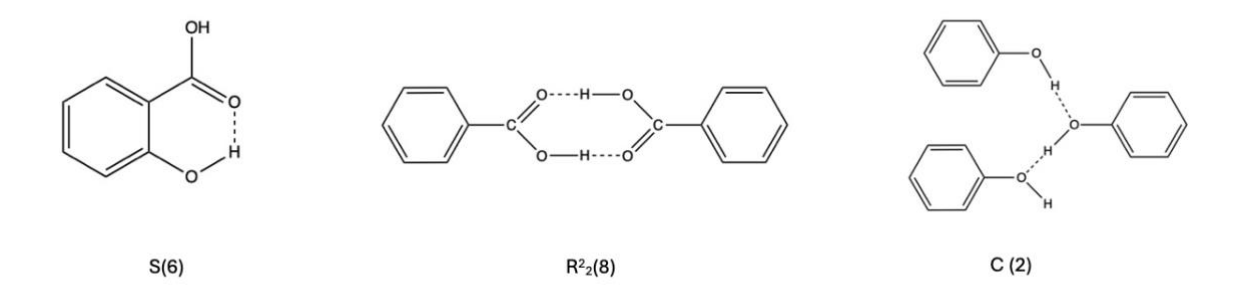


Figure 1-5 – Examples of common graph set notations.

Hydrogen bonds are important non-covalent interactions, and a single HB can greatly change the characteristics of a whole molecule <sup>95</sup>. Hydrogen bond strength can be estimated by their Gibbs free energy (DG) and substantial work to measure HB donor and acceptor strengths has been undertaken. <sup>96-99</sup> Raevesky created a package; the HYBOT (Hydrogen bond Thermodynamics) program for estimation of HB strength, which includes one for the largest databases of its kind till date. It contains data on over 11000 hydrogen bonds, from over 600 donors and 2000 acceptors, and information on their free energy and enthalpy. This package has also been used for prediction, and harnesses huge potential for the application of machine learning. <sup>100</sup>

In practical terms, hydrogen bonds can be classified into 3 categories according to their properties. In Jeffrey's book, 'an introduction to hydrogen bonding', <sup>101</sup> he groups hydrogen bonds by strength; weak, moderate (normal), and strong, Table 1.1 shows some properties of the three categories. Normal HBs can be likened to those between water molecules, which typically have an energy range of 4-15 kcal/mol. HBs with energy greater than 15kcal/mol are 'strong', and less than 4 are 'weak'. However, it must be noted that there are no 'hard' boundaries, and this classification is merely a guideline. <sup>102</sup> It is through the increased understanding of hydrogen bonds that the field of crystal engineering has advanced, and we now have the concept of supramolecular synthons.

**Table 1-1** - Guidance on properties of weak, normal and strong HBs as classified by Jeffrey.

101 Adapted from 102

	Weak	Moderate (Normal)	Strong
Bond length HA (Å)	>2.2	1.5-2.2	1.2-1.5
Bond angles (°)	>90	>130	170-180
Bond energy (kcal/mol)	<4	4-15	15-40
Directionality	Weak	Moderate	Strong
Type of interaction	Electrostatic	Mostly electrostatic	Strongly covalent

#### 1.4.2 The supramolecular synthon

Gautam R. Desiraju defined crystal engineering as "the understanding of intermolecular interactions in the context of crystal packing and in the utilization of such understanding in the design of new solids with desired physical and chemical properties". <sup>43</sup> The purpose of crystal engineering was to create dependable links between a molecule and the supramolecules it is a member of based on its intermolecular interactions. This field has now progressed greatly, with heavy interest in the synthesis of new compounds with supramolecular synthons as the building blocks. To achieve this, a deeper understanding of the chemistry of the functional groups present in a molecule is essential. <sup>44</sup>

Supramolecular synthons are described as the smallest structural units containing the characteristic information through which molecules assemble into supramolecules. However, the interactions that determine crystal structures are generally weak, and as a result, closely related structures often have differing crystal structures. Therefore, supramolecular synthons must be robust in order to be generalised. The hierarchy of supramolecular synthons has been addressed widely, <sup>27, 44, 83, 103-115</sup> and there are some functional groups, including those in this report such as carboxylic acids, phenols, amides, and aromatic nitrogen atoms that are commonly observed as reliable supramolecular heterosynthons; groups on different but

compatible molecules participating in non-covalent bonding<sup>116</sup> and supramolecular homosynthons, such as carboxylic acid dimers or amide dimers.

## 1.5 In-situ NMR for observing crystallisation

Nuclear Magnetic Resonance (NMR) spectroscopy has long been a cornerstone technique in the analysis of molecular structure and dynamics. Its unique ability to observe specific chemical environments, makes it perfect for probing the intricacies in molecular systems at the atomic level. The versatility of NMR stems from its capacity to detect subtle changes in the electronic environment of atomic nuclei, which are influenced by their chemical surroundings. This non-invasive sensitivity allows research to elucidate complex molecular structures, study reaction mechanisms, and investigate intermolecular interactions. 117, 119 NMR has also been used to further understanding on reaction kinetics, with chemical shift (.ppm) being measured as a function of time. 120-122

Solid-state NMR emerged as a powerful tool for real-time monitoring of chemical processes, particularly in the context of crystallization studies. Early efforts focused on developing techniques that could selectively detect the solid phase in heterogeneous solid-liquid systems, effectively rendering the liquid phase "invisible" to the measurement. This selectivity allowed Hughes *et al* to observe and identify the first solid particles produced during crystallization and monitor the evolution of different solid phases, such as polymorphs, as a function of time. <sup>123</sup>

In recent years, a novel application of NMR, known as CLASSIC NMR (Combined Liquid- And Solid-State In-situ Crystallization NMR), which alternates between two different pulse sequences to record both solid-state and liquid-state NMR spectra as a function of time <sup>119,</sup> <sup>124</sup> has emerged as a powerful tool for studying crystallization processes in unprecedented detail. The ability to measure solid and solution state spectra simultaneously, provides valuable information on the interplay of both phases during pre-nucleation, nucleation and crystal growth in one NMR rotor. <sup>125</sup> <sup>119, 124-128</sup>

Another key strength of in situ NMR is its ability to reveal the existence of transitionary phases during crystallisation. By capturing the evolution of both solid and liquid phases over time, we can now identify and characterize intermediate states. This complements data gained from other characterisation techniques such as X-ray diffraction and Raman spectroscopy, providing a wholistic report of the crystallisation process.

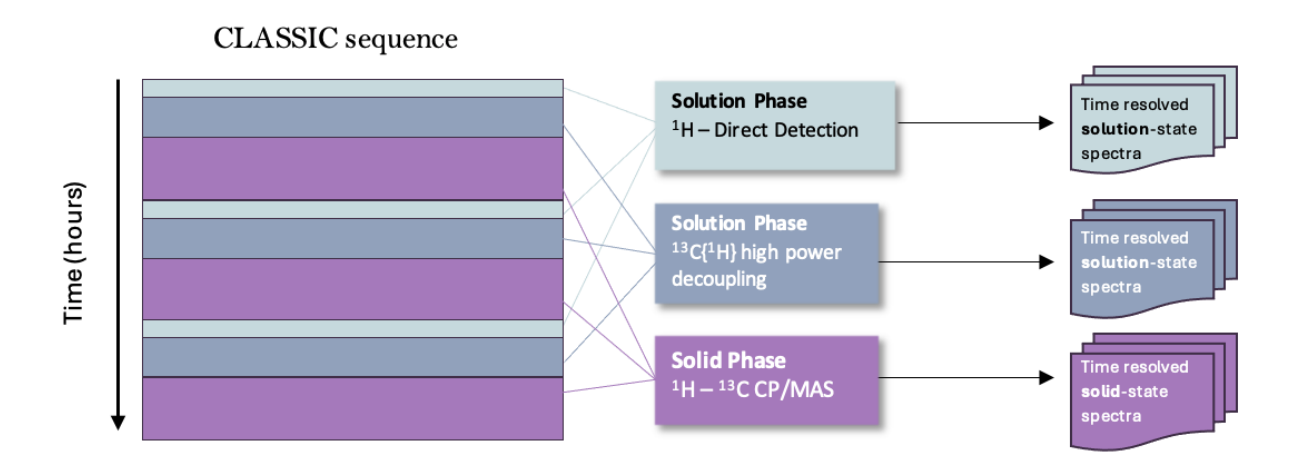


**Figure 1-6** - Schematic representation of CLASSIC NMR sequence used in this study. One acquisition of <sup>1</sup>H direct detection, <sup>13</sup>C {<sup>1</sup>H} high power decoupling and <sup>13</sup>C CP/MAS solid state makes one CLASSIC cycle.

## 1.6 Project overview and aims

This study significantly advances the understanding of intermolecular interactions in pharmaceutical systems, with particular emphasis on hydrogen bonding in multicomponent crystals. We employ a multifaceted approach that integrates statistical analysis, machine learning, experimental screening, and advanced characterization methods to systematically explore cocrystal formation and behaviour.

Our research begins with a comprehensive analysis of hydrogen bonding patterns in cocrystals using the Cambridge Structural Database (CSD). This establishes a hierarchy of supramolecular synthons in binary crystals, providing a foundation for subsequent investigations. Building on these insights, we evaluate multiple machine learning algorithms for their ability to predict cocrystal formation between potential coformers.

A significant innovation in our approach is the deliberate inclusion of data from "failed" cocrystal screening attempts. We recognize that these outcomes-whether resulting in unintended products or no change to pure coformers-provide valuable negative data that is essential for refining predictive models. By documenting both successful and unsuccessful results, this thesis creates a more complete resource for future researchers.

The experimental phase encompasses extensive cocrystal screening with selected active pharmaceutical ingredients (APIs) and coformers chosen for their hydrogen bonding potential. Our methodology systematically investigates various stoichiometric ratios between coformers, acknowledging this critical factor in cocrystal formation. We characterize screening outcomes using solid-state analytical techniques and complement these findings with solution-state NMR spectroscopy to examine intermolecular interactions in the liquid phase. This dual approach provides comprehensive insights into molecular behaviour across different physical states.

We further extend our investigation to explore solvent effects by testing solvent with various polarities with the same coformer pairs and stoichiometries, yielding valuable information about solvate, hydrate, and cocrystal formation under different conditions.

In the final phase, we present a transformation mechanism showing how cocrystals evolve from pure coformers through intermediate stoichiometric ratios to reach their final form. This process is observed using time-resolved powder X-ray diffraction and verified through an innovative application of combined liquid- and solid-state NMR for *in situ* crystallization studies. The comprehensive database of screening results and mechanistic insights developed through this research offers a valuable resource for crystal engineering and pharmaceutical development, advancing the field from empirical exploration toward systematic, prediction - driven design.

# Chapter 2 - Main principles of characterisation methods

# 2.1 Thermal analysis

## 2.1.1 Thermogravimetric analysis (TGA)

TGA is a powerful, yet simple thermal analysis technique used to investigate thermal stability, composition and degradation behaviour of materials. Fundamentally, TGA involves continuously monitoring the mass of a sample as it is subjected to a controlled temperature program within a specific atmosphere. This approach yields important insights into a range of physical and chemical processes, such as thermal decomposition, material degradation, sublimation, evaporation, adsorption and desorption events, as well as oxidation and reduction reactions. TGA operates by measuring the change in mass of a sample as a function of temperature or time in a controlled environment, T31 providing valuable insights into material properties.

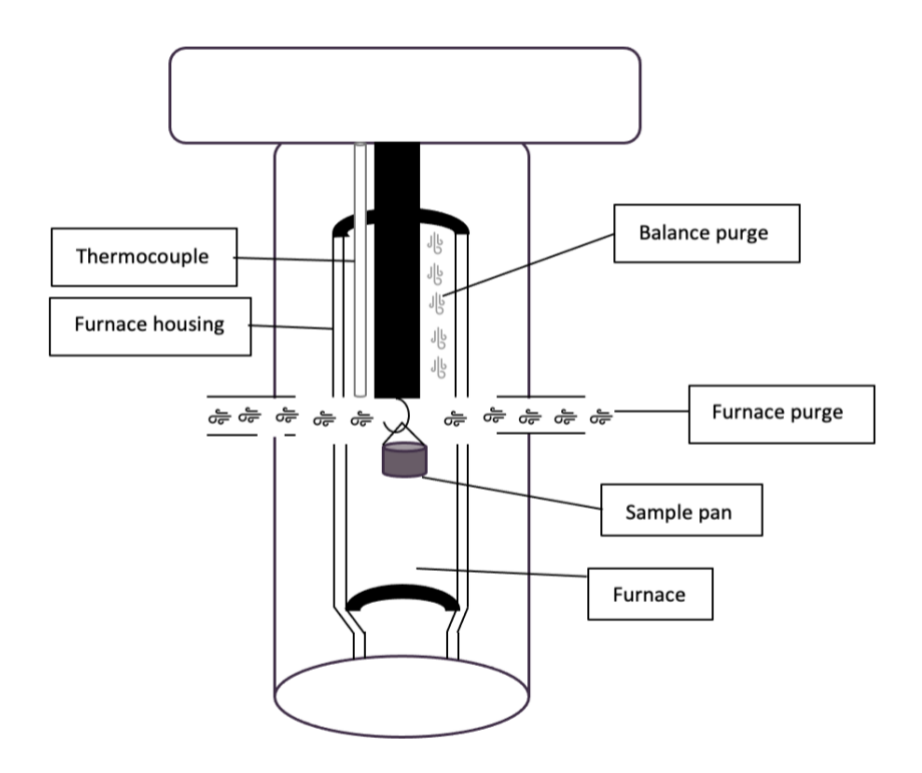


**Figure 2-1** Schematic cross section of TGA instrument sample area. Adapted from TA instruments <sup>132</sup>

A standard thermogravimetric analysis (TGA) instrument is comprised of several key components: a highly sensitive microbalance capable of registering extremely small changes in mass (often down to  $0.1~\mu g$ ), a temperature-controlled furnace that allows for precise thermal programming, and an advanced purge gas delivery system.

The sample holder, commonly referred to as a crucible or pan, is made from materials selected for their exceptional thermal stability and chemical inertness. Aluminium pans serve adequately for lower temperature analyses (below 600°C), while platinum crucibles are preferred for higher temperature investigations due to their superior thermal stability and resistance to oxidation. Sample preparation plays a pivotal role in ensuring both the accuracy <sup>133</sup>and reproducibility of TGA measurements. Reliable results can often be obtained with as little as 1 mg, <sup>134</sup> particularly when sample material is scarce. The morphology of the sample is also important; finely powdered samples with greater surface area tend to promote more consistent heating and efficient release of evolved gases, whereas larger, solid pieces may experience uneven temperature distribution and slower diffusion of decomposition products.

The furnace system constitutes another critical component, engineered to provide highly controlled, programmable temperature environments. Contemporary TGA furnaces typically operate from ambient temperature to  $1000^{\circ}$ C, with specialized systems capable of achieving temperatures up to  $1600^{\circ}$ C for high-temperature applications. Sophisticated temperature controllers maintain precise heating rates, typically between 0.1 and  $100^{\circ}$ C/min, with temperature accuracy of  $\pm 0.1^{\circ}$ C.

The data acquisition systems in modern TGA instruments capture mass, temperature, and time data at precisely defined intervals, typically collecting several data points per second. This high sampling rate enables accurate determination of rapid thermal events and facilitates sophisticated kinetic analysis. Modern, more advanced TGA instruments also combine TGA with other analytical techniques like Differential Scanning Calorimetry (DSC)<sup>135</sup>. Thermogravimetric analysis (TGA) was selected as a characterisation technique in this study due to its precise, quantitative assessment of thermal stability, composition, and decomposition behaviour. This makes it valuable for identifying critical transitions such as dehydration, degradation, or loss of volatile components in complex multicomponent formulations.

#### 2.1.2 Differential scanning calorimetry (DSC)

DSC is another powerful thermal analysis technique used in materials science to provide quantitative and qualitative data about the physiochemical changes occurring in a sample as heat is applied. Modern DSC instruments operate under two principal designs: *heat flux* and *power compensation* configurations. Heat flux is the class utilised in this study. Heat flux instruments typically consist of a furnace housing two platforms: a sample pan and a reference pan, which is usually empty. The furnace is heated at a user-defined, constant heating rate (from 0.1 to 40°C/min), with a thermoelectric disk transferring heat to the sample and reference pans. Based on the heat capacity of the sample (C<sub>p</sub>), there will be a difference between the sample and reference pan. This difference is measured by area thermocouples by the thermal equivalent Ohm's law.

$$q = \frac{\Delta T}{R}$$
 Equation 2-1

Where q is sample heat flow,  $\Delta T$  is temperature difference between sample and reference and R is resistance of thermoelectric disk. Power compensation DSC employs separate furnaces for the sample and reference, dynamically adjusting energy input to maintain thermal equilibrium. This design minimises thermal lag, enhancing resolution for rapid transitions. Both configurations achieve comparable results, though heat flux systems are preferred for pharmaceutical applications due to superior baseline stability.  $^{137}$ 

DSC measures endothermic and exothermic differences in heat flow between a sample pan and reference pan as a function of time or temperature. As the temperature changes, any physical or chemical transformations in the sample will require either the absorption (endothermic) or release (exothermic) of heat. These thermal events manifest as deviations from the baseline in the DSC thermogram, which plots heat flow against temperature or time. The area under these peaks is directly proportional to the enthalpy change associated with the thermal event, providing quantitative information about the energy involved in the process. DSC was selected as a characterisation technique due to its high sensitivity, allowing

for the detection of various thermal events such as melting, crystallization, glass transitions, and chemical reactions. 138

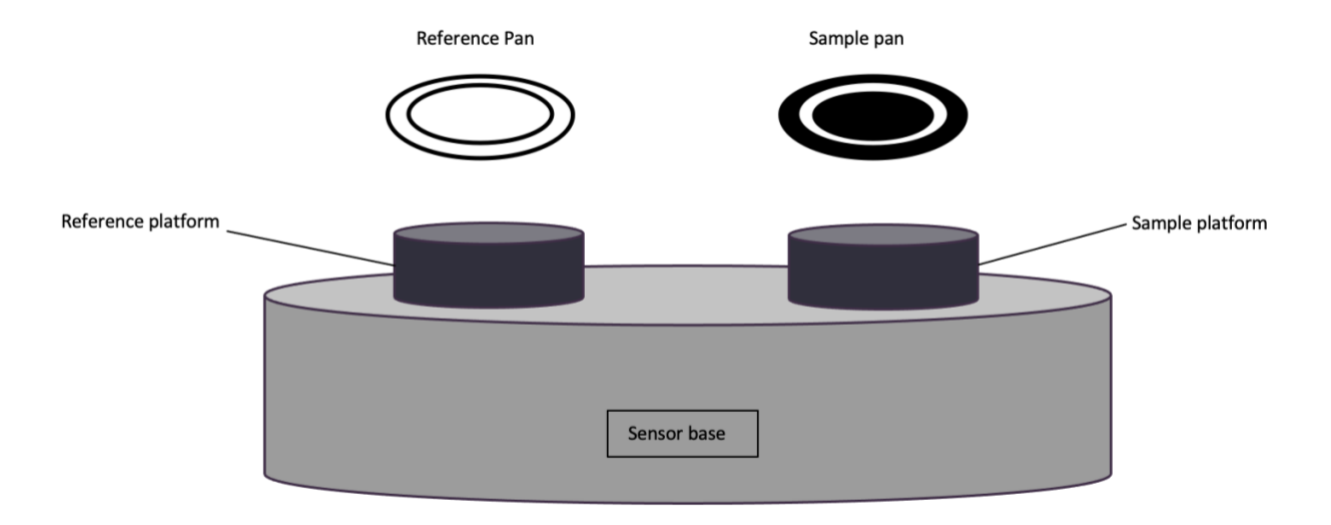


**Figure 2-2** Schematic representation of DSC oven showing sensor base, sample and reference pans and platforms.

# 2.2 Powder X-ray Diffraction (PXRD)

Powder X-ray diffraction is a versatile analytical tool for the identification of compounds based on their diffraction pattern, which is a unique fingerprint for crystalline material. X-ray diffraction relies on the occurrence of constructive interference between X-ray waves that are scattered by the electrons of the atoms in an ordered arrangement within a crystalline structure. These scattered X-rays can interfere with each other in two ways: constructively or destructively. Constructive interference occurs when the scattered waves are in phase, resulting in amplification of the signal and producing a characteristic diffraction pattern that reflects the crystal structure of the material. This phenomenon only occurs is Bragg's law conditions are satisfied.

$$n\lambda = 2d\sin\theta$$
 Equation 2-2

Where n is an integer,  $\lambda$  is the wavelength of the incident X-rays, d is the interplanar spacing of the crystal lattice, and  $\theta$  is the angle between the incident X-rays and the crystal plane.

PXRD typically employs a monochromatic X-ray source, a sample hold and a detector to measure the intensity of diffracted X-rays as a function of the scattering angle. X-rays are generated in a vacuum tube by accelerating electrons towards a metal target, often copper or molybdenum, in a sealed tube or rotating anode system. The choice of target material affects the wavelength of the X-rays produced, which is crucial for the analysis. The resulting diffraction pattern is often presented as a plot of intensity versus scattering angle (2θ), containing peaks corresponding to specific crystal planes in the sample.

PXRD, as the name suggests, has the ability to analyse powdered samples, eliminating the need for large, high-quality single crystals needed for single crystal X-ray diffraction. Sample preparation typically involves grinding the material into a fine powder and packing it into a sample holder, ensuring a random orientation of crystallites. While the ideal PXRD sample consists of randomly oriented crystallites, many materials, particularly those with anisotropic crystal morphologies, exhibit a tendency for crystallites to align preferentially along specific crystallographic directions.

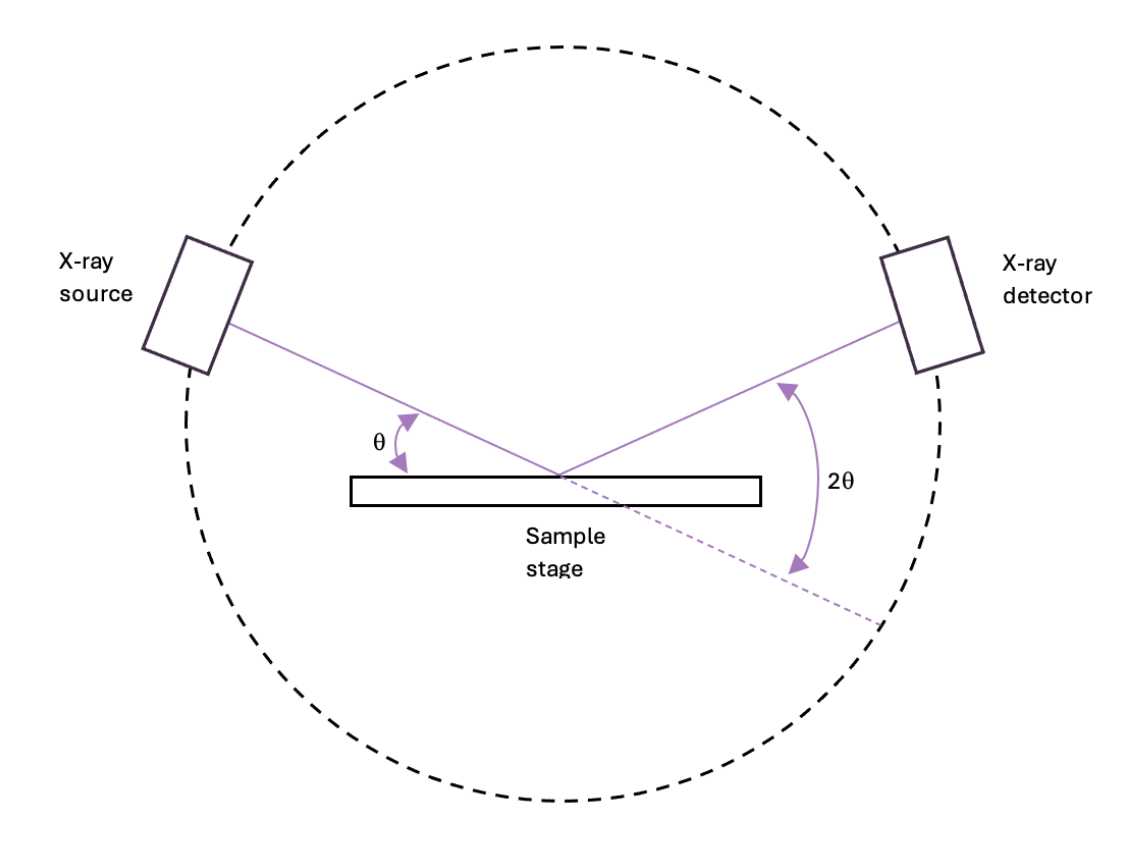


Figure 2-3 Schematic representation of X-ray diffractometer components

Powder X-ray diffraction (PXRD) is an invaluable characterisation tool for multicomponent pharmaceuticals because it enables precise identification and differentiation of crystalline phases within complex mixtures. Each component in a formulation produces a unique diffraction pattern, allowing for the detection of polymorphs, co-crystals, and impurities even at low concentrations. This makes PXRD essential for confirming the formation of new solid forms, monitoring phase purity, and ensuring the stability and quality of pharmaceutical products throughout development and manufacturing.

## 2.3 Nuclear Magnetic Resonance spectroscopy

## 2.3.1 Basic NMR principles 118, 140-144

Nuclear magnetic resonance spectroscopy is a robust characterisation tool used throughout this thesis, effective in its ability to investigate solutions, gels, semi-solids and solids. NMR spectroscopy exploits the interactions between atomic nuclei, an applied oscillating radio frequency signal and an external magnetic field.

NMR relies on the unique properties of atomic nuclei to probe molecular structure and dynamics. Atomic nuclei possess a quantum chemical property called nuclear spin (I), combined with the nucleus's charge, generates a magnetic field, resulting in a magnetic moment ( $\mu$ ). The relationship between the magnetic moment and nuclear spin is described by the equation:

$$\mu = \gamma I$$
 Equation 2-3

Where  $\gamma$  represents the nuclear gyromagnetic ratio, a constant specific to each type of nucleus. Both  $\mu$  and I are vector quantities, having both magnitude and direction.

The ability of a nucleus to generate an NMR signal depends on its spin quantum number. Nuclei with non-zero spin quantum numbers (I = 1/2, 1, 3/2, etc.) are NMR-active, while those with I = 0 do not produce detectable signals.

In an NMR experiment, the collective behaviour of these nuclear magnetic moments is observed. The net magnetization in a sample, denoted as (M), represents the sum of all individual nuclear magnetic moments. The net magnetization vector M experiences a torque from the external magnetic field ( $B_0$ ), causing it to precess around the direction of  $B_0$  at a fixed rate.

This precession occurs at the Larmor frequency  $(\omega_0)$ , which is given by:

$$\omega_0 = -\gamma B_0$$
 Equation 2-4

When a sample containing an NMR-active nuclei is placed in a strong external magnetic field  $(B_0)$ , the nuclear spins align either parallel (lower energy state) or antiparallel (higher energy state) to this field in a phenomenon called Zeeman splitting. This alignment is governed by the Boltzmann distribution, resulting in a slight excess of spins in the lower energy state. This population difference creates a net macroscopic magnetization  $(M_0)$  aligned with  $B_0$ .

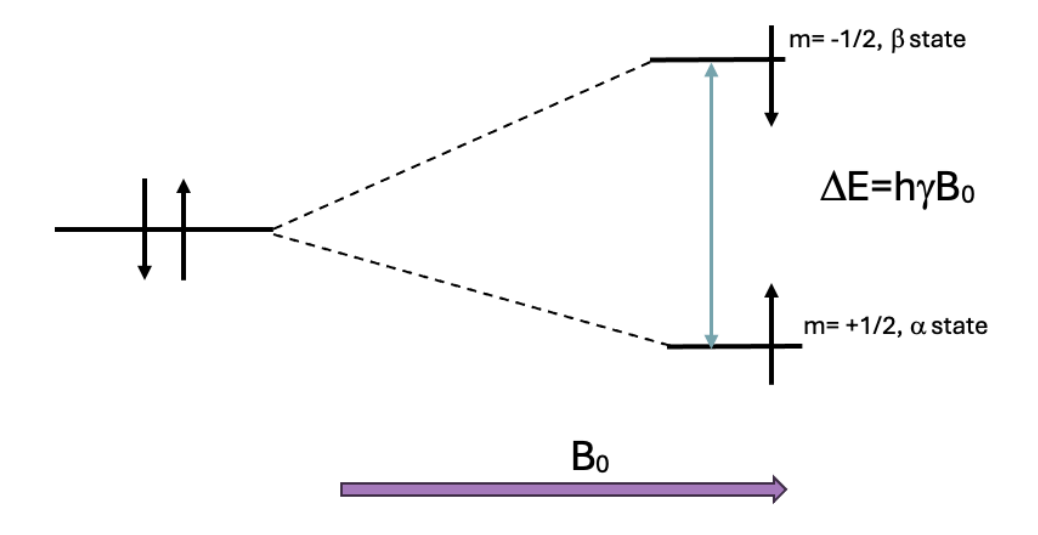


**Figure 2-4** Schematic representation of magnetic spin states of spin 1/2 nucleus Where h is the reduced Planck constant,  $\gamma$  is the gyromagnetic ratio, and  $B_0$  is the magnetic field strength.

During acquisition, an oscillating radiofrequency (RF) pulse is applied perpendicular to the main magnetic field  $B_0$ . This pulse is tuned to match the Larmor frequency of the nuclei of

interest, for example in this work we use a 400MHz solid state magnet, hence a  $^{13}$ C pulse is tuned to 100.6MHz. For a spin-1/2 nucleus, there are two energy states:  $\alpha$  (aligned with B<sub>0</sub>) and  $\beta$  (aligned against B<sub>0</sub>) as seen in Figure 2-4.

When the frequency of the applied RF pulse matches the Larmor frequency of the nuclei, a condition called resonance occurs. This is crucial for efficient energy transfer between the RF field and the nuclear spin system. At resonance, the RF field's oscillations match the precession of the nuclear spins. This synchronization allows for cumulative effects of the RF field on the spin system, resulting in efficient nuclei energy absorption and inducing transitions between spin states. The resonance condition is highly specific, allowing for selective excitation of different nuclear species in a sample.

Initially, the net magnetization vector (M) of the sample aligns with the strong external magnetic field  $B_0$ . When an RF pulse is applied, it generates a magnetic field  $B_1$  perpendicular to  $B_0$ . This  $B_1$  field exerts a torque on M, causing it to precess around  $B_1$  and tip away from its initial alignment along the z-axis. The extent of this tipping is quantified by the flip angle ( $\theta$ ), which represents the angle through which M rotates from its original position. The flip angle is determined by two key factors: the duration of the RF pulse ( $\tau$ ) and the strength of the  $B_1$  field. Two common flip angles are  $90^{\circ}$  and  $180^{\circ}$ . A  $90^{\circ}$  pulse rotates M into the transverse (xy) plane, maximizing the transverse magnetization and resulting in the strongest detectable signal as seen in Figure 2-5. A  $180^{\circ}$  pulse, on the other hand, inverts M, flipping it to point along the negative z-axis. By controlling the flip angle, we can manipulate the balance between longitudinal (z-axis) and transverse (xy-plane) magnetization, which is crucial for various NMR pulse sequences and experiments.

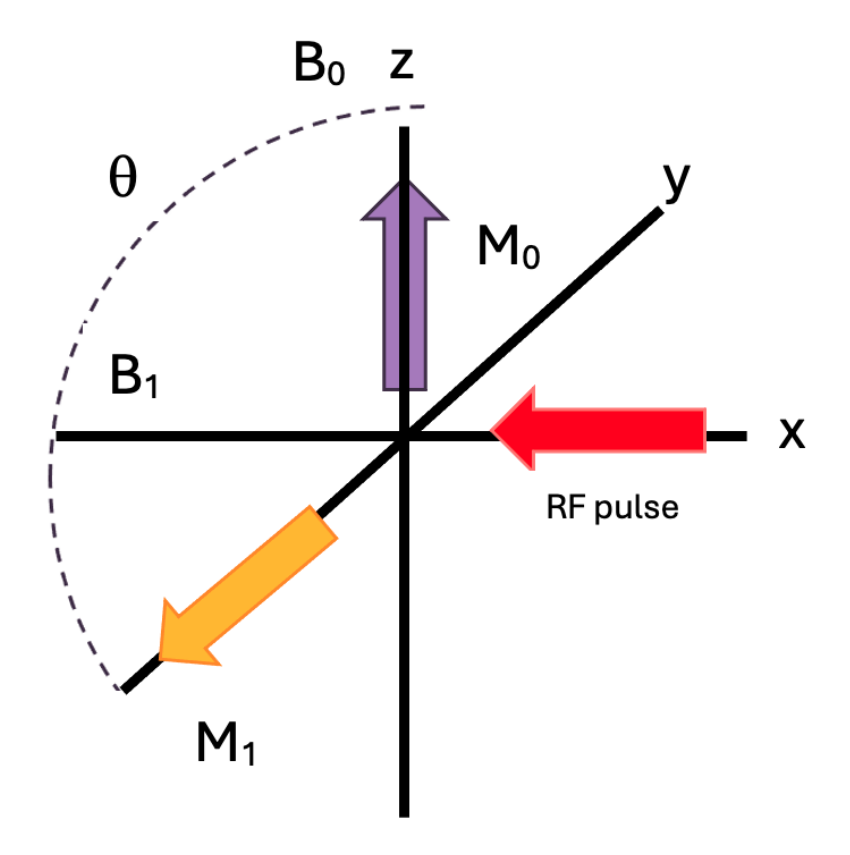


**Figure 2-5** Schematic representation of change in bulk magnetisation around flip angle as a result of RF pulse. 90° pulse shown here.

After the RF pulse, the excited spins return to equilibrium, producing a time-dependent signal called the Free Induction Decay (FID). The FID encodes the superposition of all sample resonance frequencies, modulated by their relaxation rates. This time-domain signal, when subjected to Fourier transformation, produces the frequency-domain NMR spectrum.

In this thesis, interactions within multicomponent pharmaceutical systems are investigated using both solution and solid-state NMR spectroscopy. A key factor considered in these studies is chemical shift anisotropy (CSA). Chemical shift anisotropy arises from the orientation-dependent electronic shielding of nuclei in molecules. In solution NMR, rapid molecular tumbling averages out CSA effects, resulting in sharp, isotropic peaks. However, in solid-state NMR, the restricted molecular motion preserves CSA, leading to broad, asymmetric chemical shifts. This anisotropic interaction provides valuable information about local electronic environments, molecular orientation, and structural features in solid pharmaceutical

# 2.3.2 Cross Polarisation Magic Angle Spinning (CP/MAS)<sup>145-151</sup>

CP/MAS is a powerful technique that greatly enhances spectral resolution in solid state NMR. As mentioned above, chemical shift anisotropy along with other anisotropic interactions such as dipolar couplings can lead to broad peaks in solid state NMR spectra. The magic angle spinning component of CP/MAS addresses this issue. Magic angle spinning (MAS) is the most significant tool in solid state NMR. This technique averages the anisotropic interactions, by rotating the sample at an angle relative to the external magnetic field; the magic angle which is derived from equation:

$$3cos^2\theta - 1 = 0$$
 Equation 2-5

By rotating the sample at an angle of 54.74°, the geometric term  $3\cos^2\theta$  - 1 averages to zero over a complete rotation. This averaging effectively nullifies the anisotropic interactions, including CSA, resulting in narrower spectral lines and improved resolution. For MAS to be effective, the sample rotation frequency must be greater than spectral width in Hz. Recent developments in probe technology now allows samples to be spun at 150KHz and above, however MAS alone is often insufficient to produce well-resolved ¹H spectra for most organic solids. To overcome this, we employ multiple-pulse sequences such as cross polarisation (CP), in conjunction with MAS.

Nuclei studied in this thesis have low natural abundance <sup>13</sup>C (1.1 %) and <sup>15</sup>N (0.37 %), making it extremely difficult to obtain high quality NMR spectra in a reasonable time frame. Cross polarisation is a method that transfers magnetization from abundant, high gyromagnetic ratio nuclei such as <sup>1</sup>H to less abundant, low gyromagnetic ratio nuclei such as <sup>13</sup>C or <sup>15</sup>N. In organics, abundant nuclei are usually in close proximity and coupled through dipolar interactions to low abundant nuclei. For CP to occur, the Hartmann-Hahn condition must be satisfied. The Hartmann-Hahn condition states that the precession frequencies of the two types of nuclei must be matched in their respective rotating frames. This is expressed mathematically as:

$$\gamma_H B_{1H} = \gamma_C B_{1C}$$
 Equation 2-6

Where  $\gamma_H$  and  $\gamma_C$  are the gyromagnetic ratios of the two nuclei, and  $B_{1H}$  and  $B_{1C}$  are the applied radiofrequency field strengths of each nucleus. When this condition is met, energy conservation allows for efficient dipolar coupling between the two spin systems, enabling magnetization transfer. This transfer significantly improves the signal-to-noise ratio of the low abundance nuclei, allowing for faster data acquisition and better spectral quality.

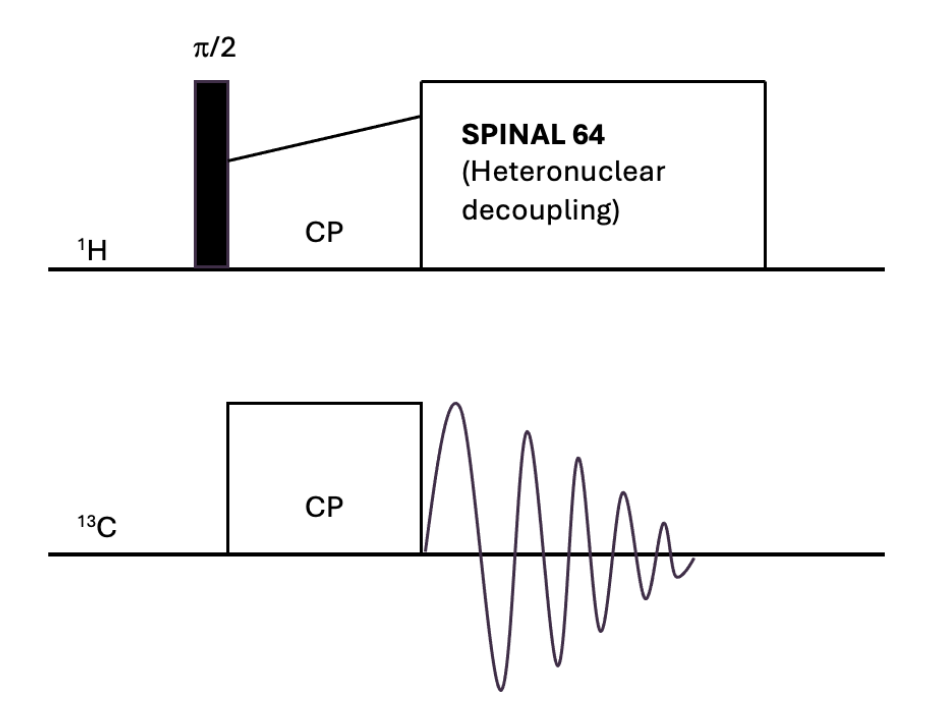


**Figure 2-6** Schematic representation of the cross-polarisation pulse sequence. First, a 90° pulse is applied to the <sup>1</sup>H nuclei, rotating their magnetisation into the transverse plane. Immediately after the 90°, a ramped RF field is applied to the <sup>1</sup>H channel. Simultaneously, a constant RF field is applied to the <sup>13</sup>C channel. Ramped pulse helps broaden the Hartmann-Hahn matching conditions, improving efficiency of magnetization transfer. Following contact time, the <sup>13</sup>C FID is recorded. During this acquisition period, SPINAL-64 decoupling is applied on the <sup>1</sup>H channel. SPINAL-64 is an advanced decoupling scheme that provides improved heteronuclear decoupling compared to traditional continuous wave (CW) decoupling. After acquisition, a delay period allows for relaxation before next scan.

# 2.3.3 Combined Liquid and Solid State In-situ Crystallisation NMR (CLASSIC)<sup>119,</sup> 123-125, 127, 152

CLASSIC NMR is an advanced in-situ method for probing crystallisation from solution in a solidstate NMR rotor. This technique was originally used to detect the crystallisation of different polymorphs from solution. Here we leverage the efficiency and accuracy of CP/MAS to exclusively detect the change in local environments at the transformation of one cocrystal ratio to another, in the presence of a liquid. The same instrument is able to view both the liquid phase and the solid phase, simply by applying different pulse sequences. Therefore, by alternating between two/three different pulse programs, we can observe evolution of both phases in real time. We are able to ascertain the changes in a qualitative way by changes in chemical shift peak positions, but also a quantitative way by the change in integrals of these peak, provided the acquisition time remains the same throughout the cycle. The most crucial factor is the selection of pulse sequences that selectively detect signals from only the solid phase and only the solution phase. As previously determined, CP/MAS is effective in determining the solid phase. The method used in detecting the solution phase here is a direct <sup>13</sup>C pulse with High Power <sup>1</sup>H Decoupling (HDPEC) and a relatively short relaxation delay (d1= 5-10s), to ensure no signal is detected from solid phase (d1 > 45s). We also utilise <sup>1</sup>H direct detection; this is possible because we obtain a reference of the broad solid state <sup>1</sup>H peak(s), which clearly contrasts the narrow <sup>1</sup>H peak(s) observed in the sample containing the solution.

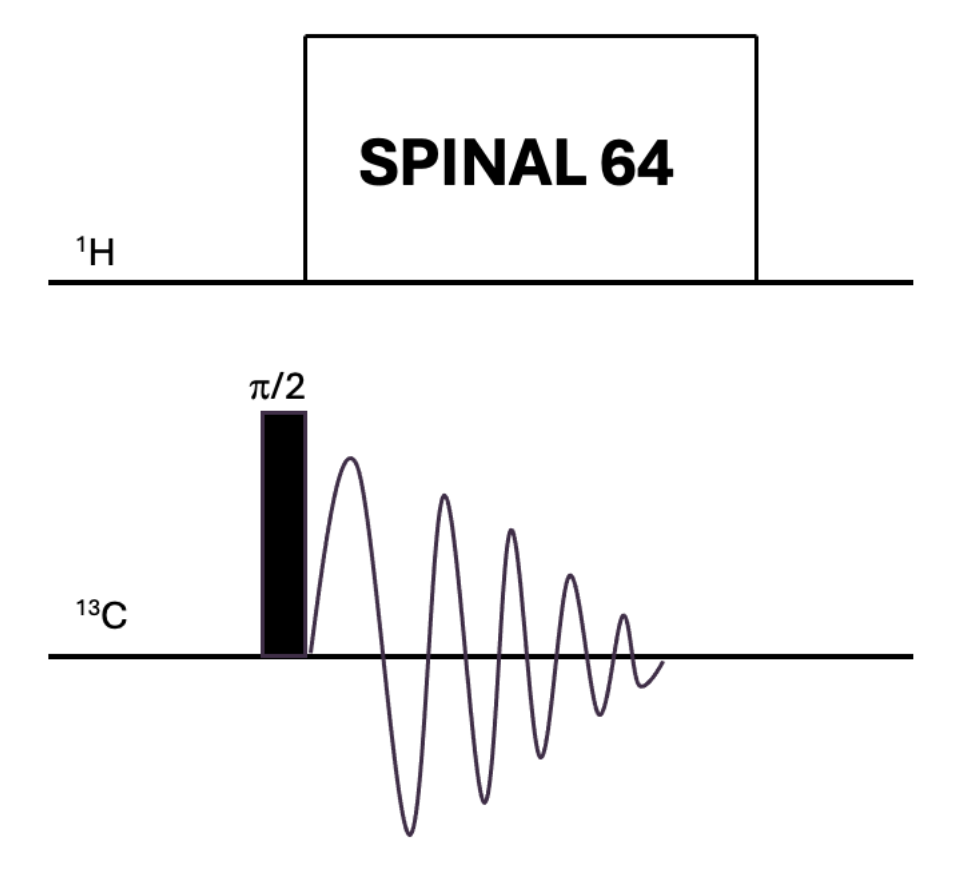


**Figure 2-7** <sup>13</sup>C{<sup>1</sup>H} High power decoupling pulse sequence. Directly apply 90° pulse on <sup>13</sup>C followed by FID acquisition and simultaneous heteronuclear decoupling.

# 2.3.4 Solution state NMR <sup>153-156</sup>

In Chapter 4, we study intermolecular interaction dynamics of cocrystal coformer combinations in solution using <sup>1</sup>H solution NMR. This is possible due to the enhanced sensitivity of solution state NMR to chemical exchange processes. Solution state NMR involves the use of solvent species, here EtOH is the only solvent used, as we are trying to mimic the environs of a cocrystal formed in the solid state by LAG. We also utilise 2D NMR techniques; Insensitive Nuclei Enhanced by Polarization Transfer (INEPT) and Nuclear Overhauser Effect Spectroscopy (NOESY). INEPT is solution state pulse sequence designed to enhance sensitivity of low-abundance nuclei, in our case <sup>15</sup>N, by transferring magnetisation from abundant nuclei like <sup>1</sup>H through scalar (J-coupling) interactions.

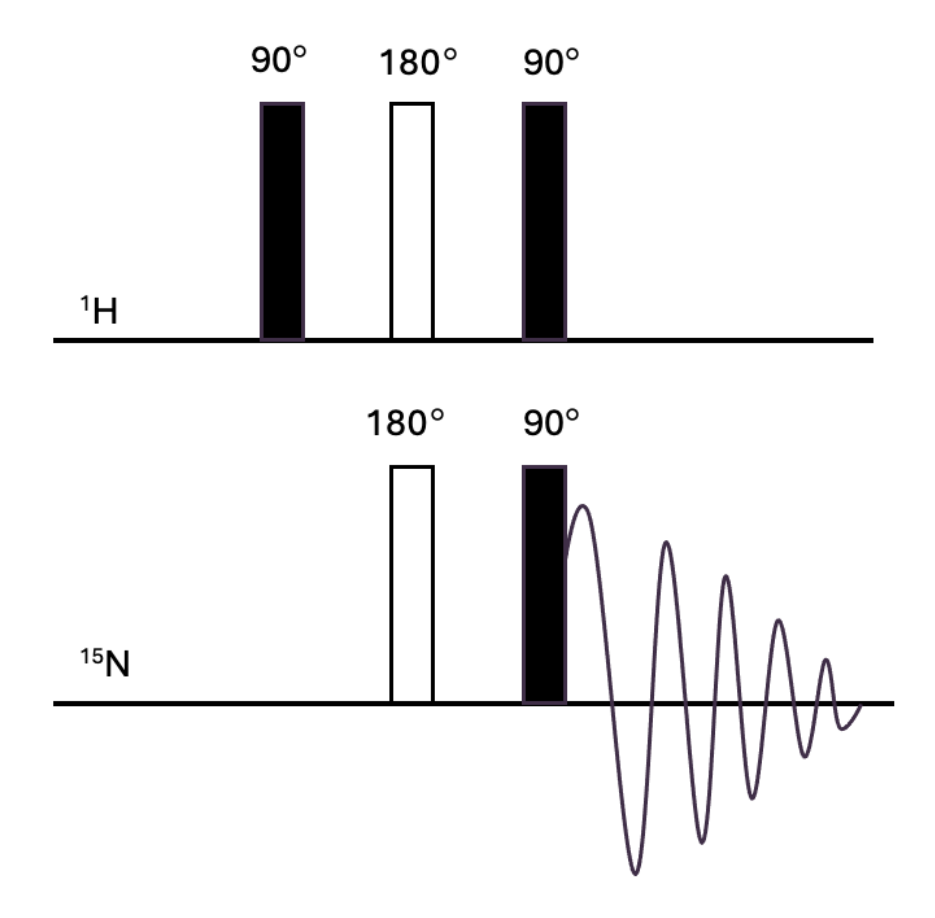


**Figure 2-8** INEPT pulse sequence. 90° pulse is first applied to the <sup>1</sup>H nuclei to rotate magnetisation plane, followed by a delay for j-coupling evolution. Simultaneous 180° pulses are applied to the <sup>15</sup>N and <sup>1</sup>H nuclei to refocus chemical shift evolution. A final 90° pulse to transfer magnetisation to <sup>15</sup>N nucleus and signal is acquired.

NOESY is a 2D NMR technique used to study through-space relationships between nuclei in molecules. It provides important information about molecular aggregation in solution, through spatial correlations between nuclei that are close in proximity, typically within 5 Å but not connected through bonds. The idea of NOESY is to detect specific inter and intramolecular interactions in solution. NOESY has been used to study host-guest complexes and supramolecular assemblies, making it ideal for studying cocrystal systems.

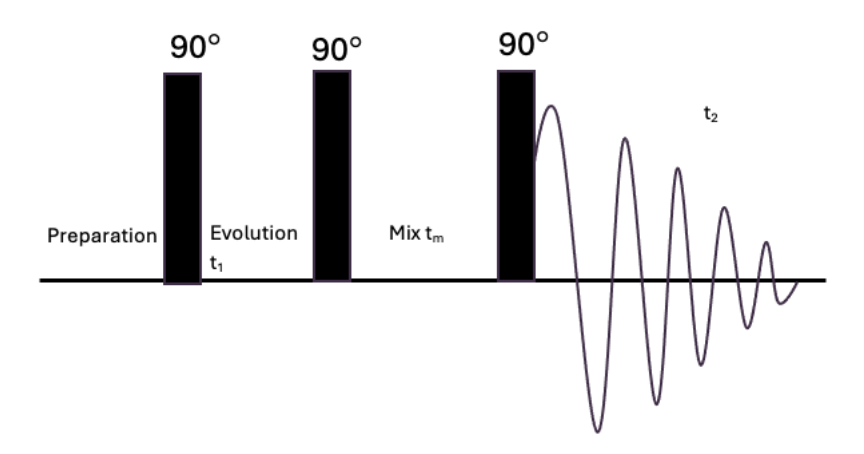


**Figure 2-9** – 2D NOESY pulse program. Three 90° pulses are applied. The first pulse is applied to create transverse magnetisation to xy plane. Time t1 allows for chemical shift evolution, with duration incrementally increased to create the 2nd dimension of the spectrum. The second pulse returns magnetisation to z-axis and beings mixing time. Mixing time is the key parameter in NOESY experiments, allowing for cross relaxation between proximal nuclei. Shorter mixing times favour stronger NOEs from smaller molecules or closely situated nuclei, longer mixing times allow detection of weaker NOEs from larger molecules or those further apart. The third pulse returns magnetisation to transverse plane for detection. t2 is the acquisition period.

In a nutshell, NMR is well suited for this study of multicomponent pharmaceutical systems because it directly probes the local environments and dynamics of atomic nuclei, providing both structural and interactional information at the molecular level. The use of both solid-state and solution-state NMR in this thesis is particularly advantageous: solid-state NMR, especially with techniques such as cross-polarisation magic angle spinning (CP/MAS), allows for the investigation of crystalline and amorphous phases, quantification of polymorphs, and the elucidation of intermolecular interactions and local order in complex solid formulations-capabilities that are critical for characterising cocrystals, hydrates, and other multicomponent solids where molecular mobility is restricted and chemical shift anisotropy (CSA) is significant. Conversely, solution-state NMR provides high-resolution insights into dynamic processes, molecular aggregation, and chemical exchange in the liquid phase, enabling the study of how components interact, aggregate, or dissociate in environments relevant to dissolution and

formulation. By employing both approaches, this thesis leverages the strengths of NMR to comprehensively characterise the structure, dynamics, and interactions of pharmaceutical systems across different physical states, thereby yielding a deeper understanding of the factors governing cocrystal formation, stability, and transformation.

# Chapter 3 – Experimental methods

# 3.1 Liquid-Assisted Grinding (LAG)

Liquid-assisted grinding (LAG) was employed as a mechanochemical technique to facilitate cocrystal screening and synthesis. All LAG experiments were performed using a Retsch MM400 ball mill. For each experiment, the required coformers were weighed out in their precise stoichiometric ratios (for example, 1:1, 1:2, or 2:1) as detailed in Appendix Table 3.5 of the thesis. Typically, 122.1 mg of either isonicotinamide or nicotinamide (corresponding to 1 mmol) was combined with the appropriate mass of the selected coformer. The solid components were transferred to a 10 mL stainless steel grinding jar along with one 7 mm stainless steel balls. To each mixture, 50  $\mu$ L of ethanol was added using a calibrated micropipette to act as the grinding liquid. The addition of this small volume of solvent was intended to enhance molecular mobility and facilitate the formation of cocrystals without introducing excess solvent or dissolving the reactants entirely. The loaded jars were sealed and subjected to grinding at a frequency of 30 Hz for 30 minutes unless stated otherwise. After completion of the grinding cycle, the resulting solid was carefully collected from the jar using a PTFE spatula and transferred to a glass vial for storage at ambient conditions until further analysis.

All LAG experiments were performed in at least duplicate to ensure reproducibility. The products were subsequently characterised by powder X-ray diffraction (PXRD), thermogravimetric analysis (TGA), differential scanning calorimetry (DSC), and, where relevant, solid-state NMR spectroscopy to confirm cocrystal formation and determine phase purity. This protocol ensured precise control over stoichiometry and solvent volume, providing a reproducible and efficient route for the screening and synthesis of multicomponent pharmaceutical solid forms.

## 3.2 Thermogravimetric Analysis (TGA)

Thermogravimetric analysis was performed using a TA Instruments TGA Q5500 analyser. Prior to analysis, all samples were finely ground, where necessary, to ensure homogeneity and to maximise surface area for uniform heating. Approximately 5–10 mg of each sample was accurately weighed using a microbalance and placed in a clean aluminium pan. The pan was then loaded onto the TGA sample holder, and the instrument chamber was purged with high-purity nitrogen gas at a flow rate of 10–25 mL/min to provide an inert atmosphere and prevent oxidative degradation during heating. The temperature program was set to heat the samples from room temperature (ca. 25°C) to 400°C at a constant rate of either 5°C/min or 10°C/min, depending on the specific experiment. These heating rates were chosen to balance resolution of thermal events with practical analysis time. The mass of each sample was continuously recorded as a function of temperature throughout the heating process.

After completion of the run, the resulting thermograms-plots of mass versus temperature-were analysed using TA Trios software. The onset temperature of decomposition was determined as the point where the mass loss curve deviated from the baseline, and the percentage weight loss was calculated for each thermal event. Residual mass at the end of the experiment (400°C) was also recorded to assess the presence of non-volatile components or inorganic residues. All TGA experiments were repeated at least twice to ensure reproducibility of the results.

# 3.3 Differential Scanning Calorimetry

Differential scanning calorimetry (DSC) analysis was conducted using a TA Instruments DSC Q2500 differential scanning calorimeter. Prior to measurement, all samples were finely ground, where necessary, to ensure homogeneity and to maximise surface contact within the pan. Approximately 2–5 mg of each sample was accurately weighed using a microbalance and sealed in an aluminium pan. An empty, hermetically sealed aluminium pan was used as the reference for all measurements. The samples were heated from room temperature to 300°C at a rate of either 5°C/min or 10°C/min, depending on the nature of the experiment. A nitrogen purge was maintained throughout the analysis at a flow rate of 50 mL/min to prevent

oxidative degradation and to ensure a consistent thermal environment. The heat flow as a function of temperature was recorded for each sample using TA Trios v5.1.1 software. Thermal events were identified from the resulting DSC thermograms, with onset temperatures, peak temperatures, and melting points determined for each sample. The presence of multiple endothermic or exothermic events was used to identify potential polymorphic transitions or the presence of solvates. Each measurement was performed at least in duplicate, using separately prepared batches, to confirm reproducibility.

This approach allowed for the precise characterisation of melting behaviour, phase transitions, and thermal stability in the multicomponent pharmaceutical systems under investigation.

# 3.4 Powder X-ray Diffraction (PXRD)

Powder X-ray diffraction (PXRD) analysis was carried out using both a Rigaku Smartlab SE powder diffractometer and, when necessary, due to equipment availability, a Rigaku Miniflex benchtop diffractometer. Both instruments were equipped with a copper Kα radiation source  $(\lambda = 1.5418 \text{ Å})$  operating at 40 kV and 15 mA. Prior to measurement, all samples were finely ground using an agate mortar and pestle to ensure homogeneity and to minimize the effects of preferred orientation. The powdered samples were then carefully packed into a custom 3D-printed, reduced-volume sample holder, ensuring a flat and even surface for optimal data collection. Care was taken to avoid air gaps and to achieve a random orientation of crystallites. For each measurement, data were collected over a  $2\theta$  range of 5° to 35°, with a step size of 0.02° and a scan speed of 2° per minute. These parameters were chosen to provide sufficient resolution for distinguishing between different crystalline phases and to allow for accurate comparison with reference patterns. The resulting diffraction patterns were analysed using Rigaku software. Phase identification was performed by comparing the experimental patterns with those of individual coformers as well as with reference patterns from the Cambridge Structural Database (CSD). The PXRD technique was used to confirm the formation of new multicomponent pharmaceutical solid forms, to detect any changes in crystal structure, and to assess the presence of multiple phases or impurities in the products.

All PXRD measurements were repeated at least twice, and, where possible, on independently prepared batches to confirm reproducibility. In cases where the benchtop instrument was used due to technical issues with the Smartlab SE, it was noted that the lower resolution may limit the ability to distinguish subtle differences between closely related phases; however, key features for phase identification remained accessible. This PXRD protocol ensured reliable and reproducible characterisation of crystalline phases, supporting the identification and analysis of new cocrystals, hydrates, solvates, and other multicomponent forms throughout the study.

### 3.5 Solid-State NMR

Solid-state nuclear magnetic resonance experiments were carried out using Bruker Avance III HD spectrometers operating at 300, 400, and 850 MHz, with the 850 MHz system at the UK High-Field Solid-State NMR Facility used for high-resolution and in situ studies. Samples were finely ground as needed and approximately 50–60 mg was packed into 4 mm zirconia rotors. For moisture-sensitive materials, all sample handling and rotor packing were performed in a nitrogen-filled glovebox to minimise exposure to atmospheric moisture. The rotors were then sealed and inserted into the MAS probe. For routine characterisation, <sup>13</sup>C cross-polarisation magic angle spinning (CP/MAS) experiments were conducted with MAS rates of 10–12 kHz. Typical parameters included a contact time of 2 ms, a recycle delay between 10 and 1200 seconds (depending on the relaxation properties of the sample), and between 32 and 1028 scans to achieve adequate signal-to-noise. The <sup>13</sup>C chemical shifts were referenced to tetramethyl silane (TMS) using the methyl peak of hexamethylbenzene at 17.35 ppm as a secondary standard. Spectra were processed using Bruker TopSpin software, applying exponential line broadening and manual phase and baseline correction. For in situ studies of phase transformations and crystallisation, the CLASSIC NMR technique was employed on the 850 MHz spectrometer using a 4 mm HXY probe. Samples were prepared with both solid and a small amount of liquid phase (typically 20 µL ethanol), and the rotor was spun at 12 kHz. The experimental protocol alternated between three pulse sequences: direct <sup>1</sup>H detection, <sup>13</sup>C direct detection with high-power <sup>1</sup>H decoupling and short recycle delay for the liquid phase, and  ${}^{1}H\rightarrow {}^{13}C$  CP/MAS for the solid phase. This approach enabled simultaneous

monitoring of both solid-state and solution-state environments within the same experiment, allowing real-time observation of cocrystal formation and transformation.

All solid-state NMR experiments were performed at least in duplicate to confirm reproducibility. The combined use of CP/MAS and CLASSIC NMR provided detailed insight into the local structure, hydrogen bonding, and dynamic processes in multicomponent pharmaceutical systems, complementing the results obtained from PXRD and thermal analysis.

### 3.6 Solution State NMR

Solution-state NMR experiments were performed primarily to investigate intermolecular interactions, aggregation behaviour, and dynamic processes of cocrystal coformers in solution. All one-dimensional (1D) and two-dimensional (2D) NMR measurements were carried out on Bruker AVANCE III 500 MHz and AVANCE NEO spectrometers. For all experiments, 3-(trimethylsilyl)propionic-2,2,3,3-d4 acid sodium salt (TSP,  $\delta$  = 0 ppm) was used as the internal reference standard. Sample solutions were prepared by dissolving accurately weighed amounts of the relevant coformers (e.g., 3-hydroxybenzoic acid, 2-hydroxybenzoic acid, nicotinamide, and isonicotinamide) in ethanol. Serial dilutions were performed to achieve a range of concentrations, typically from 0.05 M to 0.5 M, depending on the experiment and solubility of the analyte. For titration studies, stock solutions of each coformer were prepared, and mixtures were made in varying acid:amide ratios as described in Table 4-1 of the thesis, allowing systematic investigation of concentration-dependent chemical shift changes and intermolecular interactions. For temperature-dependent studies, the probe temperature was calibrated and maintained using the variable temperature control unit. <sup>1</sup>H NMR spectra were acquired with standard single-pulse sequences, using a typical relaxation delay of 2-5 seconds and sufficient scans (usually 8-64) to achieve an adequate signal-to-noise ratio. For 2D experiments, such as COSY (Correlation Spectroscopy), NOESY (Nuclear Overhauser Effect Spectroscopy), and INEPT (Insensitive Nuclei Enhanced by Polarization Transfer), standard Bruker pulse programs were used with parameters optimised for each system. Mixing times for NOESY experiments were varied (typically 200-600 ms) to probe through-space interactions and aggregation phenomena. For INEPT experiments targeting <sup>15</sup>N, magnetisation transfer from <sup>1</sup>H was employed to enhance the sensitivity of lowabundance nuclei. All spectra were processed using Bruker TopSpin 4.2 software. Chemical shifts were referenced to the TSP standard, and spectra were manually phased and baseline corrected. Integration and peak assignment were performed with reference to literature values and authenticated standards. All solution-state NMR measurements were conducted at least in duplicate to ensure reproducibility. The resulting data provided detailed insight into the molecular interactions, aggregation, and stoichiometry of coformer pairs in solution, complementing the findings from solid-state characterisation techniques.

# Chapter 4 Computational studies

# 4.1 Statistical analysis, screening and characterisation of nicotinamide and isonicotinamide cocrystals

Nicotinamide (NA) and isonicotinamide (INA) are two widely available amides, commonly used as coformers in cocrystals. Nicotinamide is a naturally occurring, water-soluble form of vitamin B3.<sup>157</sup> It has many dermatological applications, and is present in food items such as meat, fish, nuts and legumes.<sup>158, 159</sup> It is a good cocrystal coformer due to its hydrogen bonding abilities, and has been reported to improve the solubilities of known pharmaceuticals such as antimalarial halofantrine,<sup>160</sup> calcium channel blocking antihypertensive nifedipine<sup>161</sup> and non-steroidal anti-inflammatory drug indomethacin.<sup>162</sup>

Isonicotinamide, is a FDA Generally Recognised As Safe (GRAS) molecules, meaning it is acceptable for pharmaceutical use regarding quality and safety. <sup>163</sup> It is a structural isomer of nicotinamide and for this reason, INA and NA are of particular interest in cocrystal screening and design. They both contain 2 hydrogen bond acceptor sites: N-pyridine ring and carboxyl oxygen. The pyridine ring also contributes to intermolecular interactions through  $\pi$ - $\pi$  stacking. INA and NA possess the same functional groups, but in different positions. The nitrogen group is in the meta position in NA, but in the para position in INA. Despite possessing the same functional groups, these 2 coformers exhibit different hydrogen bonding patterns.

Figure 4-1- Chemical structure of Nicotinamide (left) and Isonicotinamide (right)

The amide is one of the most prevalent functional groups in crystal engineering, and commonly present in hydrogen bonding supramolecular synthons. <sup>164</sup> The -CONH<sub>2</sub> group

contains two hydrogens that can be donated and two lone pairs on the carbonyl O that can act as acceptors, giving it the ability to self-associate through a supramolecular homosynthon.  $^{165, 166}$  Amides are commonly known to form centrosymmetric dimers, with graph set  $R_2^2(8)$  and catemers, depicted in Figure 4-2. The amide group, coupled with carboxylic acid forms the acid-amide heterosynthon. This is a pivotal structural moiety in experimental crystal engineering, that has been utilised for decades.  $^{167, 168}$  Similarly, to the amides in Figure 4-1, acids and amides can also form dimers and catemers, and much research into making cocrystals of them has been carried out.  $^{105, 166, 169-171}$ 

$$\begin{array}{c|c} & & & & \\ & & \\ & & & \\ & & & \\ & & \\ & & & \\ & & & \\ & & & \\ & & & \\ & & & \\ & & & \\ & & & \\$$

**Figure 4-2**. Hydrogen bonding patterns between amide-amide centrosymmetric dimer (**left**) and catemer (**right**)

The pyridine group found in both coformers is another widely studied functional group in the field of crystal engineering. Pyridines are strong hydrogen bond acceptors due to the lone pair on the nitrogen and the delocalization from the aromatic ring, which makes it perfect for competing for donors. <sup>40</sup> The presence of the weak CH···O bond (Figure 4-3) makes this mixed weak-strong hydrogen bond easily exploitable in crystal engineering. <sup>115</sup> There are readily available data advocating that pyridines hydrogen bond to carboxylic acids and phenols. Steiner conducted a Cambridge Structural Database (CSD) study that signified the carboxylic acid pyridine bond in particular is favoured 10-fold compared to the carboxylic acid dimer. <sup>172</sup> Experimental data suggest that acid-pyridine synthon is preferred to the phenol-pyridine synthon when both are present.

Figure 4-3 - Carboxylic acid – pyridine synthon

# 4.2 CSD analysis of supramolecular synthon hierarchy in NA and INA cocrystals

The Cambridge Structural Database (CSD)<sup>1</sup> is a repository of small-molecule organic and metal-organic structures, with over 1 million chemical structures.<sup>2</sup> Using CSD version 2020.2.0, we conducted searches using ConQuest 2020.2.0 and analysed intermolecular interactions with Mercury 2020.2.0. Our search criteria were refined to focus on relevant structures: organic compounds without errors, excluding polymeric and metallic structures. We defined non-bonded contacts as inter- and intramolecular interactions separated by 4-999 bonds, with D-H···A angles ≥ 120° and contact distances shorter than the sum of 0 to -5 van der Waals radii. Donor atoms were limited to nitrogen and oxygen, while all atom types were accepted as acceptors. At the time of searching, there were ca. 170 nicotinamide cocrystals and ca. 230 isonicotinamide co-crystals and in the CSD. Some molecules formed cocrystals with NA, but not INA and vice versa, whilst some formed with both NA and INA. In these reported cocrystals, the seven most frequently observed cocrystal synthons are carboxylic acid – amide heterosynthon, amide – amide dimer, alcohol – amide heterosynthon, phenol – amide heterosynthon, carboxylic acid – pyridine heterosynthon, phenol – pyridine heterosynthon and phenol – amide heterosynthon (Figure 4-5). Understanding the prevalence (Figure 4-4) and nature of these synthons provides crucial insights into the molecular recognition processes governing cocrystal formation with NA and INA. This information guides our experimental design and aids in predicting potential new cocrystal systems, forming the foundation for our subsequent investigations into cocrystal screening and characterization.

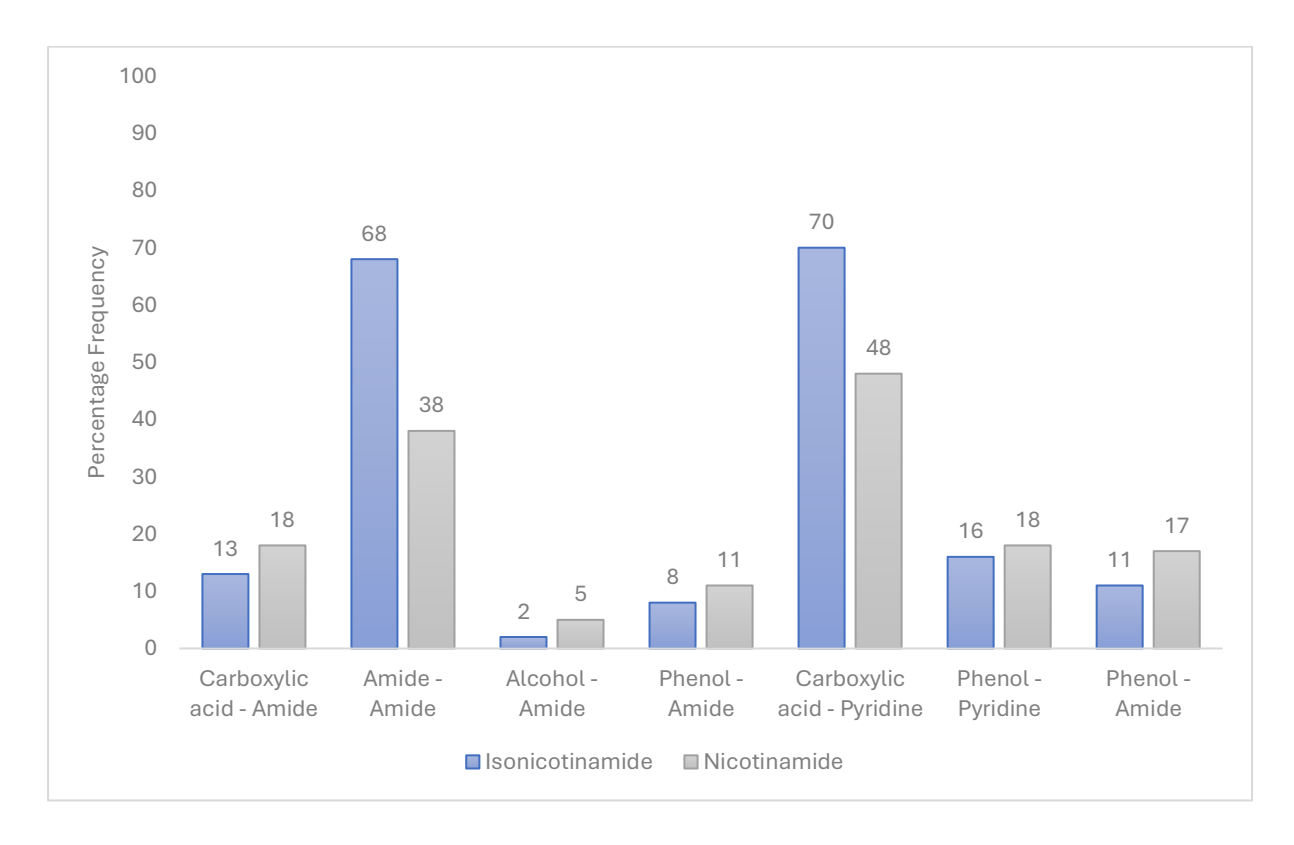


**Figure 4-4** - Graph showing prevalence of synthon occurrence as a percentage, where 100% means this synthon is present in all cocrystals.

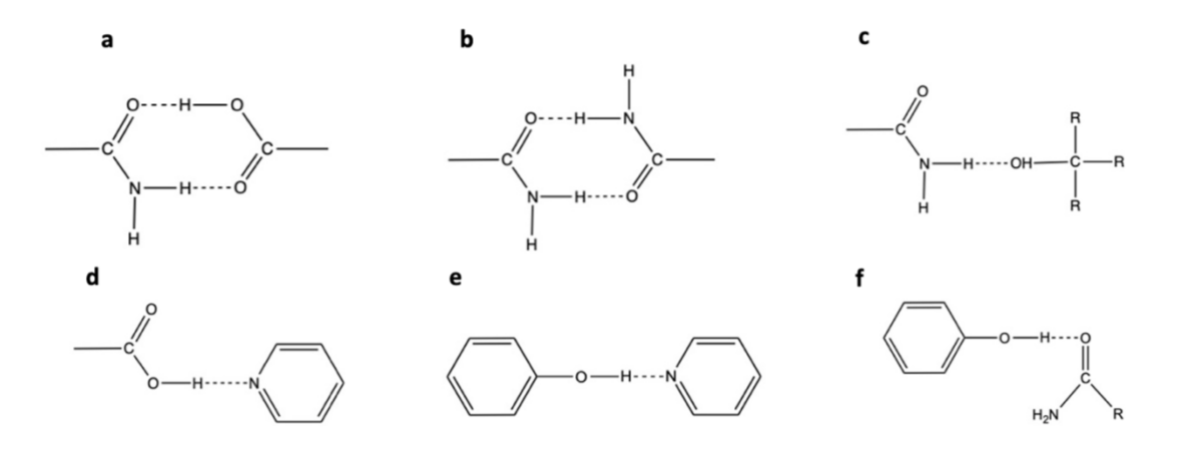


**Figure 4-5** - a) Amide - carboxylic acid heterosynthon, b) Amide – Amide homodimer, c)

Amide – Alcohol heterosynthon, d) Carboxylic acid – Pyridine heterosynthon, e) Phenol –

Pyridine heterosynthon, f) Phenol – Amide heterosynthon.

## 4.2.1 Carboxylic acid - amide

This supramolecular synthon is frequently observed in crystal engineering due to its strength, reliability and predictability. The highly directional N-H···O=C and O-H···O=C bonds make this synthon robust. Interestingly from our results, this dimer was only seen in 13% of INA cocrystals, and 18% of NA cocrystals. The -COOH preferred to donate the proton to the N-pyridine in lieu of the CONH2 as the N-pyridine is the better acceptor. We know this because of Etter's rule, strong donors prefer strong acceptors. We observed that the amide-acid synthon was present mainly in cocrystals of both INA and NA, that had more than one donor group present. These extra donor groups included functional groups on coformers, ternary crystals and cocrystals containing water. In these cocrystals the N-pyridine group is occupied with a different hydrogen bond donor, hence the amide group is available to bond with the acid.

#### 4.2.2 Amide - amide

Interestingly, this synthon was observed in 68% of INA cocrystals, yet only 38% of NA cocrystals. The amide-amide dimer primarily arises due to the absence of other strong donor/acceptor groups. When another strong hydrogen bond donor is present, this synthon is rarely present. In cocrystal engineering, heteromeric interactions are typically preferred over homomeric intermolecular bonds. This synthon was observed mostly between molecules of INA/NA hydrogen bonding with another molecule of INA/NA respectively. We also noticed amide-amide dimers combining to form tetramers, as seen in Figure 4-6.

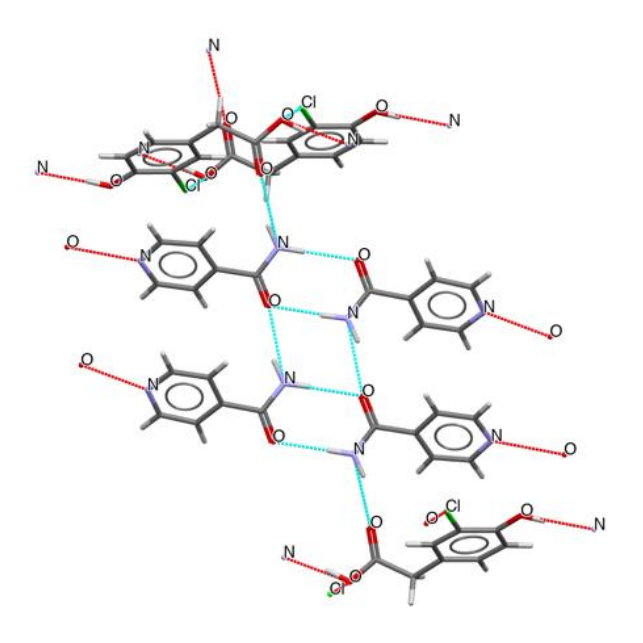


Figure 4-6. Amide-amide dimer and catemer observed in cocrystals of INA and NA

#### 4.2.3 Alcohol – amide

The alcohol - amide hydrogen bond was the least frequent synthon in cocrystals of INA and NA in the CSD. This supramolecular synthon was seen in only 2% of all INA cocrystals and 5% of all NA cocrystals. This comes as no surprise, even though alcohols possess the ability to act as hydrogen bond donors and acceptors, the presence of aliphatic chains decrease their potency compared to aromatic amides, phenols, and carboxylic acids. <sup>174</sup> For this reason, aliphatic alcohols are rarely seen in cocrystals. Interestingly, in the few cocrystal structures that did possess aliphatic alcohols, in INA, only 31% (4/13) exhibited the alcohol-amide heterosynthon, the rest were either involved in intramolecular hydrogen bonding or bonded to the N-pyridine. However, this was 53% (9/17) in NA, suggesting that this synthon is preferred in NA compared to INA. It is important to note these lists are not mutually exclusive, as the same coformers had not all been tried with both INA and NA. These lists also included a few ternary crystals, but the presence of these in both groups' levels the playing field.

## 4.2.4 Carboxylic acid – pyridine

Similar to the findings reported by Aakeroy and co-workers, 103 the carboxylic acid - pyridine and amide – amide synthons were the most common synthons in this study. Here we have the strongest donor and acceptor bond pair, making it the most favourable synthon.<sup>40</sup> This synthon was seen in 70% of cocrystals of INA, but only 48% of cocrystals of nicotinamide. It was interesting to note this significant difference is explained by the fact that there are more phenol groups in the reported cocrystals of NA. Further analysis of the hydrogen bonding competition in cocrystals containing this synthon, reveals that in INA, when there was a carboxylic acid group present in the coformer, this synthon formed in 95% of such examples. In the 5% that did not contain this synthon, it was observed that the N-pyridine had accepted a hydrogen from -SO<sub>2</sub>NH<sub>2</sub>, -OH or -CONH<sub>2</sub>, whilst the -COOH mostly formed R<sub>2</sub><sup>2</sup>(8) dimers with -COOH or -CONH2 groups. Shattock conducted a CSD analysis study on the hierarchy of supramolecular heterosynthons, concluding that from their data set, the COOH – N-pyridine supramolecular synthon formed in 98% of structures that contained carboxylic acid and pyridine moieties capable of intermolecular bonding. 112 Analysis of hydrogen bonding competition in NA showed that this synthon was observed in 81% of cocrystals with -COOH present. The remaining 19% can be rationalised; with the majority containing carboxylic acid - amide dimers. In these, the N-pyridine accepted from phenol-OH instead, there was also one cocrystal-hydrate present. We observed that the N-pyridine group in nicotinamide did not participate in hydrogen bonding in the cocrystal of NA 1-((2,4-dichlorophenyl)methyl)-1Hindazole-3-carboxylic acid (DAQZUT), contradicting Etter's rule.

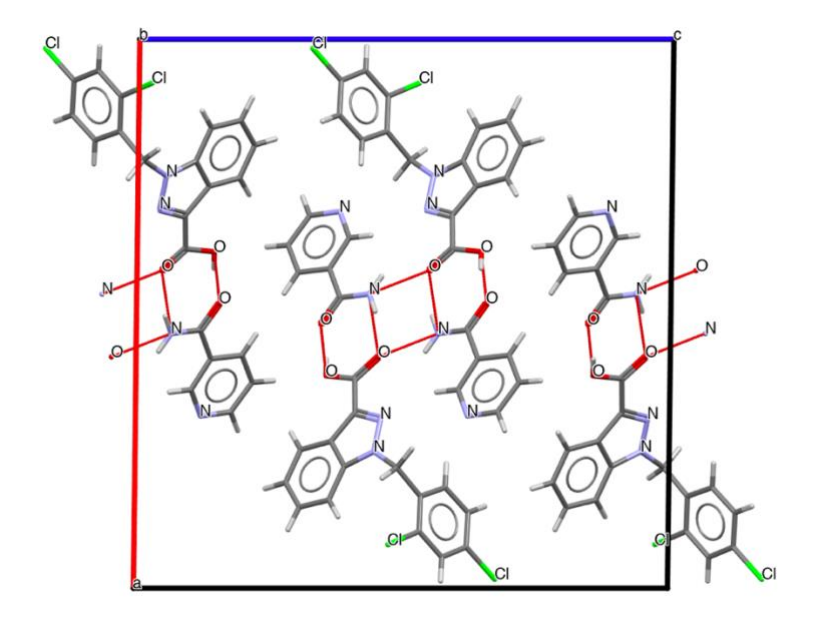


**Figure 4-7**. Hydrogen bonding in cocrystal of 1-((2,4-dichlorophenyl)methyl)-1H-indazole-3-carboxylic acid and nicotinamide DAQZUT.

#### 4.2.5 Phenol – pyridine

This supramolecular synthon contains the combination of the best hydrogen acceptor, N-pyridine and the second-best hydrogen bond donor in this dataset, phenol. We observed a similar prevalence of this hydrogen bonding interaction in INA (16%) and NA (18%). Literature cites that the carboxylic acid - pyridine synthon is a stronger bond, with larger interaction energies (kjmol<sup>-1</sup>) and shorter O/N...O/N distances (Å).<sup>175</sup> We observed that in cocrystals of INA and NA that contained a phenol group, this synthon formed in 69% and 60% respectively. It is important to note that this bond predominantly formed in structures that **did not** have a carboxylic acid group present. If the coformer had both a COOH and a Ph-OH, the acid – pyridine synthon was preferred.

#### 4.2.6 Phenol – amide carbonyl

According to Etter's third rule, the strongest hydrogen bond donors, will bond with the strongest hydrogen bond acceptors to form cocrystals.<sup>41, 175</sup> In our study dataset, the second strongest hydrogen bond donor is the phenol OH, after the carboxylic acid OH. The second strongest hydrogen bond acceptor is the amide group, after the N-pyridine.<sup>175</sup> This synthon

has a similar prevalence in INA and NA cocrystals, with the interaction observed in 8% and 11% of all cocrystals, respectively. When phenol and amide functional groups were present, this synthon was found in 35% of INA cocrystals and 36% of NA cocrystals. Further analysis showed that this synthon **only** formed if the N-pyridine of INA or NA was already engaged in a hydrogen bond, further confirming Etters rule.

**Table 4-1**. Competition for HB donors between synthons, where 100% means that when this HB D/A pair is present it will always form, 0% means when this HB D/A is present, it will never form.

HB donors	Acceptor	INA	NA
Carboxylic acid-COOH	-CONH <sub>2</sub>	19%	30%
	N-pyridine	95%	81%
Aliphatic alcohol-OH	-CONH <sub>2</sub>	31%	53%
Phenol-OH	-CONH <sub>2</sub>	35%	35 %
	N-pyridine	69%	60%
	-CONH <sub>2</sub>	46%	59%

#### 4.2.7 Summary of findings

Nicotinamide and isonicotinamide are common cocrystal coformers reported in the CSD. Through detailed analysis of the hydrogen bonding in cocrystals of these amides using Conquest and Mercury, a statistical hierarchy of supramolecular synthons has been established. We have been able to confirm Etter's rule in many instances. The most important factor is the strengths of the donor and the acceptor in predicting which bonds are most likely to form. The strongest donor is most likely to bond with the strongest acceptor. In the occasion that the strongest donor/acceptor is occupied, the second strongest donor/acceptor is likely to bond etc. Despite some interesting observations, we conclude that our sample size

was too small to confirm or deny any definitive rules for prediction of hydrogen bonding in cocrystals of INA and NA. Our database initially consisted of approximately 400 cocrystals of INA and NA. However, many of the coformers had only been screened for cocrystallisation with only INA or NA.

# 4.3 Machine learning towards the prediction of NA and INA cocrystals

Traditional experimental screening methods for cocrystals, whether solid-state (such as mechanochemical grinding) or solution-based (such as solvent evaporation), are inherently time-consuming, resource-intensive, and low-throughput. For example, as detailed later in this thesis, preparing and producing a single LAG cocrystal screen typically requires 45 minutes, with subsequent characterisation taking from several hours to multiple days depending on the chosen analytical techniques. This combinatorial burden is further compounded when multiple stoichiometries and solvent systems are considered, resulting in significant bottlenecks for pharmaceutical development where both cost and time are critical. Recent studies have demonstrated that machine learning (ML) can achieve >90% accuracy in predicting cocrystal formation, enabling rapid virtual screening and reducing the need for traditional trial and error techniques. <sup>89, 176</sup>

This study evaluates four ML algorithms-SVM, logistic regression, Naïve Bayes, and gradient-boosted trees using a dataset of **224 cocrystals** from the CSD, focusing on nicotinamide (NA) and isonicotinamide (INA) systems. The choice of algorithms reflects their complementary strengths under data constraints.

#### **Logistic Regression**

Logistic regression is a binomial classification system that accounts for numerous descriptors, each with differing 'weights', giving a final value between them that represents the probability of an event occurring.  $^{86}$  It is based on the logistic function below. Where x is the probability, the outcome is 1 for a given set of inputs of x.  $B_0$  is the intercept.

 $B_i$ ,...  $B_n$  are the coefficients for each input variable  $x_i$ ,  $x_n$  e is the base of the natural logarithm.

$$x = \frac{1}{1 + e^{-(\beta_0 + \beta_i x_i + \dots + \beta_n x_n)}}$$
 Equation 4-1

Logistic regression provides a transparent approach, estimating the probability that a given pair of molecules will form a cocrystal. It is computationally efficient and less prone to overfitting when regularization is applied, making it a good baseline model for smaller datasets. Logistic regression also allows for direct assessment of the influence of individual molecular features, which can yield mechanistic insights into the factors most associated with cocrystal formation. In recent cocrystal prediction studies, logistic regression has been used to benchmark the performance of more complex algorithms and to identify key molecular descriptors. <sup>89</sup>

#### **Support Vector Machines (SVM)**

SVMs are particularly advantageous for cocrystal prediction tasks because they excel at classifying data with many features, even when the number of samples is relatively small, as is often the case in pharmaceutical datasets. By employing kernel functions; a mathematical tool that measures the similarity between two data points in a transformed feature space, such as the radial basis function (RBF), SVMs can model complex, non-linear relationships between molecular descriptors and cocrystal formation outcomes. This makes them well suited for capturing subtle effects of hydrogen bonding, molecular shape, and polarity, which are critical for predicting whether two compounds will form a cocrystal. SVMs have demonstrated high accuracy in cocrystal screening applications, as reported by Wicker et al.,

who achieved strong predictive performance using SVMs trained on Cambridge Structural Database.<sup>85</sup>

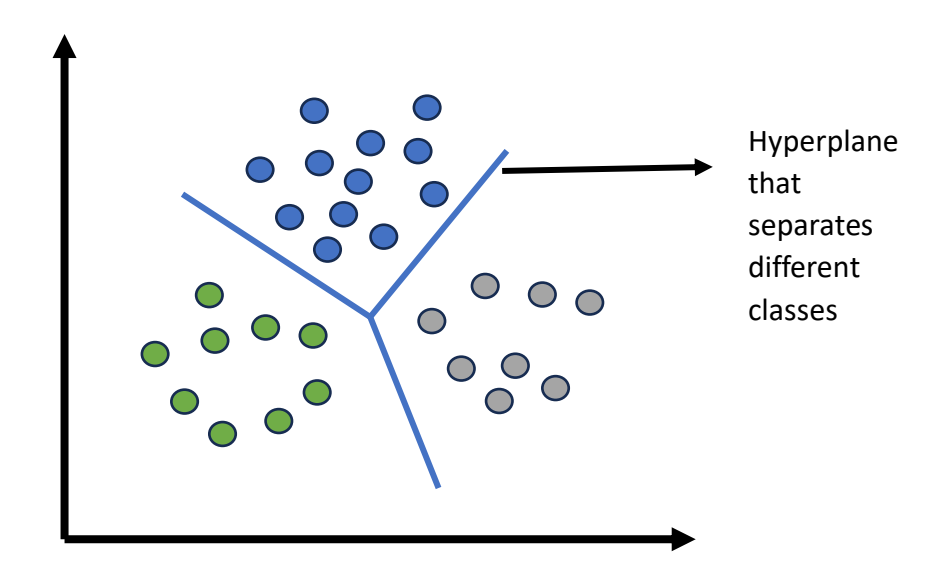


Figure 4-8 Schematic showing Support Vector Machine schematic

#### Naïve Bayes'

Naïve Bayes' classification algorithm is based on Bayes' theorem that identifies the most probable hypothesis based on previous data. The word 'naïve' explains that features are assumed to be independent of each other. This algorithm seems relatively simple, however it is capable of handling multiple classes and has been shown to be computationally efficient.

The formula for Bayes' Theorem is

$$P\{A|B\} = \frac{P\{A \cap B\}}{P\{B\}} = \frac{P\{A\} \cdot P\{B|A\}}{P\{B\}}$$
 Equation 4-2

P{A} = Probability of A occurring (outcomes)

P{B} = Probability of B occurring (descriptors)

P{A|B} = Probability of A(outcomes) given B (descriptors)

 $P\{B|A\}$  = Probability of B given A

 $P\{A \cap B\}$  = Probability of both A and B occurring

#### **Gradient Boosted Trees (XGBoost)**

XGBoost is an advanced machine learning algorithm that builds a series of decision trees, where each new tree focuses on correcting the errors made by the previous ones. This sequential approach enables the model to capture complex, non-linear relationships between molecular descriptors, which is particularly important for predicting cocrystal formation where interactions between features can be subtle. XGBoost stands out for its ability to automatically identify and prioritize the most informative features, such as functional group counts or hydrogen bond donors and acceptors, while also incorporating regularization techniques to prevent overfitting. Its scalability and efficiency make it suitable for handling larger datasets and high-throughput screening. Recent studies in pharmaceutical and materials science have shown that XGBoost and related tree-based models often outperform simpler algorithms in cocrystal prediction tasks, due to their robustness and ability to model intricate feature interactions. <sup>88, 178</sup>

In this study, we filtered our database, originally derived from statistical analysis to only include coformers that have a record of forming cocrystals with both INA and NA. Using Python 3 in Jupyter notebooks, we extract the SMILES strings of coformers in the CSD that meet this criterion (Appendix 3.1). Tightening our coformer standards will allow us to elucidate the molecular characteristics crucial for successful cocrystal formation with NA and INA, informing future screening attempts. All collected data formed part of our internal cocrystal database, which will be used to train our ML algorithm discussed below. At the time of searching, there were a total of 224 cocrystals which were noted in our internal database for machine learning model training. We used Knime analytics platform<sup>179</sup> to create, train and run our machine learning algorithms. Appendix 3.2 shows a selection of these coformers with their SMILES strings and chemical names.

#### 4.3.1 Preprocessing of data for machine learning

In materials science, machine learning processes typically follow a consistent workflow. Raw data undergoes preprocessing to rectify invalid data points and is converted into a format readable by the model or program. This crucial step prevents errors in input data from

misleading the algorithm and producing false positives or negatives. The data format is refined, extraneous information is eliminated, and relevant features are extracted. 180

For this study, the preprocessing involved:

- Importing mol2/SDF files of cocrystal coformers of INA into our workflow. These files
  contain atomic coordinates and connectivity information, useful for calculating bond
  lengths and angles.
- 2. Converting the imported files to KNIME CDK<sup>179</sup> (Chemistry Development Kit) molecules. CDK is an open-source Java library for cheminformatics, providing tools for handling chemical structures.
- 3. Removing empty rows from the dataset to ensure data integrity and eliminate potential errors caused by missing information.
- 4. Appending canonical SMILES<sup>181</sup> strings to the resulting table. Canonical SMILES (Simplified Molecular Input Line Entry System) provide a standardized text representation of chemical structures, ensuring a unique representation for each molecule.
- 5. Using the Mol2/SDF files to create RDKit<sup>182</sup> molecules. RDkit was chosen as the cheminformatics toolkit due to its ability to generate 2D and 3D molecular descriptors for machine learning.
- 6. Generating molecular descriptors using RDkit. These descriptors encode structural and physicochemical properties of molecules, including topological indices, molecular fingerprints, and quantum chemical properties. Scheme showing pre-processing can be seen in Appendix 3.3.

The legitimacy and applicability of the model hinges greatly on the descriptors. A list of descriptors; including number of hydrogen bond donors and acceptors used for model training can be found in Appendix 3.4. Each molecule was analysed using knime 3D viewer as a final check. This process was independently repeated for NA cocrystals, resulting in total of 224 (136 formed with INA, 88 formed with NA); cocrystals as input data. A column was appended for 1= cocrystal with Isonicotinamide and 0=cocrystal with nicotinamide). Whilst this number is smaller than the total number of INA (230) and NA (170) reported cocrystals, it represented our interests better.

## 4.3.2 Selection, training and comparison of machine learning algorithms

The selection of a suitable machine learning algorithm is another vital step in the machine learning pathway. This involves choosing between supervised, semi-supervised and unsupervised learning. The model is selected based on the nature of the problem to be solved, for example, classification, regression or clustering. We trialled logistic regression, Naïve Bayes classifiers, support vector machines (SVM) and extreme gradient boosted trees (XGB).

For all algorithms, we partitioned 90% for training, with the remaining 10% used for testing. Training data was drawn randomly, using a random seed. Default parameters were used for each algorithm.

Feature selection algorithms that identify and prioritize the most relevant descriptors have proven valuable in machine learning tasks. These methods reduce dimensionality by excluding irrelevant or redundant features while retaining those with high predictive power.<sup>90</sup>

However, we did not utilise these, rather we compared prediction accuracy when all RDkit molecular descriptors are used, D<sub>all</sub>, and when only integer descriptors such as such as number of bonds, molecular weight, number of donors/acceptors, D<sub>num</sub>. A summary is shown in Appendix 3.4.

Our analysis revealed varying effects when reducing the number of descriptors in our machine learning models. The Support Vector Machine and XGBoost algorithms experienced a decrease in overall accuracy. In contrast, Logistic Regression showed a notable 25% improvement in accuracy, while Naïve Bayes demonstrated a 15% increase. Among all tested algorithms, SVM consistently exhibited the best predictive ability for cocrystal classification problems, aligning with previous findings in the literature.<sup>85, 183</sup> However, it is crucial to interpret these results cautiously. Despite the improvements observed in some models, the Cohen's kappa statistic, which measures inter-rater agreement, indicated either no agreement or only slight agreement across all models. This proves that the overall accuracy of all algorithms remains poor, and any apparent correlations may be spurious.<sup>85</sup>

**Table 4-2**. Accuracy<sub>all</sub> vs Accuracy<sub>num</sub> of each model based on their confusion matrices , overall accuracy, and Cohens Kappa.

Model	Overall accuracy <sub>all</sub>	Overall accuracy <sub>num</sub>
SVM	0.609	0.565↓
Naïve Bayes	0.478	0.522 ↑
Gradient boosted trees	0.435	0.391↓
Logistic Regression	0.345	0.601 1

The variation in model performance observed with the reduction in number of descriptors can be attributed to the correlation between model complexity and overfitting tendences. SVM and XGB are complex algorithms, capable of capturing intricate patterns in chemical data sets. <sup>89</sup> A reduction in accuracy with fewer descriptors suggests that reducing the number of descriptors results in a loss of potentially useful information. These models are capable of utilising complex relationships between a large number of features to make accurate predictions. On the other hand, too many descriptors may lead to the model overfitting the noise in the data, hence a balance between retaining enough useful descriptors and avoiding irrelevant ones is crucial and thus the appeal of feature selection algorithms. <sup>184</sup>

In contrast, Naïve Bayes and logistic regression are simpler models with a lower tendency to overfit. Reducing the feature set can mitigate the risk of overfitting for these models, enabling them to focus on the most relevant patterns, benefitting for the more streamlined feature set.<sup>185</sup>

A significant limitation of this machine learning study was the lack of negative data, on failed cocrystallisation experiments, from literature and experimentally. The input data only contained positive information on successfully formed cocrystals, which introduces an inherent bias in the training dataset.<sup>85</sup> Consequently, having two sets of "positive" inputs - cocrystals formed with INA and those formed with NA - does not provide sufficient contrast for training an accurate predictive algorithm. Another limitation was the relatively small

sample size used in this study. In contrast, Wicker *et al.* conducted a more comprehensive study, training their model with 657 cocrystal data inputs that included both successful and unsuccessful attempts. This larger, balanced dataset likely contributed to a more accurate predictive model<sup>85</sup>. To inform future studies, it would be beneficial to actively generate negative data from failed cocrystallisation experiments. Our analysis of the Cambridge Structural Database (CSD) revealed intriguing patterns in the stoichiometric ratios of cocrystals formed with isonicotinamide (INA) and nicotinamide (NA). This observation prompted us to conduct a comprehensive screening and characterization of cocrystal combinations in various stoichiometries (1:1, 1:2, 2:1), with the aim of developing a robust database containing both successful and failed cocrystallisation attempts.

# Chapter 5 – Studying stoichiometry in cocrystals

From our database of cocrystals, we selected 5 coformers for our stoichiometry screening. These coformers are known to form at least a 1:1 cocrystal with both INA and NA and were easily accessible. We also selected one common drug molecule sulfasalazine that has not been reported to form cocrystals with INA and NA, but has the supramolecular synthons ideal for cocrystallisation, and therefore should form a cocrystal.

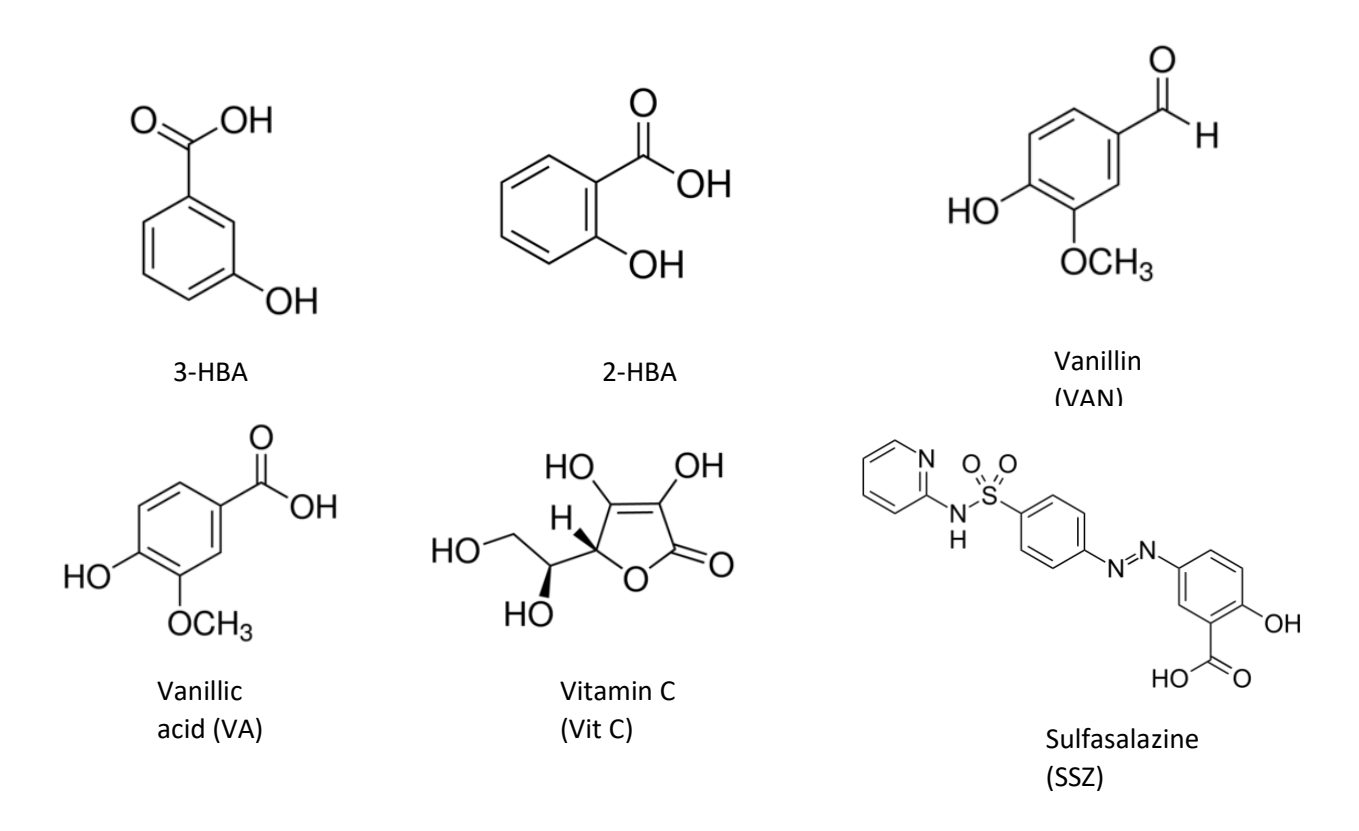


**Figure 5-1** Six coformers of interest. 3-hydroxybenzoic acid, 2-hydroxybenzoic acid, vanillin, vanillic acid, vitamin C and sulfasalazine

#### 5.1 Solid State

#### Liquid assisted grinding

Cocrystal screening was performed by liquid assisted grinding (LAG) using a Retsch Ball Mill MM400 model. For 1:1 and 2:1 grinding experiments, 122.1 mg of INA and NA was added to the stoichiometric amount of the coformer as seen in Appendix table 3.5, and 50  $\mu$ l of ethanol into 10 ml jars, and ground at 30 Hz for 30 minutes. The products were analysed and

characterised by IR, TGA, DSC, PXRD and where relevant, solid-state NMR. Full table of coformer masses can be found in appendix.

#### Screening results and analysis

As mentioned above, each product was initially analysed using PXRD. This was to compare the powder patterns with those of the individual coformers, and with any other known cocrystal structure. If these were visually confirmed as different to previously reported patterns, then thermal analysis was conducted. Solid-state NMR spectra were measured for products that were clearly different in PXRD and DSC, for cocrystals which did not have solidstate NMR spectra reported, and for any product that proved ambiguous by other characterisation techniques. A summary of screening results can be found in Table 5. 32 cocrystal screening attempts were made via LAG, of which twelve produced cocrystals reported in literature. Nine screening experiments produced new solid forms. It is interesting to note, that all the 'failed' cocrystallisation attempts actually yielded a different stoichiometric ratio cocrystal for example, a screening attempt for a 1:2 cocrystal actually resulted in a 1:1 cocrystal and excess of the pure stoichiometric coformer. No combination resulted in two pure starting materials post grinding – confirming the supramolecular synthon theory that specific intermolecular interactions guide cocrystal formation. 186 The fact that excess coformer remained pure while the 1:1 cocrystal formed suggests a hierarchy of interactions, with the cocrystal synthons being more favourable than those in the pure coformer crystal.44, 187-189

Table 5-1 Cocrystal screening results showing products formed from LAG.

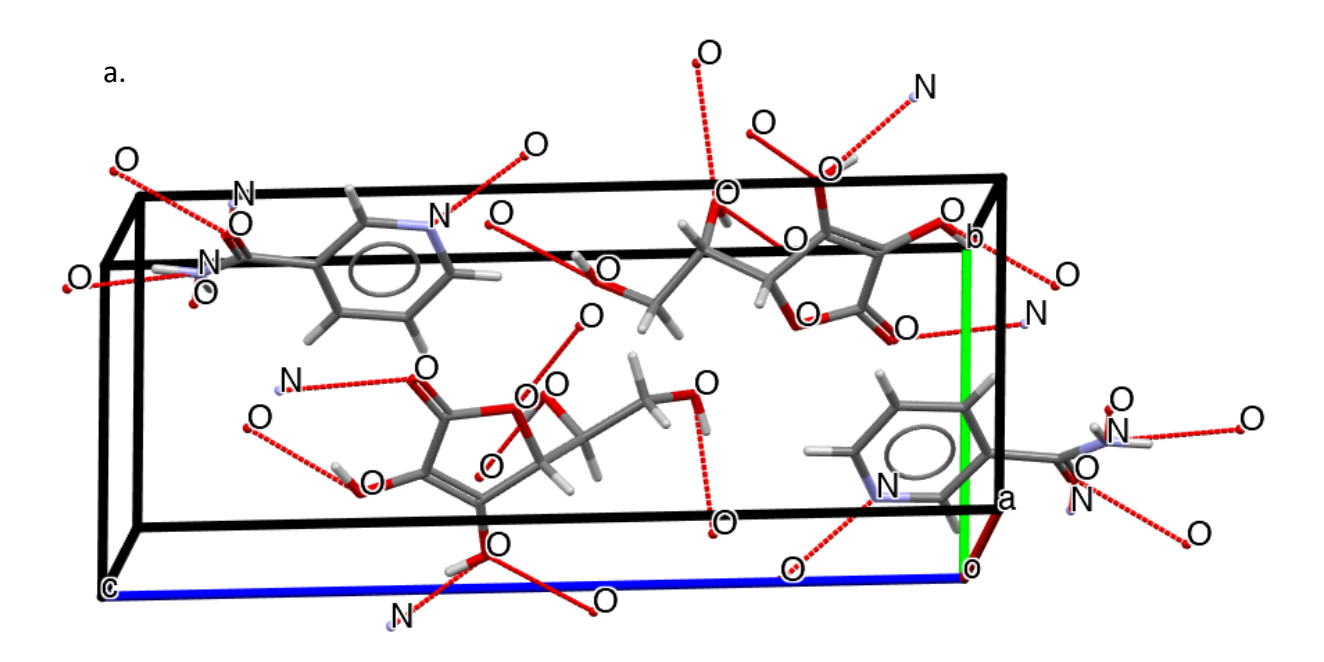
Coformer	INA/NA	Stoichiometry	New LAG	Previously	
			product formed	reported	Result
Vitamin C	Nicotinamide	1:1	Yes	Yes	Cocrystal
Vitamin C	Nicotinamide	1:2	No	No	1:1 cocrystal + excess NA
Vitamin C	Nicotinamide	2:1	Yes	No	NEW SOLID FORM
Vitamin C	Isonicotinamide	1:1	Yes	Yes	Cocrystal
Vitamin C	Isonicotinamide	1:2	Yes	Yes	Cocrystal

Vitamin C	Isonicotinamide	2:1	No	No	1:1 + excess Vit C
Vanillin	Nicotinamide	1:1	Yes	Yes	Cocrystal
Vanillin	Nicotinamide	1:2	No	No	1:1 cocrystal + excess NA
Vanillin	Nicotinamide	2:1	No	No	1:1 cocrystal + excess vanillin
Vanillin	Isonicotinamide	1:1	Yes	Yes	Cocrystal
Vanillin	Isonicotinamide	1:2	No	No	1:1 cocrystal + excess INA
Vanillin	Isonicotinamide	2:1	No	No	1:1 cocrystal + Excess VAN
Vanillic Acid	Isonicotinamide	1:1	No	Yes	1:2 (0.5:1) cocrystal and excess Vanillic acid
Vanillic Acid	Isonicotinamide	1:2	Yes	Yes	1:2 cocrystal form <sup>190</sup>
Vanillic Acid	Isonicotinamide	2:1	No	No	1:2 cocrystal + excess Vanillic acid
Vanillic Acid	Nicotinamide	1:1	Yes	Yes	Cocrystal
Vanillic Acid	Nicotinamide	1:2	Yes	No	NEW SOLID FORM
Vanillic Acid	Nicotinamide	2:1	No	No	1to1 cocrystal + excess Vanillic acid
2-HBA	Isonicotinamide	1:1	Yes	Yes	Cocrystal
2-HBA	Isonicotinamide	1:2	Yes	No	NEW SOLID FORM
2-HBA	Isonicotinamide	2:1	Yes	Yes	Cocrystal
2-HBA	Nicotinamide	1:1	Yes	Yes	Cocrystal
2-HBA	Nicotinamide	1:2	No	No	1:1 + excess NA
2-HBA	Nicotinamide	2:1	No	No	1:1 + excess 2- HBA

3-HBA	Isonicotinamide	1:1	Yes	Yes	Cocrystal
3-НВА	Isonicotinamide	1:2	No	No	1:1 cocrystal + excess INA
3-HBA	Isonicotinamide	2:1	No	No	1:1 cocrystal + excess 3HBA
3-HBA	Nicotinamide	1:1	Yes	Yes	Cocrystal
3-HBA	Nicotinamide	1:2	Yes	No	NEW SOLID FORM
3-НВА	Nicotinamide	2:1	No	No	1:1 cocrystal + excess 3-HBA
Sulfasalazine	Isonicotinamide	1:1	Yes	No	NEW SOLID FORM
Sulfasalazine	Nicotinamide	1:1	Yes	Yes	NEW SOLID FORM

## 5.1.1 Vitamin C<sub>2</sub>:Nicotinamide<sub>1</sub>

Vitamin C, also known as L-ascorbic acid, is one of four possible stereoisomers of ascorbic acid. It is a common cocrystal coformer and has many pharmaceutical applications in neurology, endocrinology, digestion, absorption and immunology<sup>191</sup>. Vitamin C has the ability to act as a hydrogen bond donor through its aromatic -OH and aliphatic alcohol groups and acceptor and through its oxygen atoms. Vitamin C and nicotinamide have been reported to form cocrystals in 1:1 and 1:3 ratios.<sup>192, 193</sup> The 1:1 cocrystal has 2 known polymorphs, CSD REFCODE OXOHEQ and OXOHEQ01.<sup>194</sup> Both polymorphs have 2 molecules each in the asymmetric unit, as seen in Figure 5-2. The network forms through an aromatic-OH···N-pyridine bonds between vitamin C and NA. The amide group bonds to 2 different NA molecules via a C=O···NH bond, and to another vitamin c molecule by the aromatic OH···O=C bond. The 1:3 cocrystal however, forms a complex network of stacks of Vit C and NA, bonded by a OH···N-pyridine. NA molecules are joined together by a NA-NA homodimer. The unit cell contains the coformers in a 2:6 ratio. Shockingly, two out of the six NA N-pyridine groups do not participate in hydrogen bonding.



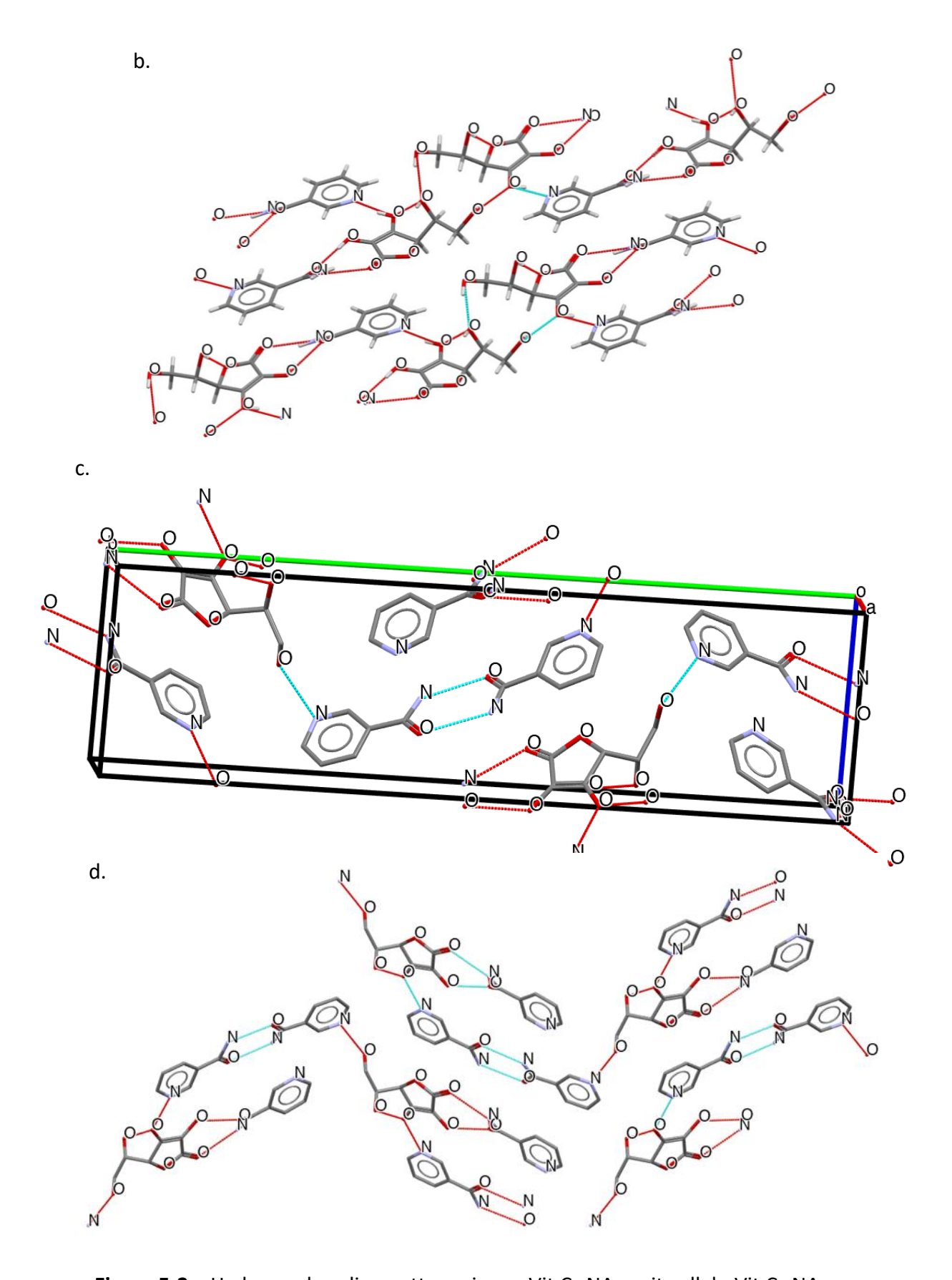


**Figure 5-2** – Hydrogen bonding patterns in - a. Vit  $C_1$ :NA<sub>1</sub> unit cell, b. Vit  $C_1$ :NA<sub>1</sub> intermolecular interactions, c. Vit  $C_1$ :NA<sub>3</sub> unit cell, d. Vit  $C_1$ :NA<sub>3</sub> intermolecular interactions.

Characterisation of the LAG product "Vit  $C_2$ :NA<sub>1</sub>" reveals a melting point different to starting materials, and the 1:1 cocrystal. Pure nicotinamide has a melting point at ca. 128°C, vitamin C decomposes between 190 and 192°C and the 1:1 cocrystal melts at 145.6 °C. However, the product with 2:1 ratio has a melting point at ca. 140°C. Interestingly, we see a small endothermic peak in this product at ca. 145°C, overlapping with the 1:1 co-crystal peak. This confirms a small amount of 1:1 co-crystal is present, but also suggests that the product contains another compound, different to the 1:1 cocrystal.

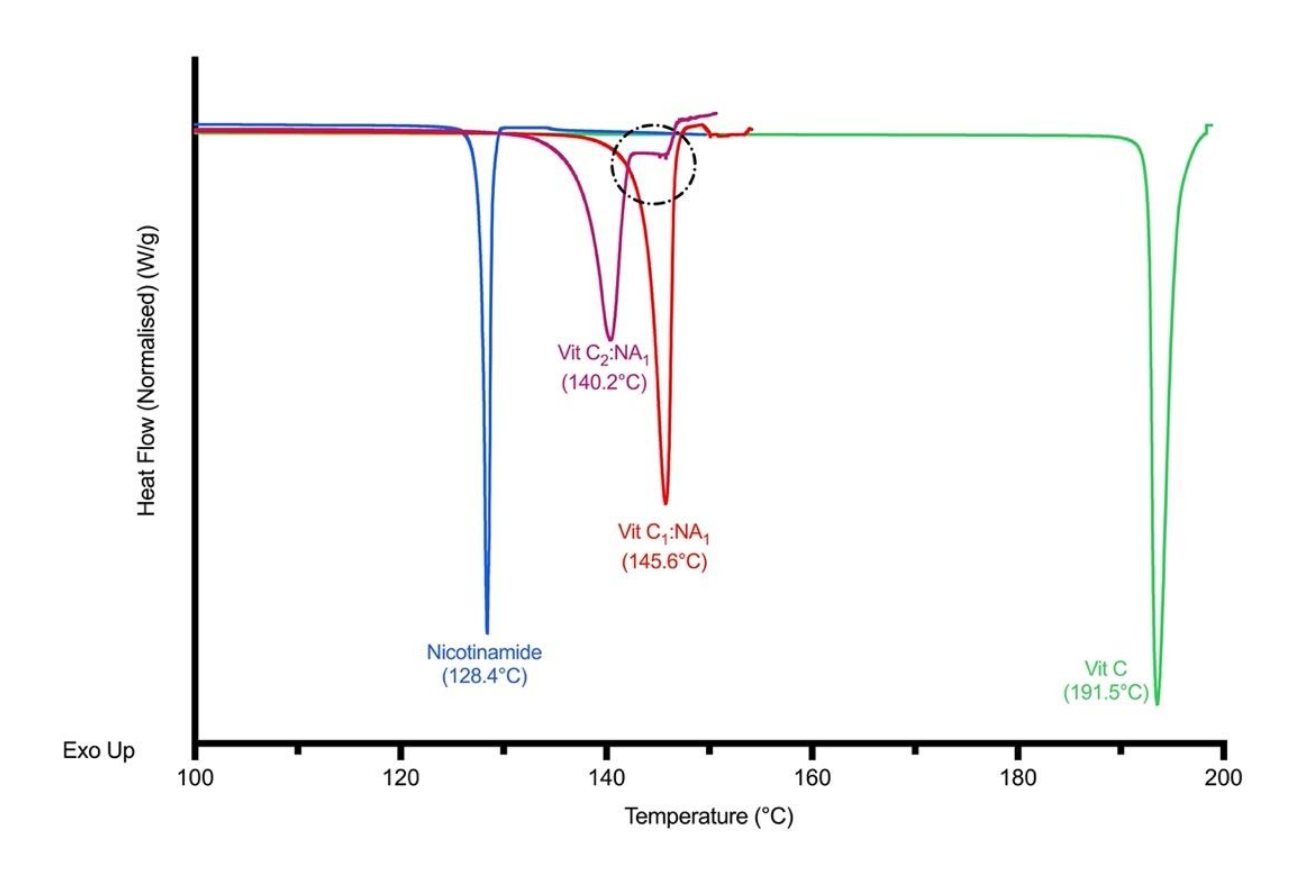
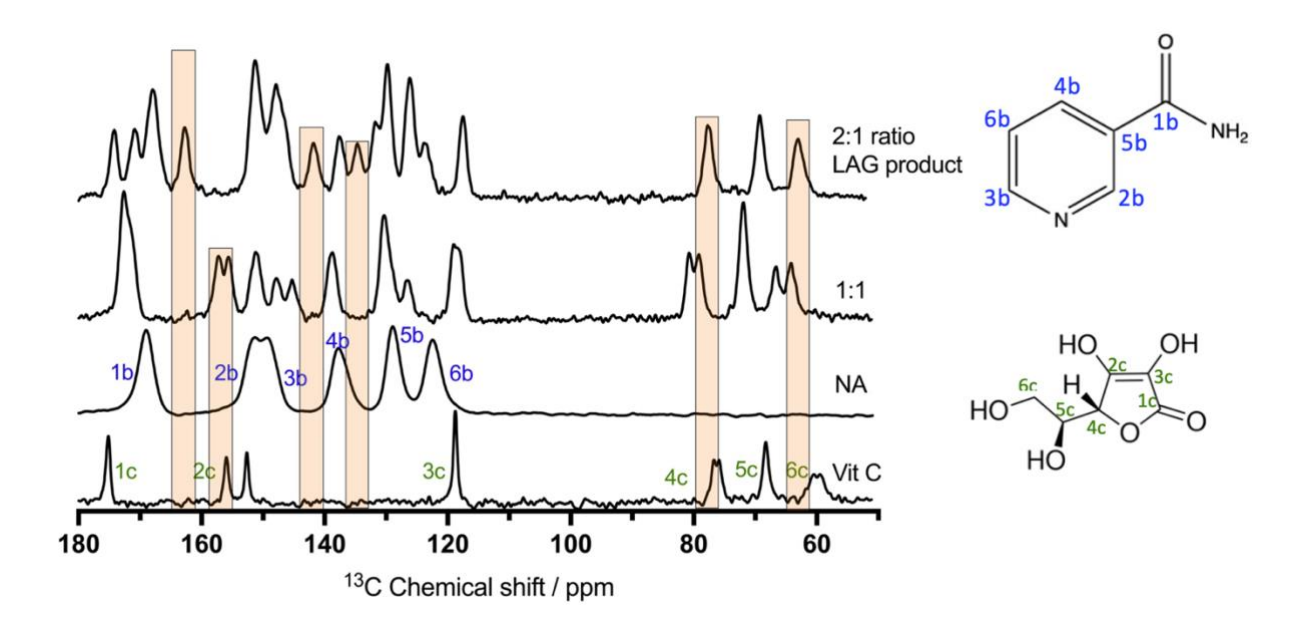


Figure 5-3 - DSC thermograms of Vitamin C, NA, 1:1 and suspected 2:1 cocrystal



**Figure 5-4** - <sup>1</sup>H-<sup>13</sup>C CP/MAS NMR spectra of Vitamin C, NA, 1:1 (OXOHEQ) and suspected 2:1 cocrystal.

<sup>13</sup>C CP/MAS NMR spectroscopy reveals distinct differences in chemical shift positions of the 2:1 LAG product, the 1:1 cocrystal and the starting materials. In the region between 180 and 160 ppm, in the spectrum of the 1:1 cocrystal, we observe 2 peaks. However, in the 2:1 LAG product, there are 4 peaks present, with only one peak traceable to its position in the Vit C spectra. In the 2:1 cocrystal, we note many changes in peak positions compared to 1:1 and starting materials (highlighted in Figure 5-4). In the 160-120 ppm range, new peaks arise at 134 and 142ppm ppm. The peaks at the aliphatic region between 55 and 85 ppm also shift considerably, and combine, suggesting a different packing arrangement compared to pure Vit C and the 1:1 cocrystal.

The powder X-ray diffraction (PXRD) analysis yielded intriguing results that provide further insights into the structure of our cocrystal products. We were able to confirm that the 1:1 polymorph produced from our liquid-assisted grinding (LAG) attempt is identical to the previously reported structure with the Cambridge Structural Database reference code OXOHEQ<sup>192</sup>. Unfortunately, due to technical issues, our Rigaku smartlab LE PXRD diffractometer was out of service, rendering us unable to obtain high-resolution data for the 2:1 LAG product that would be directly comparable to the 1:1 cocrystal pattern. Instead, we had to rely on a benchtop Rigaku diffractometer, which, while functional, offers significantly

lower resolution. This limitation somewhat hampers our ability to make precise comparisons between the 1:1 and 2:1 product by PXRD.

Despite the lower resolution, the PXRD pattern of the 2:1 LAG product still provides valuable information. We observed that some peaks in the 2:1 pattern overlap with those of the 1:1 cocrystal, suggesting similarities in certain aspects of their crystal structures. However, the appearance of new, distinct peaks in the 2:1 pattern indicates the presence of a novel crystal structure, different from both the 1:1 cocrystal and the starting materials. These PXRD findings, although limited by the resolution constraints, corroborate our other analytical results, particularly the DSC and solid-state NMR data. They support the conclusion that the 2:1 LAG product represents a new cocrystal form, distinct from the known 1:1 cocrystal, while potentially sharing some structural features. Further high-resolution PXRD analysis, once equipment is available, would be beneficial to fully characterize this new cocrystal form.

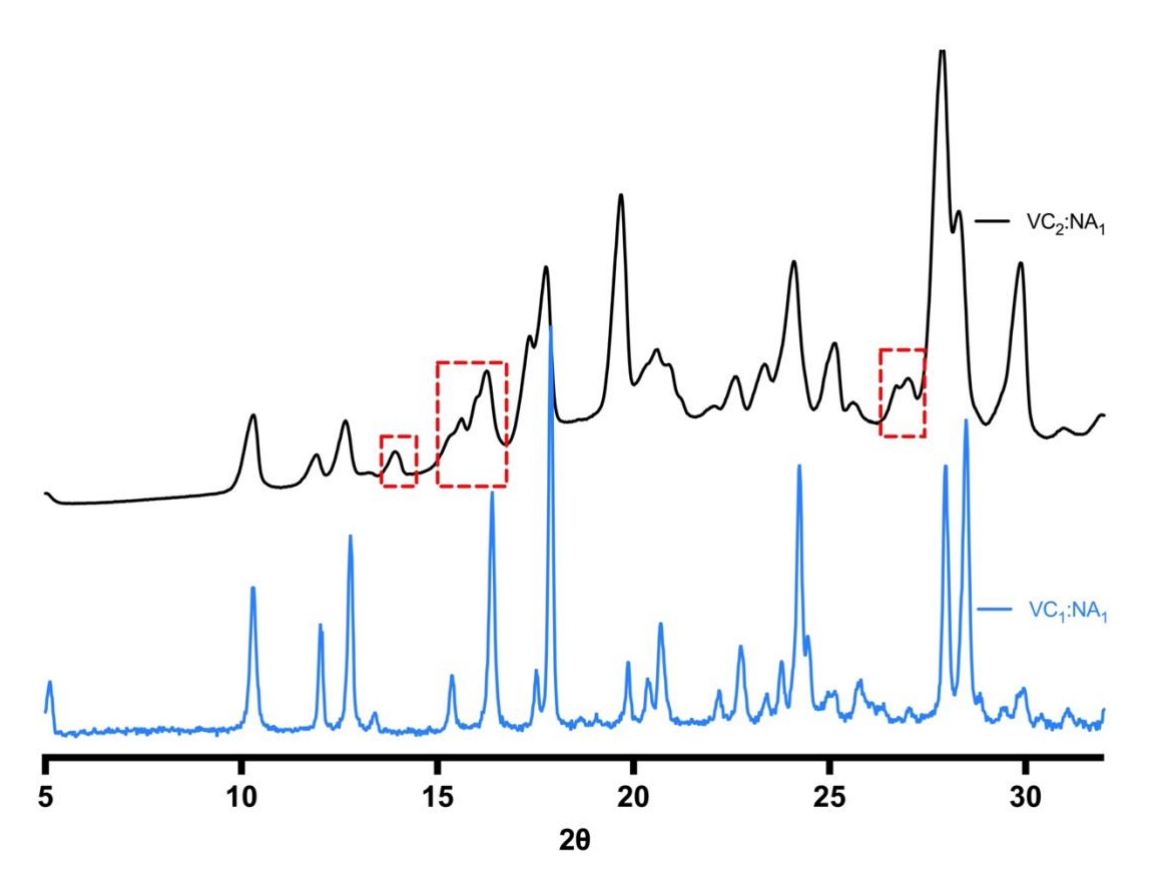


**Figure 5-5** PXRD patterns of VC<sub>2</sub>:NA<sub>1</sub> (Rigaku Smartlab SE) and VC<sub>1</sub>:NA<sub>1</sub> (Rigaku benchtop diffractometer). Key differences highlighted in red. Differing instrument resolutions limit direct peak comparisons.

#### 5.1.2 Vanillic Acid<sub>1</sub>:Isonicotinamide<sub>2</sub>

Vanillic acid is the oxidized form of vanillin and has similar properties and applications in various industrial sectors as mentioned above. Natural VA can be found in foods such as guava, rice, oranges as well as drinks such as scotch and Canadian whisky. VA has been shown to possess cardioprotective properties, antioxidant ability and to prevent apoptosis. <sup>195-197</sup> This dihydroxybenzoic acid is an intermediate in the formation of vanillin from ferulic acid. It is of relevant in supramolecular engineering due to its possession of phenolic-OH and a carboxylic acid, both HBA and HBD and an ether functional group which can accept hydrogen bonds. VA has been reported to form cocrystals with amides such as ethenzamide<sup>198</sup>, pyrazinecarboxamide, <sup>199</sup> nicotinamide<sup>190</sup> and isonicotinamide. Interestingly, VA molecules adopt an R<sub>2</sub><sup>2</sup> (8) acid-acid homosynthon formation. <sup>200</sup> However, in some cocrystals with amides such as ethenzamide, the acid-amide synthon is formed, and with others such as pyrazinecarboxamide, the acid-acid homosynthon is maintained.

 $VA_1$ :INA<sub>2</sub> has been reported<sup>190</sup> as forming a cocrystal from a mixture of chloroform and diethyl ether. Noa *et al.* also report a PXRD pattern from their attempt to form a 1:2 cocrystal by LAG. They report this as a failed attempt and describe the result as a physical mixture.

On comparison, the PXRD patterns from Noa *et al* 'failed' LAG attempt and the LAG attempt presented in this work display the same peaks, however our higher resolution PXRD pattern, in addition to thermal analysis, <sup>13</sup>C CP/MAS sheds more light on this situation.

DSC analysis of our VA<sub>1</sub>:INA<sub>2</sub> LAG product produced a single peak, at 136.2°C, slightly lower than the 1:2 cocrystal produced from solution, at 142.4°C. However, a single peak is observed until decomposition begins, therefore we can assume that the product is a single phase.

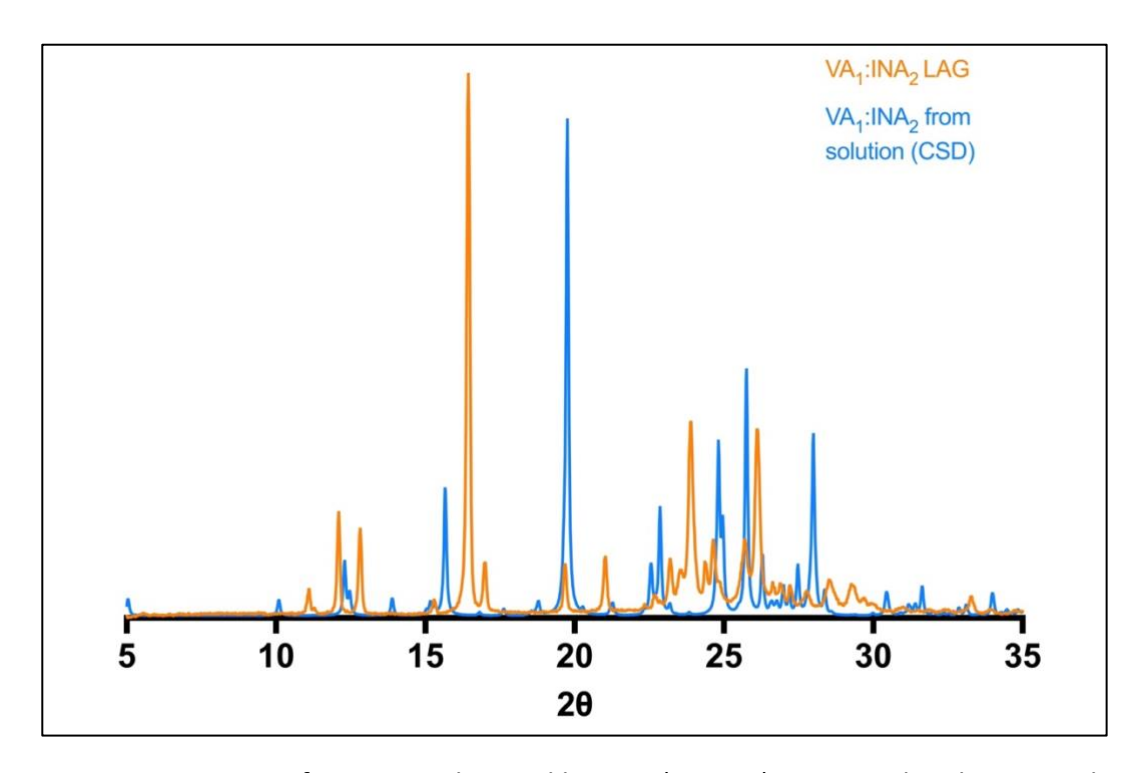


**Figure 5-6** - PXRD pattern of VA<sub>1</sub>:INA<sub>2</sub> obtained by LAG (orange) compared with cocrystal obtained from solution CSD – Noa *et al*<sup>190</sup>.

Interestingly, when we performed LAG with a ratio of VA<sub>1</sub>:INA<sub>1</sub>, we observe melting at the same temperature of 136°C without subsequent decomposition. This is because when these coformers undergo LAG in a 1:1 ratio, the 1:2 (0.5:1) LAG product is observed with an excess of Vanillic Acid. We observe this clearly from DSC, as no excess INA is observed and <sup>13</sup>C CP/MAS, where VA peaks are seen in addition to the new 1:2 form.

As mentioned above, Noa et~al. suggest that this LAG product is a physical mixture. However, on comparing PXRD patterns, we see that there is minimal overlap. For example, peaks at 9.34, 10.2, 21.9° 20 from vanillic acid, and peaks at 17.86, 19.38 and 31.2° 20 from isonicotinamide are not present. We see new, distinct peaks at 11.2, 12.1, 16.4 and 24.6° 20, which rather suggest that it is a different solid form.

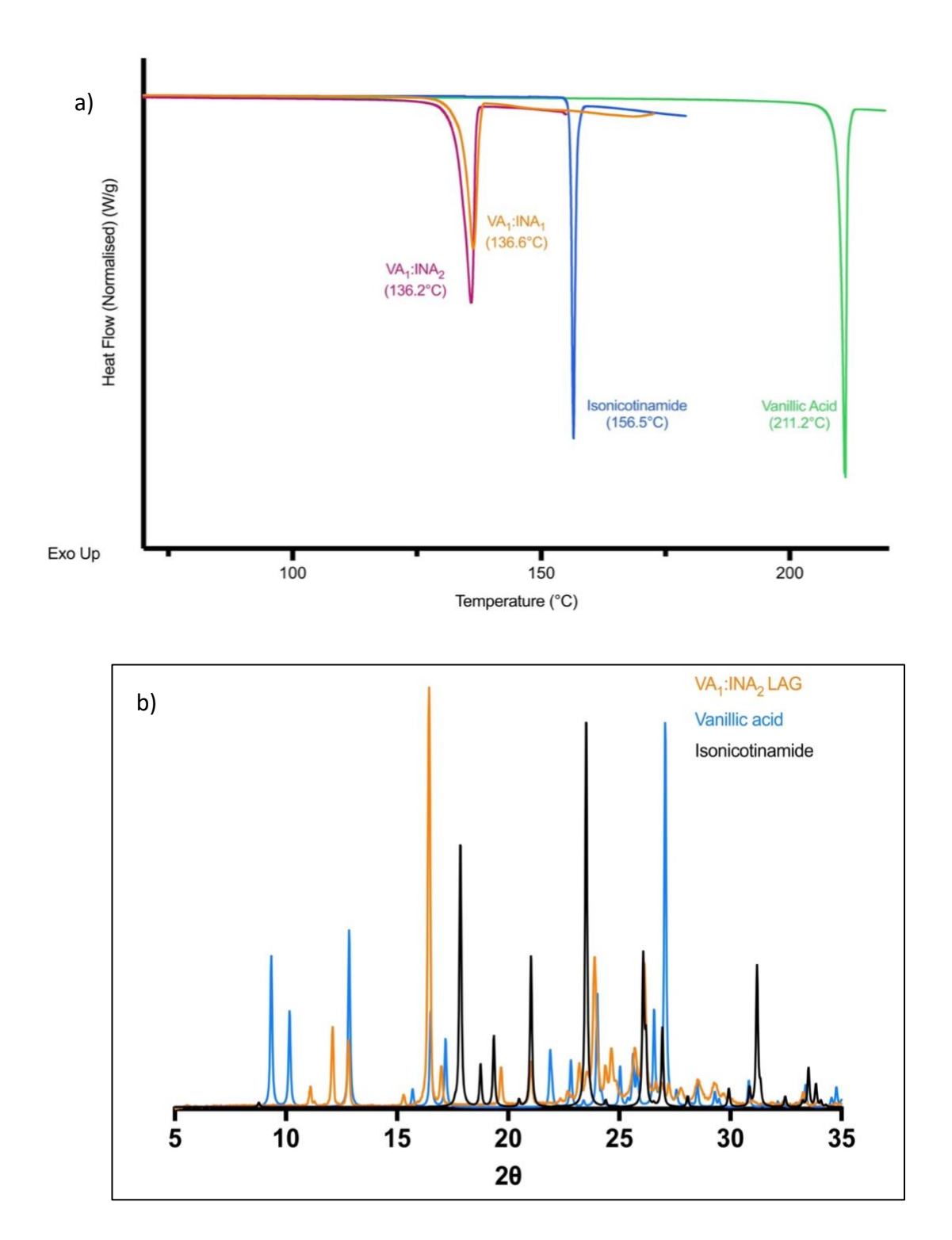


**Figure 5-7** – a) DSC plot of VA, INA, 1:1 LAG product and 1:2 LAG product. B) PXRD pattern of VA, INA and 1:2

<sup>1</sup>H-<sup>13</sup>C CP/MAS NMR corroborates the findings from DSC and PXRD. We see clear changes in chemical shifts, and the rise of new peaks. The VA carboxylic peak at 173.7 ppm shifts to 169.4 ppm in the LAG product, with the amide from INA shifting from 172.9 to 171 ppm. We also see changes in peak positions in the aromatic region between 140 and 160 ppm. INA aromatic carbon shifts from 153 to 148.9 ppm. The methyl carbon shifts from 57.1 to 56.3 ppm. Comparing the <sup>1</sup>H-<sup>13</sup>C CP/MAS NMR spectra of the 1:1 and 1:2 products clearly corroborate the findings from the DSC, the formation of a '0.5:1 cocrystal' with the excess of vanillic acid, can be seen from the direct overlap and missing peaks. We observe sharp peaks at 173.7ppm and 111ppm from pure VA, in the spectrum from the 1:1 LAG product.

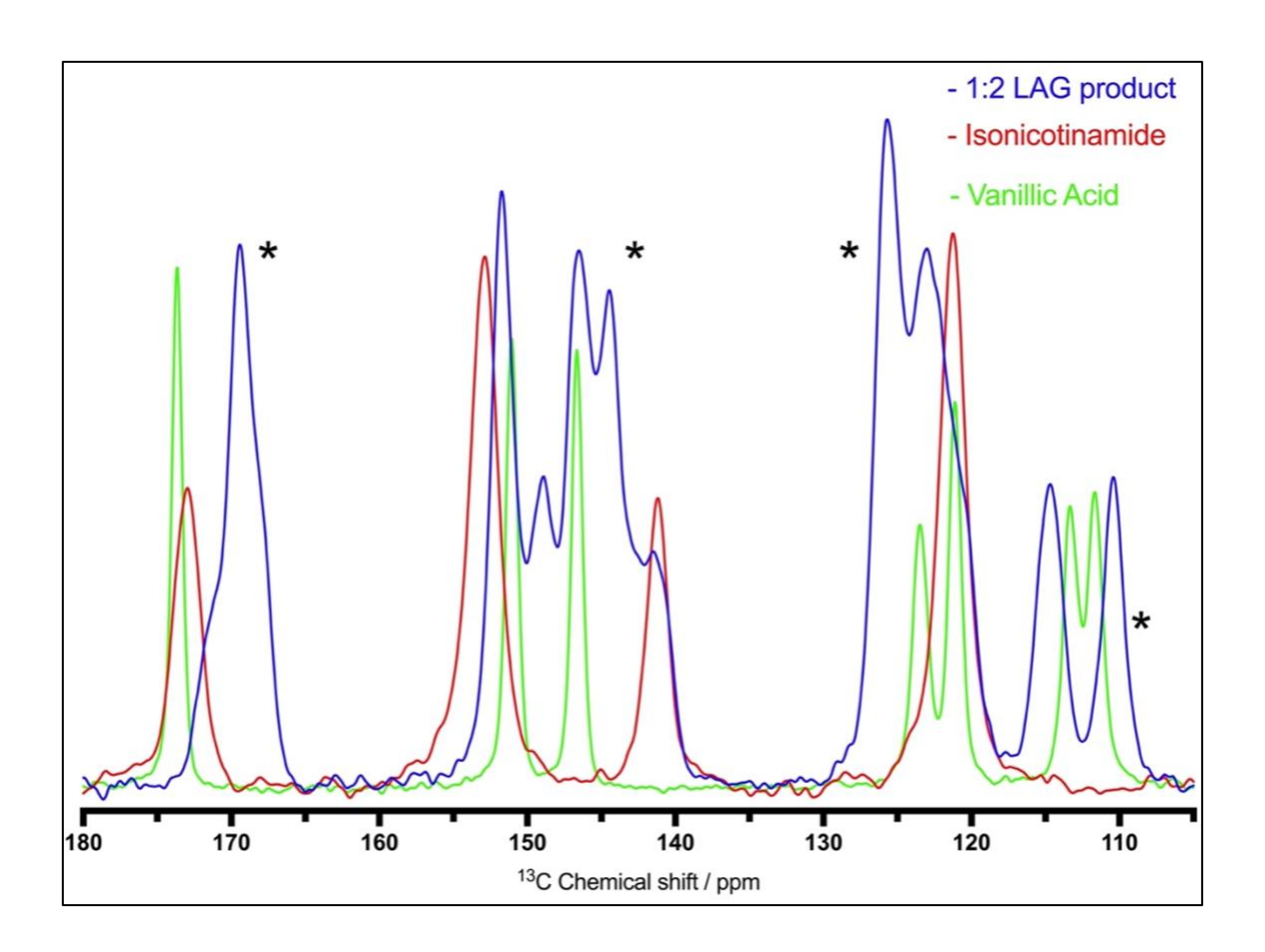
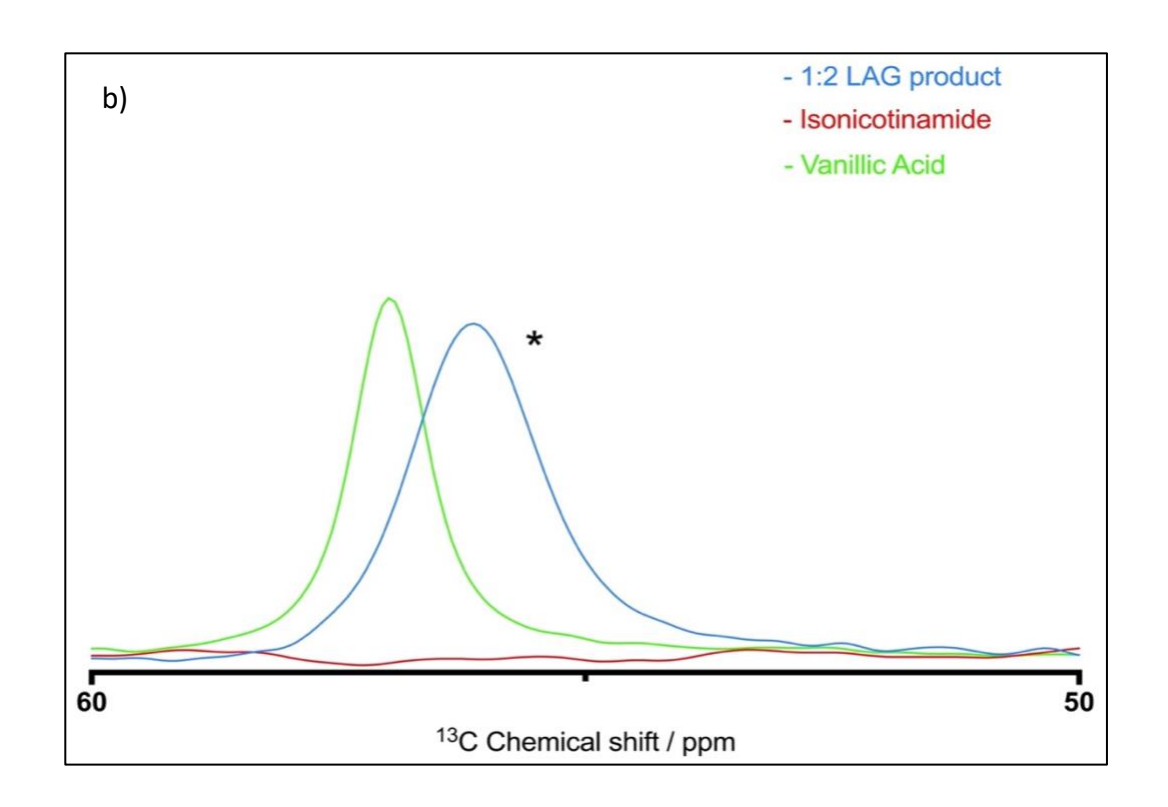
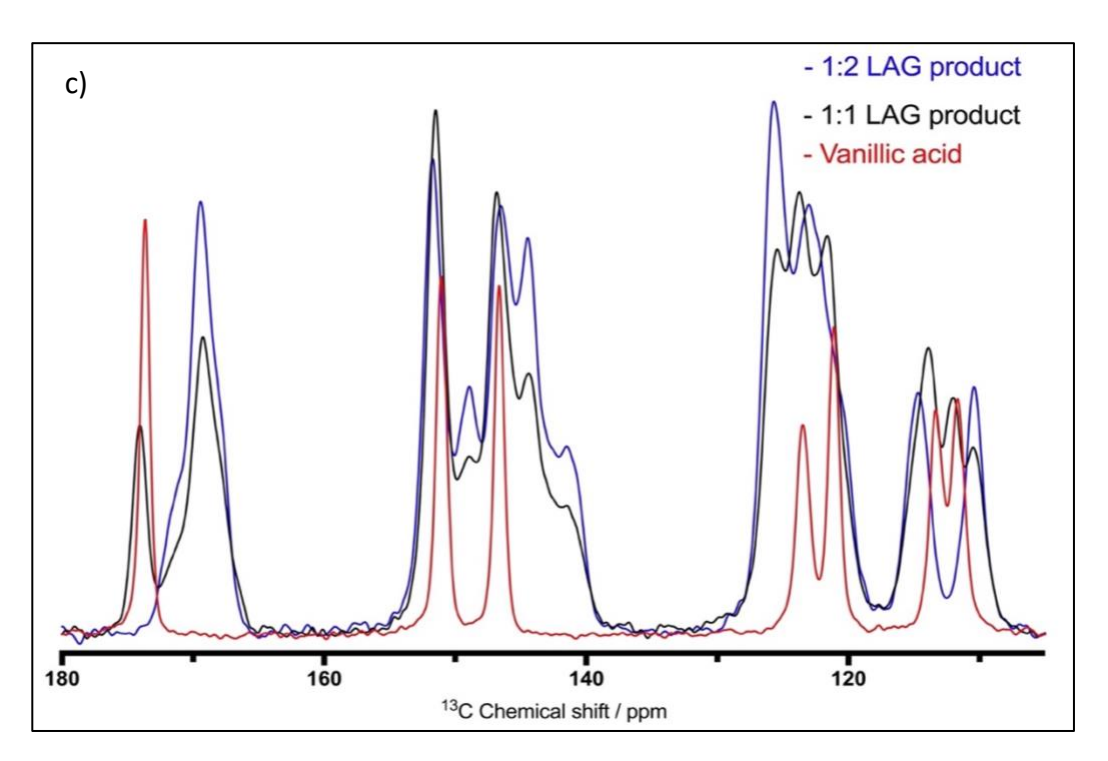


Figure 5-8 a) <sup>1</sup>H-<sup>13</sup>C CP/MAS 1:2 LAG product compared to pure VA and INA.





**Figure 5-9** – b)  $^{1}$ H- $^{13}$ C CP/MAS 1:2 LAG product compared to pure VA and INA, zoomed in on the aldehyde region. c)  $^{1}$ H- $^{13}$ C CP/MAS comparing 1:2 LAG product, 1:1 LAG product and Vanillic Acid

## 5.1.3 Vanillic Acid<sub>1</sub>:Nicotinamide<sub>2</sub>

In the reported  $VA_1:NA_1$  cocrystal, we see this  $R_2^2$  (8) acid-acid homosynthon, with the VA and NA molecules interacting via only a N-pyridine – Phenol -OH bond. The amide group bonds with neighbouring amide molecules via a C=O---NH<sub>2</sub> to form a chain.

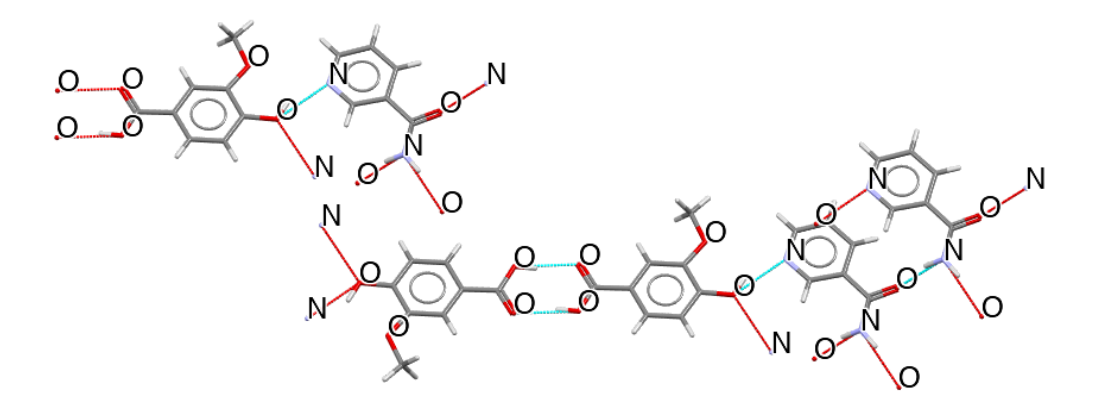


Figure 5-10. Hydrogen bonding pattern in VA<sub>1</sub>:NA<sub>1</sub>

Thermal analysis of the VA<sub>1</sub>:NA<sub>2</sub> LAG product shows a distinct, sharp peak at 124.8°C, which differs from the 1:1 cocrystal's melting point of 134.2°C. There is a small peak at 128.4°C, suggesting a small impurity of NA present, however the size of it suggests that the amount is minute, compared to the large peak representing a new material.

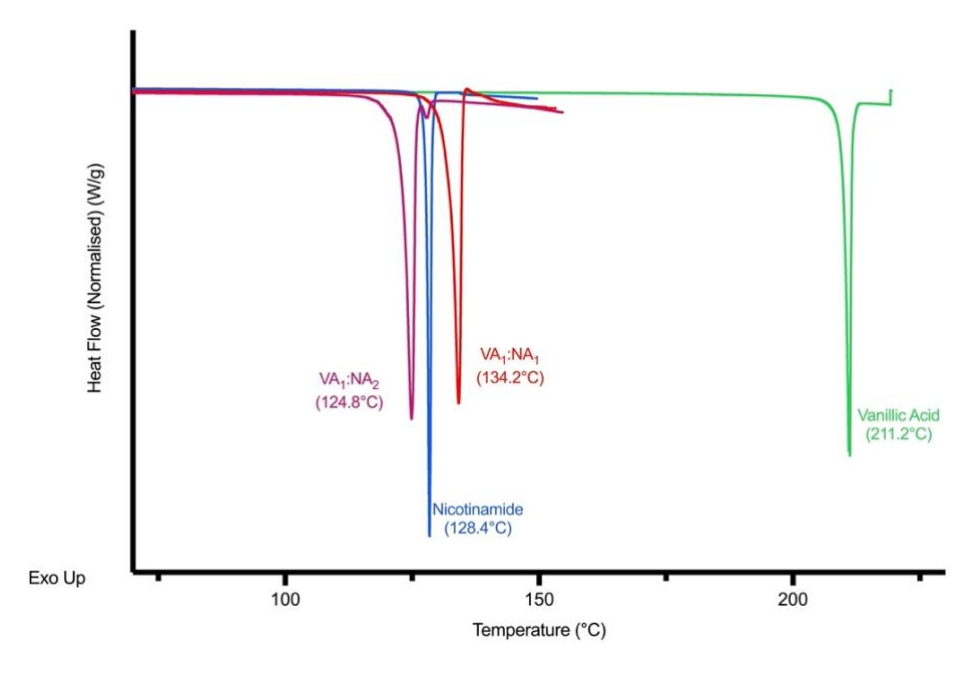


Figure 5-11. DSC thermograms of VA, NA, VA<sub>1</sub>:NA<sub>1</sub> and VA<sub>1</sub>:NA<sub>2</sub>.

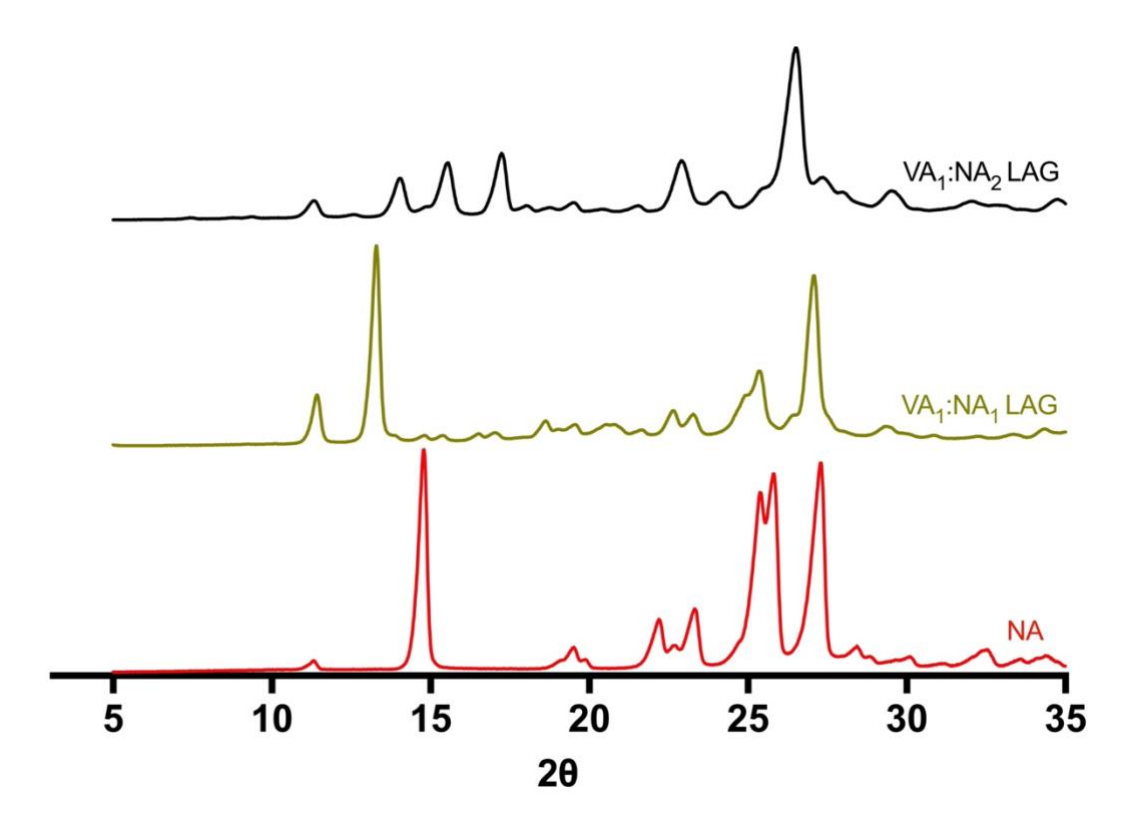
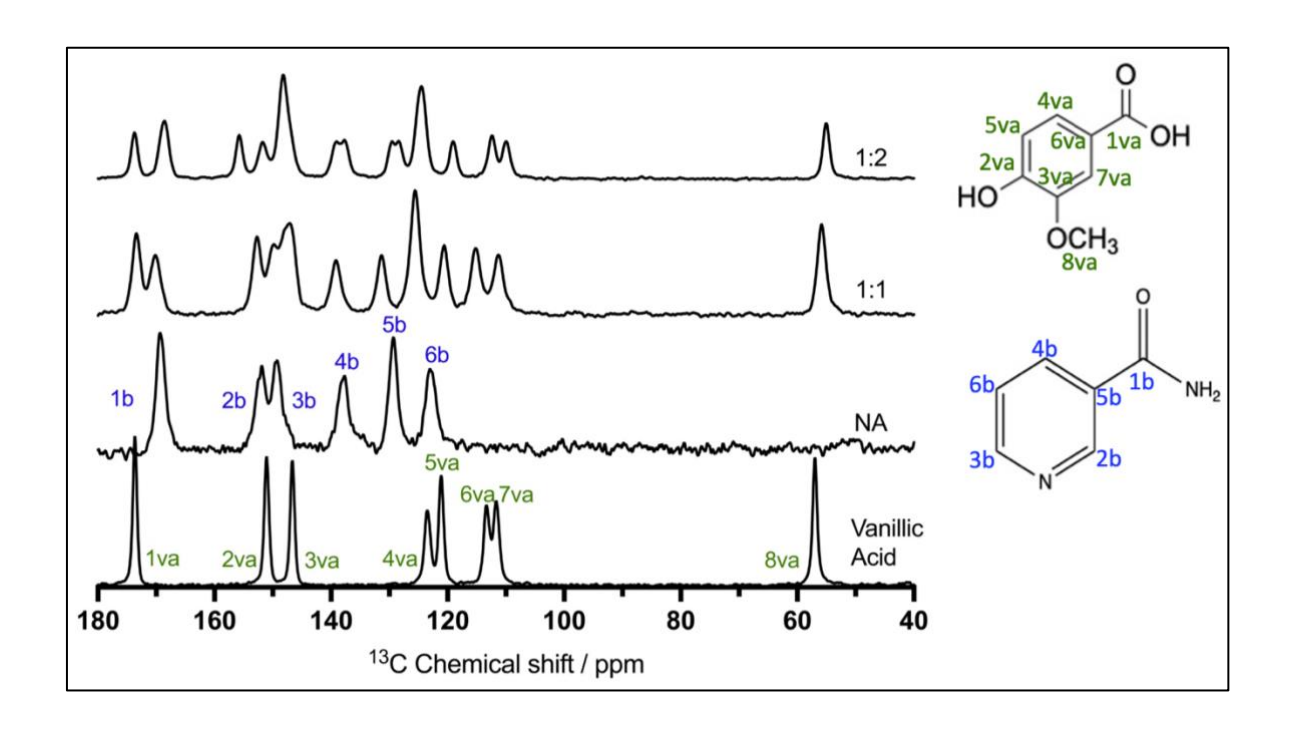
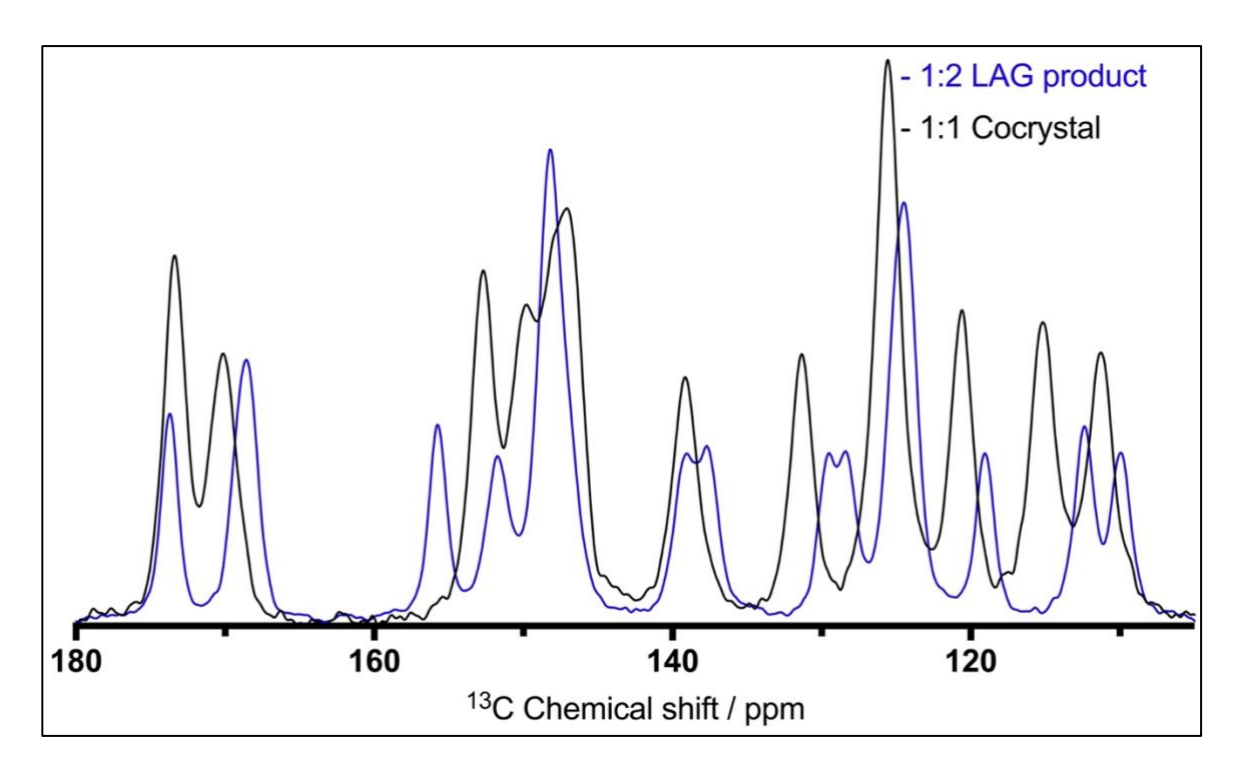


Figure 5-12. PXRD pattern of VA<sub>1</sub>:NA<sub>2</sub> compared to those of VA<sub>1</sub>:NA<sub>1</sub> and pure NA

PXRD pattern shows differences in peak positions with a large peak at 17.3° 2θ, confirming a different solid form. Comparing <sup>1</sup>H-<sup>13</sup>CP/MAS NMR spectra, we can clearly see changes in peak positions, suggesting a different packing arrangement of the coformers. The peak at 169.4 ppm, which represents the NA amide group, shifts downfield in the 1:1 cocrystal to 170.3 ppm, whilst in the 1:2 LAG product it shifts upfield to 168.6 ppm. There is a new peak present at 155.5 ppm, which is not seen in either starting material or 1:1 cocrystal. The value of chemical shift suggests that this peak arises as a result of an interaction between the pyridine-N and the phenol group. Single peaks observed in the 1:1 cocrystal at 139.2 and 132.3 ppm, are seen as double peaks at 139.3, 137.7 ppm and at 129.6 and 128.33 ppm respectively, implying the presence of 2 different nicotinamide molecules. A further shift in the peak representing the vanillic acid methyl carbon group, is observed – from 57.0ppm in pure VA, to 55.9ppm in 1:1 cocrystal and 55.0ppm in the 1:2 LAG product.





**Figure 5-13**.  $^1\text{H-}^{13}\text{C CP/MAS NMR}$  spectra, comparing peaks of pure VA, NA, 1:1 cocrystal and 1:2 LAG product

# 5.1.4 Sulfasalazine<sub>1</sub>:Isonicotinamide<sub>1</sub>

Sulfasalazine (SSZ) is a drug that has 2 main, licensed indications in the UK<sup>201</sup>: treatment of mild, moderate and severe ulcerative colitis (UC) and active Crohn's disease, remission

maintenance of mild, moderate and severe ulcerative colitis and treatment of active rheumatoid arthritis by experts advice. SSZ is a prodrug of 5-aminosalicylic acid and sulphapyridine, linked by an azo bond (R-N=N-R') that is selectively metabolised in the intestines. 5-aminosalyciclic acid is the active moiety for UC treatment, <sup>202-205</sup> however the mechanism of action of sulfasalazine in rheumatoid arthritis is not fully understood. <sup>206</sup> Sulfasalazine has a very low bioavailability following oral administration, approximately 10-30% hence cocrystallisation would be beneficial, and due to the supramolecular synthons SSZ possess, it, should be possible from a crystal engineering point of view. SSZ is capable of accepting and donating hydrogen bonds, due to the possession a carboxylic acid, phenol sulphonamide and pyridine group. The sulphonamide group is known to exist as 2 tautomers; the amide (Figure 5-14) and the imide (Figure 5-15) tautomer. <sup>207</sup>

**Figure 5-14**. Sulphonamide amide form (left) and crystal packing structure (right). CSD refcode: QIZJOY

The amide tautomer (triclinic desmotrope) $^{208}$  assembles with a carboxylic acid-pyridine synthon, with the phenol group forming an intramolecular bond with the carboxyl C=O group. The C=O group also forms intermolecular hydrogen bonds with the sulphonamide-NH group, making a  $R_2^2(8)$  motif. The packing structure is extended by sulphonamide S=O forming an intermolecular hydrogen bond with a neighbouring proton from a different sulfasalazine molecule's sulphonamide.

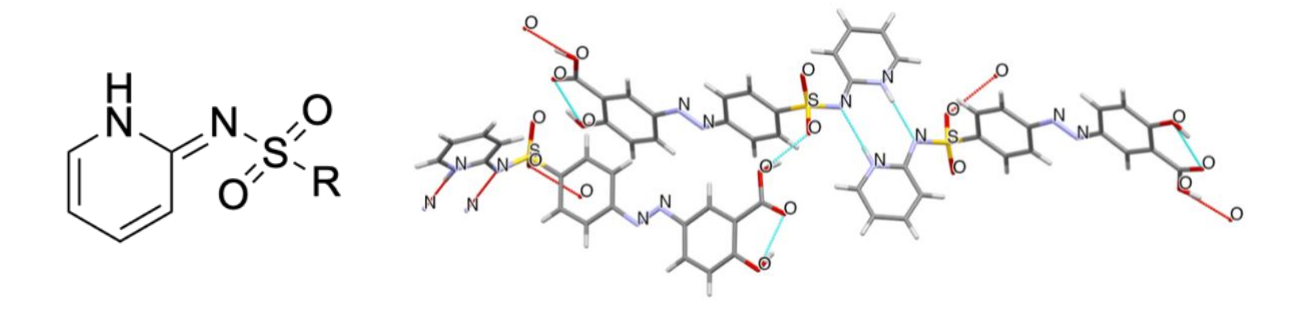


Figure 5-15. Imide tautomer (left) and crystal packing structure (right). CSD refcode: KIJBOX

The imide tautomer (monoclinic desmotrope) $^{208}$  exhibits a completely different packing arrangement – with two SSZ molecules bonded together via a sulphonamide – NH...N-pyridine bond, graph set  $R_2^2(8)$ , with the S=O stabilised with a C-H...O bond graph set  $R_2^2(7)$ . The small change of the position of the double bond between amide and imide, massively affects the crystal packing nature of SSZ. We attempted cocrystallisation using the monoclinic imide form. Huang *et al.* reported that their attempt to cocrystallise SSZ<sub>1</sub>:INA<sub>1</sub> was unsuccessful. <sup>209</sup> Herein we present our cocrystallisation attempt and characterisation. High resolution PXRD results show a new pattern, with clear, new peaks at 6.6, 8.1, 12.6, 13.1, 13.3, 14.3, 16.2, 20.3, 25.2 - 2 $\theta$ .

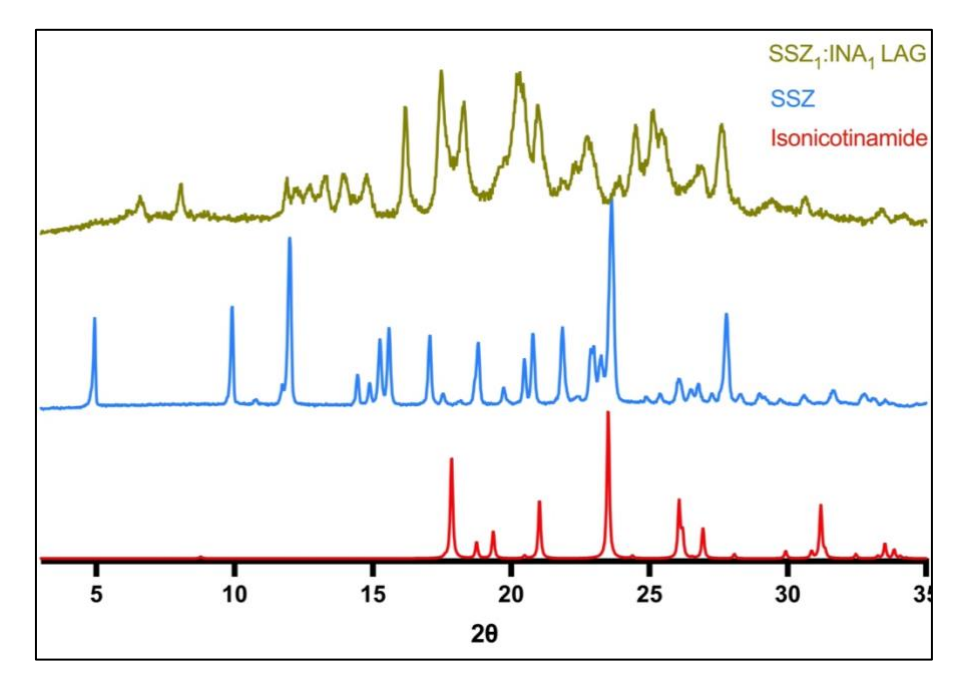


Figure 5-16. - PXRD patterns of SSZ, INA and 1:1 LAG product.

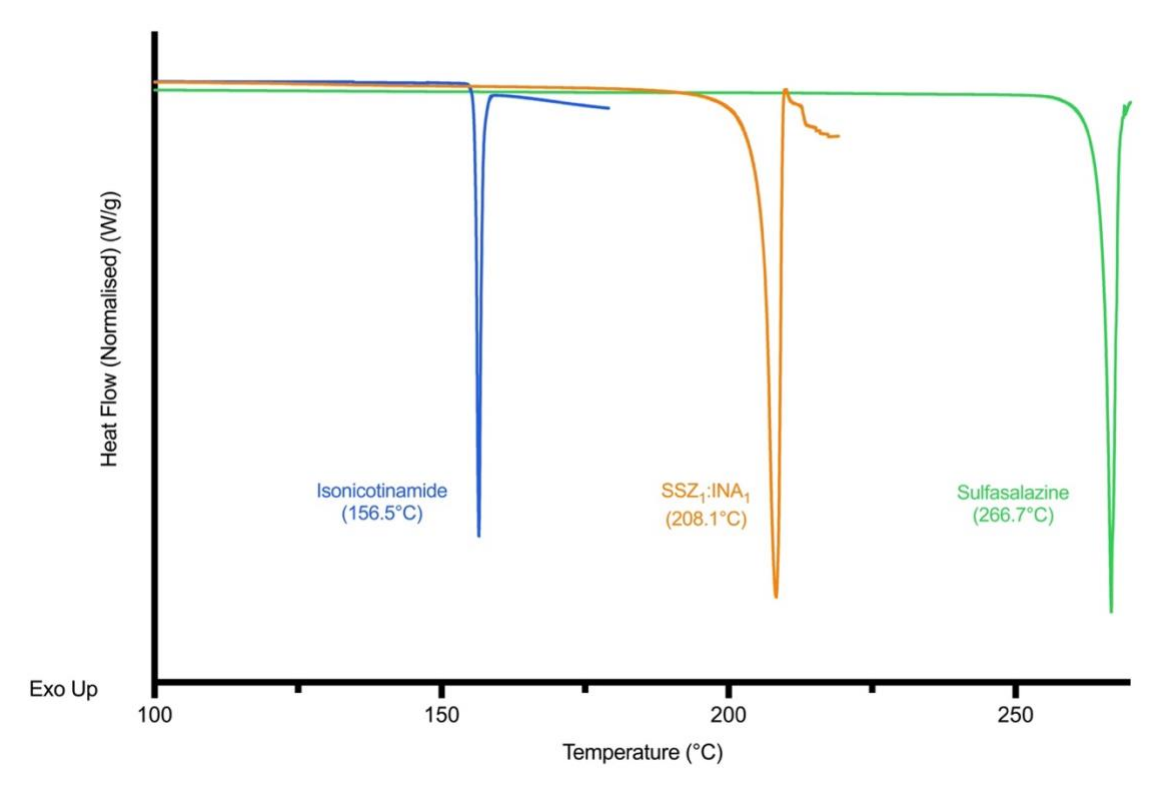


Figure 5-17. DSC thermograms showing melting points of SSZ, INA and 1:1 LAG product

Thermal analysis shows a single endothermic peak at 208.1°C, in between the melting points of the pure coformers, suggesting a new single phase solid form is present. <sup>1</sup>H-<sup>13</sup>C CP/MAS solid-state NMR spectra show changes in chemical shifts, confirming that the 1:1 LAG product is not a physical mixture of starting components.

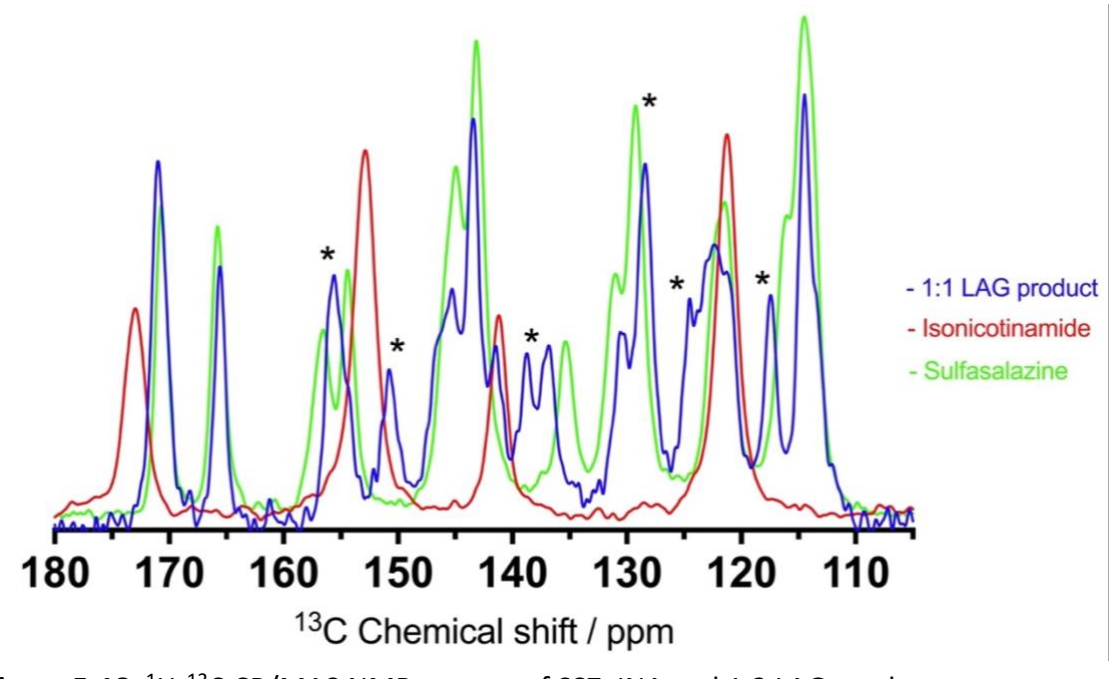


Figure 5-18. <sup>1</sup>H-<sup>13</sup>C CP/MAS NMR spectra of SSZ, INA and 1:2 LAG product

# 5.1.5 Sulfasalazine<sub>1</sub>:Nicotinamide<sub>1</sub>

Similarly to SSZ:INA, a 1:2 cocrystal of sulfasalazine and nicotinamide has been reported,<sup>210</sup> formed from melt crystallisation and was shown to possess improved dissolution characteristics. However, its crystal structure is not available in the CSD.

DSC analysis by Elbakush et~al. showed a broad peak at 192°C for the proposed 1:2 cocrystal. For our 1:1 cocrystal, we observed a sharp, narrow, endothermic peak at 194.8°C, suggesting a more crystalline product is produced by LAG, compared to melt crystallisation. We note several differences in PXRD date of SSZ<sub>1</sub>:NA1, compared to the reported pattern. We observe unique peaks at 7.2, 10.6, 11.9, 17.2, 18.2 and 27° 2 $\theta$ . Peaks representing the pure SSZ and NA are absent from the product, confirming it is not just a pure mixture.

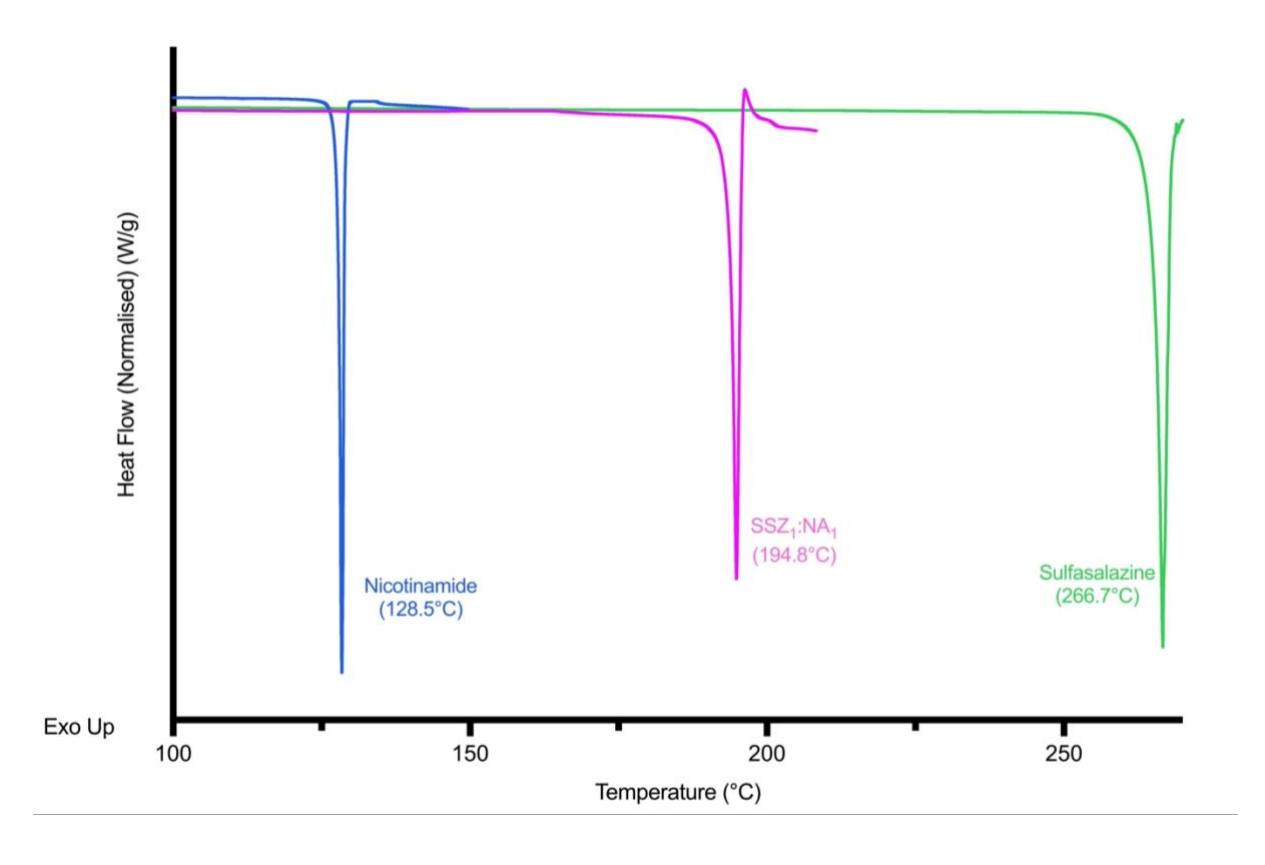


Figure 5-19. – DSC thermograms of SSZ<sub>1</sub>:NA<sub>1</sub> and pure coformers

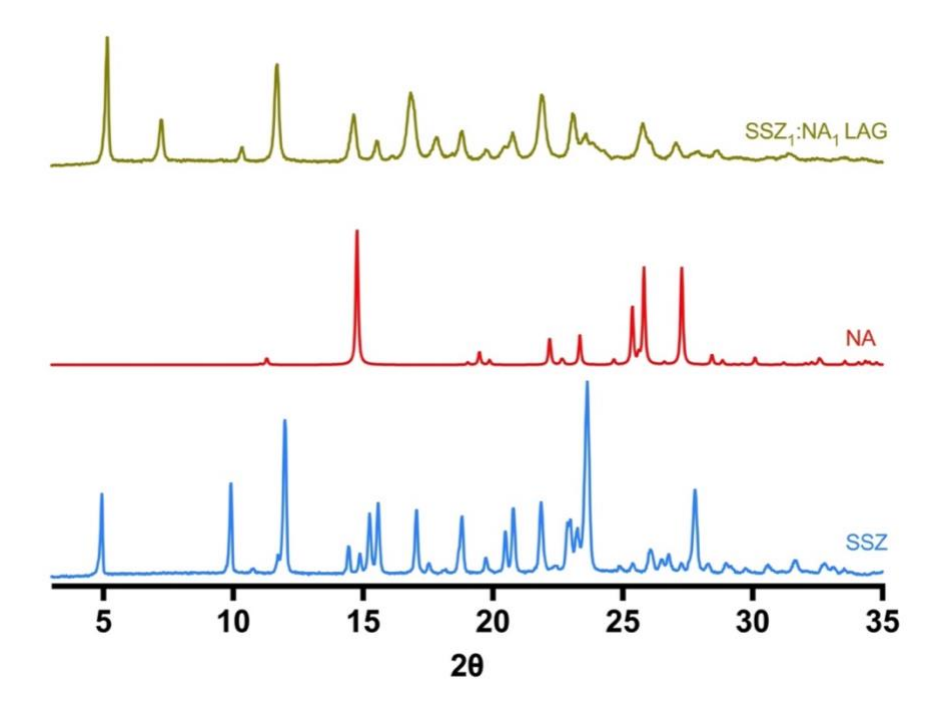


Figure 5-20. PXRD patterns for SSZ<sub>1</sub>:NA<sub>1</sub> and pure coformers

We report the <sup>1</sup>H-<sup>13</sup>C CP/MAS NMR spectrum for our SSZ<sub>1</sub>:NA<sub>1</sub> cocrystal. We observe peaks in the 165 to 175ppm region, which correspond to the -COOH and -CONH<sub>2</sub> groups from both coformers. Shifts are observed in the 140-160 ppm region, which correspond to the carbons connected to the N-pyridine regions in SSZ and NA. We also see substantial changes in chemical shifts in the aromatic regions, suggesting that this LAG product contains new hydrogen bonds.

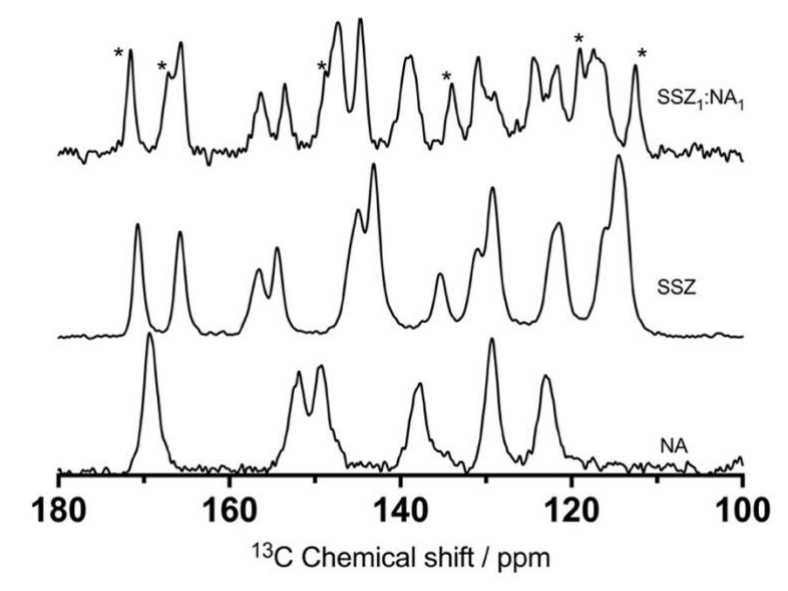


Figure 5-21. <sup>1</sup>H-<sup>13</sup>C CP/MAS NMR spectra of SSZ, NA and SSZ<sub>1</sub>:NA<sub>1</sub>.

## 3-Hydroxybenzoic acid<sub>1</sub>:nicotinamide and 2-hydroxybenzoic acid<sub>1</sub>:isonicotinamide<sub>2</sub>

3-hydroxybenzoic acid is an isomer of common pharmaceutical, 2-hydroxybenzoic acid, i.e., salicylic acid differing in only the position of the phenol group. Both 2HBA and 3HBA are discussed extensively in Chapter 6.

#### 5.1.6 Discussion and conclusions

The coformers selected for this study exhibit a propensity for multiple ratio cocrystallisation, primarily due to their diverse functional groups. A critical consideration in the selection process was the presence and distribution of multiple hydrogen bond donor and acceptor sites within these molecules. The selection was strategically guided by their hydrogen bonding capabilities, with particular emphasis on the carboxylic acid (COOH) and phenol (-OH) donor groups. The -COOH group, present in four out of six selected coformers, has been identified as the most effective hydrogen bond donor<sup>115</sup> and is prevalent in cocrystals, as confirmed by our CSD analysis. The pairing of COOH with the N-pyridine group, recognized as the strongest hydrogen bond acceptor, was anticipated to facilitate robust intermolecular interactions.

While this principle generally holds true, our research exposes nuances that deviate from this expectation, highlighting the necessity of screening cocrystals across various stoichiometric ratios. A notable example is the vitamin C<sub>1</sub>:nicotinamide<sub>3</sub> cocrystal, which exhibits a complex arrangement of stacks and homodimers. Surprisingly, some pyridine groups in this structure do not participate in hydrogen bonding, despite the N-pyridine typically being considered the strongest acceptor. This observation challenges conventional understanding of cocrystal formation principles and suggests that factors beyond simple hydrogen bonding play a crucial role in determining cocrystal stability.

The vanillic acid: isonicotinamide system presents a compelling case study in cocrystal stoichiometry, challenging previous assumptions about cocrystal formation. Contrary to earlier reports<sup>190</sup> which were unable to successfully form a 1:2 cocrystal via liquid-assisted grinding (LAG), our comprehensive analysis employing differential scanning calorimetry,

powder X-ray diffraction, and solid-state nuclear magnetic resonance spectroscopy strongly demonstrates the formation of a distinct 1:2 cocrystal. This finding underscores the superiority of solid state NMR,<sup>18</sup> and the importance of using multiple analytical techniques for accurate characterization. This system also illustrates that while 1:1 stoichiometry is the most prevalent cocrystal ratio in the Cambridge Structural Database (CSD), alternative ratios may exhibit greater stability and preferential formation under certain conditions. In this case, the VA<sub>1</sub>:INA<sub>2</sub> cocrystal emerges as the stable form, contradicting the general trend observed in the CSD.

Previous studies reported unsuccessful attempts to form an SSZ:INA 1:1 cocrystal, while our comprehensive analysis provides compelling evidence for the formation of a novel solid form, once again showing how a combination of DSC, PXRD and solid-state NMR offers a robust, three-fold characterization strategy that can reveal subtle structural changes and confirm the formation of new cocrystal forms. Our attempts to obtain single crystals of the newly discovered cocrystal forms proved ultimately unsuccessful, primarily due to time constraints inherent in the slow evaporation method, which can require days to weeks for crystal growth. A recurring challenge was the formation of unintended crystal forms. For instance, efforts to grow a 1:2 vanillic acid: nicotinamide cocrystal resulted in the formation of 1:1 single crystal instead. This phenomenon can be likely attributed to the complex interplay between thermodynamic and kinetic factors during the crystallization process.<sup>211</sup> The desired 1:2 stoichiometric ratio did not represent the most thermodynamically stable form under the experimental conditions, despite exaggerating the ratio to as high as 1:4. Instead, the 1:1 ratio could exhibit greater stability, leading to its preferential formation.

Thermodynamically stable forms tend to predominate as they minimize the system's free energy. However, kinetic factors, including nucleation rates and crystal growth dynamics, also play a crucial role in determining which form crystallizes first. If the 1:1 form nucleates more rapidly or exhibits faster growth kinetics compared to the 1:2 form, it is likely to dominate the crystallization process.

# 5.2 Solution state investigation of cocrystal aggregation dynamics

#### 5.2.1 Introduction

One of the primary advantages of solution-state NMR spectroscopy is its capacity to characterise the aggregation of biomolecules and small molecules alike. Proton ( $^{1}$ H) NMR is a powerful analytical technique that provides insight into the molecular dynamics and interactions of small molecules in solution. Cocrystals are typically formed through noncovalent interactions, such as hydrogen bonding, van der Waals forces, and  $\pi$ - $\pi$  stacking, and the aggregation of cocrystals in solution is a complex process influenced by various factors such as the nature of the coformers, their relative concentrations, the solvent environment, temperature and the presence of additives. The concentration of coformers is particularly crucial, as it can dictate the extent of interaction and aggregation in solution.  $^{212}$ 

The presence of specific functional groups can enhance hydrogen bonding interactions, leading to increased stability of the aggregated forms.<sup>213</sup> The ability of NMR to illuminate important facets of molecular interactions is demonstrated in studies, such as Carney et al. on anthraquinone disulphonic acid (AQDS), where concentration-dependent dimerization was assessed.<sup>214</sup> Here, <sup>1</sup>H NMR is used to monitor changes in the chemical shifts of AQDS protons as the concentration increases. The observed shifts indicate that protons in the AQDS molecule experience different electronic environments due to intermolecular interactions, particularly dimerization. This shift is a direct consequence of the formation of dimeric species, which alters the local magnetic environment around the protons. The authors also note that specific peaks corresponding to protons in the AQDS structure become broadened or shifted, which is indicative of the formation of aggregates. This phenomenon is consistent with the hypothesis that increased concentration leads to enhanced intermolecular interactions. The observed upfield shifts in NMR peaks with increasing concentration indicated enhanced shielding effects, which are indicative of molecular aggregation. This finding aligns with the general principle that molecular interactions in solution can lead to significant changes in the NMR spectral characteristics, thus providing a means to infer aggregation.<sup>215</sup>

Using NMR to study cocrystals allows for the observation of molecular interactions and the identification of aggregation behaviour.<sup>216</sup> Guo *et al.* revealed distinct solution proton

chemical shifts in flufenamic acid and nicotinamide cocrystals, compared to their individual states. These shifts indicate changes in the electronic environment of the protons due to intermolecular interactions. The authors highlight that these interactions can significantly influence the stability and solubility of the cocrystals. In this chapter, we will investigate a range of 1D and 2D solution state NMR methodology for assessing the effect of concentration, pH and stoichiometry on intermolecular interactions between hydroxybenzoic acids and cyclic amides and the conditions under which these interactions are favoured. We analyse and interpret NMR spectra to identify chemical shifts, peak broadening, and diffusion coefficients, which sheds light on the molecular interactions and aggregation dynamics in solution.<sup>217</sup> The significance of this research extends beyond understanding cocrystal behaviour; by understanding the factors that influence aggregation and solubility in cocrystal systems, we can develop more effective drug formulations that leverage the advantages of cocrystallisation.<sup>218, 219</sup>

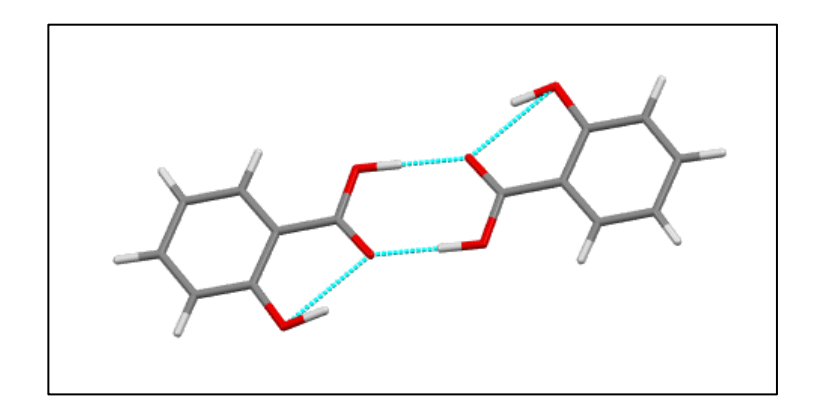
**Table 5-2** <sup>1</sup>H Titration regime for 3-HBA, 2-HBA, NA and INA

Acid:Amide ratio	Acid concentration (M)	Amide concentration (M)
0.1:1	0.025	0.25
0.2:1	0.05	0.25
0.4:1	0.1	0.25
0.6:1	0.15	0.25
0.8:1	0.2	0.25
1:1	0.25	0.25
1.2:1	0.3	0.25
1.4:1	0.35	0.25
1.6:1	0.4	0.25
1.8:1	0.45	0.25
2:1	0.5	0.25
2.2:1	0.55	0.25
2.4:1	0.6	0.25
2.6:1	0.65	0.25
2.8:1	0.7	0.25
3:1	0.75	0.25

# 5.2.2 <sup>1</sup>H analysis of pure coformers

<sup>1</sup>H analysis and assignment of pure coformers 3-HBA, 2-HBA, INA and NA have previously been reported in literature. 220-223 We recorded the <sup>1</sup>H NMR spectra of each coformer, starting with a concentrated 0.5 M coformer in ethanol solution, followed by successive dilutions to achieve a final concentration of 0.05 M. Ethanol was selected for consistency, as it was the solvent used when screening cocrystals by liquid-assisted grinding (LAG). The primary purpose of these dilutions is twofold: to determine the effect concentration of pure coformer has on chemical shift, and to establish reference spectra for comparison with coformer combinations. Our analysis revealed several noteworthy observations. Interestingly, while both 2-HBA and 3-HBA possess a phenol functional group, their <sup>1</sup>H spectra do not exhibit signals corresponding to the phenolic -OH protons. This phenomenon is most likely attributed to rapid proton exchange. Ethanol, being a protic, polar solvent facilitates <sup>1</sup>H exchange between the phenolic hydroxy group and solvent molecules, resulting in broad and sometimes imperceivable signals. The presence of hydroxyl groups in ethanol promotes strong hydrogen bonding interactions, which expedite this proton exchange process. While temperature can influence phenolic OH signal resolution, it is not a relevant factor in this particular case.<sup>224</sup>

Secondly, we note that the carboxylic acid proton for 3-HBA appears as a sharp, narrow peak at 10.2 ppm, whilst 2-HBA appears as a broad peak at 12.1 ppm. This difference can be attributed to the structural differences of the coformers and their intermolecular interactions. The spatial arrangement of 2-HBA makes intramolecular bonding<sup>225</sup> between the hydroxyl and carbonyl possible, as seen in Figure 5-22. 3-HBA in contrast, has its hydroxyl group at the meta position, preventing the formation of an intramolecular hydrogen bond. The presence of intramolecular hydrogen bonding in 2-HBA significantly affects its <sup>1</sup>H NMR spectrum. The intramolecular hydrogen bond in 2-HBA results in rapid proton exchange of the carboxylic acid group, leading to considerable peak broadening.<sup>226</sup> Consequently, the COOH signal appears diminished at low concentrations. The hydrogen bonding also alters the chemical shift of the COOH proton in 2-HBA, hence the difference in peak position further downfield.



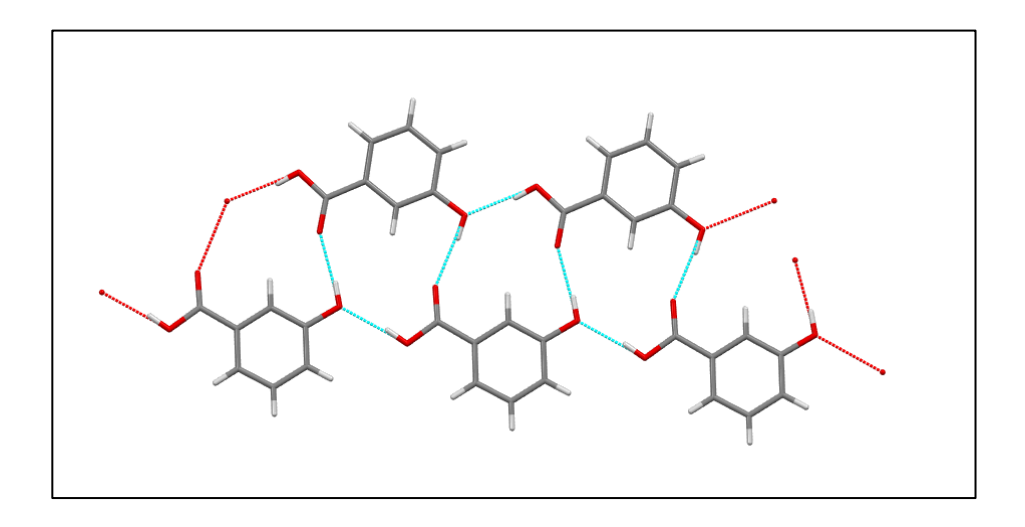
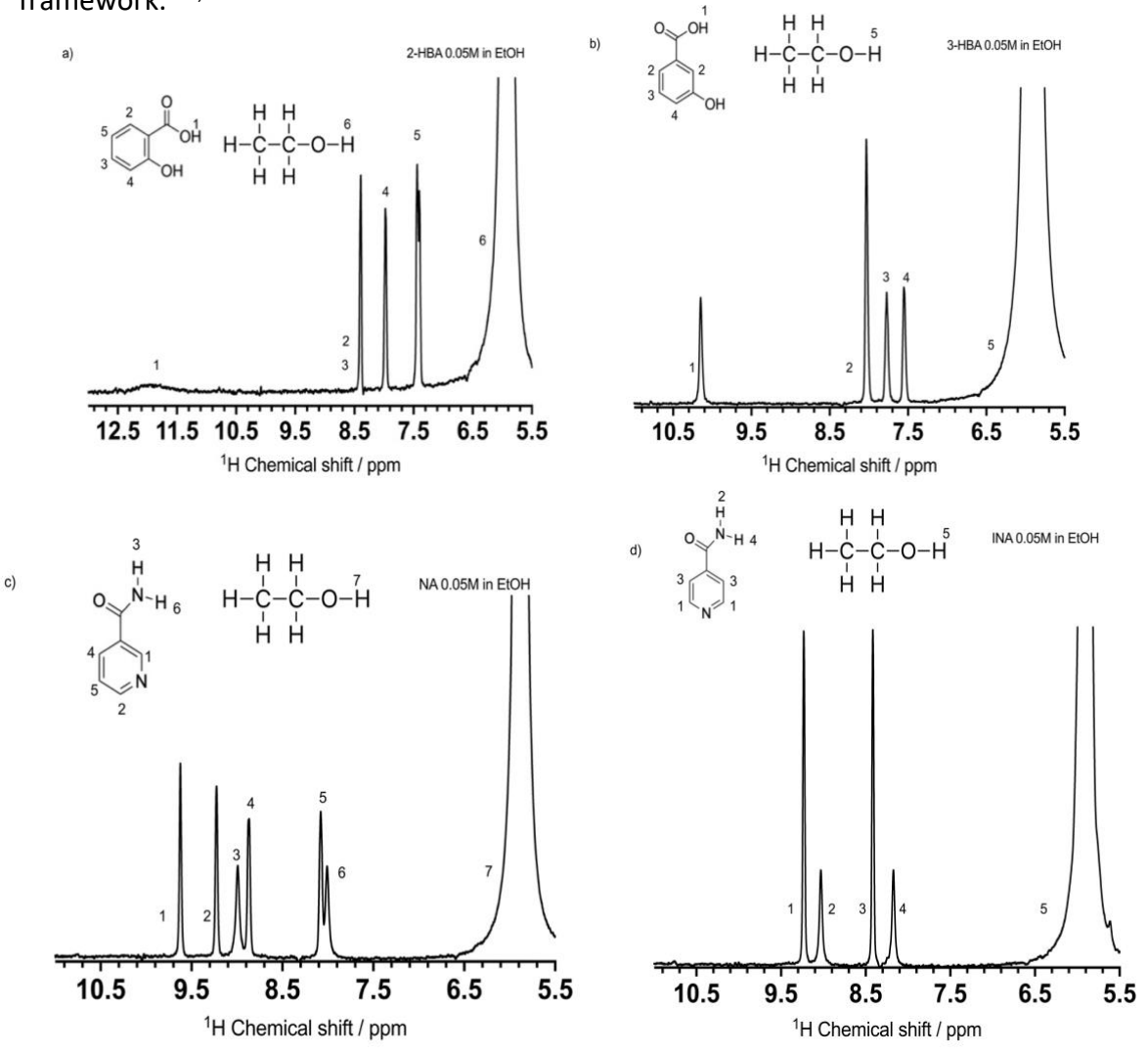


**Figure 5-22** – (**above**) Intermolecular bonding in 2-HBA. REFCODE: SALIAC. (**below**) Intermolecular bonding in 3-HBA. REFCODE: BIDLOP02

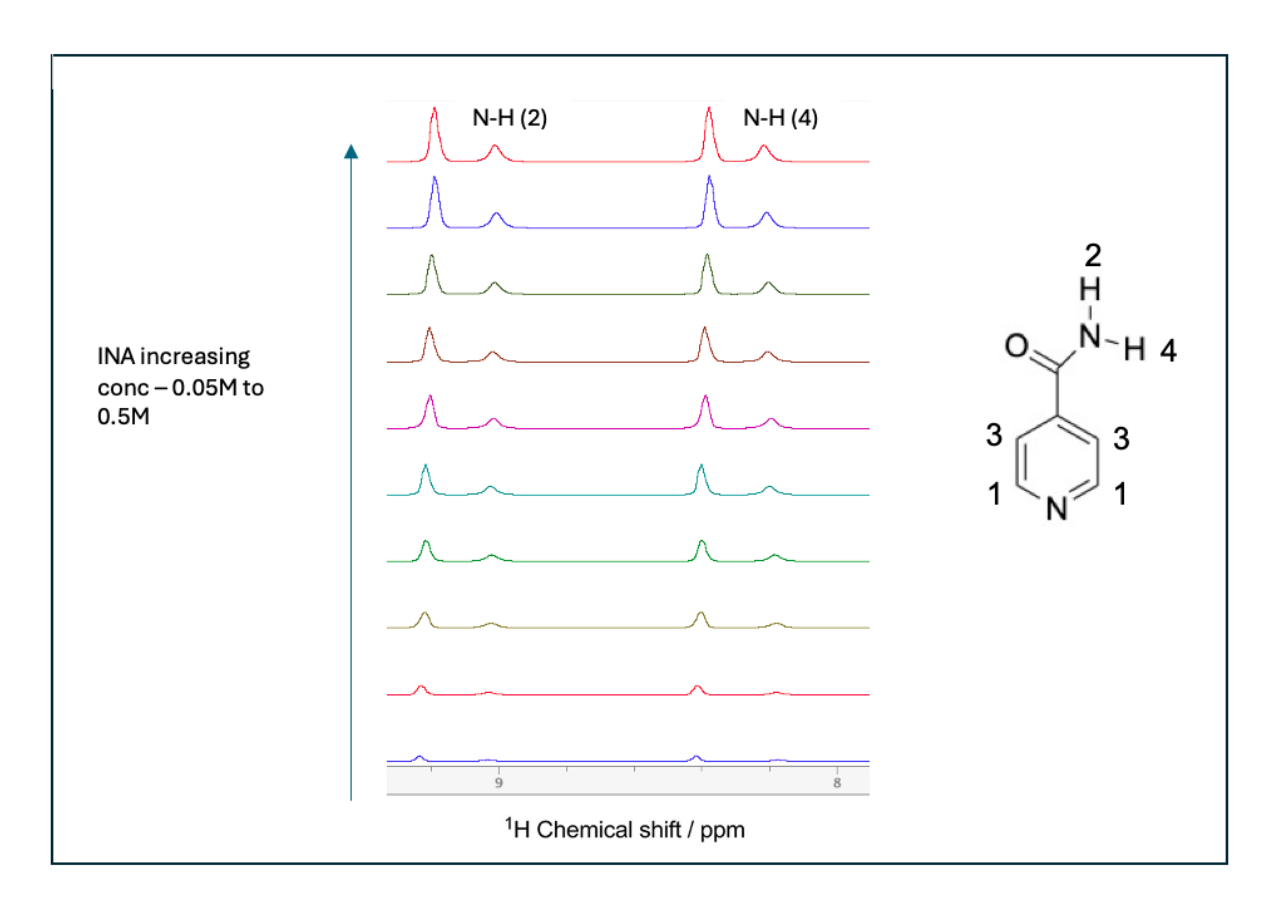
From our serial dilutions, as concentration increases, we observe that in both 3-HBA and 2-HBA, all  $^1$ H NMR peaks exhibit a consistent upfield shift. This is likely due to the shielding influence of hydrogen bonding and other intermolecular forces such as  $\pi$ - $\pi$  stacking, van der Waals interactions and dipole-dipole interactions. The observed upfield shift of peak positions is in agreement with established NMR spectroscopy concepts, where an increase in hydrogen bonding usually leads to a more shielded proton environment by increasing the surrounding electron density. As the acid concentration increases, the probability of hydrogen bonds forming with either the solvent or other acid molecules also increases, creating a more shielded environment for aromatic and hydroxyl protons. Upon increasing the concentration

of cyclic amides, we noticed a deviation in this trend: although most resonances exhibited an upfield shift, one particular amide proton, NH-6 in NA and NH-4 in INA, showed a downfield shift. This anomaly suggests that this proton is involved in a different type of molecular interaction, possibly due to unique intramolecular or solvent interactions that distinguish its behaviour from the other protons. Distinguishable amide protons suggest they are in different planes. We also note that the peak corresponding to the ethanol -OH group consistently broadens, reduces in intensity and shifts downfield as concentration of acid/amide increases suggesting intermolecular interactions with the solute.

The downfield shift of the amide proton (NH-6 in NA and NH-4 in INA) can be attributed to the potential formation of intramolecular hydrogen bonds within the cyclic amide framework.<sup>228, 229</sup>



**Figure 5-23** - <sup>1</sup>H NMR spectra of pure coformers dissolved in ethanol. A) 2-HBA, B) 3-HBA, C) NA, D) INA



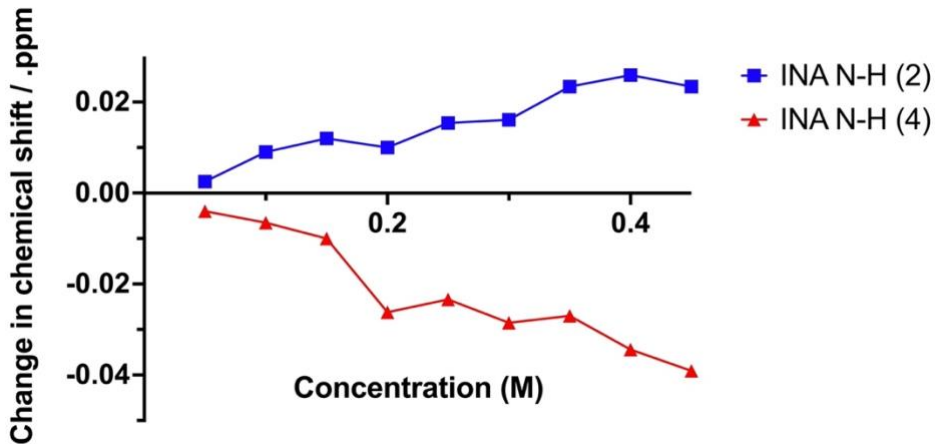


**Figure 5-24** – (above) <sup>1</sup>H NMR spectra of INA at concentrations 0.05 to 0.5 M, (below) changes in INA <sup>1</sup>H chemical shifts *vs* concentration of both N-H protons.

As the concentration increases, the amide proton may engage more strongly in intramolecular hydrogen bonding with the carbonyl oxygen of the same molecule, as suggested by Etter.<sup>40</sup> This interaction results in a deshielding effect, shifting the amide proton downfield compared to the other protons in the system.

Leskowitz et al.<sup>230</sup> studied the dynamic behaviour of amide protons in INA, highlighting the critical role of conformational flexibility around the amide bond. The amide protons can adopt multiple conformations due to the rotational freedom associated with the N-C(=O) bond. This rotational flexibility is crucial, as it allows the molecule to explore different spatial arrangements. The presence of hydrogen bonding interactions plays a pivotal role in stabilizing certain conformations of the amide protons. Hydrogen bonds can influence the energy landscape of the molecule, favouring specific orientations that minimize steric hindrance and maximize favourable interactions. For example, in isonicotinamide, the amide protons can exist in either a syn or anti orientation relative to the carbonyl oxygen. This synanti relationship leads to the formation of different rotational isomers,<sup>231</sup> each with distinct NMR signatures. The syn conformation typically places the amide proton closer to the electron-withdrawing carbonyl group, which can enhance hydrogen bonding interactions, while the anti-conformation may allow for a more sterically favourable arrangement. <sup>232</sup> The dynamic nature of these protons is reflected in the NMR spectra, where changes in chemical shifts can indicate the presence of different coformers. In our case, it seems that by increasing concentration of INA in ethanol, we observe more of the syn conformation due to the downfield shifts suggesting intramolecular hydrogen bonds<sup>233</sup>. This is later confirmed by variable temperature experiments.

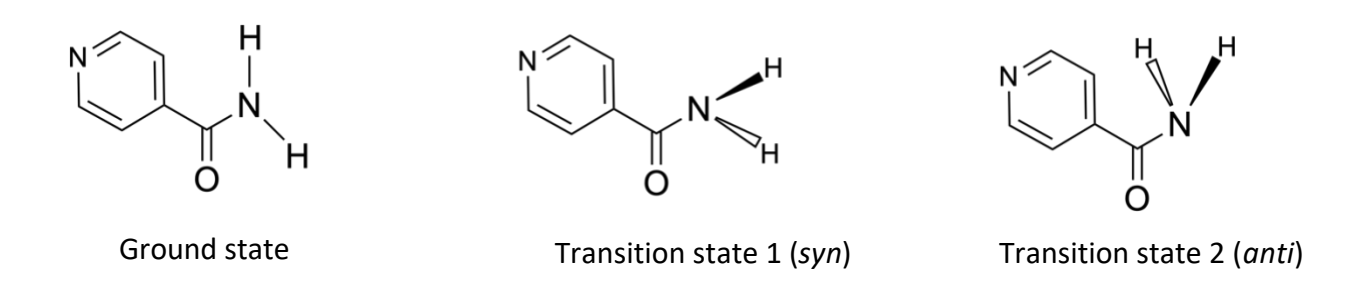


**Figure 5-25** - Rotational pathways for pyridine carboxamides: Isonicotinamide (shown) and Nicotinamide (N-pyridine position changes) for the ground state, transition state 1 and transition state 2.<sup>230</sup>

Leskowitz *et al.*<sup>230</sup> also discuss how temperature and solvent effects can further influence the conformational preferences of the amide protons. For example, increasing temperature may enhance the rotational freedom around the amide bond, allowing for a greater population of the anti-coformer, while specific solvents can stabilize certain conformations through solvation effects. This interplay between temperature, solvent, and hydrogen bonding interactions underscores the complexity of conformational dynamics in amide-containing compounds. In our case, temperature and solvent remain constant, with the only variable being concentration of the co-former. As mentioned earlier, in the NA titration spectra, NH-6 also exhibits chemical shifts contrary to the rest of the molecule.

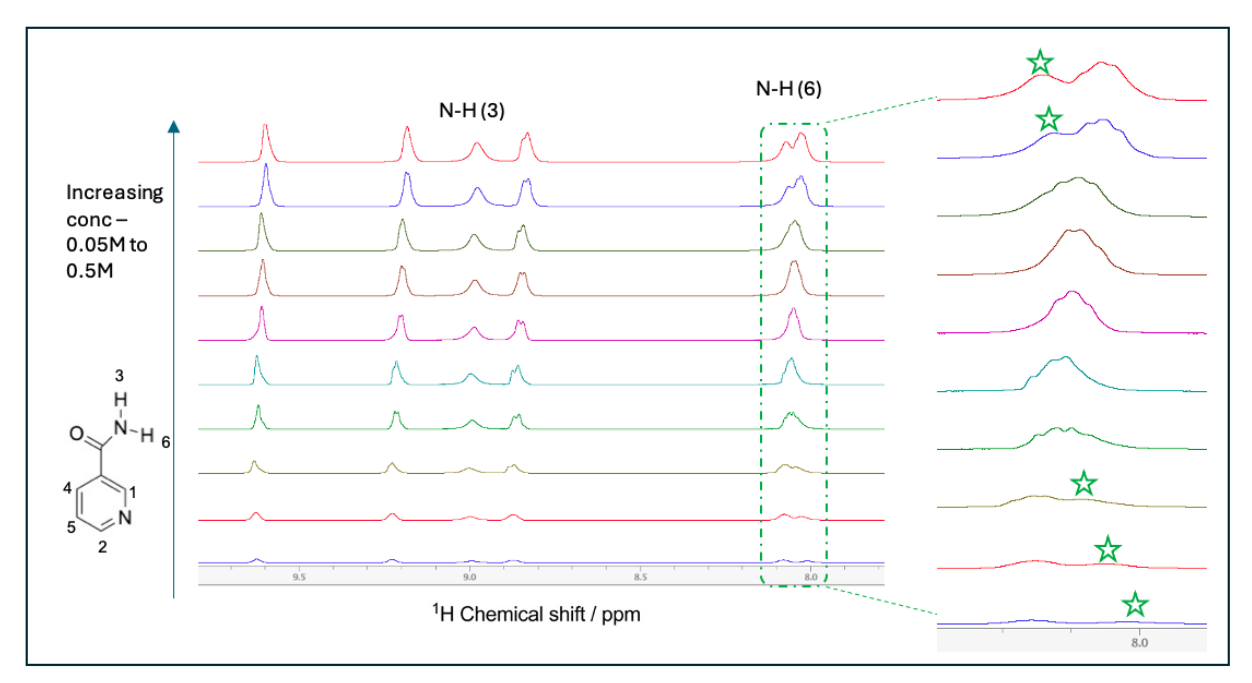
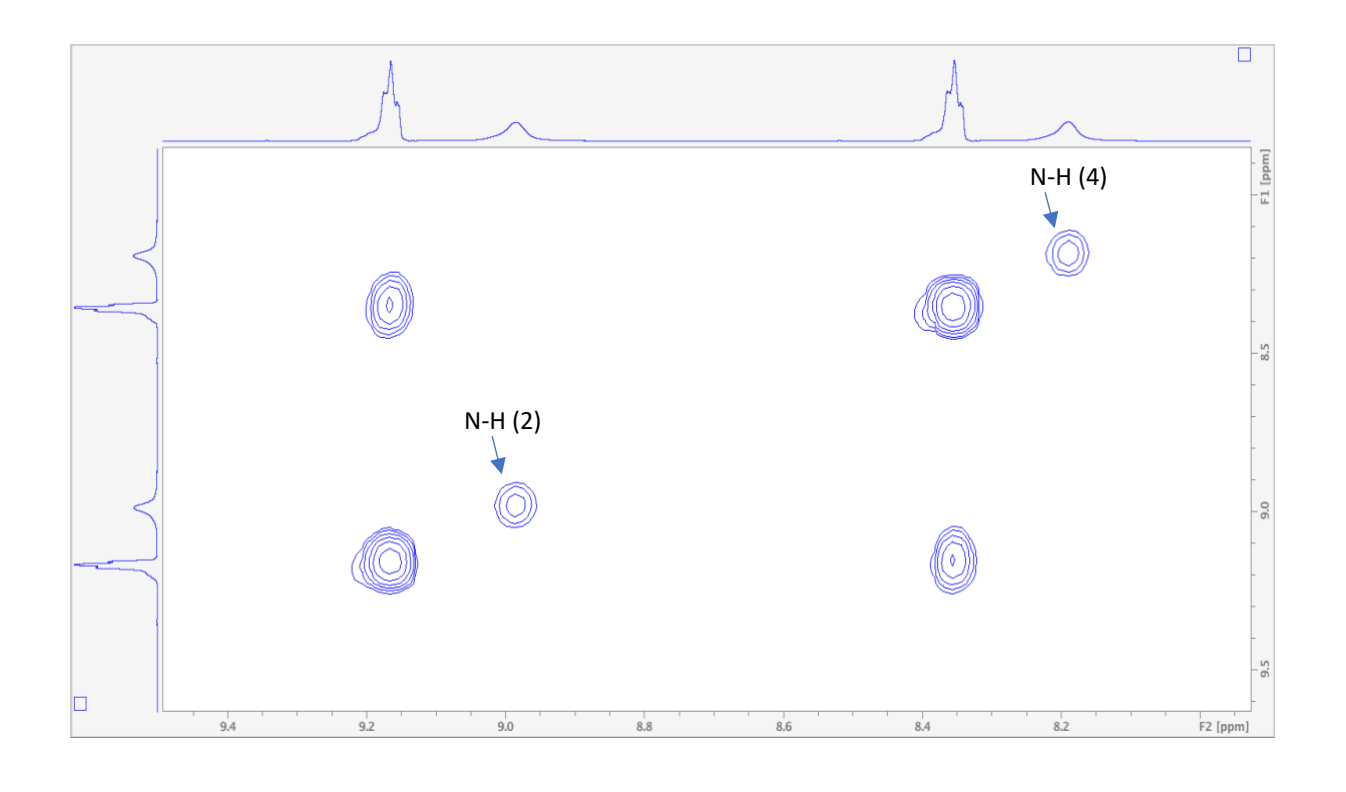
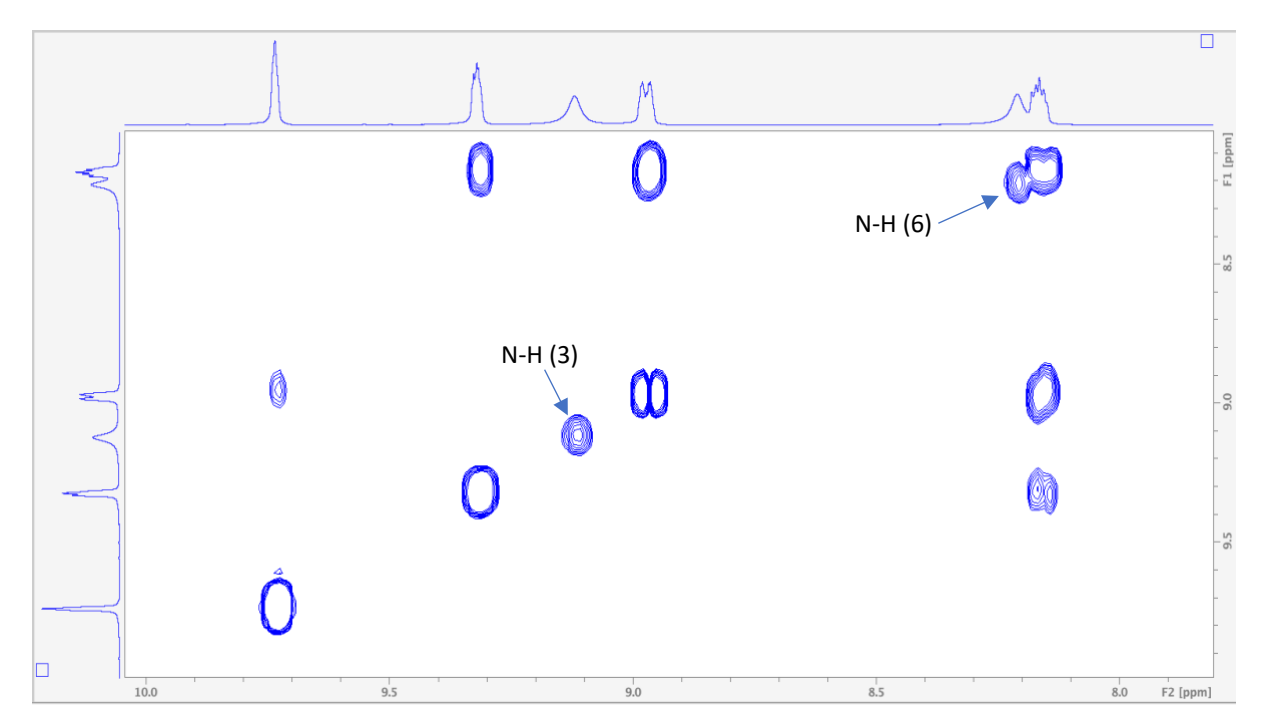


Figure 5-26 - <sup>1</sup>H NMR of NA in ethanol 0.05M to 0.5M

However, at some concentrations there is overlap between peaks, rendering the peak centre unintelligible. The peak corresponding to the N-H (6) proton, at 8.01 ppm is close to the one of the aromatic protons, C-H (5). As N-H (6) shifts, it overlaps with C-H (5) between the concentrations of 0.2 and 0.4 M, and at 0.45 M we observe it clearly at 8.07 ppm (Figure 5-5). Full list of NA titration peak shifts can be seen in appendix table 2. We report the COrrelation SpectroscopY (COSY) spectra for NA and INA, confirming the assignments of INA and NA peaks in question.





**Figure 5-27** - <sup>1</sup>H-<sup>1</sup>H COSY NMR spectrum of 0.5 M INA in ethanol (above) and 0.5 M NA in ethanol (below) identifying N-H peaks by through bond correlations

Guo *et al.*<sup>216</sup> reported <sup>1</sup>H NMR analysis of flufenamic acid (FFA) and nicotinamide (NA) at different concentrations. They noted that when FFA was dissolved in deuterated CDCl<sub>3</sub> at 500, 1000 and 5000 μg/mL, higher concentrations resulted in downfield shifts as a result of self-association *via* carboxylic acid-acid hydrogen bonding. CDCl<sub>3</sub> is a common choice for NMR experiments due to its low polarity and ability to dissolve a wide range of organic compounds, without interfering with the NMR signals. They also note that the FFA N-H proton shifts upfield, as a result of intercarboxylic acid hydrogen bonding. However as NA amide protons did not interact with CDCl<sub>3</sub> a gradual downfield shift is seen in both protons due to amideamide bonding, <sup>234</sup> whilst aromatic <sup>1</sup>H peak positions remain constant. This provides an interesting contrast to the effect on <sup>1</sup>H NMR spectra observed when NA is dissolved in ethanol.

#### Summary of findings

The <sup>1</sup>H NMR analysis of pure coformers in ethanol solution, conducted over a concentration range of 0.05 to 0.5 M revealed distinct behaviours for hydroxybenzoic acids and cyclic amides in ethanol solution. For both 3-HBA and 2-HBA, phenolic -OH protons were not visible due to proton exchange with the solvent, however the carboxylic acid proton appeared differently for each acid, reflecting structural differences and intramolecular hydrogen bonding in 2-HBA. As concentration increased, all acid peaks showed a consistent upfield shift attributed to enhanced intermolecular interactions such as  $\pi$ - $\pi$  stacking and hydrogen bonding. For cyclic amides INA and NA, most resonances exhibited an upfield shift with increasing concentration. Notably, one specific amide proton (NH-6 in NA and NH-4 in INA) showed an anomalous downfield shift. This deviation was attributed to the potential formation of intramolecular hydrogen bonds within the cyclic amide framework, possibly involving the carbonyl oxygen of the same molecule. The solvent ethanol -OH peak broadened, reduced in intensity, and shifted downfield as solute concentration increased, indicating significant intermolecular interactions between the solvent and solute molecules. These findings demonstrate the sensitivity of <sup>1</sup>H NMR to concentration-dependent changes in molecular interactions and conformations for the studied pure coformers in ethanol solution. These findings serve as crucial references for our subsequent <sup>1</sup>H NMR study of solution-state interactions in cocrystal coformers, providing a foundation for understanding the behaviour of these molecules in the context of cocrystal formation and stability.

# 5.2.3 Concentration-dependent solution-state interactions of cocrystal coformers

Understanding of the solution-state behaviour of the coformers sheds light on the nature and strength of intermolecular interactions that drive cocrystal formation. We conducted a series of  $^1H$  NMR experiments using a 1:1 stoichiometric ratio of these coformers at various concentrations. These experiments enabled us to elucidate the complex interplay of hydrogen bonding,  $\pi$ - $\pi$  stacking, and other non-covalent interactions that characterize this system. While we observed similar patterns for each acid/amide combination studied, the 3-hydroxybenzoic acid and isonicotinamide system exhibited the lowest level of peak overlap in the NMR spectra. Therefore, we will use this 3-HBA:INA system as our model to describe the observed interactions in detail.

## 3-Hydroxybenzoic Acid (3-HBA) and Isonicotinamide (INA) - 1:1

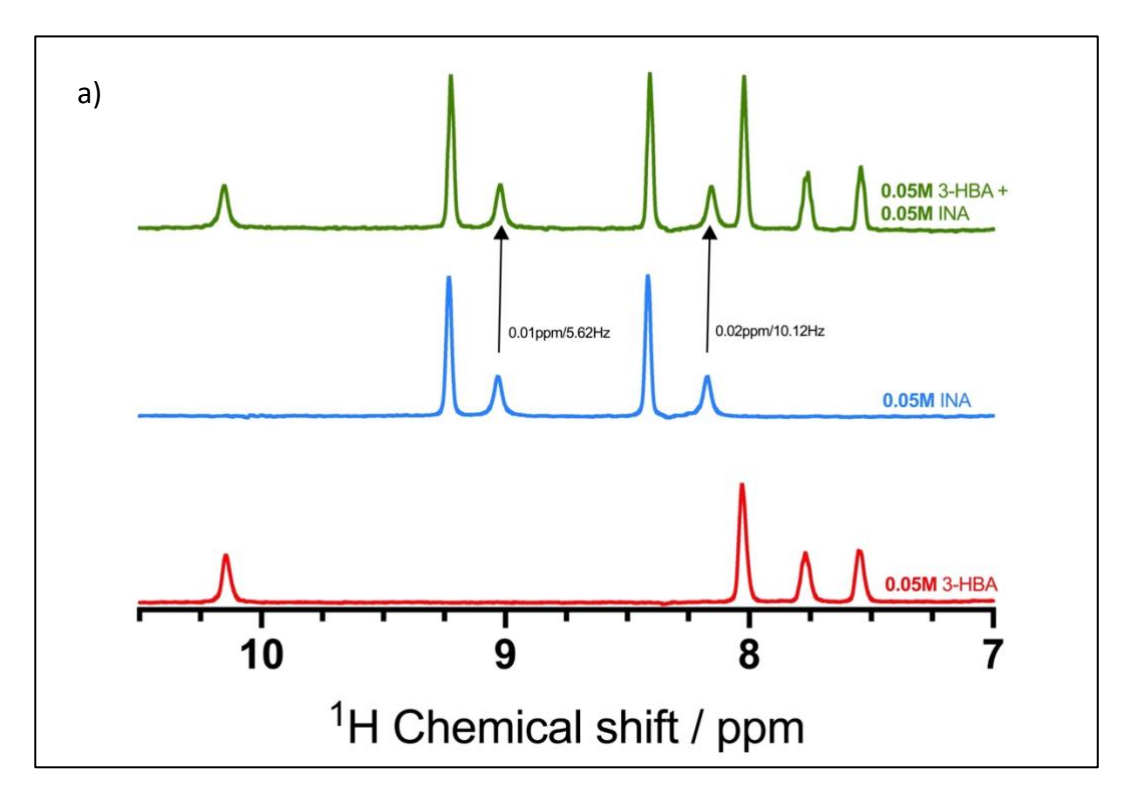
At the lowest concentration studied (0.05 M), we observe an intriguing pattern of chemical shifts. The peaks corresponding to 3-HBA exhibit a small upfield shift of 0.01 ppm relative to the TSP reference, suggesting that even at this low concentration, 3-HBA molecules are affected by the presence of INA. INA peaks also exhibit subtle but detectable shifts. The aromatic protons of INA display a small upfield shift of 0.01 ppm, which could be attributed to weak  $\pi$ - $\pi$  stacking interactions with other INA molecules and 3-HBA aromatic rings.<sup>235</sup> The amide protons of INA display a more complex behavior. The N-H (2) proton shifts 0.01 ppm upfield, consistent with the aromatic protons. However, the N-H (4) proton exhibits a larger upfield shift of 0.02 ppm. This differential shift between N-H (2) and N-H (4) suggests distinct intermolecular interactions for each amide proton, with N-H (4) potentially involved in stronger hydrogen bonding interactions.

At a concentration of 0.25 M, the peaks of 3-HBA show an upfield shift compared to pure 3-HBA at 0.05 M. However, when comparing pure 3-HBA at 0.25M in ethanol with a mixture of 0.25 M 3-HBA and 0.25 M INA, there is no observable change in peak positions of the 3-HBA peaks. Notably, the carboxylic acid peak at 10.15 ppm experiences reduction in intensity by

approximately 75%. This reduction in peak intensity suggests that the 3-HBA -carboxylic acid protons are in rapid chemical exchange with the solvent and/or the INA coformer.

The INA peaks at 0.25 M show more pronounced upfield shifts, with the aromatic peaks shifting by 0.01 ppm. The amide protons continue to exhibit differential behavior, with N-H (2) shifting upfield by 0.02 ppm and N-H (4) shifting by 0.04 ppm. This concentration-dependent increase in chemical shift magnitude suggests strengthening of intermolecular interactions as molecular proximity increases.

At the highest concentration studied (0.5 M), we observe a qualitative change in behavior. For the first time, we note a small 0.01 ppm downfield shift in the 3-HBA aromatic proton chemical shifts, indicative of hydrogen bond formation.<sup>236</sup> The COOH peak at 10.15 ppm is no longer observable, suggesting its involvement in rapid exchange processes or strong intermolecular interactions. INA aromatic protons continue their upfield trend, shifting by 0.02 ppm. The amide protons exhibit the most dramatic shifts, with N-H(2) moving upfield by 0.03 ppm and N-H(4) showing a pronounced upfield shift of 0.06 ppm.



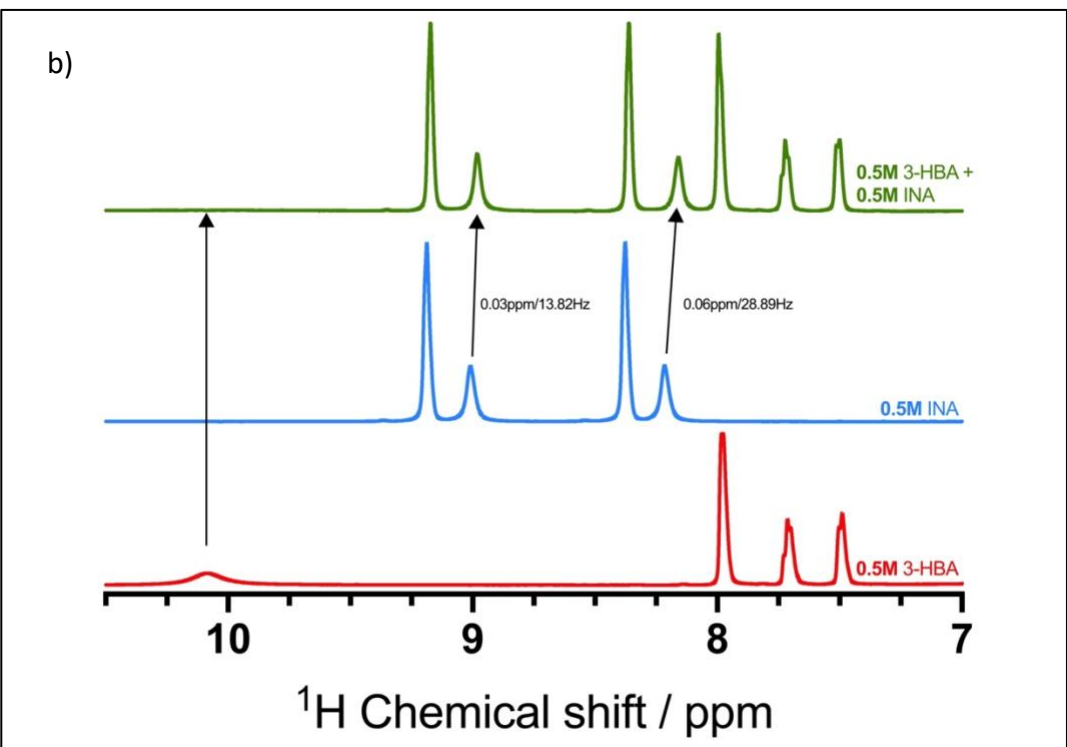


**Figure 5-28** -  $^1$ H solution NMR spectra of 3-HBA, INA and 3-HBA $_1$ :INA $_1$  at a) 0.05M and b) 0.5M

The behavior of the ethanol OH peak offers further insights into the hydrogen bonding network within the system. At higher concentrations, we observe that the ethanol -OH peak shifts downfield, becomes broader, and exhibits reduced intensity, indicating its involvement in the hydrogen bonding network.

# 5.2.3 Correlating solid-state and solution-state interactions

To fully understand these solution-state observations, it is crucial to consider the known solidstate interactions in the 3-HBA-INA cocrystal. X-ray crystallography reveals three primary hydrogen bonding interactions in the solid state as seen in table 2.

Table 5-3 - 3-HBA<sub>1</sub>:INA<sub>1</sub> (LUNMEM) cocrystal bond lengths

Hydrogen bond	Bond length, Å
(i) - Carboxylic acid C=O pyridine bond	2.624
(ii) - Amide-carboxy COOH acid bond	2.910
(iii) - Amide amide bond	2.945

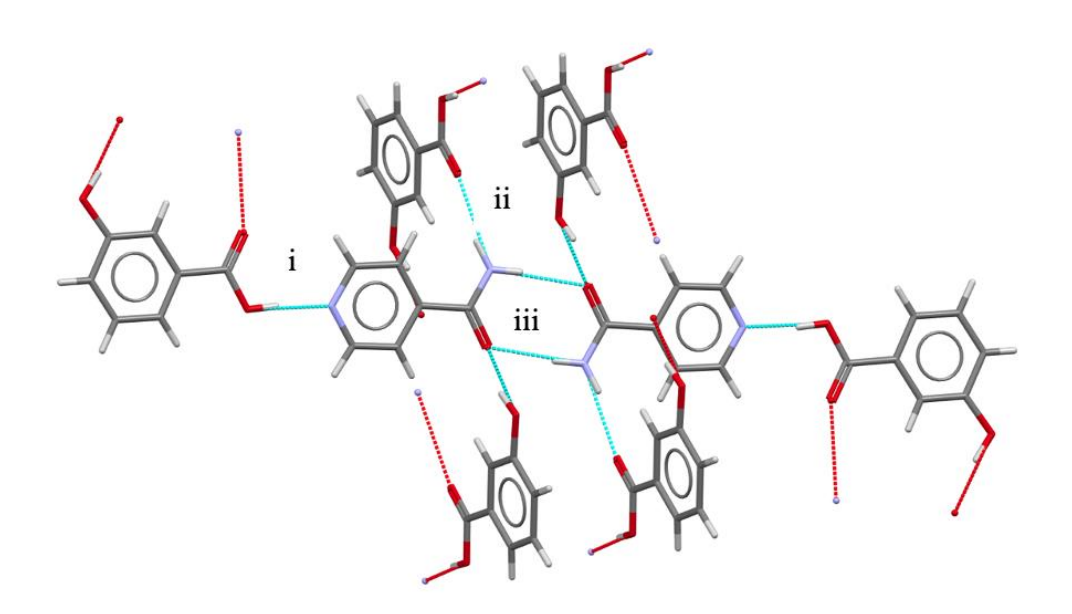


Figure 5-29 - 3-HBA<sub>1</sub>:INA<sub>1</sub> (LUNMEM) supramolecular synthons

These bond lengths indicate a hierarchy of interaction strengths, with the carboxylic acidpyridine interaction being the strongest, followed by the amide-carboxylic acid and amideamide interactions. This hierarchy provides a framework for interpreting the solution-state behavior, although it is important to note that solution interactions are more dynamic and may not perfectly mirror the solid-state structure. All these bond lengths, all under 3 Å, indicate strong hydrogen bonding interactions. For context, van der Waals interactions typically occur at larger distances and are considerably weaker than these hydrogen bonds. 102

The solid-state data aligns well with our solution-state NMR observations:

- 1. The strong carboxylic acid-pyridine interaction (2.624 Å) correlates with the disappearance of the COOH peak at high concentrations in our NMR studies, suggesting strong hydrogen bonding or rapid exchange processes.
- 2. The hierarchy of interaction strengths is reflected in the differential behaviour of the amide protons in solution, with N-H(4) showing larger chemical shift changes compared to N-H(2).
- 3. The presence of multiple hydrogen bonding interactions in the solid state supports our observation of complex, concentration-dependent behaviour in solution, including the involvement of ethanol in the hydrogen bonding network.

The changes in chemical shifts in the 3-HBA aromatic peaks, coupled with the broadening and disappearance in carboxylic acid peak with increasing concentration, suggest that the carboxylic acid-pyridine interaction may be the primary driver of association in solution. This interaction could lead to the formation of transient complexes that are in fast exchange on the NMR timescale, resulting in considerable peak broadening. The differential shifts observed for the INA amide protons can be explained by considering their roles in the solid-state hydrogen bonding network. The N-H (4) proton, which shows the largest shift, may be involved in amide-carboxylic acid interactions, while N-H (2) may participate primarily in amide-amide interactions. As concentration increases, the likelihood of forming these hydrogen bonds also increases as more molecules come into proximity, contributing to the observed changes in chemical shifts.

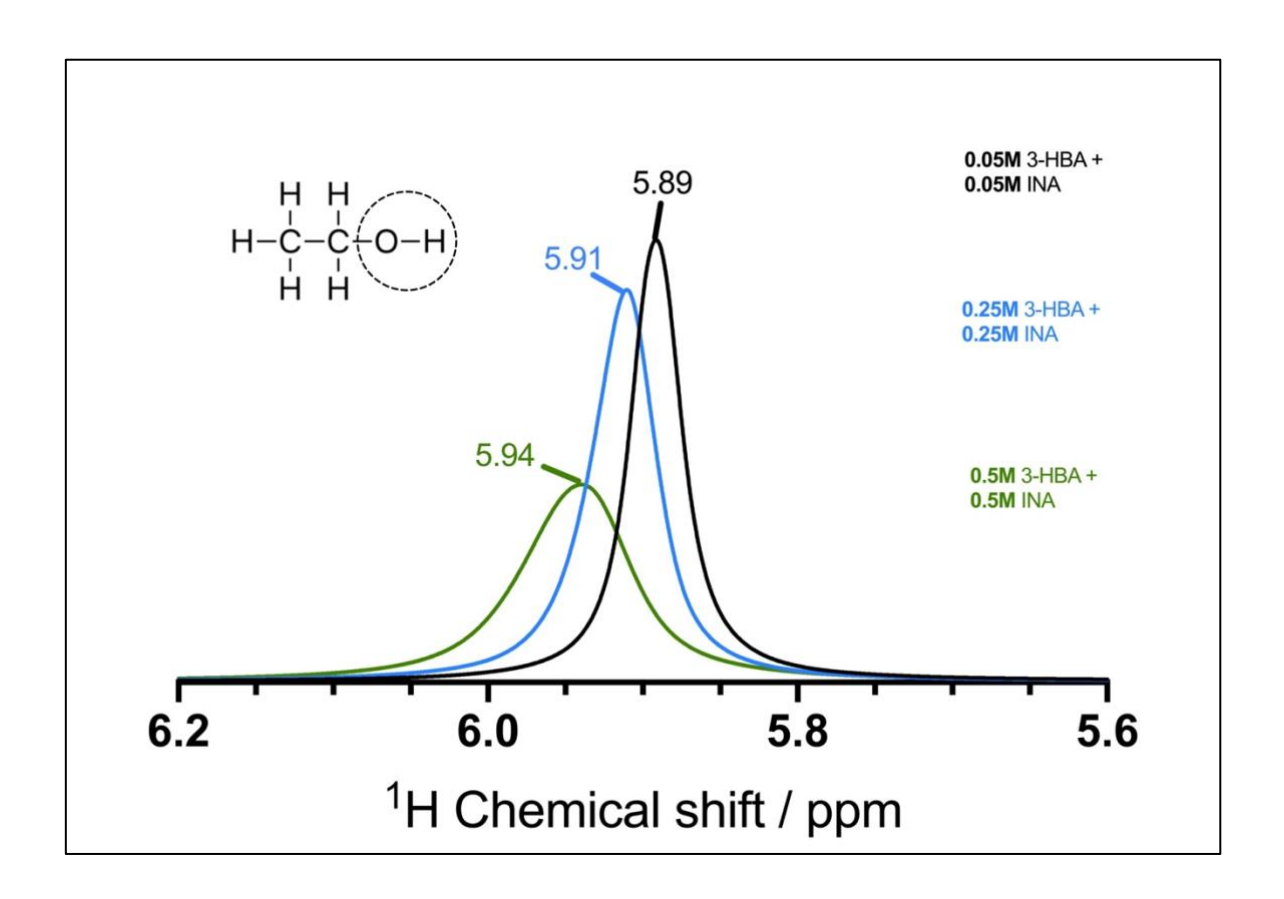


**Figure 5-30** – Changes in <sup>1</sup>H peak chemical shifts of Et-OH at different concentrations of 3-HBA and INA.

#### 5.2.4 NMR Titrations

NMR titration is an effective method for analysing the effect of concentration on intermolecular interactions between organic ligands and host molecules.<sup>237</sup> One of the primary applications of <sup>1</sup>H NMR titrations is to study the formation of host-guest complexes. By systematically varying the concentration of components, while monitoring changes in NMR peaks, we can derive quantitative information on the strength and effect of interactions between both species in a non-destructive manner. The essence of conducting <sup>1</sup>H NMR titrations lies in its ability to provide quantitative insights into binding affinities, stoichiometries, and the nature of molecular interactions.<sup>238</sup>

In this work, we conducted a series of NMR titrations to investigate the interactions between hydroxybenzoic acids (3-HBA and 2-HBA) and cyclic amides (NA and INA). We prepared

concentrated solutions of 3-HBA and 2-HBA and combined them with concentrated solutions of NA and INA, respectively, in sixteen different molar ratios ranging from 0.1:1 to 3:1 (acid:amide) in separate NMR tubes. Stock solutions were prepared and diluted accordingly to achieve the desired concentrations and ratios. Each NMR tube was filled to a total volume of  $500\mu$ L and included a capillary tube containing an internal reference (3-(Trimethylsilyl)propionic-2,2,3,3-d4 acid sodium salt,  $\delta$  = 0ppm) to ensure precise chemical shift measurements and consistency across samples.

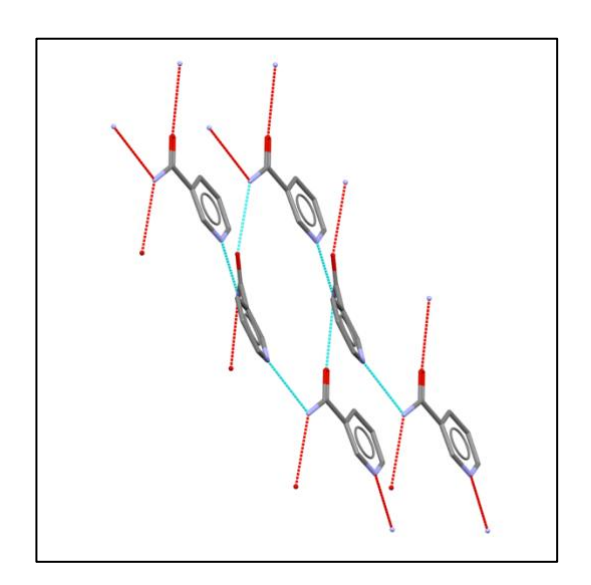
After combining the solutions in their required stoichiometries, the samples were thoroughly mixed and allowed to equilibrate for 24 hours. This equilibration period ensures that the system reaches a steady state before NMR measurements are taken, facilitating complete mixing of components, establishment of equilibrium between different molecular species, and stabilization of any hydrogen-bonded networks or complexes that may form. This experimental setup enables a comprehensive analysis of the concentration-dependent behaviour of the acid-amide systems. By varying the molar ratios over a wide range (from 0.1:1 to 3:1 acid:amide), we can observe the progression of interactions from dilute to concentrated regimes. The inclusion of a TSP internal reference enhances the accuracy of chemical shift measurements, which is crucial for detecting subtle changes in molecular environments as concentration and stoichiometry vary.

#### 2-Hydroxybenzoic Acid (2-HBA) and Nicotinamide (NA)

We observe similar patterns of chemical shifts across all acid-amide combinations studied. For the following subsections, I will focus on the 2-HBA / NA system as a representative example. This particular combination was chosen due to its clear and distinct NMR spectra, with minimal peak overlap, which allows for more straightforward interpretation of the observed chemical shifts. Additionally, the 2-HBA / NA system exhibits behaviour that is characteristic of the trends observed in the other combinations, making it an ideal candidate for detailed analysis. We note that as concentration of acid increases from 0.1:1 to 3:1 ratio, we observe a total change in chemical shift of 0.06 ppm in all peaks, suggesting an increase in aggregation behaviour due to hydrogen bonding of components. Interestingly, the NA amide peak N-H (7), exhibits a larger change in chemical shifts relative to all other chemical shifts.

The solid-state crystal structure of the 2-HBA:NA cocrystal (1:1 ratio, CSD: SODDOF)<sup>239</sup> reveals a complex hydrogen bonding network, providing crucial insights into the molecular interactions governing cocrystal formation. The primary interaction observed in this structure involves hydrogen bonding between the carboxylic acid group of 2-HBA and the pyridine nitrogen of NA. This interaction is fundamental to the cocrystal's stability and is likely to persist in solution, albeit with greater dynamic behaviour. In addition to this interaction, the crystal structure reveals a complex network of secondary interactions. NA is known to self-aggregate to form catemers. However, in the 2HBA<sub>1</sub>:NA<sub>1</sub> cocrystal, the amide proton that was bonded to a neighbouring pyridine, is now bonded to a carboxylic acid functional group. This is a stronger bond, with a shorter bond distance, hence a different chemical shift in only one N-H proton.

The NMR titration experiments revealed a consistent upfield shift of 0.05 ppm in all coformer peaks as the acid concentration increased from 0.1:1 to 3:1 ratios. This systematic change in chemical shift can be attributed to several interrelated factors. Firstly, the increasing acid concentration likely promotes molecular aggregation through enhanced hydrogen bonding, leading to changes in the electronic environment of the protons. These aggregation effects can result in increased shielding, causing the observed upfield shifts.<sup>240</sup> Secondly, the addition of acid alters the overall polarity and hydrogen bonding capacity of the solution environment. Given that ethanol is a polar, protic solvent, the introduction of increasing amounts of acid induces changes in the local chemical environment, influencing proton shielding and contributing to the upfield shifts. This effect was corroborated by a control experiment in which the addition of 100 μL of HCl to 1:1 ratios of 2-HBA and NA resulted in even larger upfield shifts for all protons. Perhaps most significantly, the magnitude and systematic nature of the shifts suggest that pH change is a major contributing factor. Carlisle et al.<sup>241</sup> examined the effect of pH changes on amino acid chemical shifts, noting variations between -0.001 to +0.19 ppm depending on the concentration of the pH-altering sample. While their study involved much higher concentration ranges (1 to 8 M urea), our observed chemical shifts are comparatively significant, considering that our coformers reach saturation point and crystallize out of solution at substantially lower concentrations.



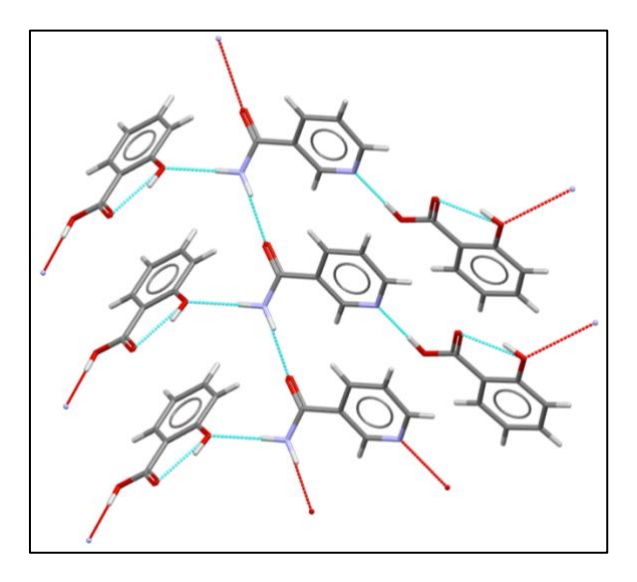


**Figure 5-31** – NA (left, CSD:NICOAM) and 2-HBA<sub>1</sub>:NA<sub>1</sub> (right, CSD:SODDOF) solid state crystal packing arrangement.

Among the observed chemical shift changes, one specific peak exhibits a more pronounced variation compared to the others. The N-H (7) peak demonstrates a shift 1.5 times larger than the rest of the coformer peaks. This unique behaviour can be attributed to a combination of factors affecting the amide group's electronic environment. The introduction of 2-HBA significantly alters the chemical surroundings of the amide protons. It disrupts the existing amide-amide hydrogen-bonded networks present in the pure NA solution, leading to substantial changes in the chemical environment of these protons. The proximity of 2-HBA molecules and the formation of intermolecular complexes further contribute to these changes. The observed chemical shift variations are a direct result of this disruption and subsequent reorganization of hydrogen bonding networks in solution. It is noteworthy that in our reference samples, increasing the concentration of pure NA in ethanol resulted in downfield shifts for this same N-H proton. Therefore, the observation of an upfield shift coinciding with the introduction of 2-HBA strongly suggests that intermolecular interactions play a crucial role in this system. While the solid-state structure provides valuable insights into potential interactions, the solution-state behaviour may not perfectly replicate the arrangement seen in the crystal structure. However, solution NMR data strongly suggests that similar interactions occur in solution, albeit with greater dynamic and possibly less ordered arrangements. This phenomenon has been observed in previous studies of related systems, where solution-state interactions are characterized by rapid exchange between different conformations and hydrogen bonding arrangements.<sup>242</sup> The gradual change in chemical shift position with increasing 2-HBA concentration indicates a dynamic equilibrium between free NA molecules, NA-NA catemers, and 2-HBA/NA complexes. As the concentration of 2-HBA increases, the equilibrium shifts towards the formation of structures more closely resembling the solid-state cocrystal arrangement. This behaviour is consistent with findings from Lamm *et al.*, who used a combination of NMR titration and diffusion NMR experiments to study the formation of host-guest complexes and identify intermediates.<sup>243</sup>

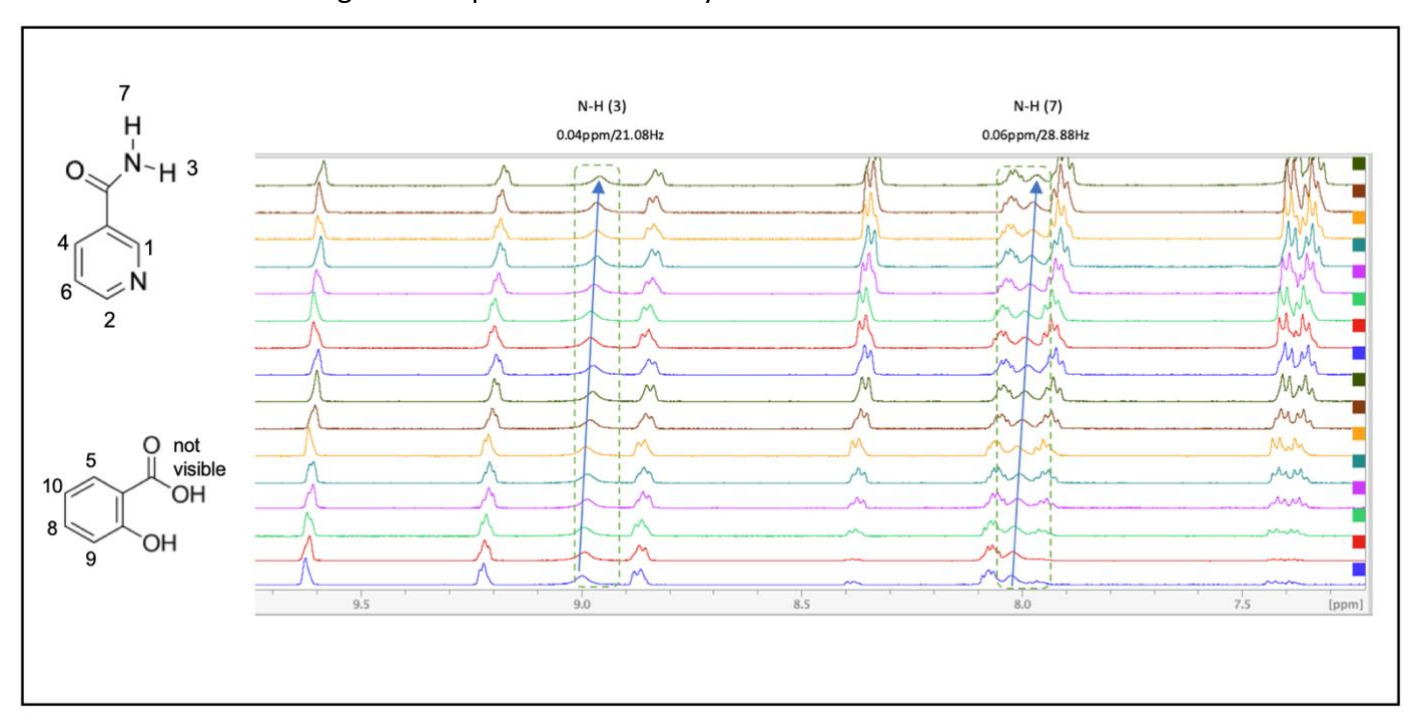


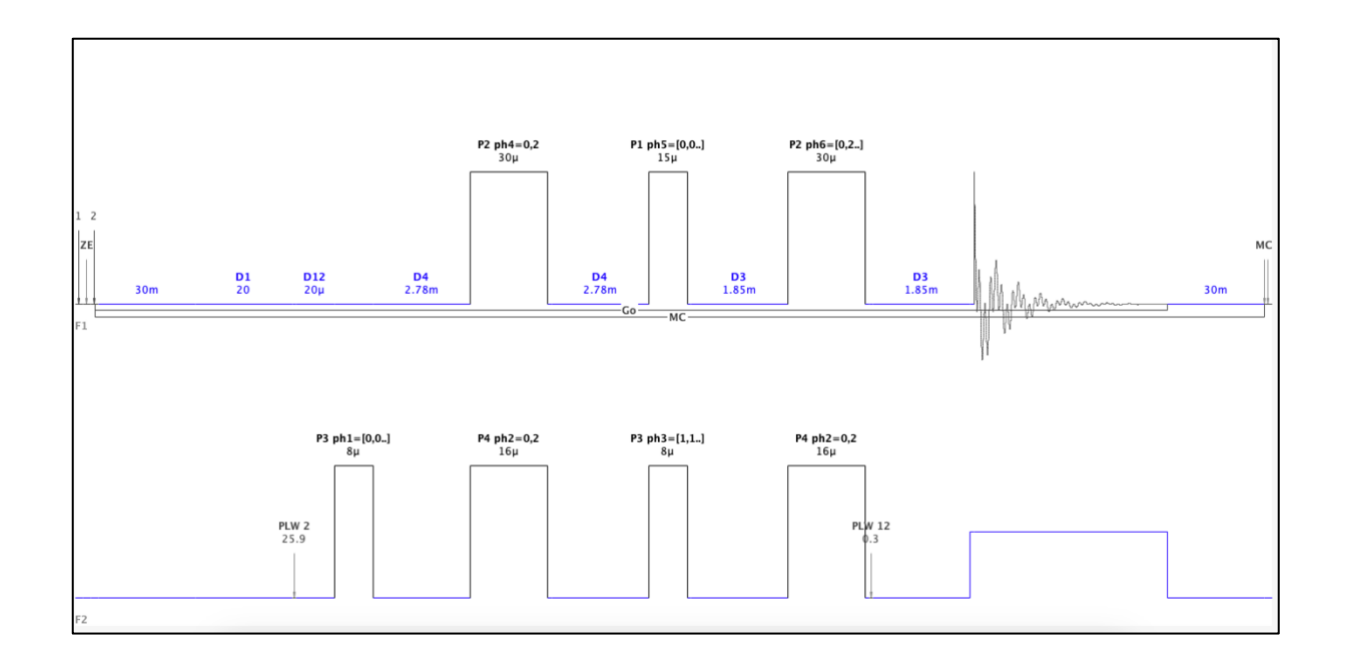
**Figure 5-32** - <sup>1</sup>H NMR titration spectra of solution of 2-HBA:NA with different ratios from 0.1:1 to 3:1 acid:amide

# 5.2.5 Insensitive Nuclei Enhanced by Polarization Transfer (INEPT) NMR spectroscopy

Building upon our understanding of the solution-state behaviour of the HBA/amide systems by <sup>1</sup>H NMR titrations, we can further enhance our insights into the intermolecular interactions by employing advanced NMR techniques. One such technique that holds particular promise for this investigation is INEPT (Insensitive Nuclei Enhanced by Polarization Transfer) NMR spectroscopy. INEPT, introduced by Ray Freeman in 1979<sup>153</sup>, is a signal enhancement method that allows for the study of insensitive nuclei, such as <sup>15</sup>N, by transferring polarization from

more sensitive nuclei like <sup>1</sup>H. This technique is particularly valuable for probing nitrogen-containing functional groups, which play a crucial role in the hydrogen bonding networks of our cocrystal systems.

INEPT allows for the detection of <sup>15</sup>N nuclei with significantly improved signal-to-noise ratios compared to direct <sup>15</sup>N observation. This enhanced sensitivity is particularly valuable for our systems, where we are interested in the nitrogen atoms of cyclic amides involved in hydrogen bonding. The technique provides a means to observe these nitrogen atoms more clearly, potentially revealing subtle changes in their chemical environment as they interact with hydroxybenzoic acids, and to monitor the extent of these interactions with changing concentration. Marion *et al.*<sup>244</sup> demonstrated that <sup>15</sup>N chemical shifts are sensitive to peptide conformation as a result of hydrogen bonding interactions. In our case, this sensitivity could reveal changes in the environment of NA as it interacts with 2-HBA for example. We conducted <sup>15</sup>N INEPT NMR experiments on the 2-HBA/NA system at various concentration ratios; 0.1:1, 1:1, 2:1, 3:1 selected from <sup>1</sup>H NMR titration experiments. The proton-nitrogen correlations provided by INEPT will allow us to directly observe changes in the chemical environment of the amide and pyridine nitrogens separately.



 $\begin{tabular}{ll} \textbf{Figure 5-33} - \textbf{Pulse} & \textbf{program for INEPT Insensitive Nuclei Enhanced by Polarization} \\ \textbf{Transfer}^{153} & \textbf{Pulse} & \textbf{Polarization} \\ \textbf{Transfer}^{154} & \textbf{Polarization} \\ \textbf{Transfer}^{1$ 

From the pulse program (Figure 5-33), our main variables to optimize, affect D3. D3 is a delay that allows for the evolution of J-coupling between the X nucleus (typically  $^{13}$ C or in our case,  $^{15}$ N) and the directly bonded proton ( $^{1}$ H). Constant 2 represents the J-coupling constant J(XH) between the X nucleus ( $^{15}$ N in our case) and the directly bonded proton ( $^{1}$ H). This value is crucial for setting the appropriate delays in the INEPT sequence to allow for optimal polarization transfer. For our 2-HBA/NA system, we estimate 1J ( $^{1}$ H- $^{15}$ N) coupling constant for the amide group in NA to be ca. 90 Hz. The pyridine nitrogen does not have a directly bonded proton, so we will not observe a one-bond J-coupling for this atom. However, we might see long-range couplings to nearby protons, which are typically much smaller (<10 Hz), hence we set cnst2 as 10 when aiming to observe the pyridine nitrogen.

Constant 11 is used to adjust the delay d3, based on the multiplicity of the X-H coupling. For our amide group, which is an XH<sub>2</sub> system, we set cnst11 to 6. This optimizes the INEPT sequence, ensuring the most efficient polarization transfer for our amide nitrogen. For our pyridine, we also set cnst11 to 6.

$$D3 = \frac{1}{(cnst2 \ x \ cnst \ 11)}$$
 Equation 5-1

We analyse our <sup>1</sup>H -<sup>15</sup>N INEPT results through the lens of hydrogen bonding, pH changes, and aggregation. The amide nitrogen, with a peak around 104 ppm, exhibits minimal shift variation (104.1-104.2 ppm) across all acid:amide ratios. This stability suggests that the amide group is likely engaged in intermolecular hydrogen bonding with other NA molecules, even at higher acid concentrations, and demonstrates less sensitivity to pH changes compared to its pyridine counterpart<sup>245</sup>.

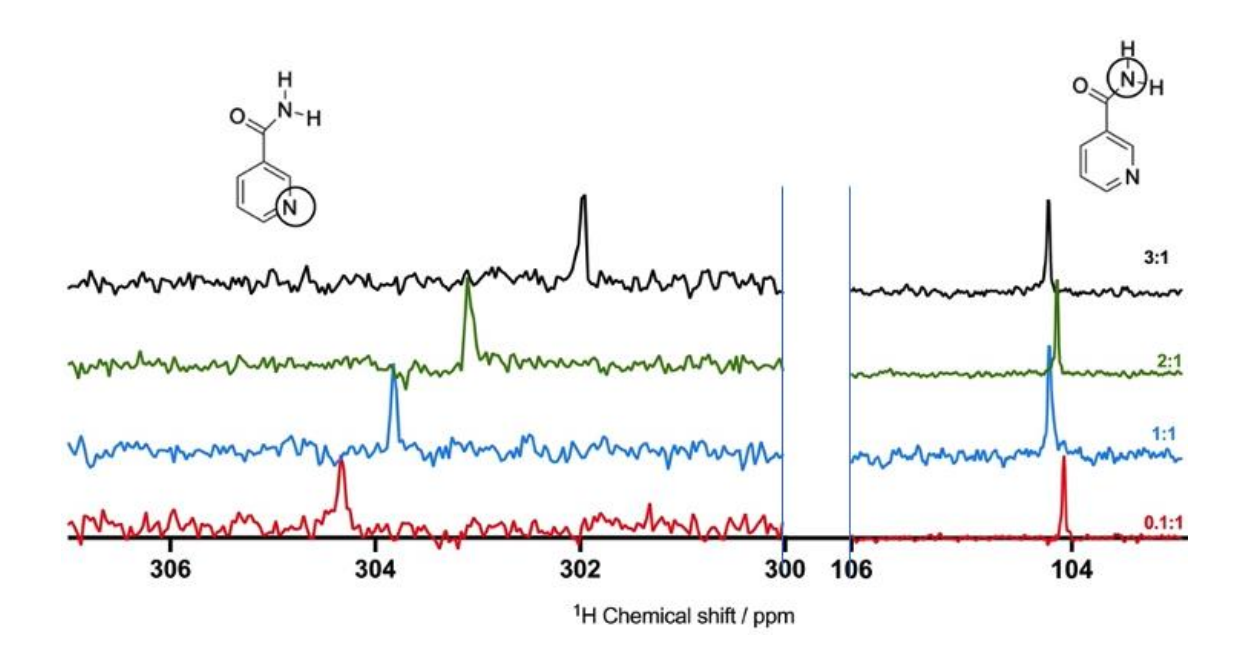


Figure 5-34 - 1H-15N INEPT NMR peaks

The pyridine nitrogen, initially observed at 304.3 ppm, undergoes a significant upfield shift, reaching 302 ppm as the acid concentration increases. These <sup>15</sup>N INEPT results reveal significant information about the behaviour of the nitrogen environments at varying acid/amide concentration ratios, and the differential behaviour raises important questions about the factors influencing chemical shifts in these nitrogen atoms. The first likely explanation is related to hydrogen bond strength and protonation. The stability of the amide nitrogen chemical shift suggests that it is engaged in robust intermolecular hydrogen bonds, likely with other NA molecules. This stability persists even at higher acid concentrations, indicating that these hydrogen bonding interactions are strong enough to maintain a consistent electronic environment around the amide nitrogen.

In contrast, the significant upfield shift observed for the pyridine can be attributed to two primary factors: protonation of the pyridine nitrogen and hydrogen bond formation. Protonation and hydrogen bonding exist on a continuum. A strong hydrogen bond can be viewed as a partial proton transfer, while full protonation represents complete proton transfer. The observed chemical shifts can reflect various stages along this continuum. As the acid concentration rises, more pyridine nitrogens become protonated, leading to increased

shielding and an upfield shift. This observation aligns with the known behaviour of pyridine in acidic environments, where protonation significantly affects its electronic structure.<sup>246</sup>

Explaining the difference in nitrogen chemical shifts of pyridines and amide by their susceptibility to protonation involves discussing their pKa. Pyridine, being a stronger base has a pKa of around 5.2 in water.<sup>247</sup> The pKa of pyridine in ethanol is less widely known, however studies in 80% ethanol – 20% water mixtures show monosubstituted pyridines have a pKa of around 3.79,<sup>248</sup> and in pure ethanol this would presumably be lower. We therefore expect it to be more readily protonated compared to the amide group, which would a much higher pKa. The higher basicity makes the pyridine nitrogen more sensitive to changes in acid concentration, resulting in the observed upfield shift. The amide nitrogen, while less prone to full protonation, can still participate in hydrogen bonding. Its relatively stable chemical shift suggests it forms consistent, strong hydrogen bonds that do not change significantly with acid concentration. Another important factor to consider is the conformational flexibility of the molecules and steric effects. Steric hindrance can affect how closely each nitrogen atom interacts with its hydrogen bonding partners.<sup>249</sup> The consistent chemical shift of the amide nitrogen suggests that steric factors may play a role in maintaining stable hydrogen bonding interactions, possibly by limiting the approach of acid molecules. For the pyridine nitrogen, the observed change in peak position could be influenced by changes in steric interactions as protonation occurs.

# 5.2.6 Nuclear Overhauser Effect NMR Spectroscopy

The next NMR technique employed is Nuclear Overhauser Effect (NOE) experiments, which offers a unique perspective on molecular structure and interactions. Building on knowledge gained from titrations and INEPT, NOE relies on through-space dipolar interactions between nuclei, providing valuable information about spatial relationships in molecules<sup>250</sup>. We aimed to observe the spatial proximities between 2HBA and NA molecules at higher concentrations, shedding light on the hydrogen bonding networks and aggregation behaviour of these coformers in solution. The power of NOE lies in its ability to detect interactions between nuclei that are close in space, typically less than 5Å<sup>251</sup>, theoretically making this useful tool for our study.

We employed both one-dimensional and two-dimensional Nuclear Overhauser Effect (NOE) experiments to probe the spatial relationships between 2HBA and NA molecules. Our approach involved selecting a variety of resonances for selective irradiation on both molecules, aiming to observe intermolecular interactions. To maximise the likelihood of detecting intermolecular NOEs, we prepared highly concentrated solutions, with 2HBA at 2M and NA at approximately 1M. The rationale was that higher concentrations would increase the probability of observing intermolecular NOE signals. We employed a mixing time of 300ms, as this has been proven effective for other small molecule systems. <sup>250, 252</sup>In our 1D

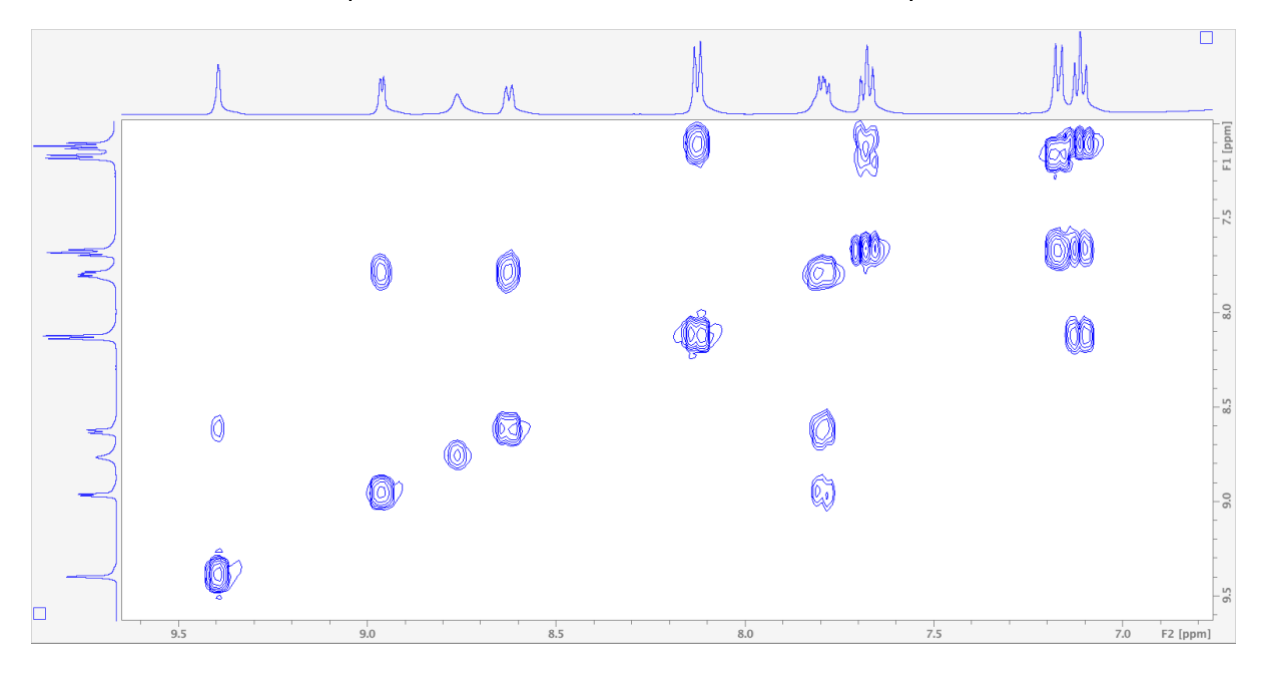


Figure 5-35 - 1H - 1H NOESY spectrum of 2-HBA and NA

NOE experiments, we applied a selective pulse to NA N-H (3) proton. However, in the corresponding negative NOE phase, we only observed the other NH<sub>2</sub> proton and ethanol peaks. We then irradiated the aromatic protons closest to the pyridine ring, but again, we only detected NOEs to other aromatic protons within the same molecule.

Further attempts to irradiate different parts of the 2HBA molecule yielded similar results, with only intramolecular NOEs observed. In our 2D NOESY experiments, we only observed intramolecular transient NOEs – intramolecular interactions between different parts of the same 2HBA molecules and the same NA molecules, but not between 2HBA and NA. The absence of observable intermolecular NOEs between the coformers in our experiments was unexpected and prompted further investigation. Several factors could potentially explain this outcome:

The molecular dynamics and diffusion characteristics of the compounds in solution play a crucial role. While NOESY is typically effective within 5 Å, intermolecular NOEs require molecules to be in close proximity with sufficient interaction time during the mixing period.

The high concentrations used (2M 2-HBA and 1M NA, both in EtOH) may have led to aggregation, potentially hindering the necessary intermolecular interactions. As Qin *et al.* noted, spin-diffusion effects can impede the observation of intermolecular NOEs, particularly in systems prone to aggregation.<sup>253</sup> The choice of a 300 ms mixing time, while generally suitable for observing NOEs, may not be optimal for this specific system. Gschwind *et al.* highlighted that longer mixing times can sometimes lead to signal attenuation due to diffusion. Observed intramolecular NOEs suggest that while the molecules interact with themselves, they may lack the necessary mobility or orientation for effective intermolecular NOE build-up<sup>254</sup>. On retrieving the NMR tube from the spectrometer, we observed some crystallisation as a solid residue had formed. This is expected at such high concentrations. To help modulate molecular mobility, we decided to run <sup>1</sup>H direct detection experiments at variable temperatures from 298 K in increments of 10 K, to 328 K and back down to 288 K.

# 5.2.7 Variable temperature <sup>1</sup>H NMR measurements

The observation of crystallization in our highly concentrated solutions (2M 2-HBA and 1M NA in EtOH) prompted us to conduct variable temperature <sup>1</sup>H NMR experiments. These experiments yielded particularly insightful results, revealing the dynamic nature of molecular interactions in our system. We note many changes in peak position and shape; however, our attention is drawn particularly to the two N-H protons from nicotinamide. As temperature changes, we observe that no other peaks shift significantly. Such changes in chemical shift position are known to be caused by restricted single bond rotation.<sup>255</sup> There are significant changes in splitting patterns, peak symmetry and multiplicity of all peaks as temperature varies, however chemical shift remains relatively similar throughout. In the case of the N-H protons and the Ethanol-OH, we see a completely different phenomenon, strongly indicating that these protons are involved in hydrogen bonding interactions. Table 4 summarizes the chemical shifts of the key protons observed.

**Table 5-4** - Chemical shifts (ppm) of key protons at different temperatures

Temp (K)	N-H (3)	N-H (7)	Ethanol OH Peaks
298 (initial)	8.99	7.86	6.23, 6.51
308	8.92	7.86	6.21, 6.48
318	8.84	7.85	6.21, 6.38, 6.52
328	8.77	7.77	6.12, 6.21, 6.42
318 (cooling)	8.86	7.86	6.27, 6.52
308 (cooling)	8.93	7.96	6.38, 6.62
298 (cooling)	9.00	8.04	6.48, 6.70
293	9.04	8.10	6.55, 6.75
288	9.08	8.14	6.59, 6.75
293 (2)	9.04	8.10	~6.64 (broad)
298 (final)	9.00	8.04	6.48, 6.70

Initially, at 298 K, we observed significant peak broadening, with relative integrations indicating that NA had crystallized to a greater extent than 2-HBA. This suggests that the 1 M NA solution had reached supersaturation more readily than 2-HBA, consistent with its lower return to solution phase. This behaviour aligns with the general principle that solubility increases with temperature for most organic compounds.<sup>256</sup>

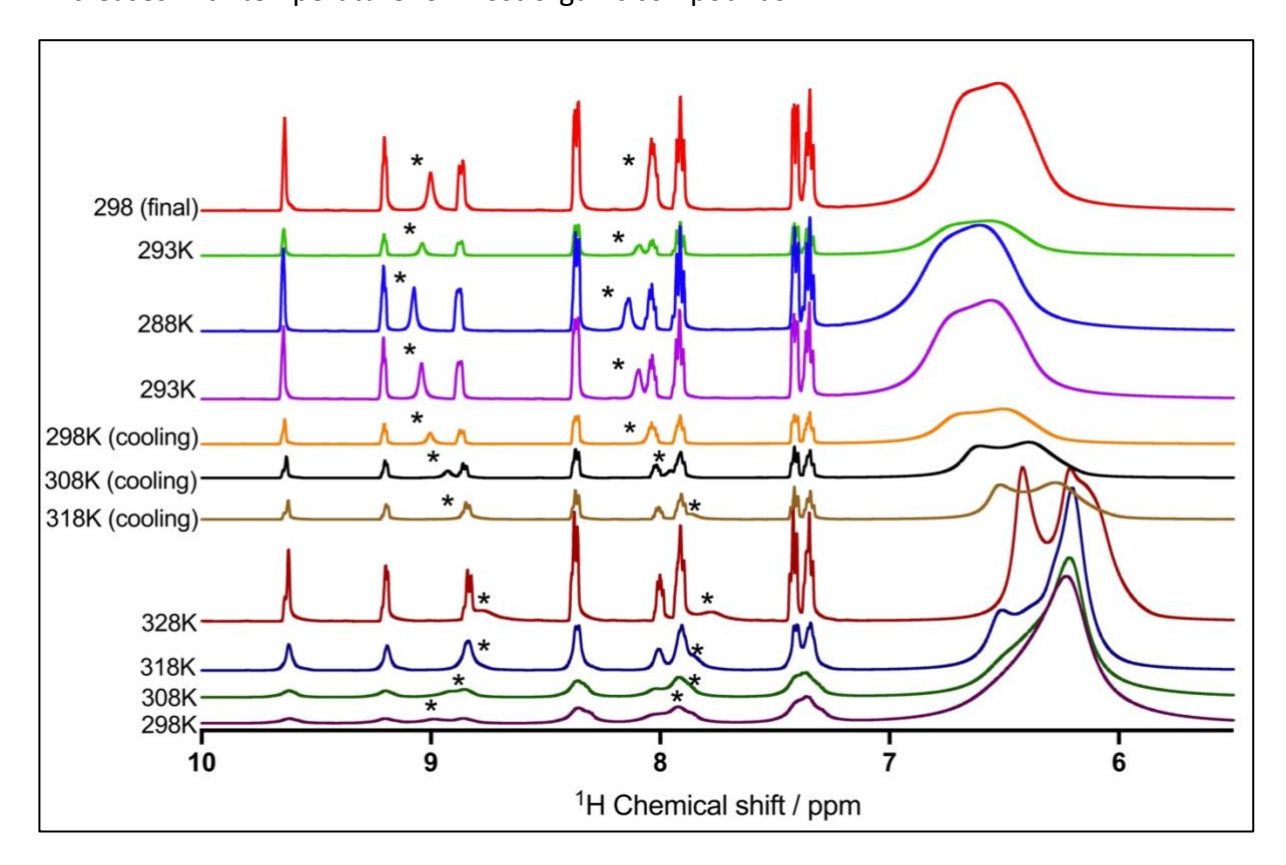


**Figure 5-36** - Variable temperature <sup>1</sup>H NMR spectra of 2HBA-NA in EtOH solution, from 298K to 328K, back down to 298K

Historically, the temperature dependencies of amide proton chemical shifts have been observed to be linear.<sup>257</sup> In our variable temperature (VT) NMR experiments, we observed that the amide proton peaks returned to their original positions at 298K after the heating and cooling cycle, despite exhibiting shifts at different temperatures during the cycle. This behaviour is consistent with the established understanding of temperature-dependent chemical shifts in proteins. The linear relationship between temperature and chemical shift allows for predictable and reversible changes as the temperature is varied. The return of the

amide proton peaks to their initial positions at 298K suggests that the temperature-induced changes in the local environment of these protons were fully reversible within the temperature range explored. <sup>258</sup> In solution, rapid rotation around bonds typically results in averaged NMR chemical shifts over all possible conformations. However, when rotation is restricted, separate signals for different coformers can be observed. This is evident from the chemical shifts observed in the amide protons<sup>232</sup>. We observed that the ethanol-OH intensity reduces in relative intensity at lower temperatures, coupled with the fact that ethanol cannot have evaporated from the sealed NMR tube, this strongly suggests that ethanol is likely participating in hydrogen bonding networks with 2-HBA and NA. These results provide strong evidence for the formation of temperature-sensitive supramolecular structures in solution, involving all three components: 2-HBA, NA, and ethanol. The system clearly appears to undergo significant reorganization with temperature change.

# 5.2.8 Summary of findings

From <sup>1</sup>H solution state analysis, we observed distinct chemical shifts for isomeric pairs (2HBA/3HBA and NA/INA), providing a robust reference framework. Concentrationdependent studies (0.05, 0.25 and 0.5 M) revealed a specific amide proton shifting downfield while other peaks shifted upfield, indicative of intramolecular hydrogen bonding due to conformational barriers in carboxamides. <sup>230, 232</sup> Upon mixing coformer solutions, we observed concentration-dependent chemical shift changes, particularly in the amide peaks. At higher concentrations, a larger relative chemical shift was noted for a specific amide proton in both NA and INA, now shifting upfield. This suggests a transition from intramolecular to intermolecular interactions. While solid-state packing data provided context, we acknowledge the potential discrepancies between solid-state and solution-state behaviour. NMR titrations across 16 different stoichiometric ratios (0.1:1 to 3:1) corroborated our initial observations. The larger shift in one specific proton compared to others, while considering factors such as pH, aggregation, and dynamic equilibrium, clearly indicates differential interactions involving this proton. INEPT and variable temperature techniques offer unique perspectives into the aggregation of these coformers in solution, particularly the difference behaviour in NA and INA nitrogens.

# Chapter 6 - Investigating cocrystal transformations by PXRD and CLASSIC NMR

#### 6.1 Introduction

Understanding structural dynamics and supramolecular assemblies in cocrystals represents a central pursuit in crystallography, encouraging the proliferation of screening efforts. In this chapter, we explore the intermolecular interactions within cocrystals formed by liquid assisted grinding of hydroxybenzoic acids and cyclic amides, focusing on 3-hydroxybenzoic acid (3-HBA), 2-hydroxybenzoic acid (2-HBA), and 2,3-dihydroxybenzoic acid (2,3-DHBA), alongside cyclic amides nicotinamide (NA) and isonicotinamide (INA). Varying stoichiometry and solvents yielded three novel cocrystals, a hydrate and a solvate from our screening experiments. These forms were characterized using a combination of solid-state techniques (TGA, DSC, FT-IR Spectroscopy, PXRD and solid-state NMR). The mechanism of cocrystal formation by grinding is often thought to be a multistage, stepwise process and can be a result of various mechanisms. Combining X-ray diffraction with Combined Liquid and Solid-State *Insitu* Crystallization (CLASSIC) NMR studies provided detailed insights into the dynamic nature of the formation of cocrystals. We were able to observe and monitor the real time interconversion of 2 known cocrystals, to 2 novel cocrystal forms, using PXRD and *in-situ* solid-state NMR techniques.

This chapter comprises two main overarching themes, the first is screening of cocrystals of hydroxybenzoic acid/cyclic amides in specific stoichiometric ratios, with solvents of varying polarity. The rationale is that varying solvents can lead to different cocrystal outcomes. This approach allows us to explore the impact of solvent polarity on the formation and stability of cocrystals, providing insights into the role of solvent-mediated interactions in crystal engineering. Solvent choice is crucial in cocrystal screening, as it can significantly influence the crystallization process and the resulting crystal forms. Solvent selection can accelerate reaction kinetics, affecting the outcome of liquid assisted grinding.<sup>259</sup>

Moreover, solvents with varying polarities can lead to the discovery of different polymorphs, stoichiometric forms and solvates/hydrates of cocrystals. For instance, Rodríguez-Hornedo and colleagues investigated the stability of 4-aminobenzoic acid/carbamazepine cocrystals

and found that the relative stability of cocrystals with 1:1 and 2:1 stoichiometries was influenced by the concentration of coformers in solution, which is directly affected by solvent choice. <sup>260</sup> The impact of solvent polarity extends beyond the screening process to the stability and properties of the resulting cocrystals. <sup>261</sup> By systematically exploring the effect of solvent polarity on cocrystal formation, this study aims to contribute to the growing body of knowledge on solvent-mediated cocrystallisation processes. This approach not only enhances our understanding of the fundamental principles governing cocrystal formation but also has practical implications for the design and optimization of pharmaceutical cocrystals with tailored physicochemical properties.

We also investigate the effect of stoichiometry on cocrystal formation. The hierarchy of hydrogen bond donor/acceptor interactions has been studied widely. Carboxylic acids, phenols, amides and aromatic nitrogens form reliable supramolecular homo/heterosynthons, and form the building blocks for this study. 27, 43, 104, 106, 108, 109, 112, 113, 262 By varying stoichiometric ratio, we change the number of donor/acceptor sites available, with the intention to affect hydrogen bonding moieties and cocrystal packing arrangements. We present the results and solid-state characterisations of screening products by a multifaceted approach, combining various analytical techniques to gain comprehensive insights into their structure and composition. We utilize techniques, including thermogravimetric analysis (TGA), differential scanning calorimetry (DSC), powder X-ray diffraction (PXRD), and solid-state nuclear magnetic resonance (ssNMR) spectroscopy. Each of these methods provides unique and complementary information, allowing for a thorough understanding of the cocrystal systems under investigation

The second section of this chapter focuses on the mechanistic understanding of cocrystal formation through *in-situ* monitoring techniques. Cocrystal formation is often considered a multistage, stepwise process that can result from various pathways. These may include amorphous intermediates, eutectic formation, or solution-mediated transformations.<sup>263</sup> We use advanced in situ monitoring techniques to observe these processes in real-time, providing insights into the complex dynamics of cocrystal formation. In-situ powder X-ray diffraction (PXRD) studies traditionally rely on synchrotron radiation due to its high intensity and time resolution capabilities.<sup>264, 265</sup> In this study, we present an alternative time-resolved technique that utilizes a laboratory-based diffractometer. This approach involves preparing multiple

batches of samples with identical stoichiometric ratios, subjecting them to grinding for specified time periods, and subsequently analysing them using PXRD to observe the evolution of X-ray diffraction patterns, whilst still observing crucial intermediate phases.

We also employ CLASSIC (Combined Liquid- and Solid-State In-situ Crystallization) NMR, a powerful technique that allows for simultaneous observation of both solid-state and solution-state species throughout the crystallization process. CLASSIC NMR leverages the strengths of NMR spectroscopy to monitor crystallization in real-time, enabling us to track the evolution of molecular interactions and the formation of supramolecular synthons that drive cocrystallisation. By leveraging alternating pulse sequences, optimized for detecting signals from either the solid or liquid phase, we are able to observe the spectra simultaneously, providing information about both environments. This dual capability is essential for elucidating the complementary changes occurring in solid and liquid phases as crystallization proceeds. This technique is particularly valuable because it can detect both dissolved species and emerging solid phases, offering a comprehensive view of the crystallization dynamics. Additionally, it provides a unique spectral fingerprint of the product, facilitating its characterization.

Figure 6-1 – Cocrystal coformers analysed in this study.

#### Materials and methods

3-Hydroxybenzoic acid (3-HBA), 2-hydroxybenzoic acid (2-HBA), 2,3-dihydroxybenzoic acid (2,3-DHBA), nicotinamide (NA), and isonicotinamide (INA) were obtained from Merck Pharmaceuticals, UK. All compounds were used as received without further purification. Solvents used for cocrystal synthesis included: toluene, acetone, 1-propanol, ethanol, methanol, ethylene glycol, and water. All solvents were of analytical grade and used without additional purification.

The experimental procedure began with the preparation of physical mixtures of hydroxybenzoic acids and the amides. Appropriate molar ratios of these compounds were weighed out based on an analysis of hydrogen bond donor/acceptor patterns observed in existing cocrystals listed in the Cambridge Structural Database (CSD). The ratios of interest were 1:1, 1:2, 2:1, and 1:3 of hydroxybenzoic acid to amide. For instance, a 1:1 ratio of 3hydroxybenzoic acid (3-HBA) to nicotinamide (NA) required 138.12 mg of 3-HBA and 122.12 mg of NA. These physical mixtures were placed in steel grinding vials, to which varying volumes of solvent (5 to 50 µL) were added. The mixtures were then subjected to grinding cycles in a Retsch MM400 ball mill. The grinding frequency was varied between 5 and 30 Hz, and cycle lengths were adjusted to determine the point at which the physical mixture converted to a cocrystal. After each grinding cycle, the resulting solids were transferred to glass vials for initial characterization using powder X-ray diffraction (PXRD). Samples showing interesting patterns were further analysed using thermogravimetric analysis (TGA), differential scanning calorimetry (DSC), and solid-state NMR. To ensure reproducibility and consistency, each combination was performed at least twice, with novel patterns being repeated a third time. The obtained powder XRD patterns were compared to those of starting materials and reported cocrystals in the CSD for identification and confirmation of new cocrystal forms.

# 6.2 Cocrystal screening by LAG with solvents of varying polarity

The use of liquid assisted grinding, previously known as solvent drop grinding as a screening tool has been widely adopted for cocrystal screening due to its high efficiency and reproducibility. <sup>56, 266</sup> The addition of a small volume of solvent increases degrees of flexibility of coformer molecules, which in turn increases the possibility of molecular collisions. <sup>267</sup> It is still unclear why LAG method improves cocrystal formation compared to neat grinding and solution methods. In this study we discovered that the solvent acts as more than a lubricating, molecular diffusion proxy. However, on some occasions, it must affect the formation of the multicomponent solid form. The 7 organic solvents selected were toluene (TOL), acetone (ACE), propanol (PrOH), ethanol (EtOH), methanol (MeOH), ethylene glycol (ETG) and water (H<sub>2</sub>O). A summary of the cocrystal screening efforts discussed in this study are shown in Table 1.

### Thermal analysis of new multicomponent solid forms

Thermal methods were helpful in screening whether a new solid form has been produced from our LAG screening using DSC. This is due to a difference in melting points of the potential new cocrystal, the starting hydroxybenzoic acid and amide coformers. The DSC thermal profile of a new cocrystal would show new indicative endothermic peaks, whereas a mixture of pure coformers should produce a thermogram with the peaks corresponding to the melting points of the starting materials. Therefore, this served as a preliminary confirmation of potential cocrystal formation, as seen in Figure 6-2.

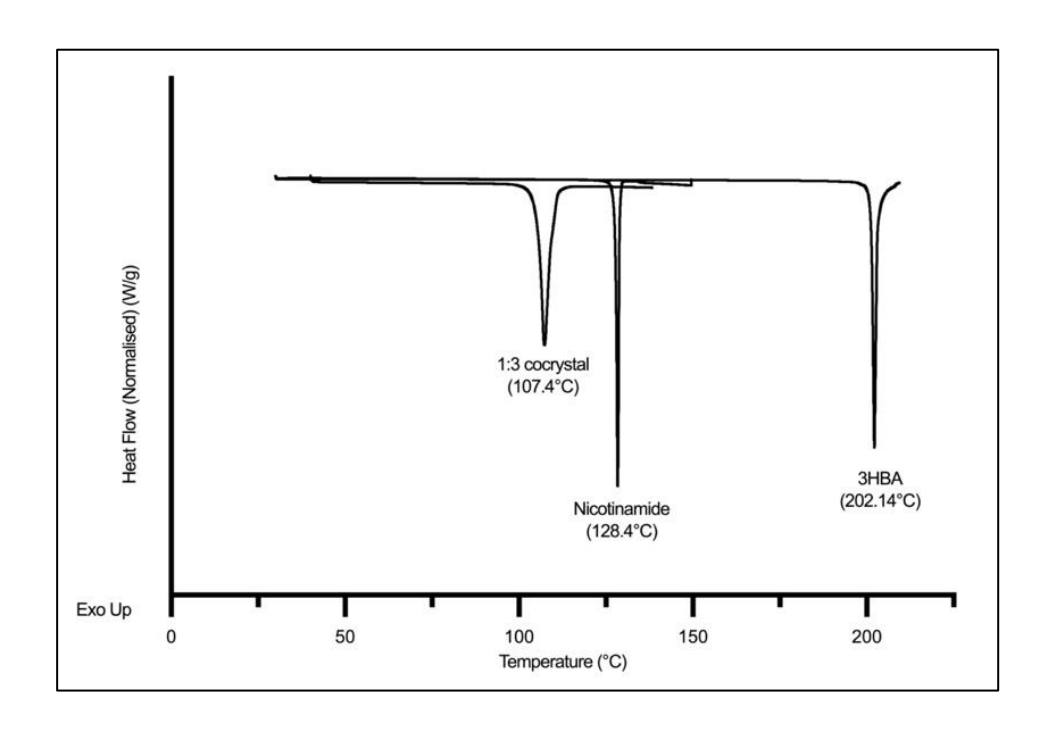


Figure 6-2 - DSC profiles of pure coformers and 3-HBA<sub>1</sub>:NA<sub>3</sub> cocrystal.

**Table 6-1** LAG screening experiments conducted in this study -  $^{*}$  star denotes cocrystals reported in CSD

COCRYSTAL	SOLVENT	RESULT
*2-HBA <sub>1</sub> :INA <sub>1</sub>	TOL	
XAQQEM	ACE	
	PrOH	
	EtOH	All formed 1:1 co-crystal
	MeOH	
	ETG	
	H <sub>2</sub> O	
2-HBA <sub>1</sub> :INA <sub>2</sub>	TOL	'Product - A'
	ACE	'Product - <b>A</b> '
	PrOH	'Product - <b>A</b> '
	EtOH	'Product - <b>A</b> '
	MeOH	'Product - <b>A</b> '
	ETG	'Product - B'
	H <sub>2</sub> O	'Product - <b>C</b> '
*2-HBA <sub>2</sub> :INA <sub>1</sub>	TOL	
QAFTID	ACE	
	PrOH	
	EtOH	All formed 2:1 co-crystal
	MeOH	
	ETG	

	H <sub>2</sub> O	
*2-HBA <sub>1</sub> :NA <sub>1</sub> SODDOF	TOL ACE PrOH EtOH MeOH ETG H <sub>2</sub> O	All form 1:1 co-crystal
2-HBA <sub>1</sub> :NA <sub>2</sub>	TOL ACE PrOH EtOH MeOH ETG H <sub>2</sub> O	All form 1:1 co-crystal with excess NA
2-HBA <sub>2</sub> :NA <sub>1</sub>	TOL ACE PrOH EtOH MeOH ETG H <sub>2</sub> O	All formed 1:1 cocrystal with excess 2-HBA
*3-HBA <sub>1</sub> :NA <sub>1</sub> XAQQIQ	TOL ACE PrOH EtOH MeOH ETG H <sub>2</sub> O	'Product - <b>D</b> ' 1:1 cocrystal 1:1 cocrystal 1:1 cocrystal 1:1 cocrystal 1:1 cocrystal 1:1 cocrystal
3-HBA <sub>1</sub> :NA <sub>2</sub>	TOL ACE PrOH EtOH MeOH ETG H <sub>2</sub> O	'Product - E' 'Product - F' 'Product - G'
3-HBA <sub>2</sub> :NA <sub>1</sub>	TOL ACE PrOH EtOH MeOH ETG H <sub>2</sub> O	All formed 1:1 cocrystal with excess 3-HBA
*3-HBA <sub>1</sub> :INA <sub>1</sub> LUNMEM	TOL ACE PrOH	

	EtOH MeOH ETG H <sub>2</sub> O	All formed 1:1 cocrystal
3-HBA <sub>1</sub> :INA <sub>2</sub>	TOL ACE PrOH EtOH MeOH ETG H <sub>2</sub> O	All formed 1:1 cocrystal with excess INA
3-HBA <sub>2</sub> :INA <sub>1</sub>	TOL ACE PrOH EtOH MeOH ETG H <sub>2</sub> O	All formed 1:1 cocrystal with excess 3-HBA
*2,3DHBA <sub>1</sub> :INA <sub>1</sub> LAGSOE	EtOH	1:1 cocrystal
2,3DHBA <sub>1</sub> :INA <sub>2</sub>	EtOH	1:1 cocrystal with excess 2,3- DHBA
2,3DHBA <sub>2</sub> :INA <sub>1</sub>	EtOH	'Product - I'
*2,3DHBA <sub>1</sub> :NA <sub>1</sub> NEFFIQ	EtOH	1:1 cocrystal
2,3DHBA <sub>1</sub> :NA <sub>2</sub>	EtOH	1:1 cocrystal with excess NA
2,3DHBA <sub>2</sub> :NA <sub>1</sub>	EtOH	1:1 cocrystal with excess 2,3- DHBA

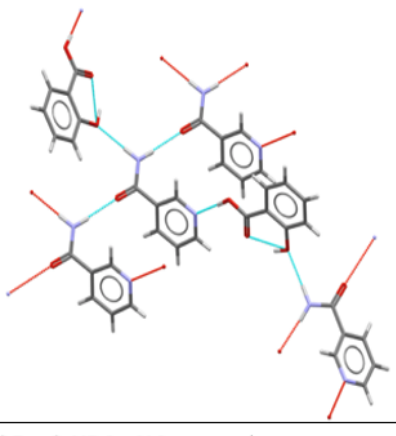
# 6.2.1 Analysis of screening results

Of the eighteen LAG screening combinations, we observe that solvent choice did not affect the result of 2-HBA<sub>1</sub>:INA<sub>1</sub>, 2-HBA<sub>1</sub>:NA<sub>1</sub>, 2-HBA<sub>1</sub>:NA<sub>2</sub>, 2-HBA<sub>2</sub>:NA<sub>1</sub>, 2-HBA<sub>2</sub>:INA<sub>1</sub>, 3-HBA<sub>2</sub>:INA<sub>1</sub>, 3-HBA<sub>1</sub>:INA<sub>2</sub> and 3-HBA<sub>2</sub>:INA<sub>1</sub>. Interestingly, literature has shown that 2-HBA<sub>1</sub>:INA<sub>1</sub> cocrystal has only previously been reported as obtained *via* slow evaporation from acetone, whilst 3-HBA<sub>1</sub>:INA<sub>1</sub> was prepared by slow evaporation from ethanol. <sup>103</sup> 2-

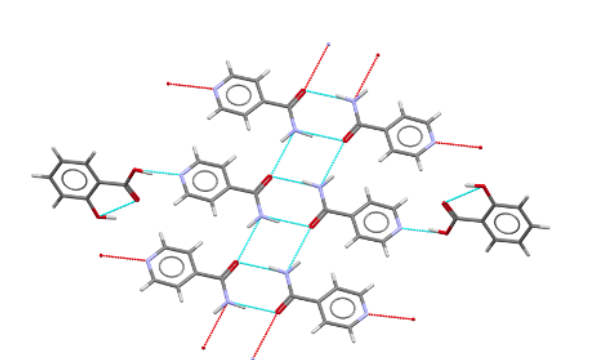
**HBA<sub>1</sub>:NA<sub>1</sub>** co-crystal has been produced *via* hot stage microscopic screening.<sup>239</sup> Of all the 2:1 combinations, only **2-HBA<sub>2</sub>:INA<sub>1</sub>** forms a pure cocrystal.<sup>269</sup> This was confirmed by PXRD and DSC.

**2-HBA<sub>2</sub>:NA<sub>1</sub>**, **3-HBA<sub>2</sub>:NA<sub>1</sub>**, **3-HBA<sub>2</sub>:INA<sub>1</sub>**, **2-HBA<sub>1</sub>:NA<sub>2</sub>** and **3-HBA<sub>1</sub>:INA<sub>2</sub>** all produced their respective 1:1 cocrystals, with an excess of pure hydroxybenzoic acid or amide. Interestingly, the increased competition from the extra hydrogen bond donors/acceptors did not change the preferred intermolecular interactions in these cases. Primary amides typically display two types of supramolecular homosynthons, namely the dimer and the catemer, when no other hydrogen bond donor is present.<sup>270</sup> However, when there is competition from other robust hydrogen bond donor/acceptors such carboxylic acids, phenols and N-pyridines, as seen in 2-HBA and 3-HBA, common supramolecular synthons present are the pyridine-acid,<sup>103</sup> amideacid,<sup>115, 271</sup> phenol-pyridine.<sup>272</sup> A closer look at the reported 1:1 cocrystals of 2-HBA:NA, 2HNA:INA, 3-HBA:NA, and 3-HBA:INA reveals they all exhibit different supramolecular synthons and hydrogen bonding patterns, as seen in Figure 6-3.

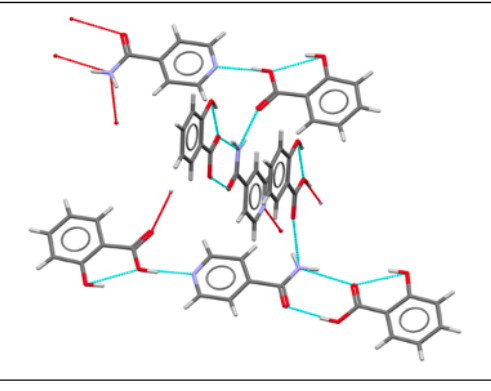
Figure 6-3 - Amide-amide centrosymmetric dimer [left] and catemer [right]



SODDOF – 2-HBA<sub>1</sub>:NA<sub>1</sub>, contains catemer with NA NH2 donating to both isonicotinamide O and 2-HBA phenol. N-pyridine accepting OH from COOH. Intramolecular bonding between C=O and Phenol OH

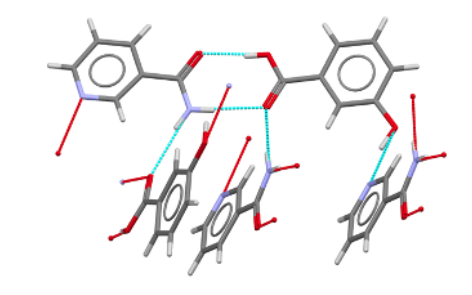


**XAQQEM – 2-HBA<sub>1</sub>:INA<sub>1</sub> –** contains amide – amide dimer, COOH – pyridine, intramolecular phenol to c=o, NH2 amide C=O.

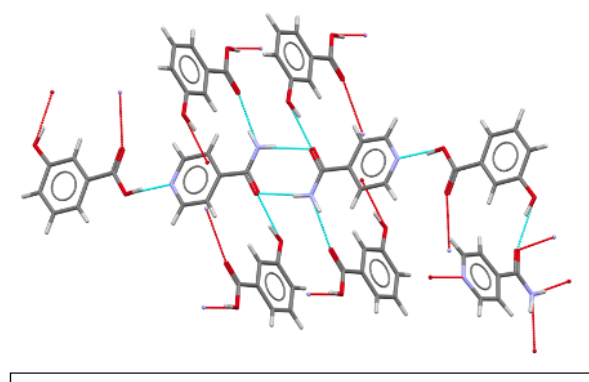


QAFTID – 2-HBA<sub>2</sub>:INA<sub>1</sub> – contains amide – acid dimer, intramolecular phenol to COOH. Amide pyridine to acid COOH. Amide NH to Acid C=O

Figure 6-4 - Supramolecular synthons of selected cocrystals in this study



**XAQQIQ – 3-HBA**<sub>1</sub>:**INA**<sub>1</sub>, contains acid-amide heterodimer. Rare Phenol-pyridine bond. Amide NH donates to amide C=O.



**LUNMEM – 3-HBA**<sub>1</sub>:**INA**<sub>1</sub> – contains amide – amide dimer, COOH - pyridine, Phenol - CONH2

#### 2-HBA<sub>1</sub>:INA<sub>2</sub>

This coformer combination yielded three different solid products. When the solvent was ethylene glycol or water, 2 new solid forms; **B** and **C** were observed.

*Product – A* — Acetone, propan-2-ol, ethanol, methanol and toluene all produced the same 'new' solid form, identified initially by its unique PXRD pattern. DSC analysis shows two, unique endothermic peaks. We determined that the peak at 132°C corresponds to the 1:1 cocrystal. Interestingly, the second peak at 130°C did not correspond to any known material from our study. <sup>13</sup>C CP/MAS NMR analysis confirmed the presence of a 1:1 component, however we also notice new peaks and multiple peak shifts. Subsequent in-depth analysis indicated that a mixture of 2-HBA<sub>1</sub>:INA<sub>1</sub> and 2-HBA<sub>1</sub>:INA<sub>3</sub> was present. This cocrystal combination is discussed in depth further on in this chapter.

#### 2-HBA:INA - ratios compared

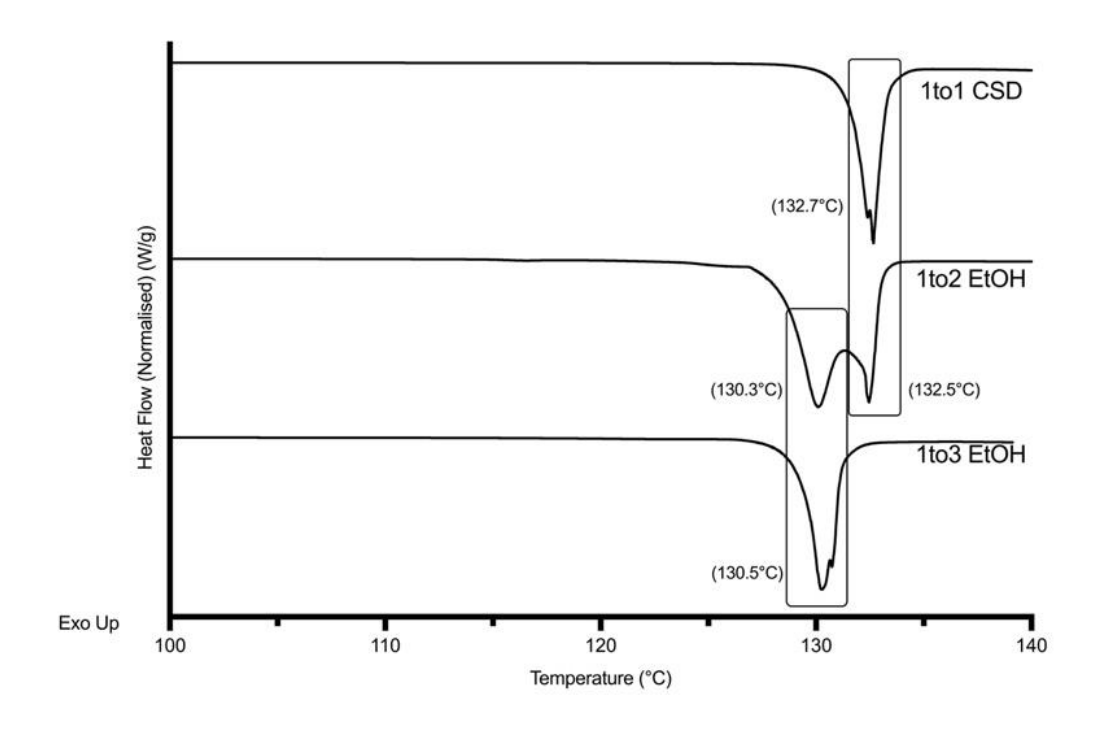


Figure 6-5 - DSC plot comparing melting points of 2-HBA:INA 1:1, 1:2, and 1:3 combination

ETG (product B) - PXRD pattern confirms a different solid form, showing sharp and narrow peaks, suggesting high degree of crystallinity. This was confirmed by DSC. We observed several endothermic peaks, none of which correspond to starting materials or known cocrystals, suggesting that this was indeed a mixture of different materials. Another hypothesis is that as heat is applied to the powder, multiple phase transitions occur. It was noted that when the rate of heating changed, from 2 to 5°C/min, we observed different DSC peaks. The presence of ETG peak in <sup>13</sup>C CP/MAS NMR suggests that the solvent has not evaporated but has rather been incorporated into the solid structure and has formed a complex mixture of products. We also note distinct differences in peak positions corresponding to the -COOH, phenol and aromatic regions.

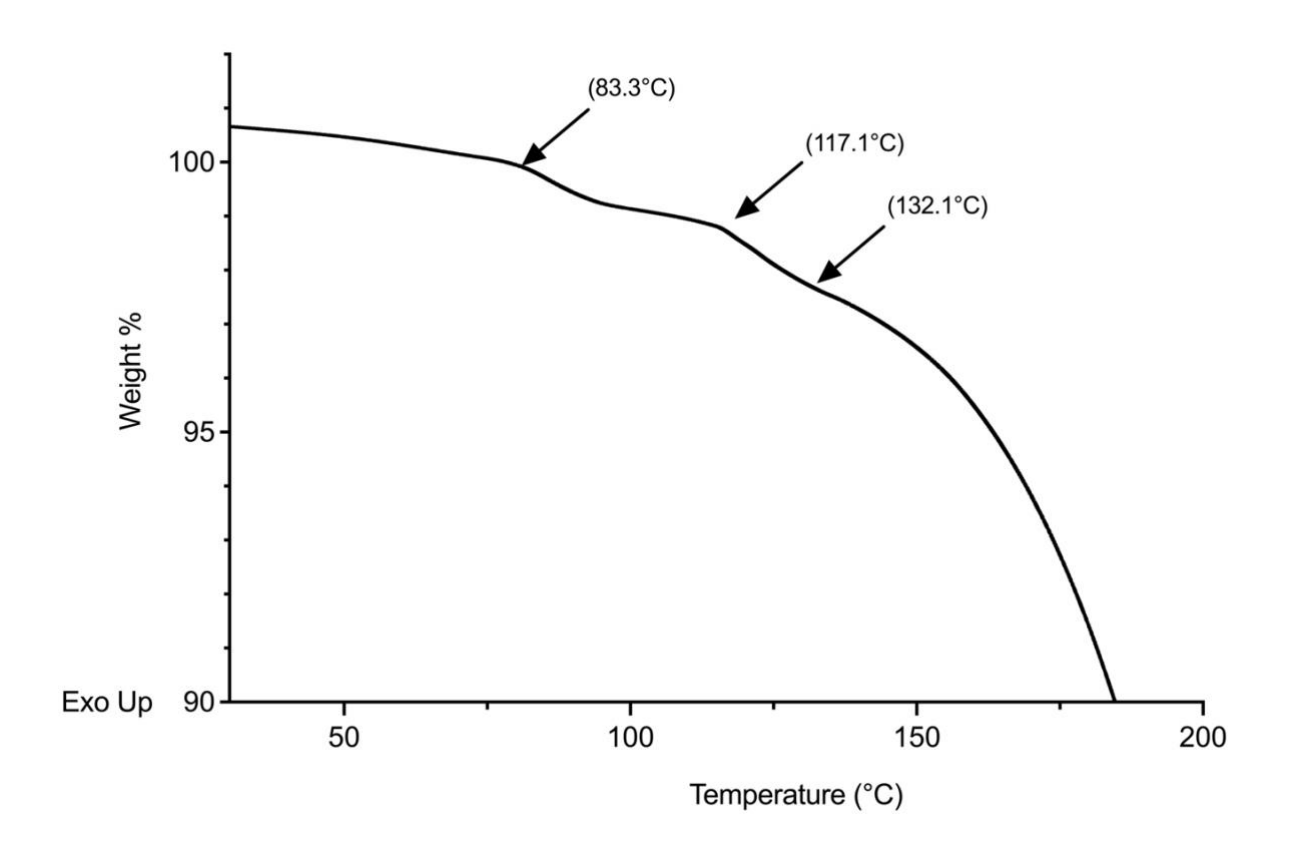
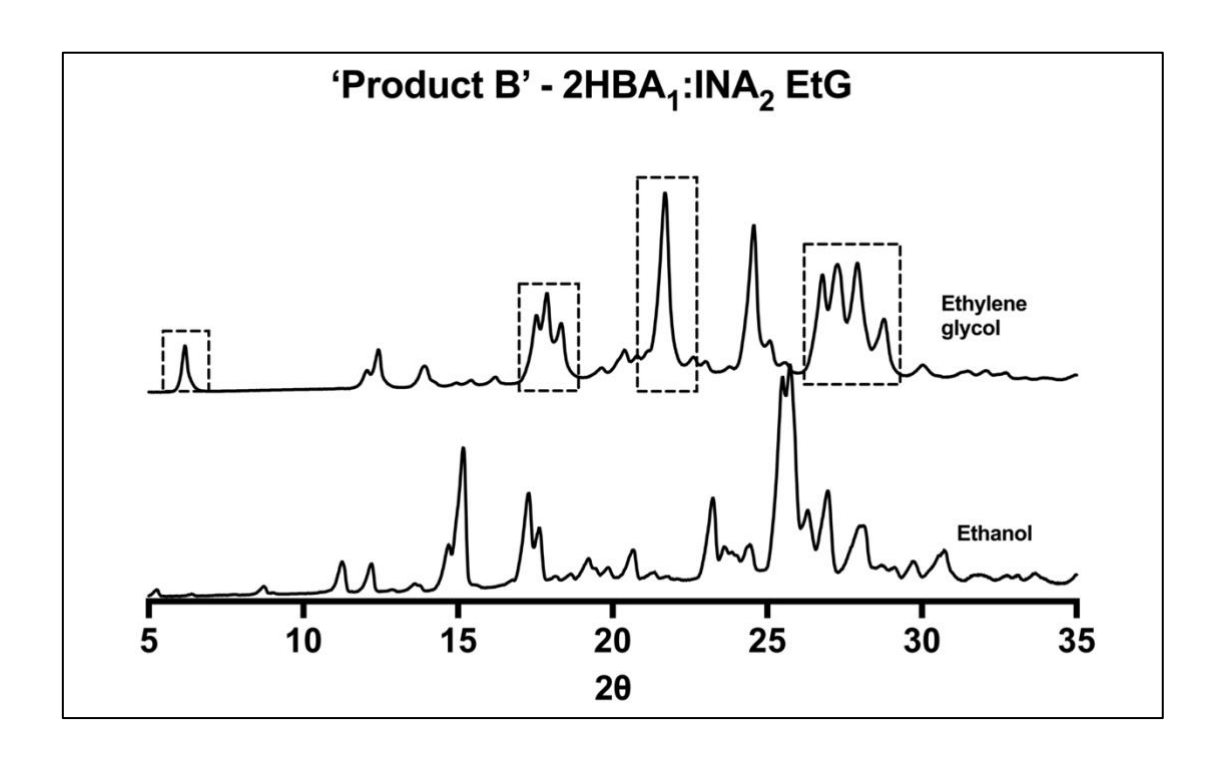
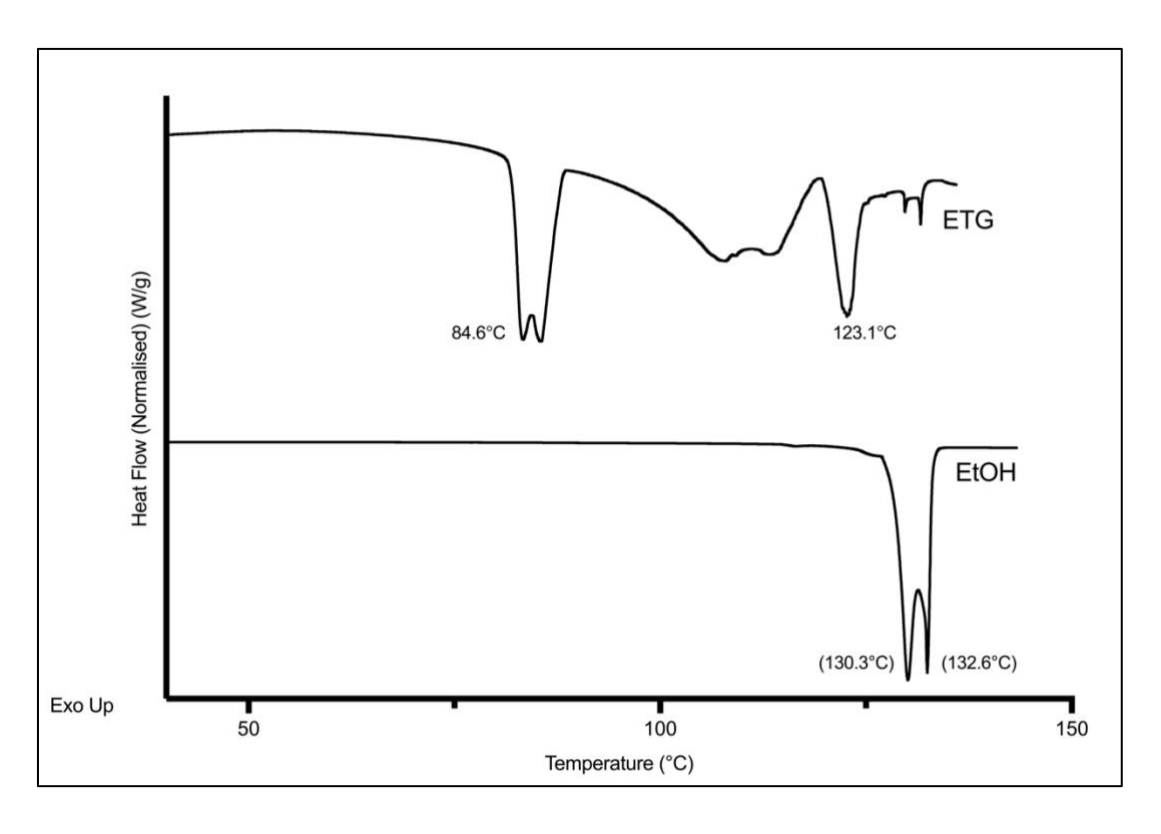
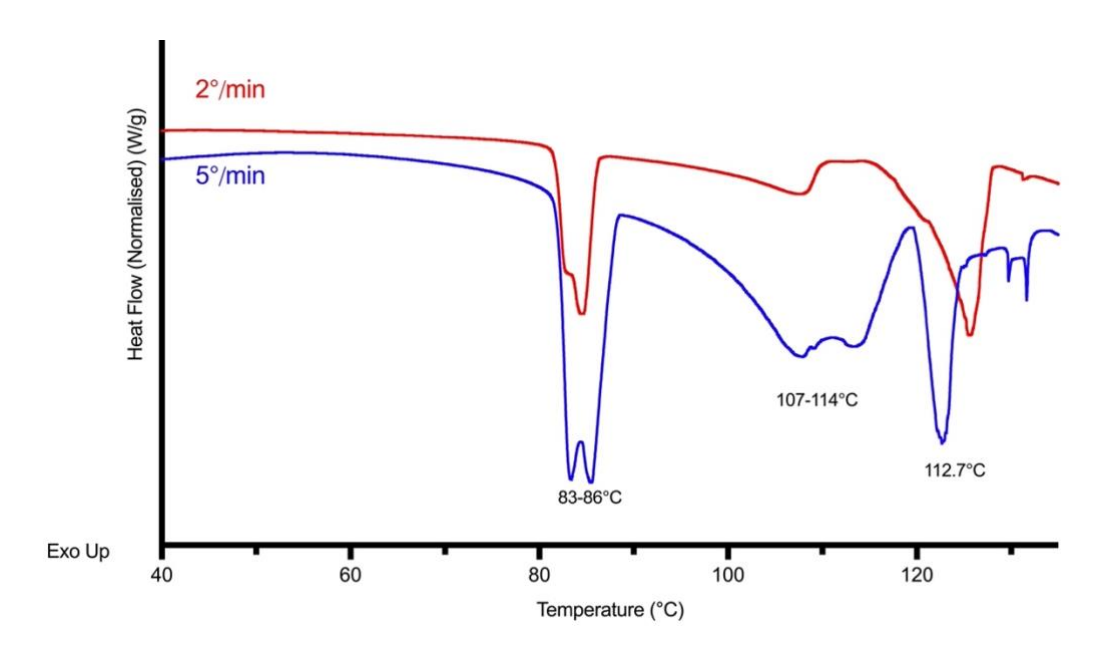


Figure 6-6 TGA plot of 2HBA1:INA2 LAG product with Ethylene glycol as the solvent.

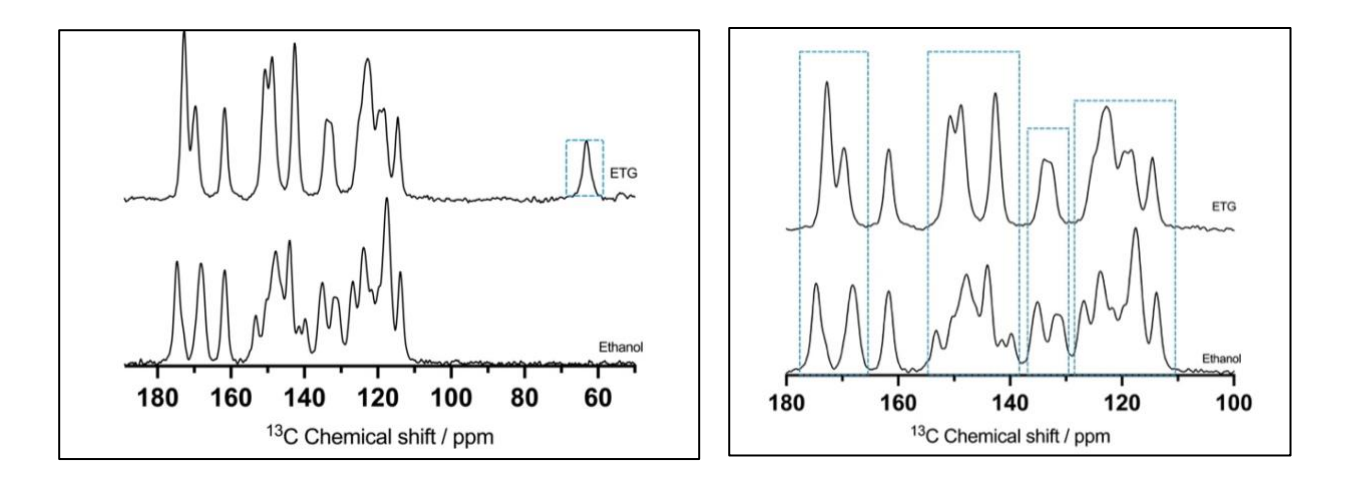




**Figure 6-7** - PXRD pattern and DSC thermograms of 2-HBA<sub>1</sub>:INA<sub>2</sub> with ETG. Multicomponent solid form 'Product B'



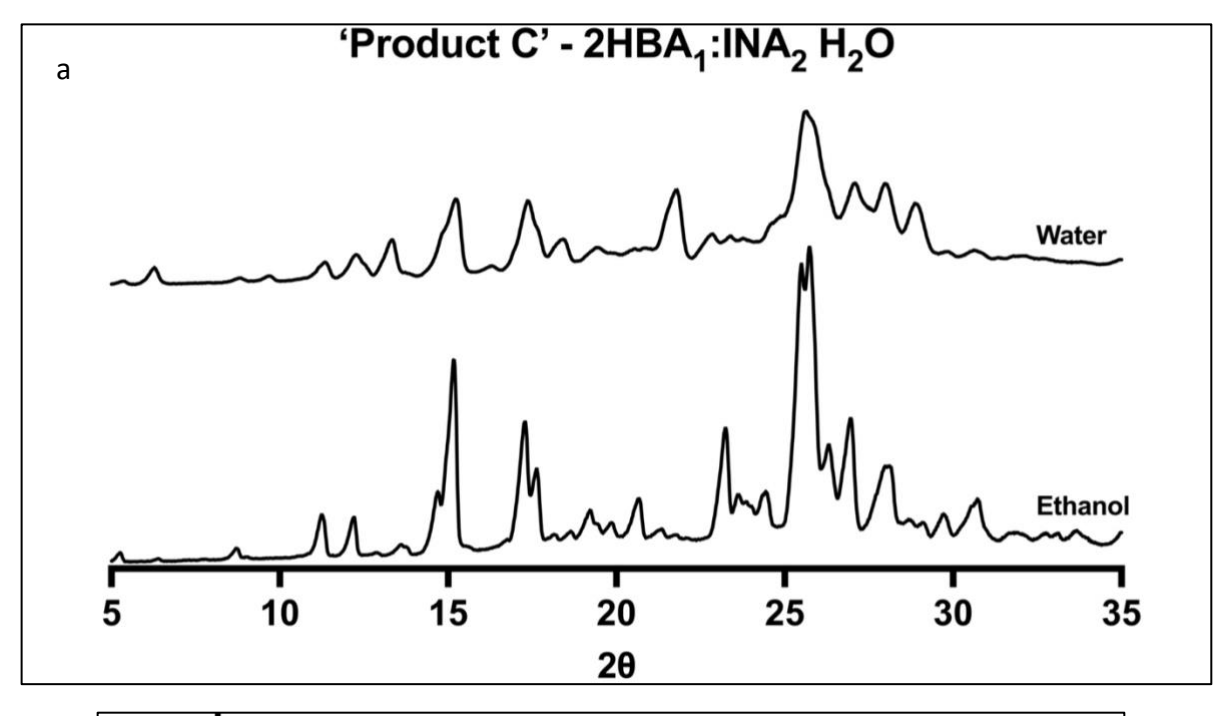
**Figure 6-8** DSC thermogram of 2HBA<sub>1</sub>:INA<sub>2</sub> LAG product with ethylene glycol at different heating rates.

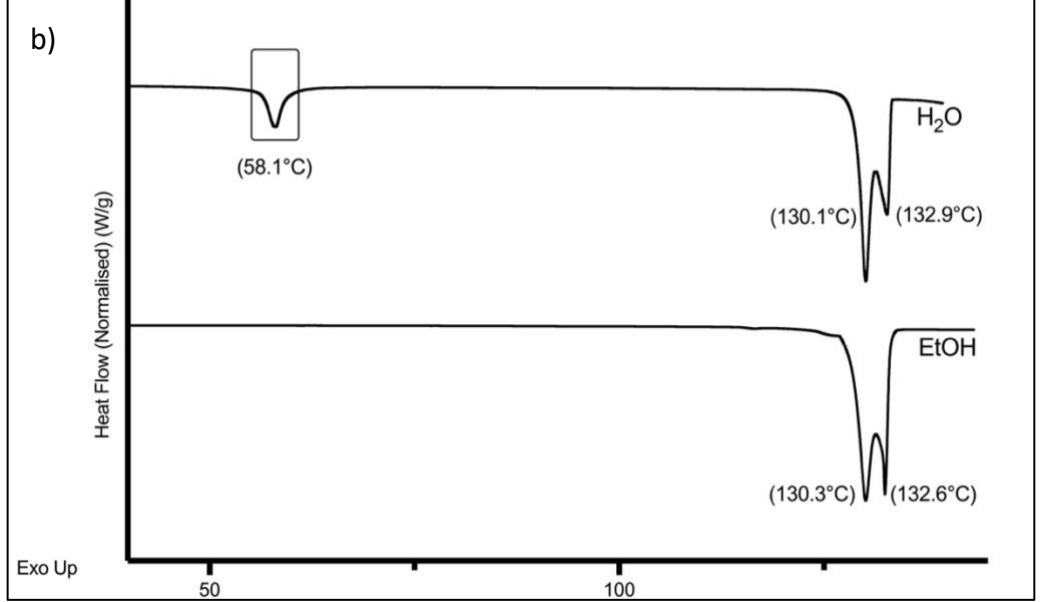


**Figure 6-9** -  $^{1}$ H- $^{13}$ C CP/MAS NMR spectra of 2-HBA<sub>1</sub>:INA<sub>2</sub> with ETG, ETG peak seen at 62 ppm. Right -  $^{1}$ H- $^{13}$ C CP/MAS NMR spectra of 2-HBA<sub>1</sub>:INA<sub>2</sub> comparing regions suspected to be involved in hydrogen bonding.

 $H_2O$  (*Product C*) – The PXRD pattern for 2-HBA<sub>1</sub>:INA<sub>2</sub> prepared with water as the solvent was similar to that of the material produced with EtOH. However, we note that all peaks are broader, suggesting that this product was less crystalline. These broader PXRD peaks are all in the same region as the product from LAG with our reference sample, ethanol which we

characterised as the same form reported in the CSD. Interestingly, DSC shows an endothermic peak at ca. 60°C, suggesting a hydrate is present. We also note the peak corresponding to the 1:1 cocrystal at 131°C, shows a reduced specific heat capacity, compared to that of 2-HBA<sub>1</sub>:INA<sub>2</sub> prepared with EtOH. TGA shows the weight loss at ca. 70°C, which corresponds to DSC within acceptable error margin.





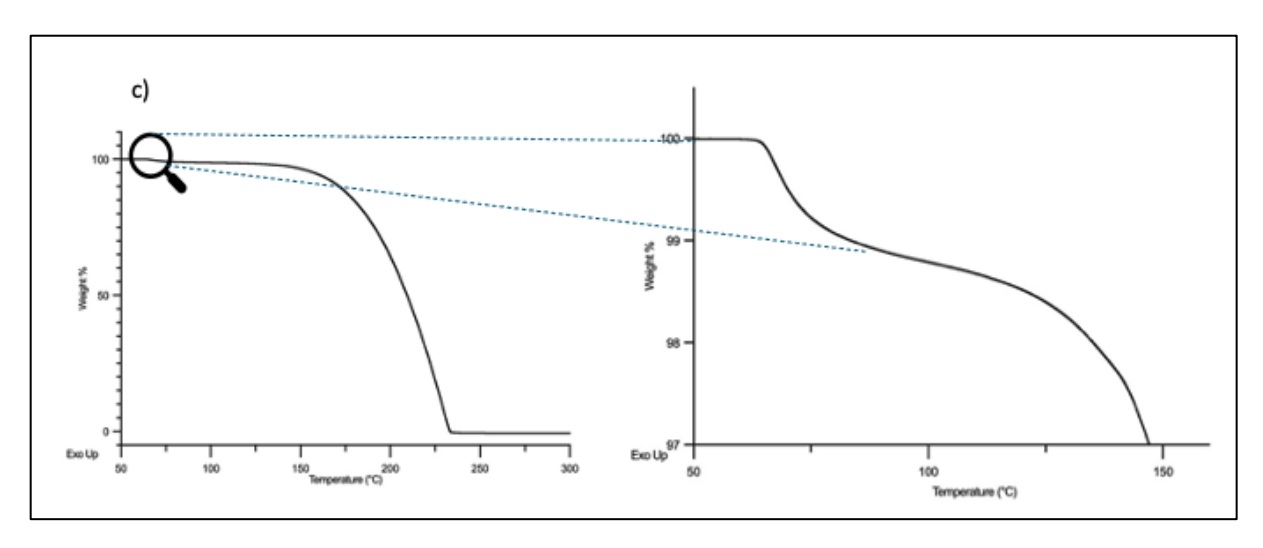
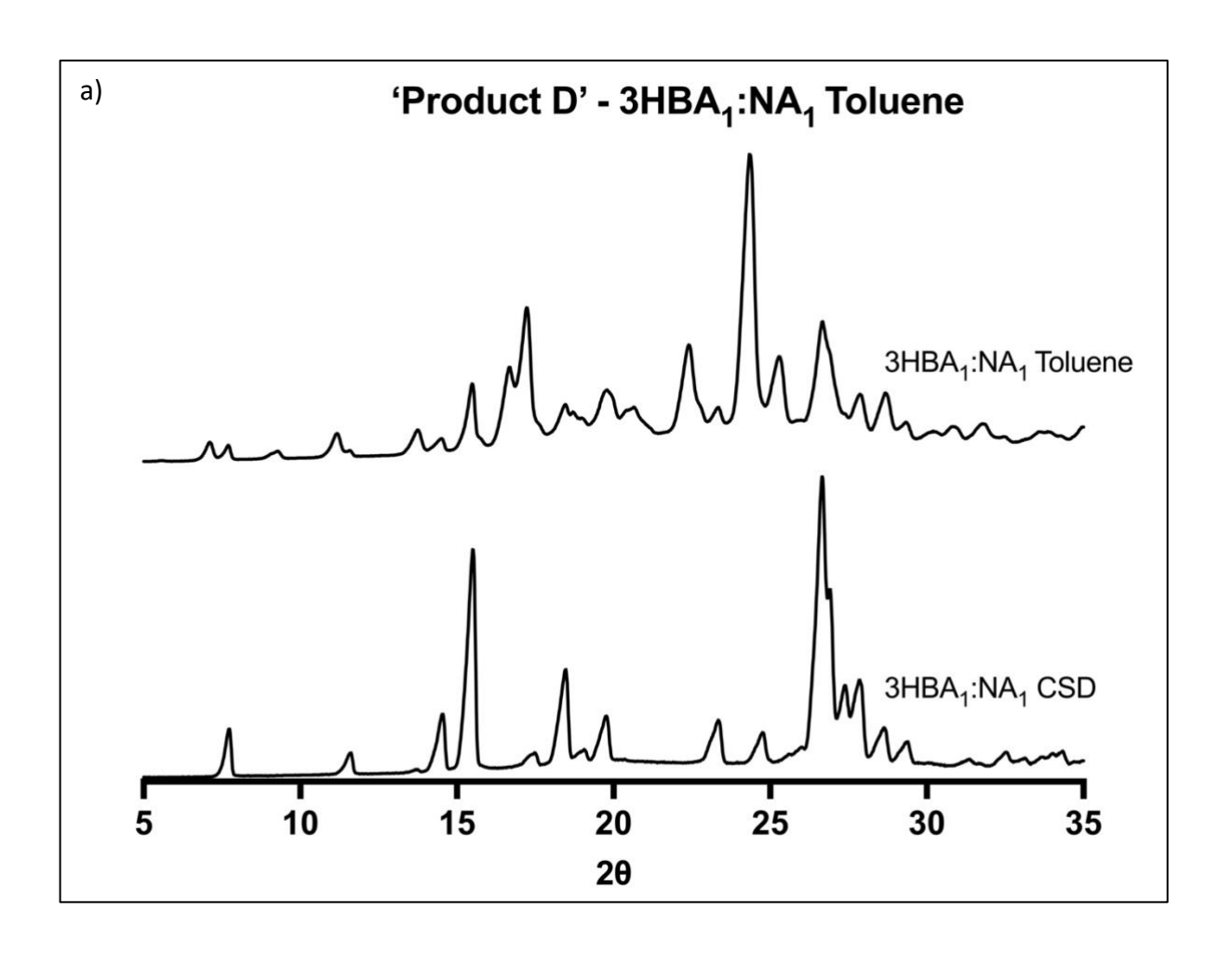


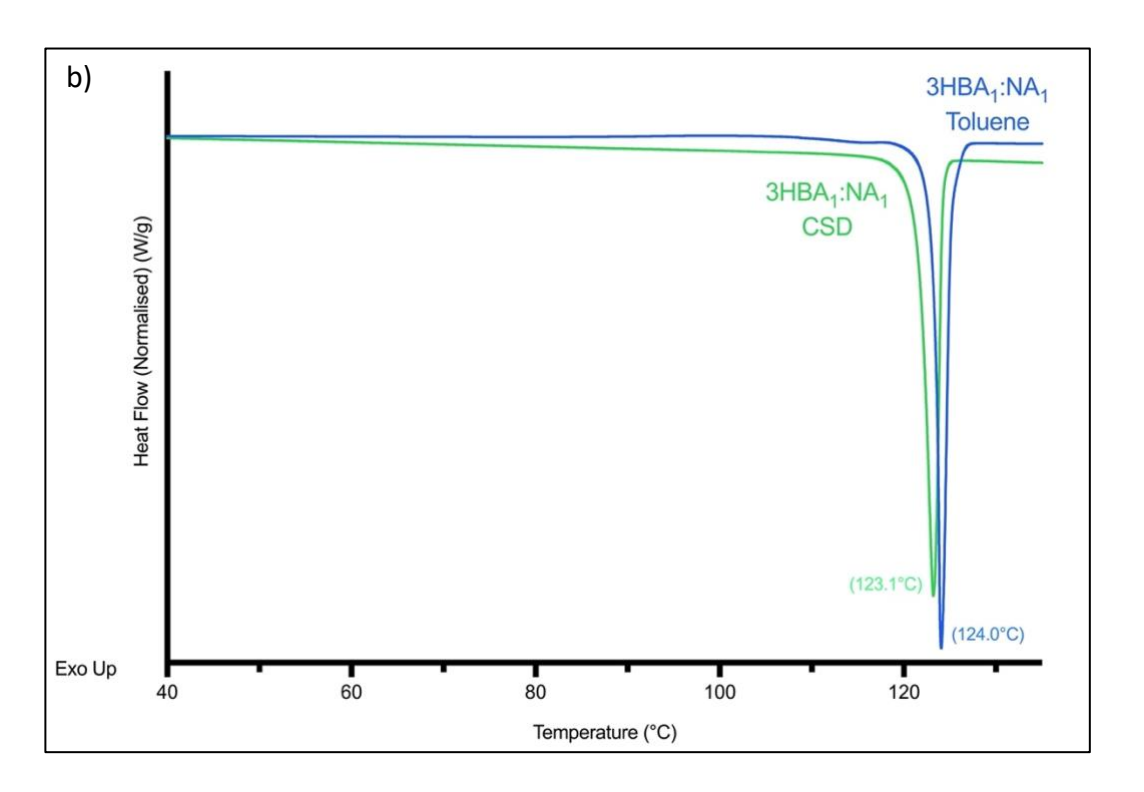
**Figure 6-10** - a) PXRD pattern, b) DSC thermogram and c) TGA plots of 2-HBA<sub>1</sub>:INA<sub>2</sub> produced by LAG with water.

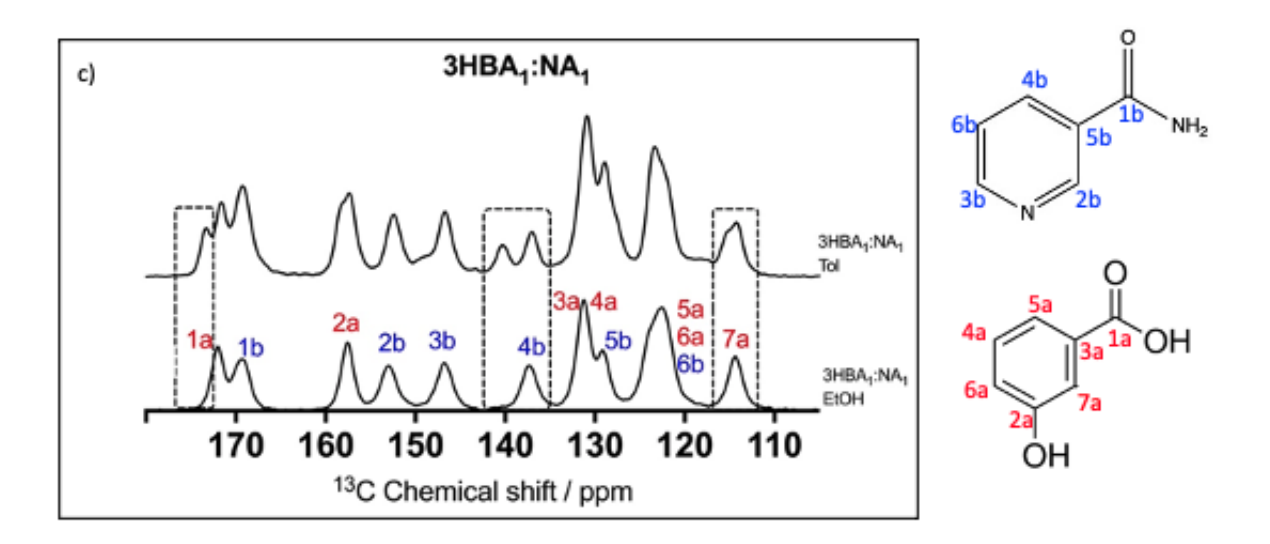
#### 3-HBA<sub>1</sub>:NA<sub>1</sub>

This cocrystal has been reported, and was obtained by slow evaporation form acetonitrile.<sup>268</sup> We also observed this co-crystal by LAG, confirmed by PXRD patterns of materials obtained in the presence of six out of the seven solvents.

Toluene (*Product D*) – The only solvent that yielded different PXRD pattern for **3-HBA**<sub>1</sub>:**NA**<sub>1</sub> was toluene. The PXRD pattern had some overlapping peaks with that reported in the CSD. However, there were new peaks that did not correspond to the known 1:1 cocrystal or the starting materials. DSC shows a slightly different endothermic peak; however, it is still a single peak. Suggesting a single-phase component is formed. <sup>13</sup>C CP/MAS NMR spectra shows the emergence of some new peaks, at 175 and 140 ppm. Interestingly, there is also a lot of overlap with the known cocrystal. The combination of these suggests a different polymorphic form, to the one reported in the CSD.



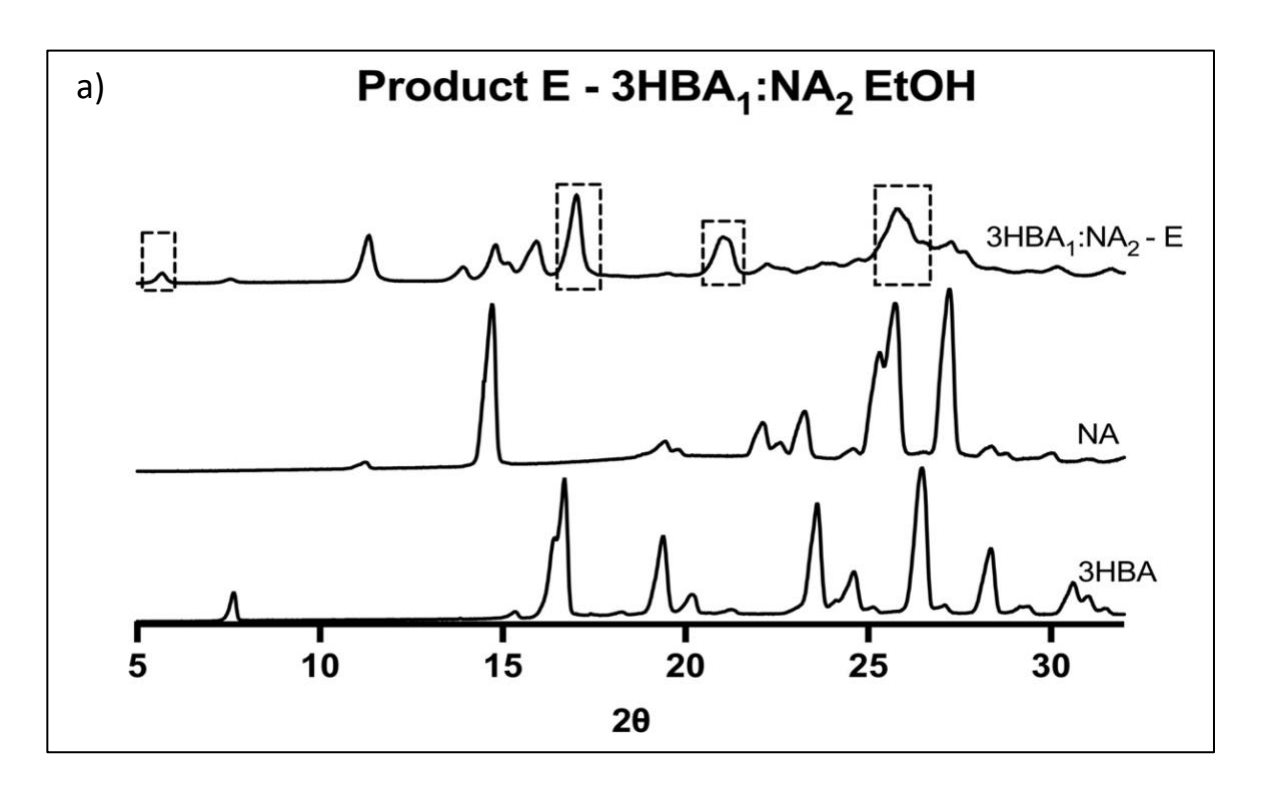


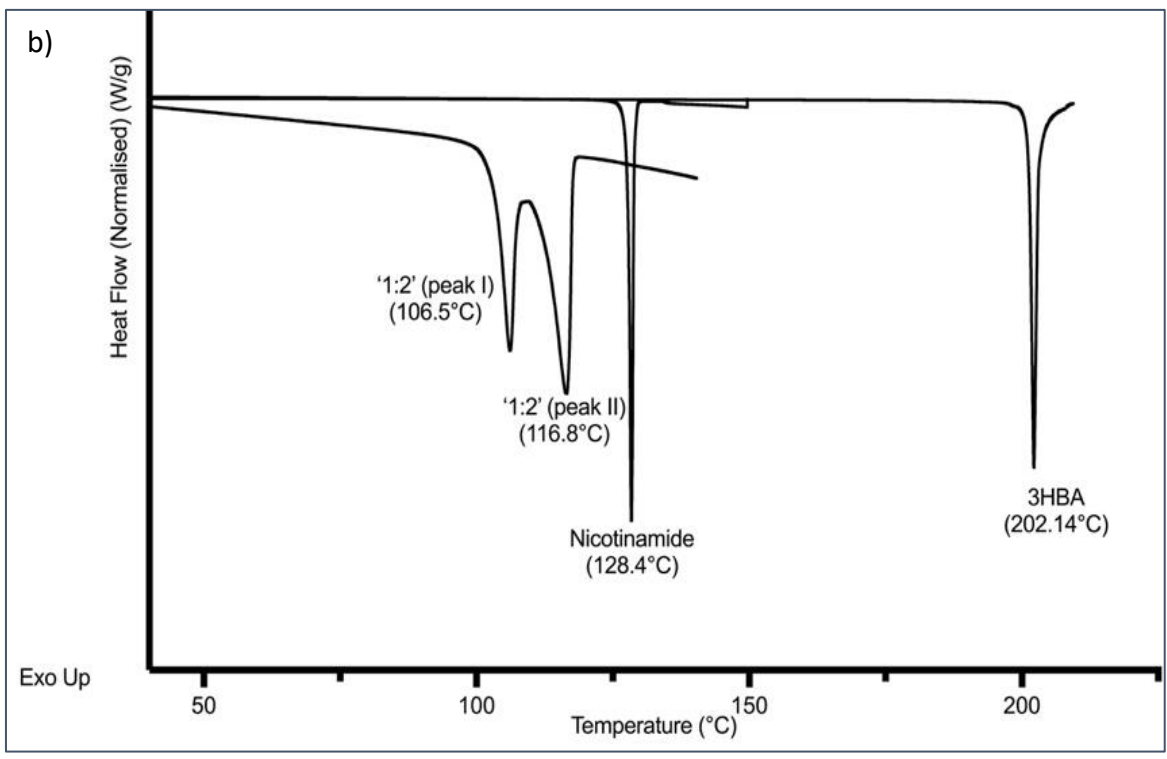


**Figure 6-11** Comparison of 3HBA<sub>1</sub>:NA<sub>1</sub> cocrystal reported in CSD vs 'product D' LAG product with toluene. a) PXRD, b) DSC and c) <sup>13</sup>C MAS NMR

#### 3-HBA<sub>1</sub>:NA<sub>2</sub>

This coformer ratio has not been reported in literature. However, all LAG screening produced the very similar results, bar two solvents: ethylene glycol and water. The rest of the solvents all produced the same product designated as **product-E**. DSC analysis of this combination shows results similar to the above mentioned 2-HBA<sub>1</sub>:INA<sub>2</sub>, we clearly see 2 endothermic peaks but no starting material, suggesting the product contains a mixture of 2 different solid forms and no starting material remains. This cocrystal combination is discussed in depth further on in this chapter.





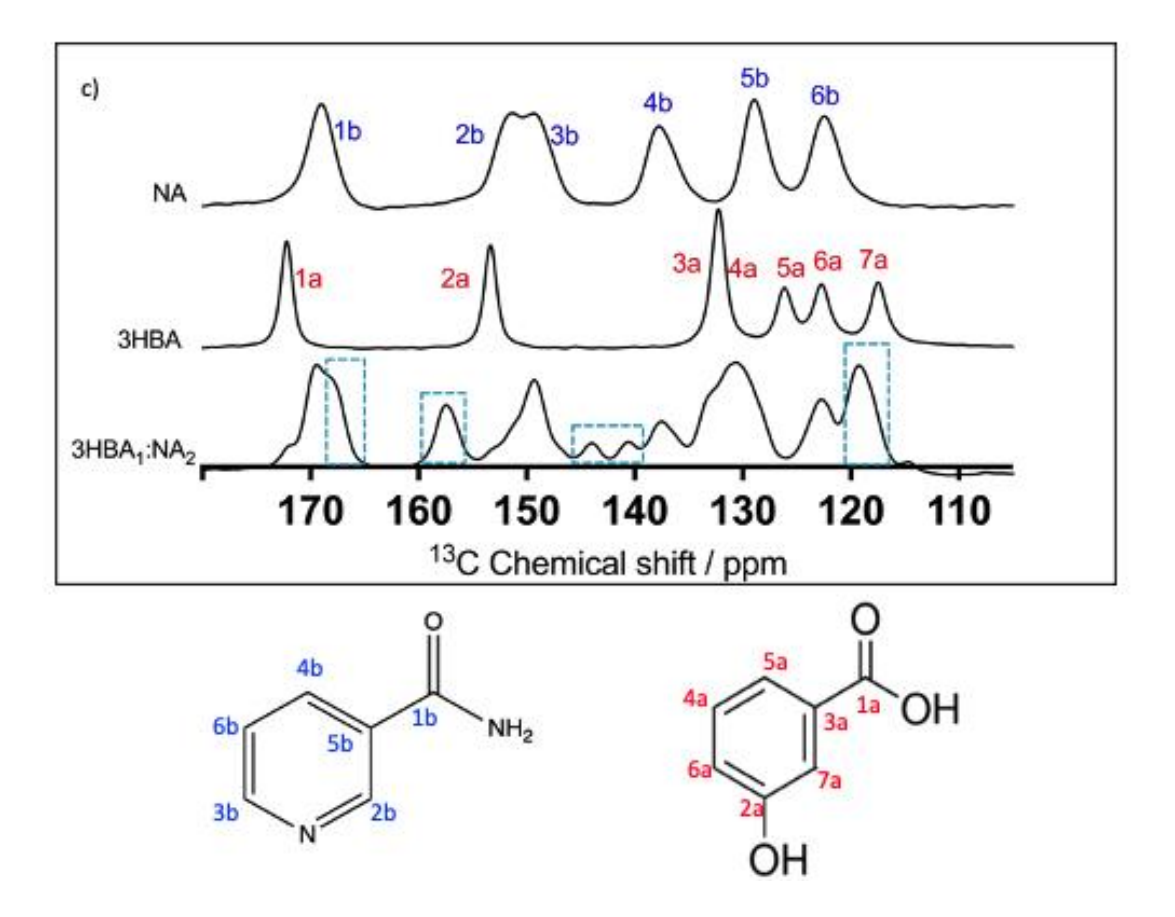
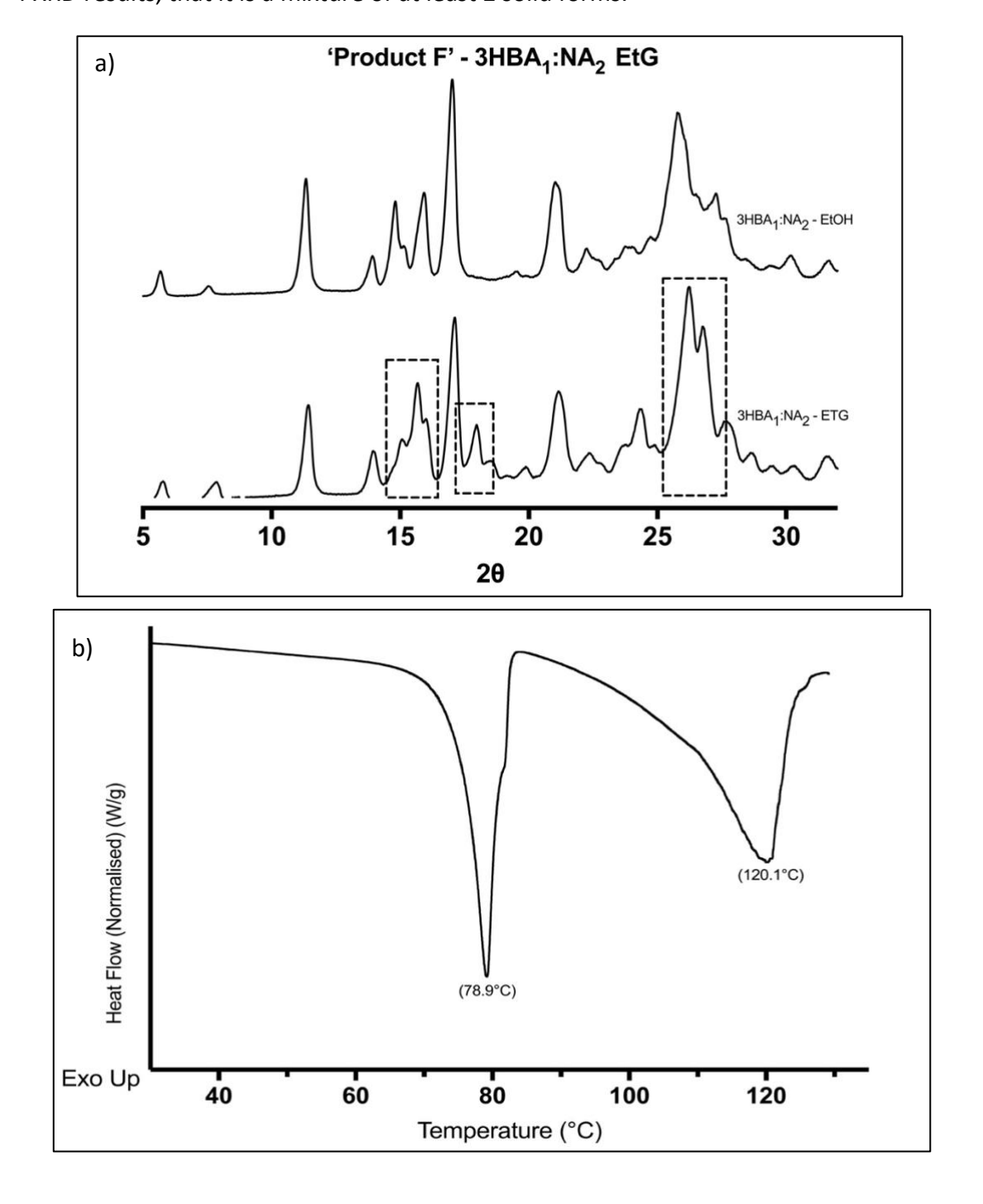


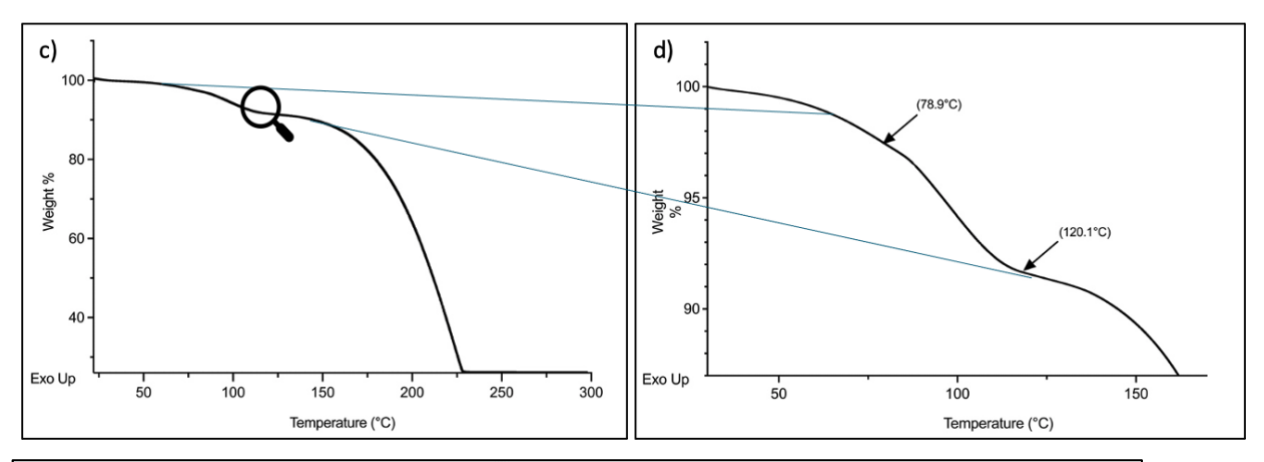
**Figure 6-12** -  $3HBA_1:NA_2$  – new solid form compared to starting materials. a) PXRD, b) DSC and c)  $^{13}C$  MAS NMR

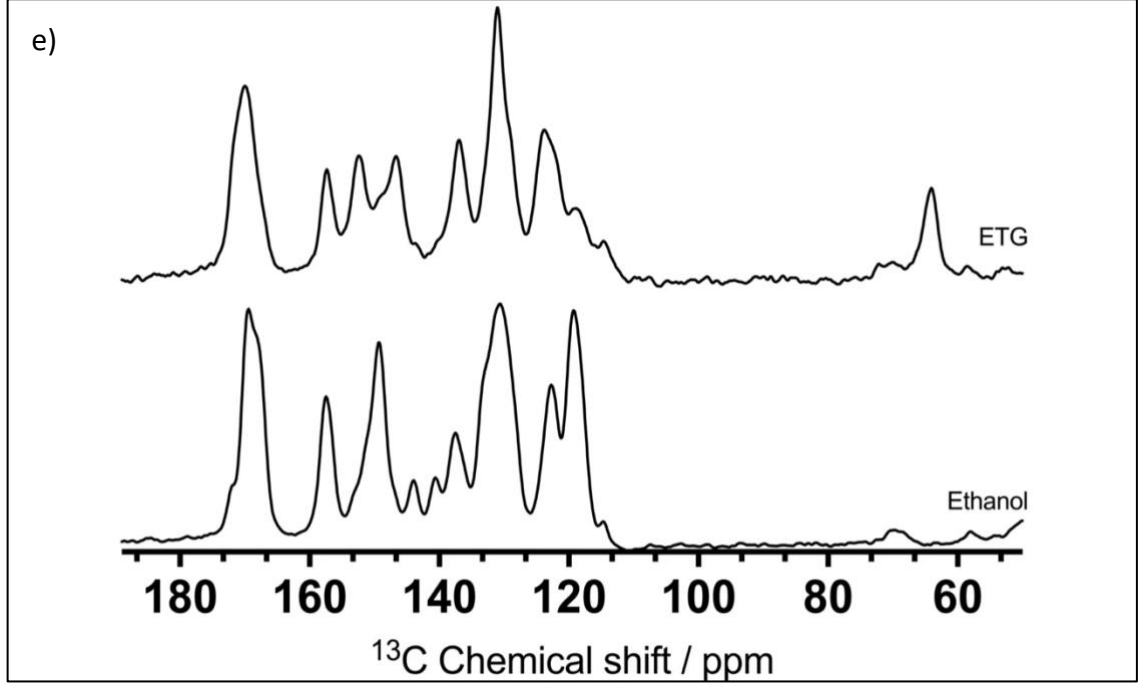
ETG (**Product F**) – The analysis of product F reveals a complex mixture is present. PXRD pattern shows both similarities to the known 3-HBA1:NA1 cocrystal however there are also new peaks present for example those seen at 15 and  $18^{\circ}$  2 $\theta$ , suggesting the presence of a novel solvate.

DSC reveals two large endothermic peaks: a peak at 78.9°C (Figure 6-12b), which has a corresponding endothermic weight reduction in TGA. This is interesting, because the boiling point of EtG is around 197°C. However, in order not to destroy DSC plate with burnt impurities, we did not heat the mixture that high. The second large peak at 120°C, which most likely corresponds to a mixture of 1:1 cocrystal, and some other impurities. This is inferred by the breadth of the peak, compared to the sharp peak observed in Figure 6-13.

From <sup>13</sup>C CP/MAS NMR spectra, we clearly see a difference in peaks in the -COOH/ -CONH<sub>2</sub> region between 165 and 180 ppm, the phenol / N-pyridine region between 140 and 157 ppm, and the aromatic region between 110 and 127 ppm. The presence of a sharp peak at *ca*. 65 ppm suggests that EtG has formed a solvate with the coformers. We can be confident that this is not an ethanol solvate, because the <sup>13</sup>C NMR only had one peak at 65ppm, representing the one carbon environment in EtG, whereas ethanol would have 2; the CH<sub>3</sub> and CH<sub>2</sub>. We can trace all the known 1:1 cocrystal NMR peaks to the new solid form, confirming the DSC and PXRD results, that it is a mixture of at least 2 solid forms.







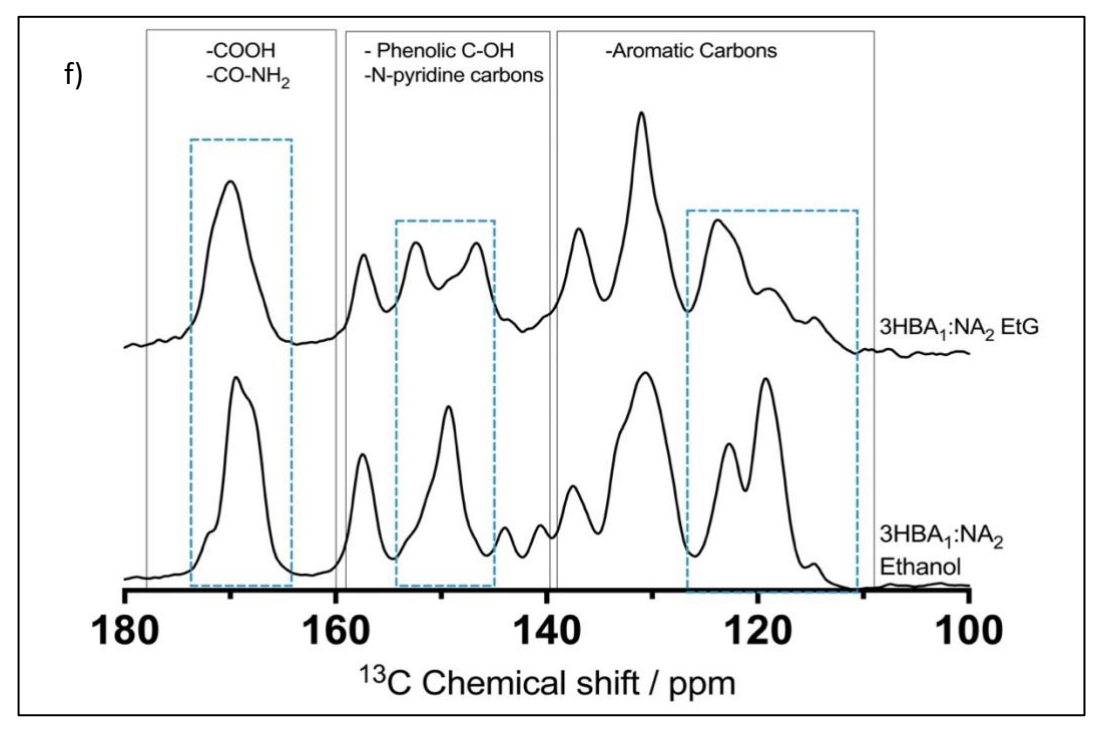


**Figure 6-13** - 3HBA<sub>1</sub>:NA<sub>2</sub> LAG with ethylene glycol 'Product F' – new solid form compared to solid form produced in ethanol. a) PXRD patterns, b) DSC thermogram, c) TGA and d) TGA magnified, e) and f) <sup>13</sup>C CP/MAS spectra recorded at 298 K, recorded on a 400 MHz spectrometer at an MAS rate of 12kHz.

 $H_2O$  (**Product G**) – From the PXRD pattern, we see narrow, sharp peaks, suggesting a high degree of crystallinity. Interestingly, we see stark differences compared to the LAG product in ethanol. We see new peaks at 7.1, 14, 14.48, 19.9, 20.7, 25.3, and 26.4 -20.

Some peaks present in this PXRD pattern are also noted in that of the known cocrystal, suggesting a mixture of the reported 1:1 cocrystal and a new polymorphic form. We suspect that DSC and <sup>13</sup>C NMR would confirm these results, however due to time constraints and equipment availability we were unable to collect this data.

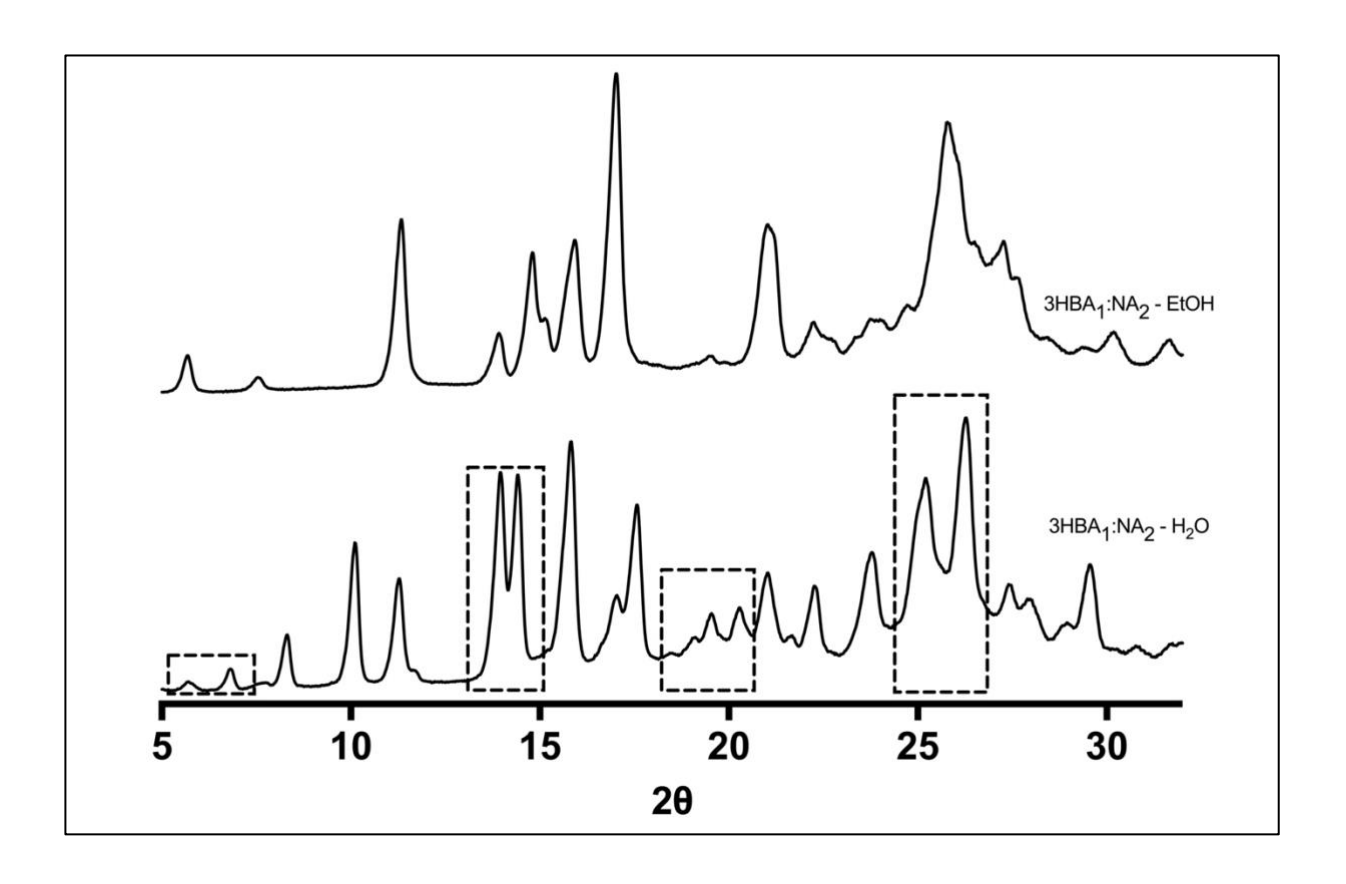


Figure 6-14 - PXRD pattern of 3HBA<sub>1</sub>:NA<sub>2</sub> LAG product with water, compared to ethanol

### 6.2.2 Summary of findings

We present a comprehensive investigation into the use of LAG to screen cocrystals of cyclic amides and hydroxybenzoic acids, varying stoichiometry and solvent choice. In many cases, we observe that 2:1 combination often resulted in 1:1 cocrystals with excess starting material. This challenges conventional wisdom as it suggests increased competition from additional hydrogen bond donors/acceptors did not alter preferred intermolecular interactions. One possible explanation is that the 1:1 cocrystal may represent the most thermodynamically stable configuration for these particular systems. The leftover excess starting material suggests that once the 1:1 cocrystal forms, it is energetically unfavourable for additional molecules to incorporate into the crystal lattice. Phase diagram studies to reveal stability regions will likely confirm this. <sup>273, 274</sup> However we see later in this chapter that in some cases, it is the opposite, with 1:1 cocrystal can act as an intermediary and excess coformer being incorporated into the unit cell. This dynamic behaviour highlights the complexity of cocrystal formation and suggests that the process may involve multiple stages or intermediate phases. For instance, in the case of 2-HBA1:INA2, we observed the formation of both 1:1 and 1:3 cocrystals, indicating that the system can accommodate different stoichiometries depending on the conditions.

These results also reveal how choice of solvent significantly influences cocrystal formation via LAG, doing more than just 'wetting the solid surface'. <sup>50</sup> We see clearly how small amounts of solvent can change the resultant cocrystal. While a direct correlation between solvent properties and LAG product has not been explicitly discovered, we make some vital observations. For the 2HBA1:INA2 combination, we see three different solid forms produced, depending on the solvent used. Non-polar to moderately polar solvents<sup>275</sup> (toluene, acetone, propan-2-ol, ethanol, methanol) produced Product A, which is later determined as a mixture of 1:1 and 1:3 cocrystals. Whilst highly polar solvents such as EtG and water produced a solvate and a hydrate respectively. We note that EtG formed a solvate with 2HBA1:INA2 and 3HBA1:NA2, but not with 2HBA1:NA2 or 3HBA1:INA2, however the reason why is not clear. These observations suggest that solvent polarity can influence LAG product formation, particularly in terms of polymorphism and solvate formation. However, the relationship is not

straightforward, and many other factors contribute to the observed outcomes. This mass screening project achieved its two primary aims: to gain a library of successful and failed screens, and to probe the intermolecular interactions governing cocrystal formation. Due to time constraints and project direction, we were not able to produce single crystals of these new solid forms, however this is a promising avenue for future study.

# 6.3 Observing cocrystal formation via time-resolved PXRD

The mechanism of cocrystal formation by grinding is often thought to be a multistage, stepwise process and can be a result of various mechanisms. For neat grinding, molecular diffusion is mentioned in literature as the likely mechanism when either or both reactants have considerably high vapour pressures. Contact between these reactants is expected to initiate cocrystal formation. However, when a solvent is added, it is observed that sometimes an intermediate phase forms, which is thought to facilitate cocrystal formation. For the cocrystals mentioned above, we wanted to elucidate if their formation was a multistage process. The initial LAG studies were carried out using a steel ball mill, and characterisation of the products was achieved by DSC, PXRD and TAC MAS NMR. Starting materials were weighed out and placed in ball milling jars, but instead of the standard procedure of 30 Hz grinding frequency for 30 mins, frequency, grinding time and solvent volume were varied as shown in Table 2. Solvent used was ethanol, as this was seen to produce new multicomponent pharmaceuticals in the selected cocrystal coformer ratios.

**Table 6-2** 3-HBA<sub>1</sub>:NA<sub>1</sub> Frequencies, solvent volumes and timepoints for time resolved LAG.

COFORMERRATIO	TIME	MILLING	SOLVENT	RESULTS
	POINT	FREQUENCY	VOLUME	
	1 min			1:1 cocrystal
	5 mins			1:1 cocrystal
3-HBA <sub>1</sub> :NA <sub>1</sub>	10 mins	30 Hz	50 μl	1:1 cocrystal
	15mins			1:1 cocrystal
	30mins			1:1 cocrystal
	1min	5Hz		1:1 cocrystal
3-HBA <sub>1</sub> :NA <sub>1</sub>	1min	10Hz	50ul	1:1 cocrystal
	1min	15Hz		1:1 cocrystal
	1min	20Hz		1:1 cocrystal
	1min		Dry	Mixture of pure coformers
	1min		5ul	Pure coformers + 1:1
				cocrystal
3-HBA <sub>1</sub> :NA <sub>1</sub>	1min		10ul	Pure coformers + 1:1
				cocrystal
	1min		20ul	1:1 cocrystal

1min	30ul	1:1 cocrystal
1min	40ul	1:1 cocrystal

 $\textbf{Table 6-3} \ 3\text{-HBA}_1: NA_2 \ Frequencies, solvent \ volumes \ and \ time points \ for \ time \ resolved \ LAG.$ 

COFORMERRATIO	TIME POINT	FREQUENCY	SOLVENT VOLUME	RESULTS
	1min			1:1 cocrystal + Excess NA
	5mins			1:1 cocrystal + Excess NA + new solid form
3-HBA <sub>1</sub> :NA <sub>2</sub>	10mins	30Hz	50ul	New solid form
	15mins			New solid form
	30mins			New solid form
	1min		Dry	Mixture of pure coformers
	1min		5ul	Excess NA + intermediate peaks + 1:1 cocrystal
3-HBA <sub>1</sub> :NA <sub>2</sub>	1min		10ul	Excess NA + intermediate peaks + 1:1 cocrystal
	1min	30Hz	20ul	Excess NA + intermediate peaks + 1:1 cocrystal
	1min		30ul	Excess NA + intermediate peaks + 1:1 cocrystal
	1min		40ul	Excess NA + intermediate peaks + 1:1 cocrystal
	1min		50ul	1:1 cocrystal + excess NA

 $\textbf{Table 6-4} \ \ \textbf{2-HBA} \textbf{1:INA} \textbf{2} \ \textbf{Frequencies, solvent volumes and time points for time resolved LAG.}$ 

COFORMERRATIO	TIME POINT	FREQUENCY	SOLVENT VOLUME	RESULTS
	1min			1:1 cocrystal + excess INA
	5mins			new solid form
2-HBA <sub>1</sub> :INA <sub>2</sub>	10mins	30Hz	50ul	new solid form
	15mins			new solid form
	30mins			new solid form
	1min		Dry	Pure coformers +
				intermediate peaks +
				1:1 cocrystal
	1min		5ul	Pure coformers +
				intermediate peaks +
				1:1 cocrystal
	1min		10ul	Pure coformers +
				intermediate peaks +
				1:1 cocrystal
2-HBA <sub>1</sub> :INA <sub>2</sub>	1min	30Hz	20ul	Pure coformers +
				intermediate peaks +
				1:1 cocrystal
	1min		30ul	Pure coformers +
				intermediate peaks +
				1:1 cocrystal
	1min		40ul	Pure coformers +
				intermediate peaks +
				1:1 cocrystal
	1min		50ul	1:1 cocrystal + excess INA

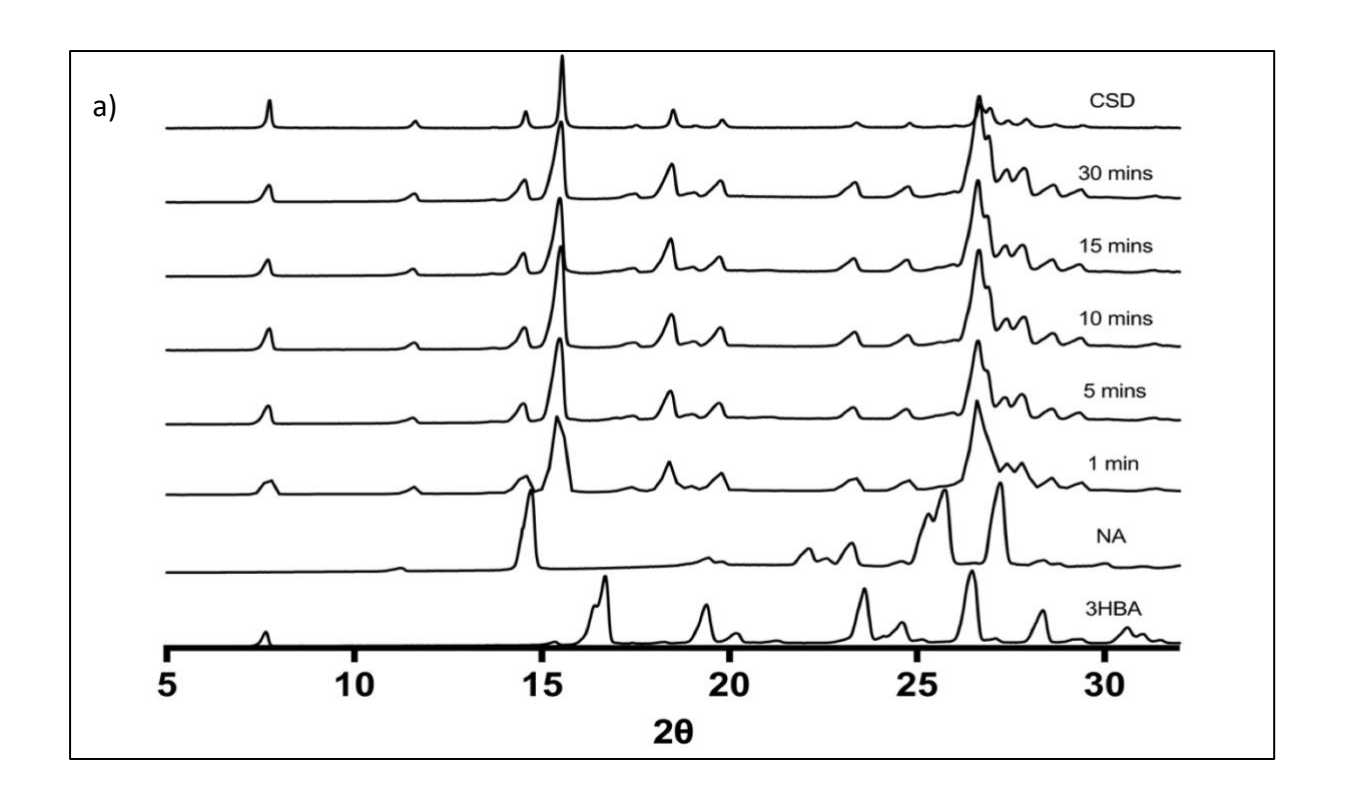
### 6.3.1 3-HBA<sub>1</sub>:NA<sub>1</sub>

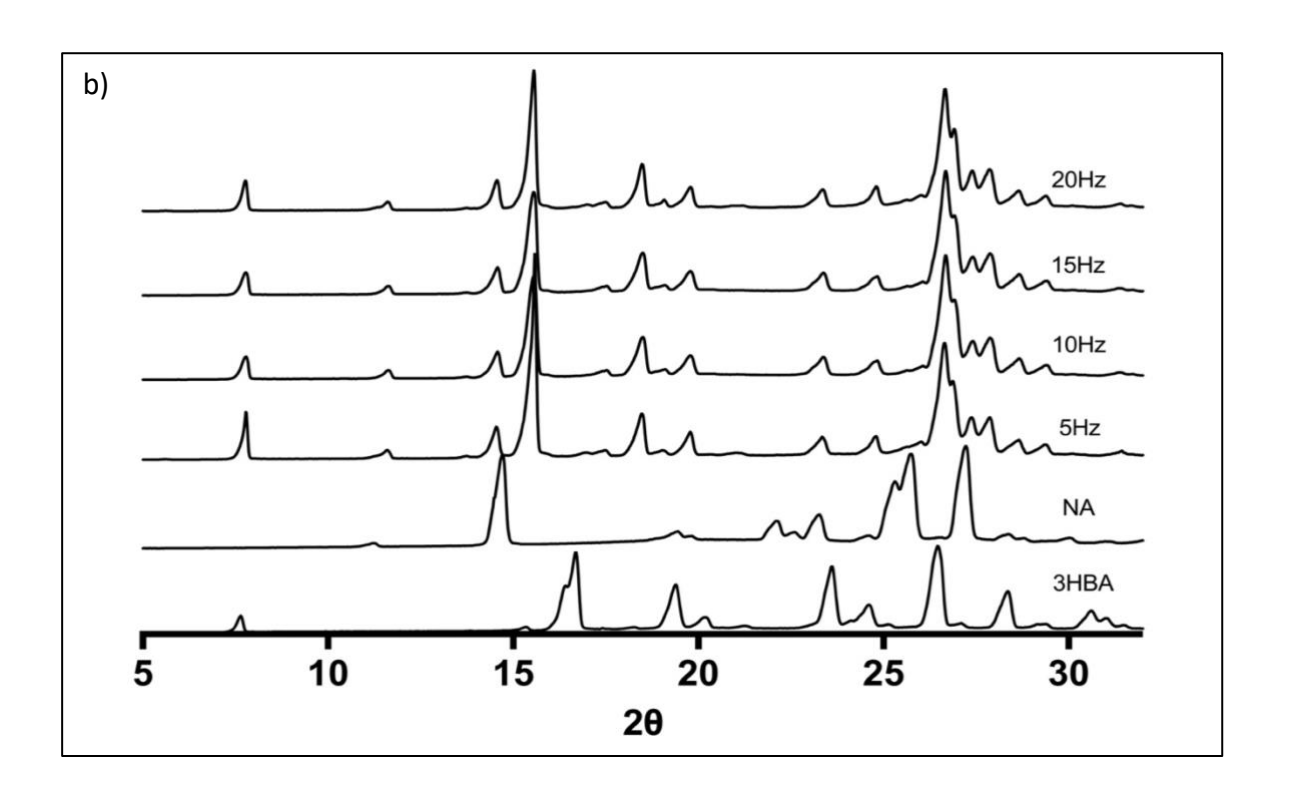
This cocrystal has been reported in the CSD (XAQQIQ).  $^{268}$  We selected this co-crystal as a test material for the time-resolved experiments. Interestingly, under the conditions selected, a 1:1 cocrystal forms after one minute of grinding. This was verified by comparing the PXRD patterns with the reported data.  $^{268}$  Varying the amount of solvent added to the LAG set up, showed that grinding with as little as 5  $\mu$ l of ethanol for 1 min was sufficient to start cocrystal formation. Volumes of ethanol of 20  $\mu$ l and above resulted in full conversion to the 1:1 cocrystal in 1 min (molar ratio of ethanol:coformers ratio 1:6). This suggests that the liquid does indeed act in a facilitating role. Using equation  $1^{56}$ , where V is solvent volume in  $\mu$ L, and m is combined mass of coformers.

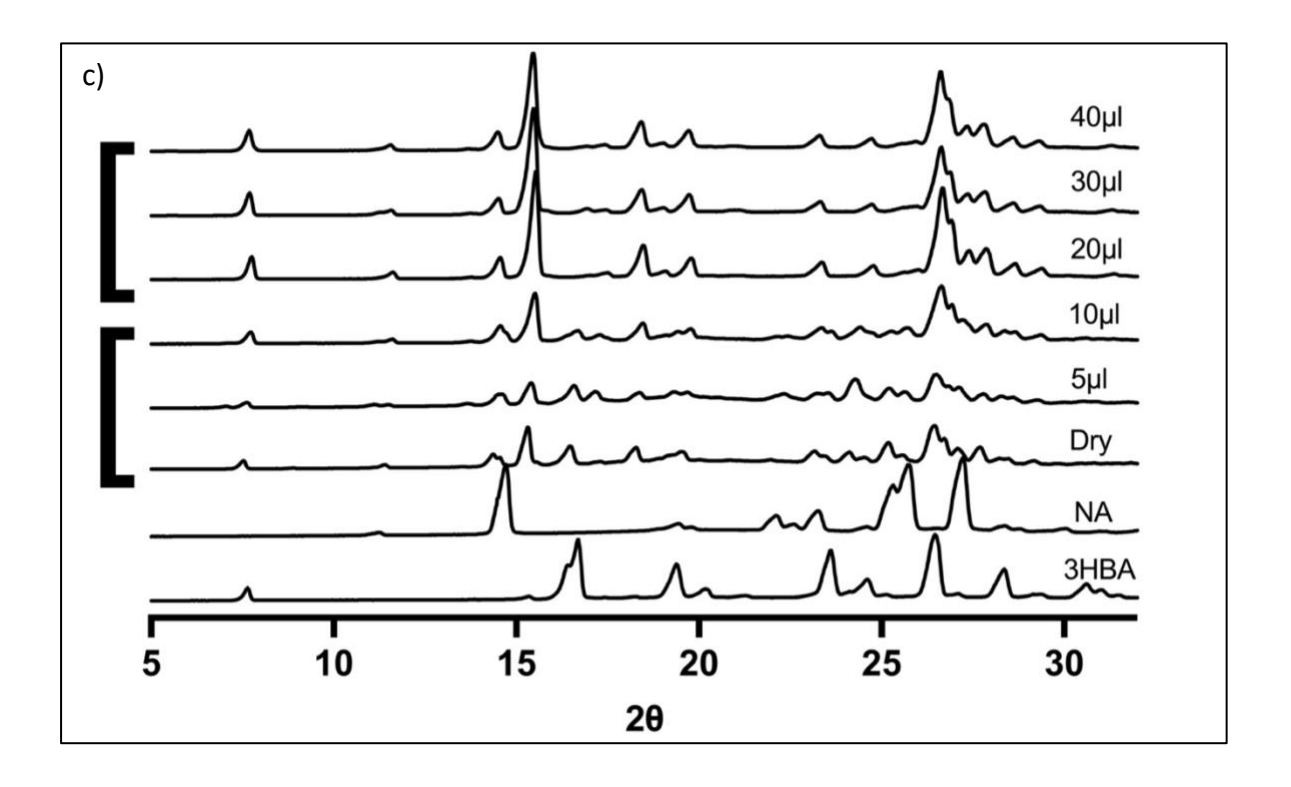
$$\eta = \frac{V \text{ (liquid,}\mu\text{L)}}{m(\text{sample,}mg)}$$
 Equation 6-1

Total sample mass for each grinding experiment, using equimolar amounts of sample is 260.24 mg. With liquid volume of 5  $\mu$ L makes  $\eta$  = 0.019  $\mu$ L/mg. This is considerably lower than for a typical LAG screening experiment, of 0.25  $\mu$ L/mg. Nonetheless, as expected, increasing the liquid volume, and thus  $\eta$  to 0.077  $\mu$ L/mg, improves cocrystal yield, consistent with the theory that the liquid acts as a catalyst. Knowing that the cocrystal formed after 1 minute of grinding, we varied the grinding frequency. Still, a 1:1 cocrystal formed after grinding for 1 minute at 5 Hz. As a control, a physical mixture of coformers left overnight did not lead to spontaneous co-crystallisation. This indicates that a small amount of agitation is required to from this cocrystal, and that the defining factor is the volume of solvent added.

As the conversion to the co-crystal occurred quickly, no intermediate was observed. Lower amounts of solvent result in incomplete conversion, highlighting the role solvent choice and volume plays in cocrystal conversion. This also suggests that the use of PXRD at different time points can show if, and when, intermediate forms.



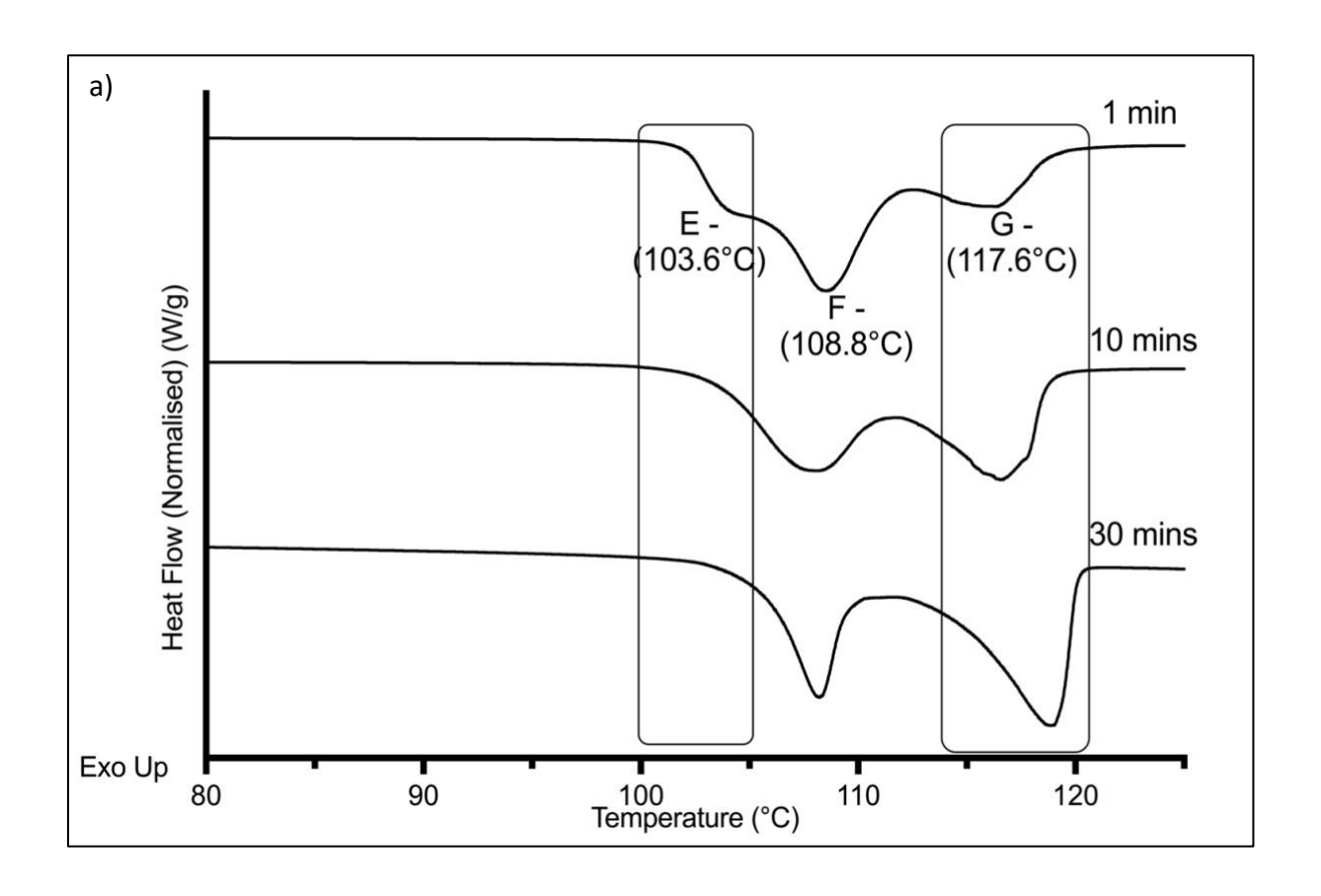


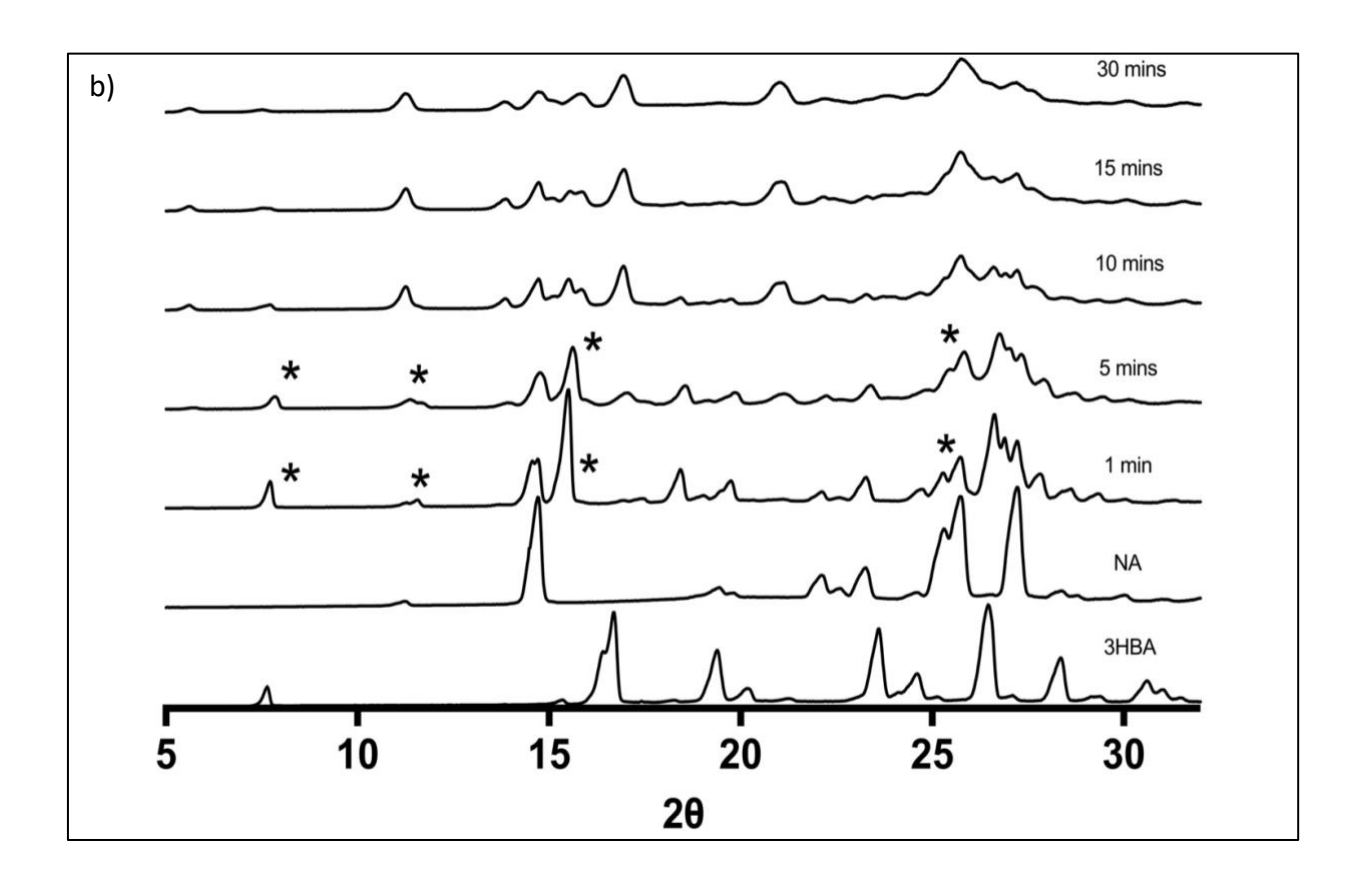


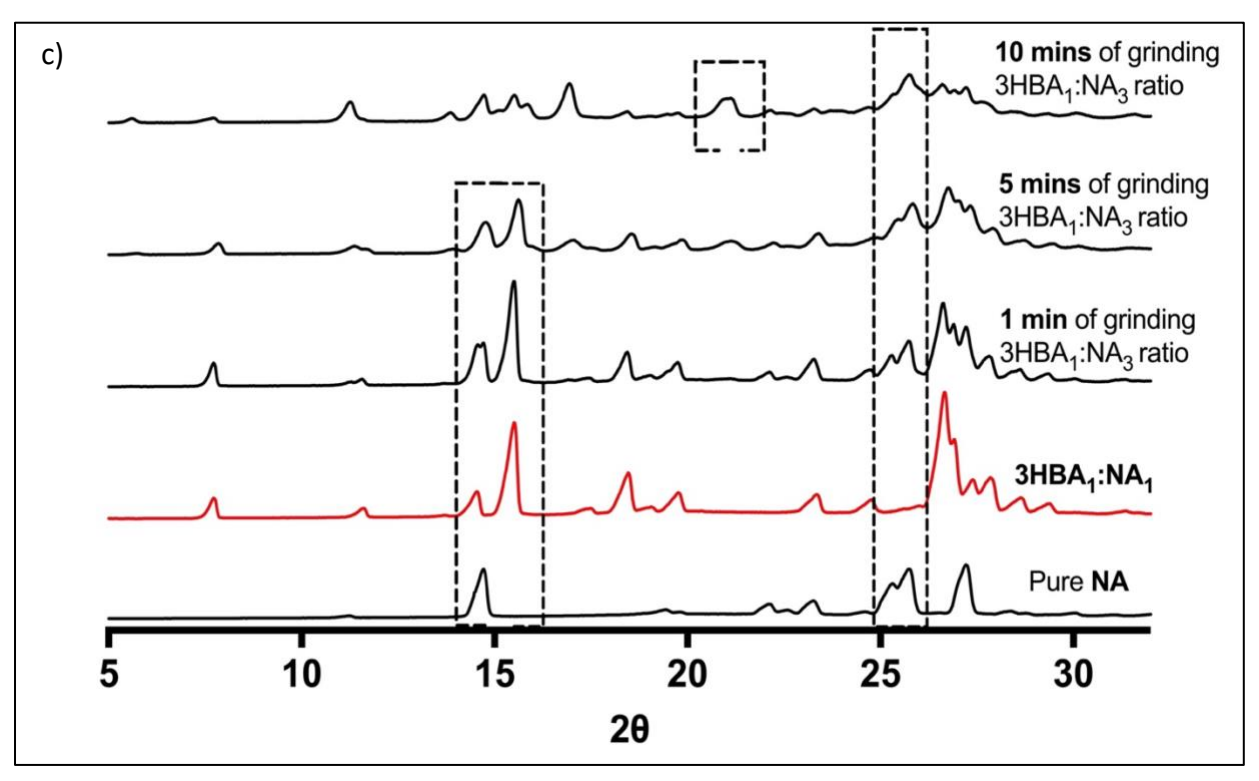
**Figure 6-15** PXRD pattern of 3HBA<sub>1</sub>:NA<sub>1</sub>. a) at different time points, b) varying frequency, c) varying ethanol volume.

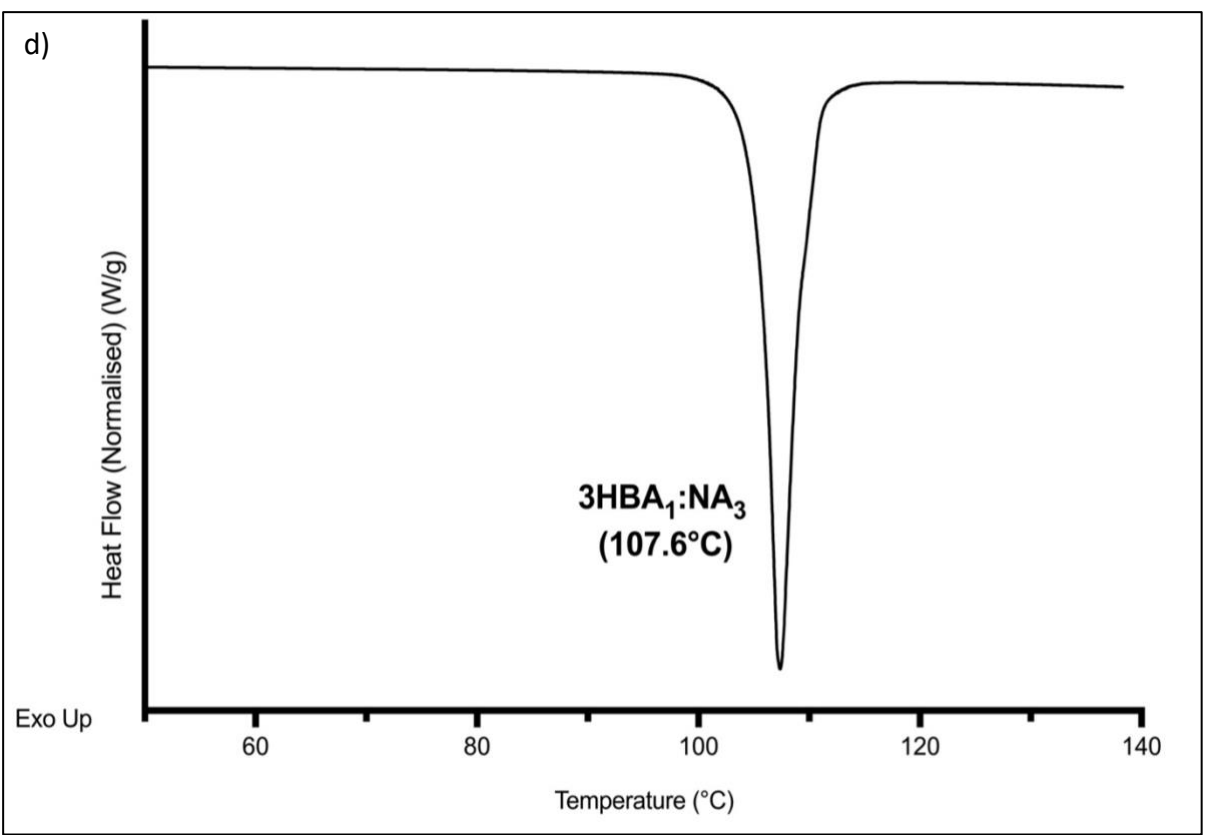
### 6.3.2 3-HBA<sub>1</sub>:NA<sub>3</sub>

This cocrystal has not been reported previously, but preliminary PXRD patterns and solid-state NMR suggested that a new multicomponent solid form is produced when these coformers are ground in this ratio. Following the same time points as in the **3-HBA<sub>1</sub>:NA<sub>1</sub> experiment** we observe some interesting developments between the products after 1 minute, 10 minutes and 30-minutes of grinding, as demonstrated in Figure 6-16. From DSC, after 1 minute, we see 3 main endothermic peaks, at *ca*. 104, 108 and 117 °C. This suggest that after 1 minute of LAG, a mixture comprising of at least 3 different components are produced: E, F and G. After 10 minutes, only the latter 2 thermal events; F and G are present in equal proportions. However, after 30minutes, peak G is larger than the peak at F. This suggests that a longer grinding time yields more of compound G. This suggests that the product is not phase pure, but a mixture of 2 forms. Our working theory was that the material obtained with 3-HBA<sub>1</sub>:NA<sub>2</sub> ratio, comprises of a mixture of 1:1 and 1:3 cocrystals, which is possible with an empirical ratio of 1:2. To test this, we repeated the grinding experiment with a ratio of 3-HBA<sub>1</sub>:NA<sub>3</sub> ratio.





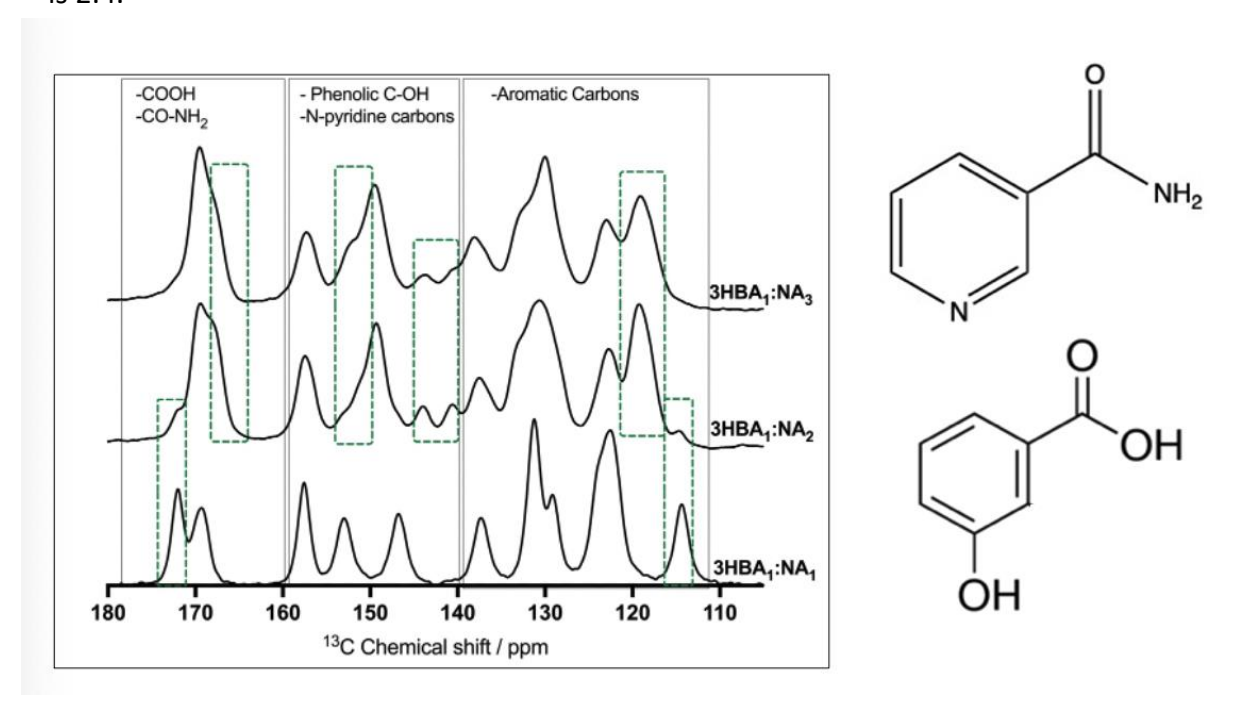




**Figure 6-16** - 3HBA<sub>1</sub>:NA<sub>2</sub>. a) DSC at different time points, b) PXRD showing transformation from 1:1 cocrystal to new form. c) PXRD showing intermediate produces is 1:1 cocrystal and excess NA. d) DSC showing single peak for phase pure 3HBA<sub>1</sub>:NA<sub>3</sub>.

As expected, DSC results for the material with 1:3 ratio of coformers now show a single peak. This was confirmed by PXRD patterns. After 1 minute, PXRD pattern shows a 1:1 cocrystal and excess NA, highlighted in Figure 6-16. Between 5 minutes and 10 minutes, a transition to a new form takes place.

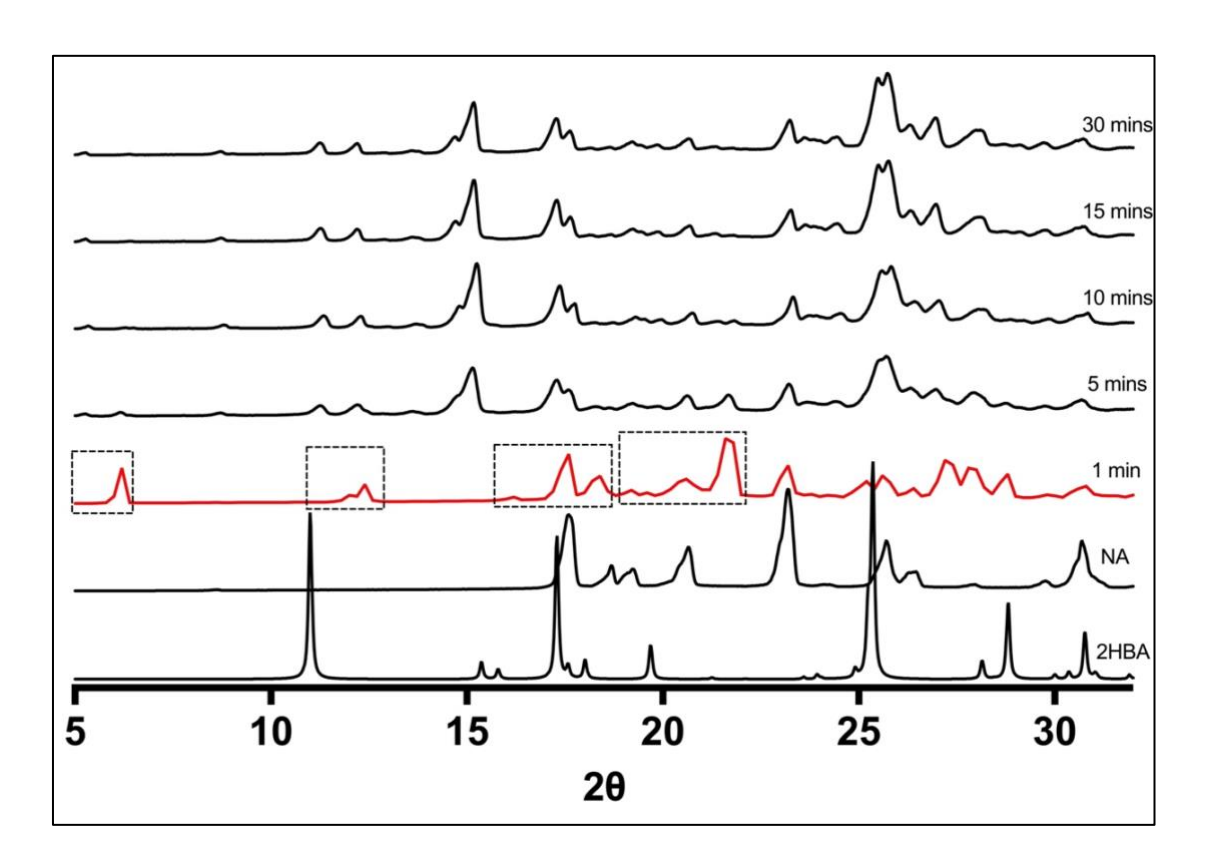
<sup>13</sup>C CP/MAS NMR measurements were carried on the products of three coformer combinations. Based on current literature available for the starting materials, peak assignments have been gleaned. Carboxylic acids and primary amides generally appear between 165 and 175 ppm. Phenol -OH carbon and the carbons next to the N-pyridine group are observed between 140 and 160 ppm. The remainder if the aromatic carbons are found between 110 and 140ppm. As suspected, peaks observed in the 3HBA<sub>1</sub>:NA<sub>2</sub> can be directly traced to 3HBA<sub>1</sub>:NA<sub>1</sub> and 3HBA<sub>1</sub>:NA<sub>3</sub>. Confirming that, when 3HBA and NA are ground in a 1:2 ratio, the product is a mixture, a 1:1 and 1:3. This is empirically possible, as the resulting ratio is 2:4.



**Figure 6-17** <sup>1</sup>H-<sup>13</sup>C CP/MAS NMR spectra of 3HBA<sub>1</sub>:NA<sub>1</sub>, 3HBA<sub>1</sub>:NA<sub>2</sub> and 3HBA<sub>1</sub>:NA<sub>3</sub> recorded at 298 K, recorded on a 400 MHz spectrometer at 12kHz MAS speed.

# 6.3.3 2-HBA<sub>1</sub>:INA<sub>3</sub>

PXRD pattern of **2-HBA<sub>1</sub>:INA<sub>3</sub>** material at different time points, showed that an intermediate is formed before a new multicomponent solid form. As shown in Fig 6-18, after 1-minute new peaks which do not correspond to the starting material are noted. On closer investigation, we observe that the PXRD pattern of a powder collected after just 1 minute of grinding, indicates the presence of 1:1 co-crystal and excess isonicotinamide. At 5 minutes, we observe that the 1:1 cocrystal and excess INA peaks are no longer visible, and a new fingerprint pattern is present. This was repeated at 30 second intervals between 1 minute and 5 minutes, and we observe the transformation takes place between the 1 minute and the 2-minute marks, at 30 Hz. New peaks, that do not correspond to starting materials or 1:1 cocrystal are observed in the PXRD pattern after grinding for 90 seconds.



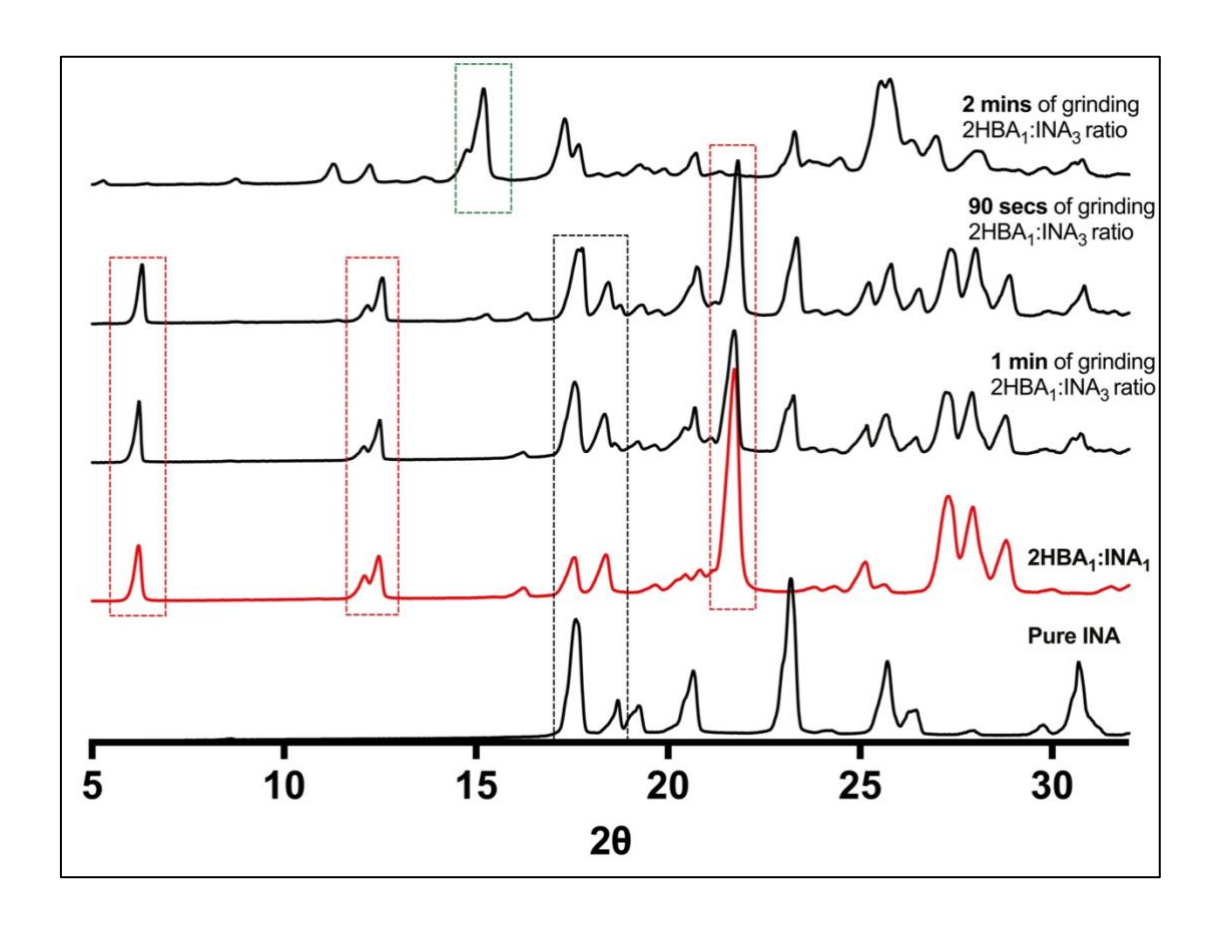


**Figure 6-18** - PXRD patterns of 2HBA<sub>1</sub>:INA<sub>3</sub> at different time points. Overlapping peaks between 1:1 cocrystal, 1:3 cocrystal and excess INA are highlighted.

### 6.3.4 2,3DHBA<sub>2</sub>:INA<sub>1</sub>

From observations of intermolecular interactions in cocrystals of 2-HBA and 3-HBA with cyclic amides, we decided to study 2,3-DHBA in the same fashion. LAG screening efforts were carried out with 2,3-DHBA, nicotinamide and isonicotinamide with ethanol as denoted in tables below.

**Table 6-5** 2,3-DHBA<sub>2</sub>:INA<sub>1</sub> Frequencies, solvent volumes and timepoints for time resolved LAG. The same NEW solid form is produced despite varied conditions.

COFORMERRATIO	TIME POINT	FREQUENCY	SOLVENT VOLUME	RESULTS
	1min			new solid form
	5mins			new solid form

2,3-DHBA <sub>2</sub> :INA <sub>1</sub>	10mins	30Hz	50ul	new solid form
	15mins			new solid form
	30mins			new solid form
	1min		Dry	new solid form
	1min		5ul	new solid form
2,3-DHBA <sub>2</sub> :INA <sub>1</sub>	1min		10ul	new solid form
	1min	30Hz	20ul	new solid form
	1min		30ul	new solid form
	1min		40ul	new solid form
	1min		50ul	new solid form
	1min	Grinding by	50ul	new solid form
		hand		
2,3-DHBA2:INA1	1min	5Hz	50ul	new solid form
	1min	10Hz	50ul	new solid form

PXRD pattern of the mixtures with composition 2,3DHBA<sub>2</sub>:INA<sub>1</sub> shows a unique fingerprint pattern to the starting materials and the known 1:1 cocrystal. We also observed that this cocrystal formed rather quickly. After 30 seconds of grinding, a new product emerges, and no further transformation is observed. To probe this, we tried manual grinding in a pestle and mortar for 30 seconds, and we observed the transformation from a white and pink mixture to a bright yellow powder.

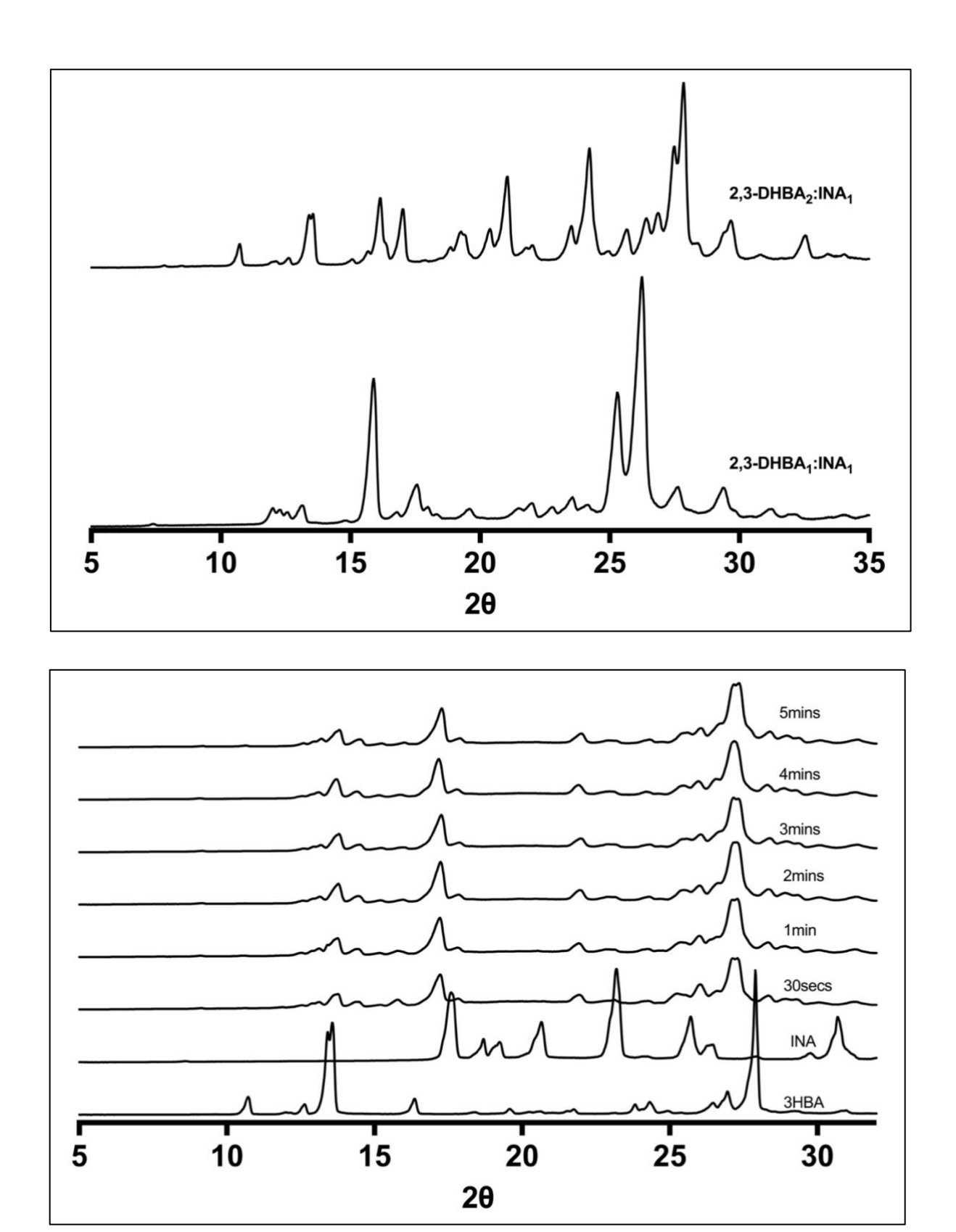


**Figure 6-19** - PXRD Pattern of 2,3-DHBA<sub>2</sub>:INA<sub>1</sub>, compared to 2,3-DHBA<sub>1</sub>:INA<sub>1</sub> and at different time points. No change observed between 30 seconds and 30 minutes of grinding.

# 6.3.5 Summary of findings

These results provide valuable insights into the mechanisms and kinetics of multicomponent solid-state reactions. For the 3-HBA<sub>1</sub>:NA<sub>1</sub> cocrystal, rapid formation was observed within one minute of grinding. We observed that as little as 5 µL of ethanol was sufficient to initiate cocrystal formation, with full conversion achieved at 20 µL and above. This suggests that the liquid plays a crucial facilitating role in the process. The  $\eta$  value (ratio of solvent volume to reactant mass) was found to be significantly lower (0.019 mL/mg) than typical LAG experiments (0.25 μL/mg),<sup>56</sup> yet still effective. Increasing the η value to 0.077 mL/mg improved cocrystal yield, emphasising the facilitating role of a solvent in LAG. Notably, no intermediate phase was observed due to the rapid conversion, and a control experiment showed that physical mixing alone did not lead to spontaneous cocrystallisation. The investigation of 3-HBA1:NA3, a previously unreported cocrystal, reveals a complex, timedependent formation process. After one minute of grinding, DSC analysis showed three distinct endothermic peaks, indicating the presence of at least three different components. As grinding time increased, the relative proportions of these components changed, suggesting a dynamic, stepwise transformation process. Solvent role is highlighted again, as dry mixing shows no cocrystal formation, however as little as 5µL is enough for some cocrystal formation. The 2-HBA<sub>1</sub>:INA<sub>3</sub> system demonstrated the formation of an intermediate phase before the final multicomponent solid form. PXRD patterns showed that after one minute of grinding, a mixture of 1:1 cocrystal and excess isonicotinamide was present. Between one and two minutes of grinding, a transformation to a new form occurred, with distinct PXRD peaks observed after 90 seconds. For the 2,3DHBA2:INA1 combination, rapid cocrystal formation was also observed, with a new product emerging after just 30 seconds of grinding. This was accompanied by a visible colour change from a white and pink mixture to a bright yellow powder during grinding (manual and LAG).

These findings display how time-resolved PXRD is a powerful tool for elucidating the pathways of cocrystal formation, capable of detecting transient intermediate phases and tracking the progression of solid-state reactions. We see that the mechanism of cocrystal formation via LAG can vary significantly between different coformer combinations, ranging from rapid, single-step processes to complex, multistage transformations involving intermediate phases.

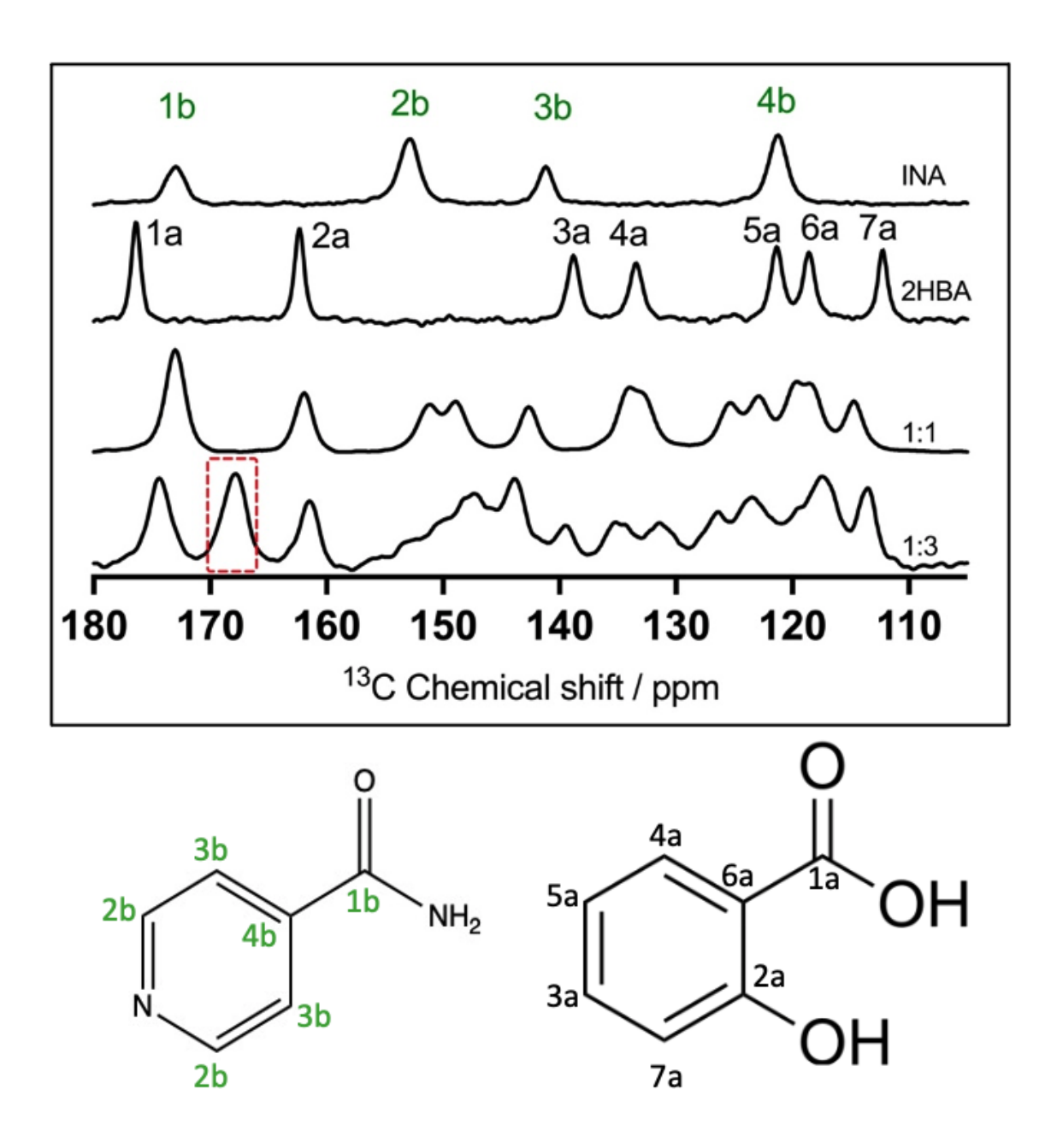
The role of the solvent in LAG extends beyond simple lubrication or molecular diffusion facilitation. Even small amounts of solvent can dramatically affect the kinetics and outcomes of cocrystal formation. Notably, the stoichiometry of the starting materials does not always directly translate to the final cocrystal composition, as evidenced by the formation of mixed-phase products in some cases. We also see how the kinetics of cocrystal formation can be influenced by factors such as grinding time, frequency, and solvent volume, highlighting the importance of optimizing these parameters in cocrystal synthesis. The stepwise transition observed by PXRD led us to attempt to further our understanding, by attempting to observe transformation *in situ* by Combined Liquid and Solid-State (CLASSIC) NMR.

# 6.4 Observing cocrystal transformation by Combined Liquid and Solid-State NMR *in situ* Crystallisation (CLASSIC)

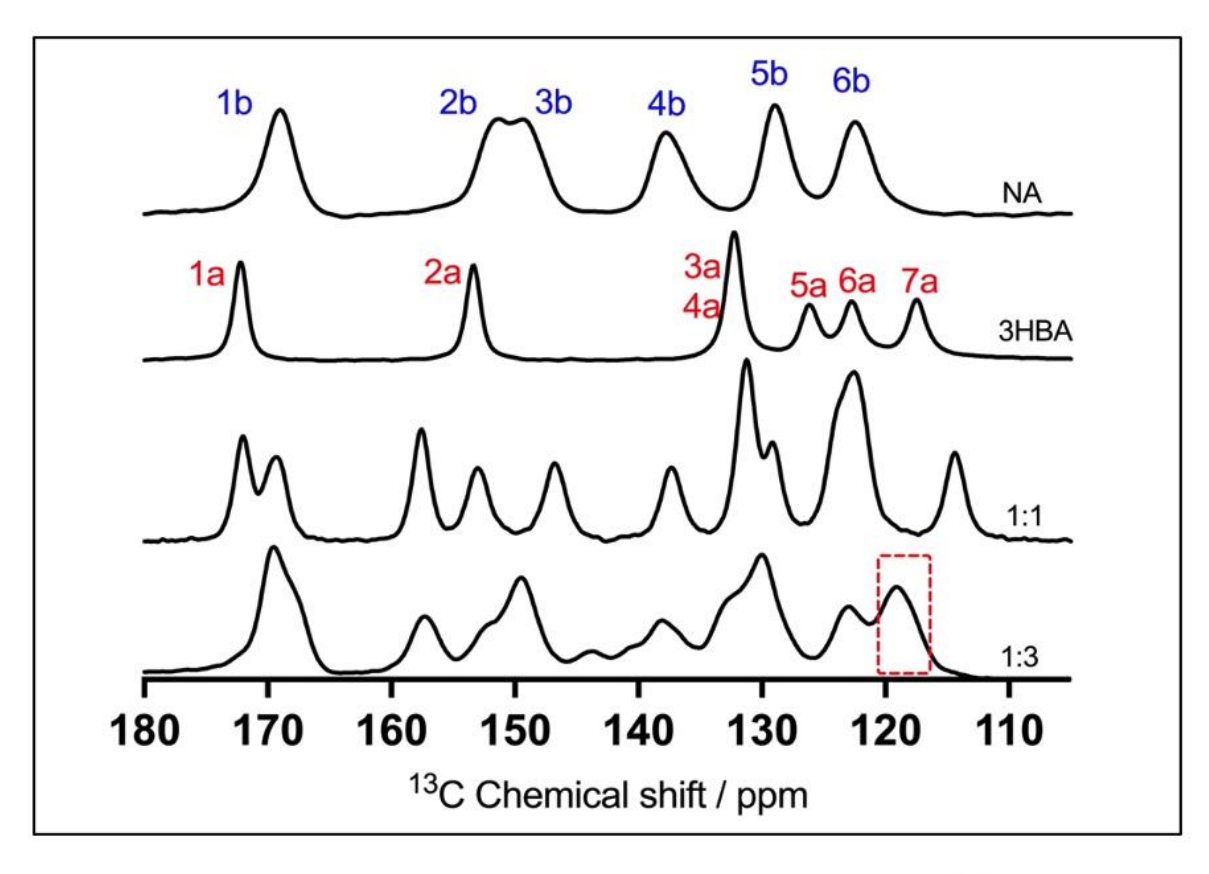
NMR spectroscopy has long been a method of choice for studies of molecular structure and dynamics. However, traditional NMR approaches have often been limited to examining either liquid-state or solid-state systems in isolation. The development of the CLASSIC NMR (Combined Liquid- And Solid-State In-situ Crystallisation NMR) technique represents a significant leap forward in our ability to probe crystallisation processes in situ, offering unprecedented insights into the complex interplay between the real-time solution-state dynamics and solid-state structure formation. CLASSIC NMR has been used widely to monitor real time reactions, including crystallisation from solution, polymorph observation and cocrystal formation. 127, 152, 278-280 In this study, we observe the transformation from one cocrystal, to a new cocrystal with a different stoichiometric ratio in a single NMR experiment.

# 6.4.1 Selection of characteristic peaks for transformation confirmation

<sup>1</sup>H MAS NMR spectra, <sup>13</sup>C with {<sup>1</sup>H} decoupling solid-state NMR, and <sup>1</sup>H-<sup>13</sup>C CP/MAS NMR spectra were recorded at 9.4 and 20.0 T for the pure coformers 2-HBA, 3-HBA, 2,3-DHBA, NA and INA. Peaks were assigned from the available literature. Cocrystals reported in literature were synthesised by LAG with ethanol as described above and verified by PXRD. For materials with reported solid-state NMR data, the spectra were verified by comparison to those previously reported in literature. For coformer ratio **2-HBA<sub>1</sub>:INA<sub>3</sub>** a new peak, observed at 167.8 ppm was selected as the characteristic peak specific to this new solid form. In the <sup>1</sup>H-<sup>13</sup>C CP/MAS NMR spectrum of **3-HBA<sub>1</sub>:NA<sub>3</sub>**, the intense, unique peak observed at 118.1 ppm was selected, which falls within the aromatic region and likely arises from the new conformation of aromatic rings, due to different hydrogen bonding in this cocrystal. In **2,3-DHBA<sub>2</sub>:INA<sub>1</sub>** a peak is observed at 167.8 ppm, which likely corresponds to either the **-C**OOH or the amide C=O sites in this new cocrystal from. In the 1:1 cocrystal, this peak is seen at 170 ppm, showing a clear shift in the 2:1 cocrystal.



**Figure 6-20** <sup>13</sup>C CP/MAS NMR spectra of 2-HBA, INA, 2-HBA<sub>1</sub>:INA<sub>1</sub>, 2-HBA<sub>1</sub>:INA<sub>3</sub> recorded at 298 K on a 400 MHz spectrometer at 12 kHz MAS speed. Characteristic peak of the new 1:3 form is highlighted in red box.



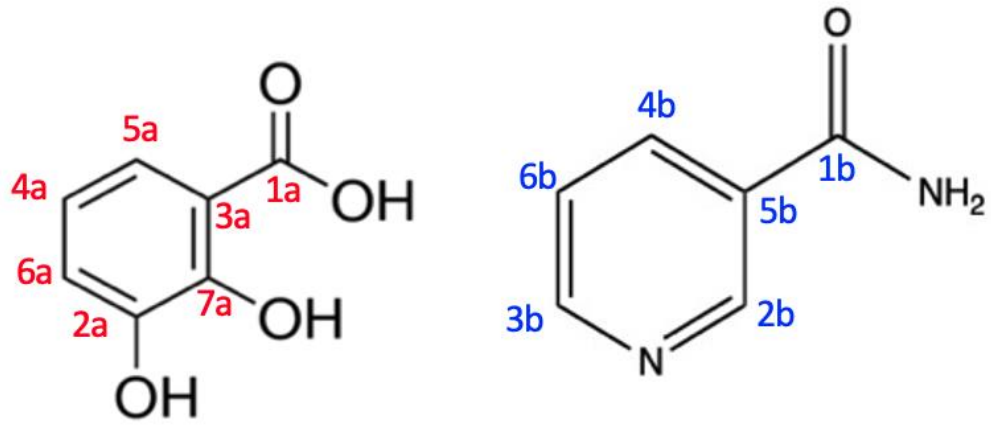


**Figure 6-21** - <sup>13</sup>C CP/MAS NMR spectra of 3-HBA, NA, 3-HBA<sub>1</sub>:NA<sub>1</sub>, 3-HBA<sub>1</sub>:NA<sub>3</sub> recorded at 298K using a 400MHz spectrometer at 12kHz spinning speed. Characteristic peak of the new 1:3 form is highlighted in red box.

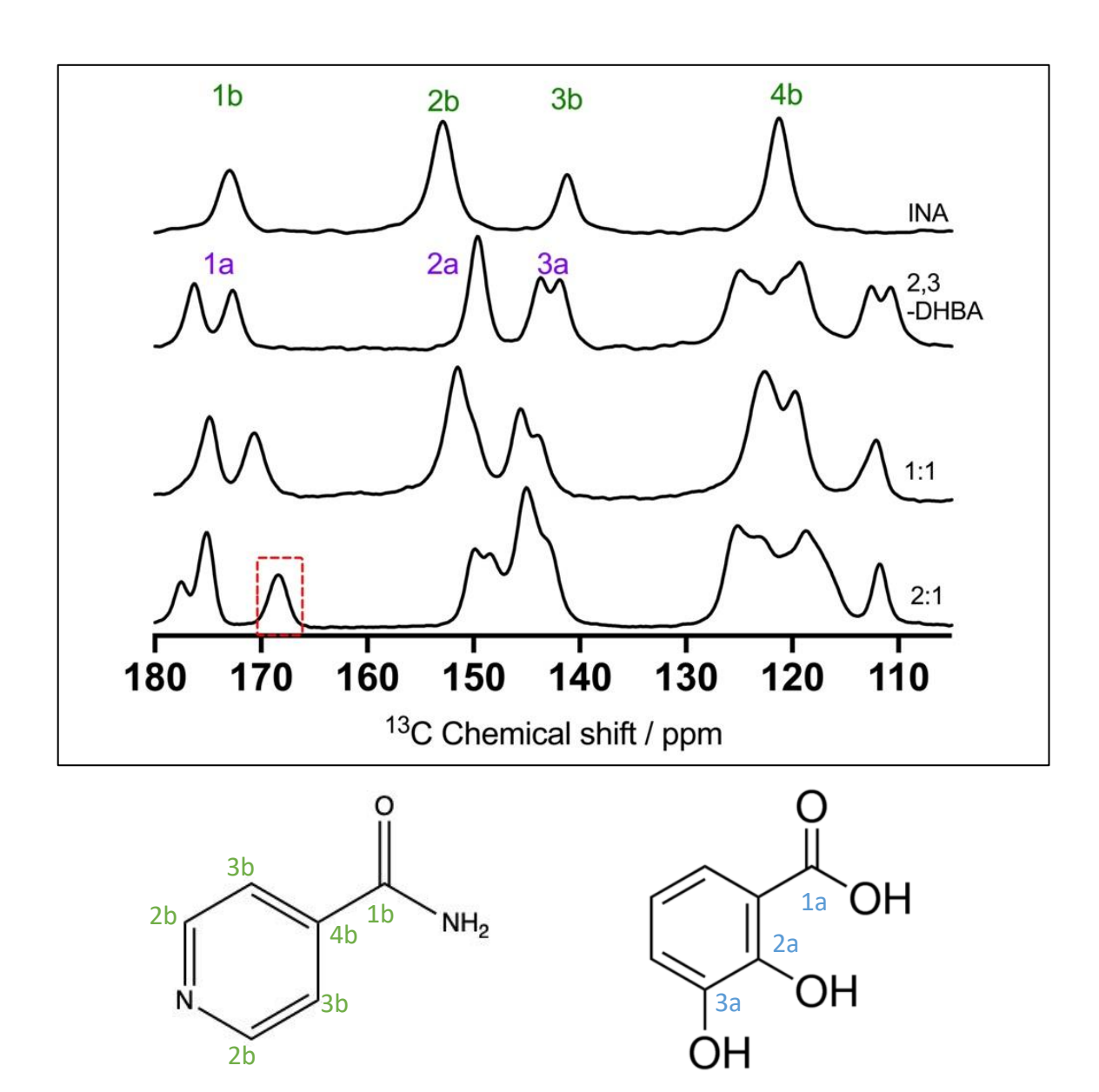


**Figure 6-22** <sup>13</sup>C CP/MAS NMR spectra of pure 2,3-DHBA, pure INA, 2,3-DHBA<sub>1</sub>:INA<sub>1</sub> and 2,3-DHBA<sub>2</sub>:INA<sub>1</sub> recorded on a 400 MHz spectrometer at 298 K and 12 KHz MAS rate. Characteristic peak of the new 2:1 form is highlighted in red box.

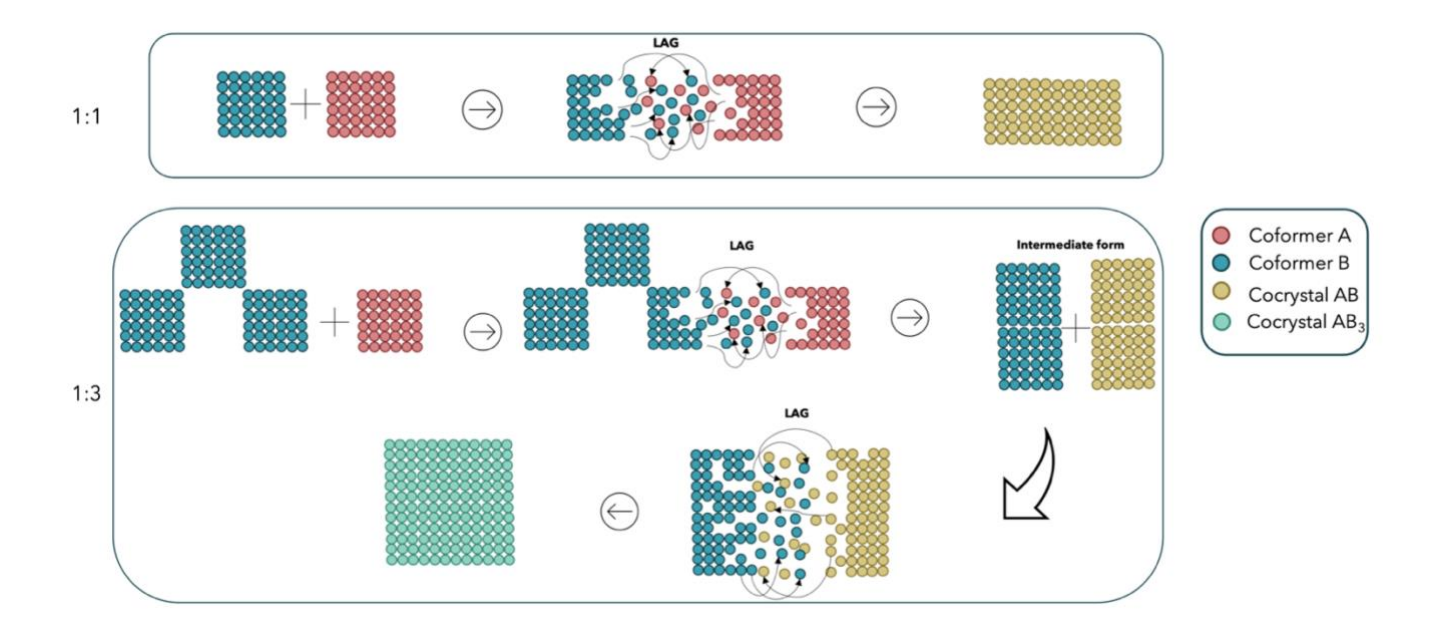


Figure 6-23 - Stepwise depiction of 1:1 and 1:3 cocrystal formation via LAG

### 6.4.2 2-HBA<sub>1</sub>:INA<sub>3</sub>

Reproducing the result achieved from cocrystal grinding *via* LAG in a ball mill,<sup>278</sup> by applying MAS in a 4mm NMR rotor proved challenging. Cocrystal formation *via* LAG is a multistep process and depends on many factors such as the nature of the solvents and reactants, stoichiometric ratio of coformers and solvent, hydrogen bonding and supramolecular synthons present, to name a few.<sup>18, 281</sup> In a ball mill, the mechanochemical force of the steel ball, the rapid tumbling and contact of the coformers, in the presence of the liquid induces the formation of a new solid form. However, in an NMR rotor, we rely on mainly on the contact and mixing of coformers during spinning at 12KHz.

From the time-resolved PXRD patterns monitoring the formation of this novel form, we observe that that conversion of pure material to 1:1 cocrystal occurs after 60 s of LAG, and the conversion of 1:1 + excess INA to 1:3 occurs between 90 and 120 s of LAG. Attempted experimental conditions to mimic this conversion in the NMR rotor are listed in **Table 6**. For

this cocrystal system we were unable to optimise the conditions suitable for in-situ NMR monitoring.

**Table 6-6** NMR experimental conditions for 2-HBA<sub>1</sub>:INA<sub>3</sub> in-situ measurements.  $^1$ H MAS (D1 = 5 s, NS = 8) ,  $^{13}$ C{ $^1$ H} high-power dipolar decoupling (D1 = 10 s, 128 transients were accumulated) , and  $^1$ H- $^{13}$ C CP/MAS (D1 = 120 s, NS=64). Each cycle duration was 2hours 42minutes.

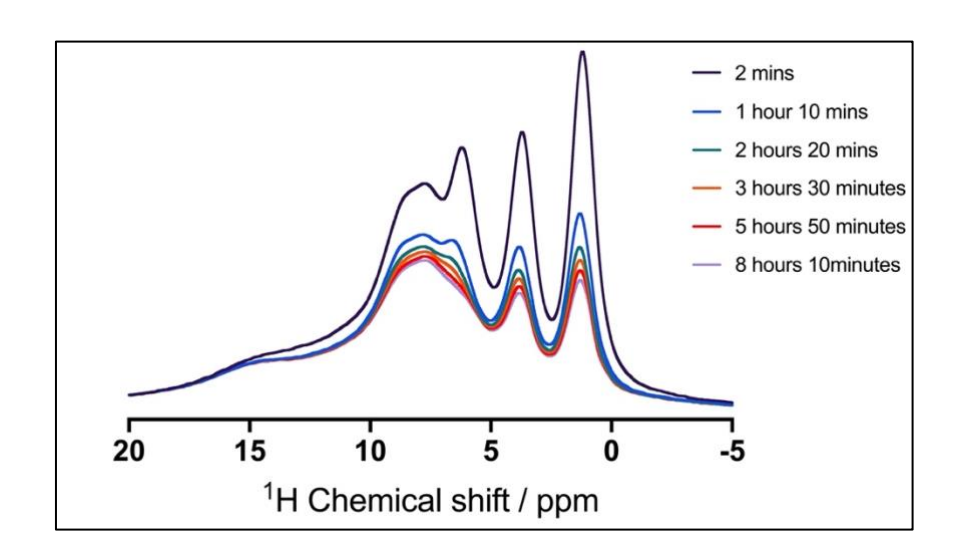
STARTING MATERIALS	<b>EXPERIMENTAL CONDITIONS</b>	OUTCOME/OBSERVATIONS
PURE 2-HBA (1) + PURE INA (3)	Gently mix coformers for 30 s, add 10 μl EtOH	Pure coformers – <b>no change</b>
PURE <b>2-HBA (1) + PURE INA (3)</b>	Gently mix coformers for 30 s, add 20 μl EtOH	INA dissolves in EtOH 2-HBA dissolves after 12 hours. No cocrystal transformation
PURE <b>2-HBA (1) + PURE INA (3)</b>	Grind coformers in pestle and mortar for 30 s, add 10 µl EtOH	1:1 cocrystal formed from grinding. no transformation to 1:3. Initially, INA dissolves in EtOH, 2-HBA dissolves after 12 hours
PURE <b>2-HBA (1) +</b> <b>PURE INA (3)</b>	Grind coformers in pestle and mortar for 30 seconds, add capillary with 10 μl EtOH	1:1 cocrystal has formed from grinding, no transformation to 1:3 cocrystal
2-HBA <sub>1</sub> :INA <sub>1</sub> COCRYSTAL (1) + PURE INA (2)	2-HBA <sub>1</sub> :INA <sub>1</sub> produced by LAG, gently mixed with pure INA, resultant molar ration 1:3. Add 10 µl EtOH	Starting materials dissolve in EtOH. No transformation observed
2-HBA <sub>1</sub> :INA <sub>1</sub> COCRYSTAL (1) + PURE INA (2)	2-HBA <sub>1</sub> :INA <sub>1</sub> produced by LAG, gently mixed with pure INA, resultant molar ration 1:3. Add 20 μI EtOH	Starting materials dissolve in EtOH. No transformation observed

### 6.4.3 3-HBA<sub>1</sub>:NA<sub>3</sub>

PXRD studies of this system indicated formation of an intermediate before the final product appears. To observe this transformation by CLASSIC NMR, two main streams were explored. Firstly, we aimed to observe the transformation of the 1:1 cocrystal to the 1:3 cocrystal and secondly, we tried to explore conversion from the 1:3 cocrystal back to the 1:1 form. Our observations are discussed below.

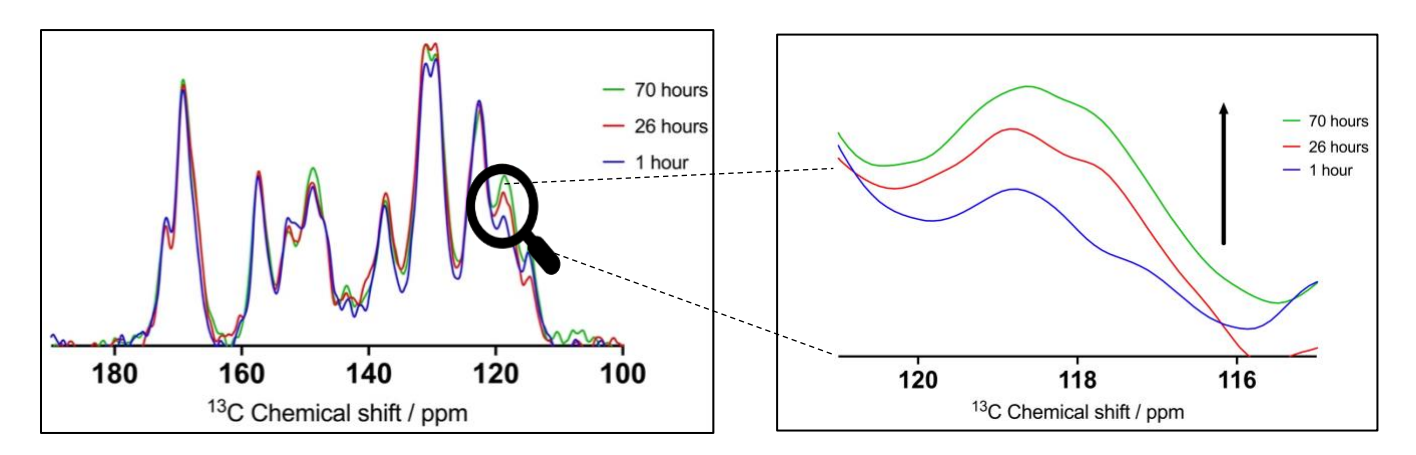
### 3-HBA<sub>1</sub>:NA<sub>1</sub> to 3H-BA<sub>1</sub>:NA<sub>3</sub>

3-HBA $_1$ :NA $_1$  cocrystal produced by LAG and verified by PXRD, was added to an Eppendorf tube with pure NA, in a 1:3 stoichiometric ratio. These were gently mixed and 10  $\mu$ l of EtOH was added. The  $^1$ H MAS NMR spectra recorded initially showed 5 distinct peaks: two at 8.20 and 9.09 ppm, which correspond to the acid and amide proton environments as seen from their individual spectra, and three peaks at 6.70, 4.23 and 1.67 ppm assigned the -OH, CH $_2$  and CH $_3$  functional groups from the ethanol $^{282}$ . Interestingly, after 2.5 hours, we noticed that all peaks reduce in intensity. This continues for the next 8 hours, after which no further change is observed, as seen in Figure 6-25. This phenomenon is also observed in the  $^{13}$ C{ $^{1}$ H} MAS NMR spectra; initially, sharp -CH $_2$  and -CH $_3$  peaks are observed at 54.8 and 14.3 ppm respectively corresponding to EtOH.  $^{283}$  Peaks corresponding to the 1:1 cocrystal are also observed in the first  $^{13}$ C{ $^{1}$ H} MAS NMR spectrum. This suggests that initially, the 1:1 cocrystal dissolves in EtOH. After 70 minutes of the process at MAS conditions, we see a reduction in intensity of all  $^{13}$ C{ $^{1}$ H} MAS NMR peaks, suggesting that the dissolved cocrystal is exiting the solution phase. This continues for the next 7 hours, after which no further change is observed.



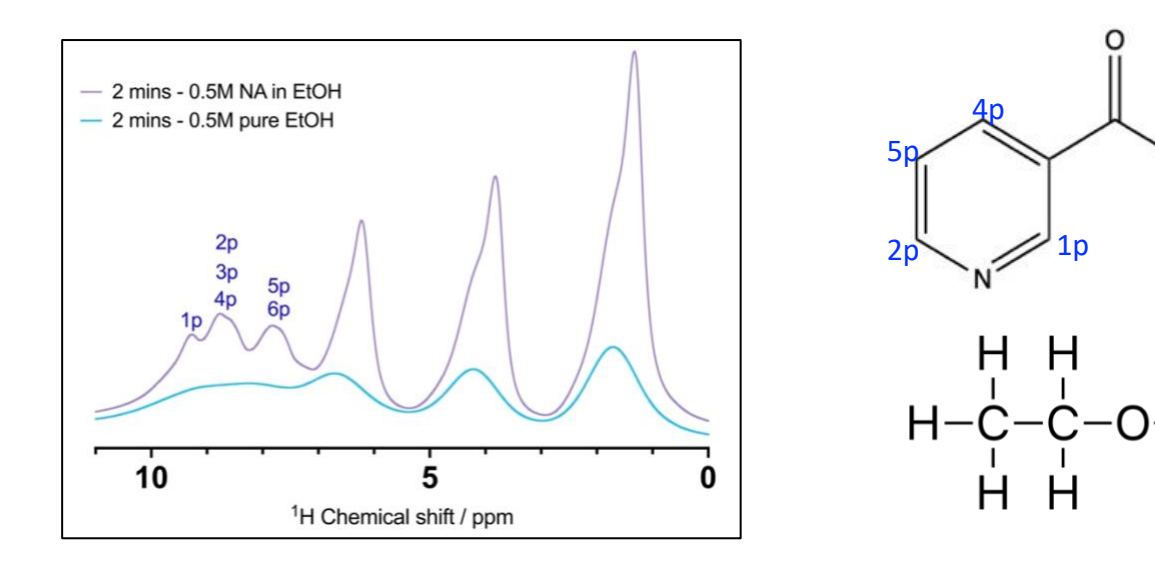
**Figure 6-24**  $^{1}$ H MAS NMR spectra of 3HBA<sub>1</sub>:NA<sub>1</sub> with excess NA and 10  $\mu$ l EtOH 3HBA<sub>1</sub>:NA<sub>1</sub> at different time points during in-situ solid-state NMR experiment. Recorded at 298 K, on a 400 MHz spectrometer at 12 kHz MAS rate.

The <sup>13</sup>C CP/MAS NMR spectral data revealed a subtle structural evolution of the co-crystal system. Initially, the spectrum remained stable for the first 24 hours, indicating minimal structural transformation. At approximately 26 hours, a notable intensity increase emerged at the 118ppm peak, suggesting the initial stages of a structural transition. By 70 hours, the relative peak intensity further increased, providing evidence of a gradual conversion from a 1:1 to a 1:3 co-crystal stoichiometry. This led to us revise our experimental set up, for an improved yield in a shorter time.



**Figure 6-25**  $^{1}$ H- $^{13}$ C CP/MAS NMR spectra of 3HBA $_{1}$ :NA $_{1}$  with excess NA and **10**  $\mu$ l EtOH, after 1, 26 and 70 hours of in-situ experiment. Recorded at 298 K, on a 400 MHz spectrometer at 12 KHz spinning speed.

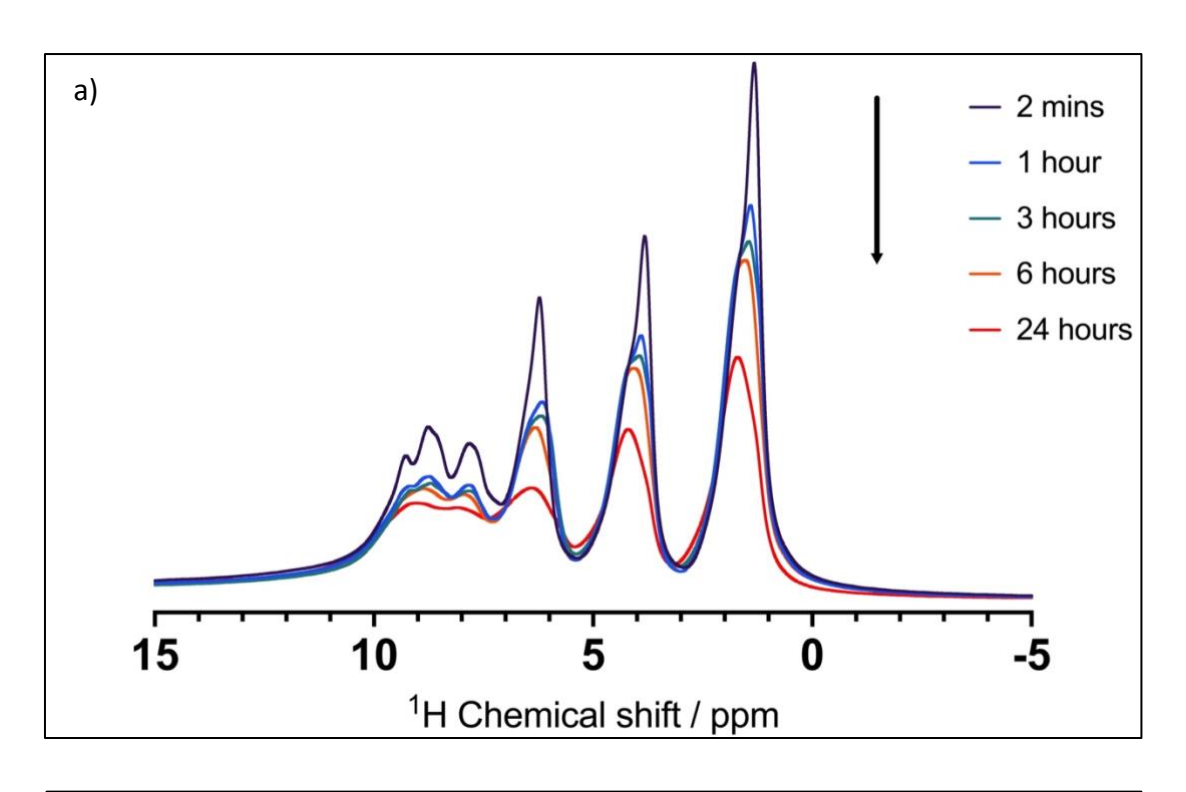
We increased the solvent volume to 20μl, which only marginally enhanced 1:3 cocrystal conversion. Subsequently, we replaced pure ethanol with 20μl of 0.5M NA in ethanol, hypothesizing that dissolved NA would accelerate conversion. This near-saturated solution led to NA crystallization upon spinning, evidenced by diminished NA peaks in the <sup>1</sup>H spectrum, influencing cocrystal formation. The <sup>1</sup>H MAS NMR spectra showed the presence of 10 peaks at the start of the experiment: 3 corresponding to the ethanol at 6.70, 4.23 and 1.67 ppm as above; we also observe peaks at 6.18 , 3.79, 1.28ppm, resulting from the concentrated solution of NA in ethanol. We now also see 4 peaks, at 8.12, 8.92, 9.11 and 9.61 ppm. From literature, and in-house solution state experiments, we know that these correspond to 6 NA proton environments.

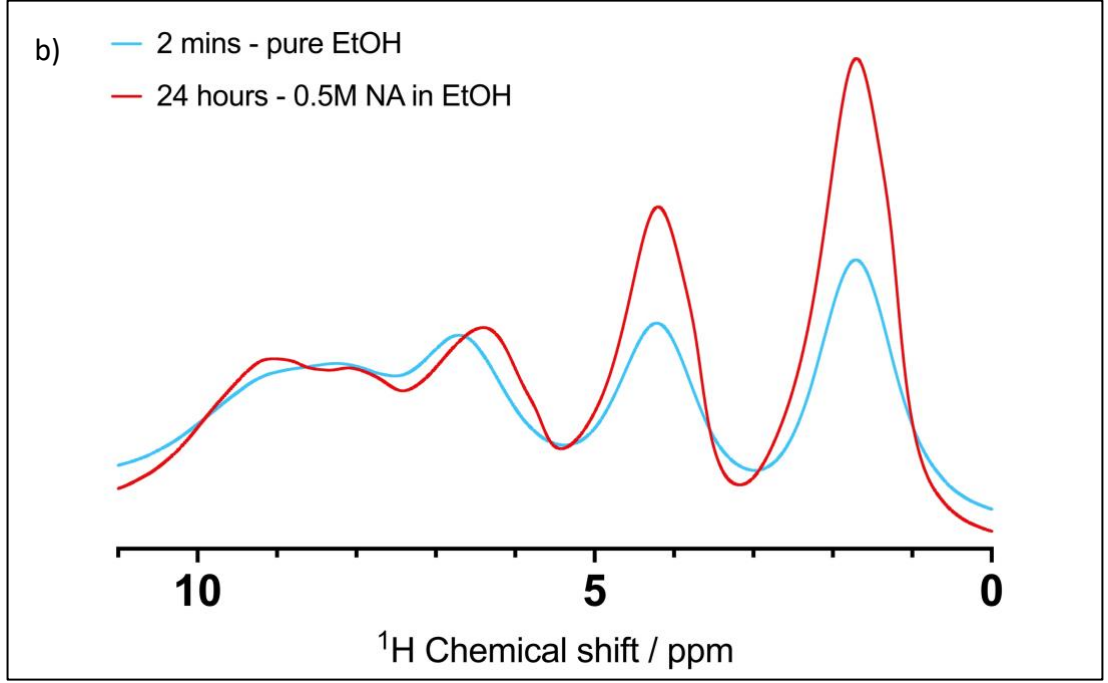


**Figure 6-26** <sup>1</sup>H NMR spectra comparing 0.5M NA in EtOH solution as solvent vs pure EtOH after 2 mins of acquisition. Recorded on 400 MHz spectrometer at 12 KHz MAS rate.

Over 24 hours, we notice a gradual reduction in the intensity of all peaks, and a shift in peaks. It is interesting to note, that after 24 hours of acquisition under MAS conditions, majority of the NA has crystallised out of solution. This can be seen from the resulting <sup>1</sup>H spectrum for the saturated solution of NA. The new peaks have reduced in intensity, resulting in a spectrum similar to that of the *in-situ* experiment with pure EtOH, as seen in Figure 6-27.

6p NH<sub>2</sub> 3p

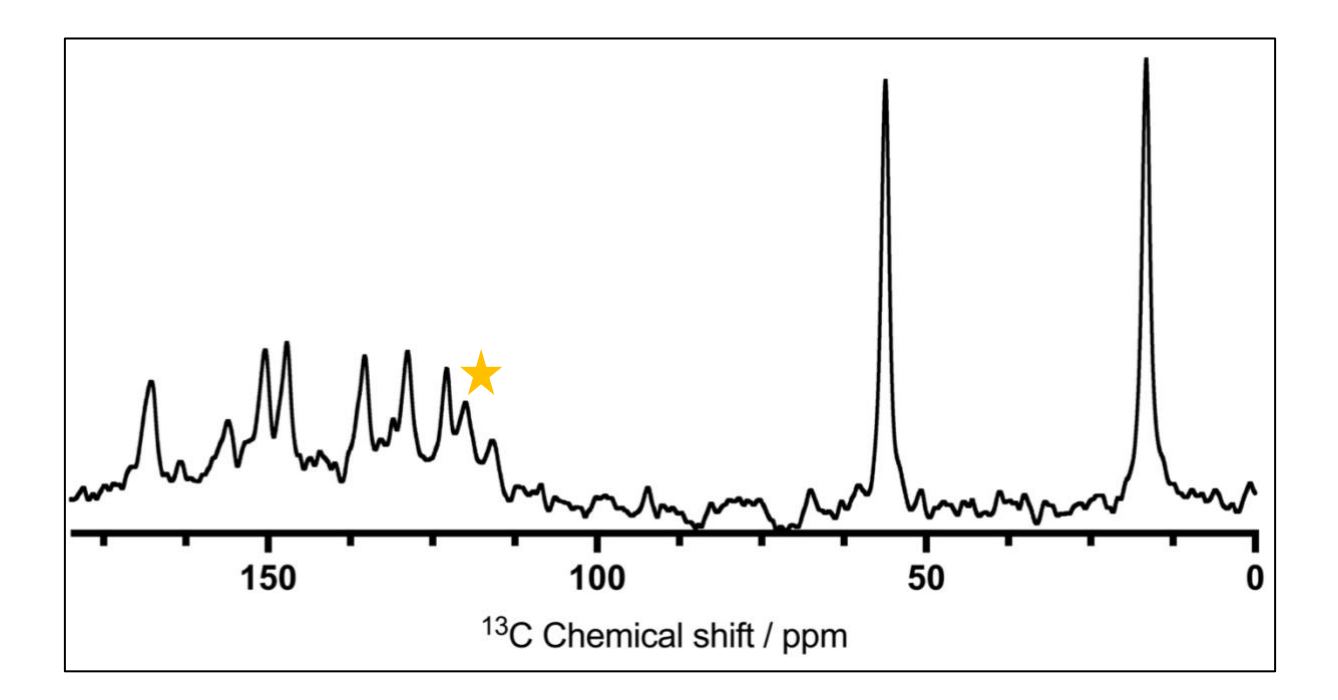




**Figure 6-27. a)** -  $^{1}$ H NMR spectra with saturated 0.5 M NA solution as solvent after 24 hours under MAS conditions. **B)** -  $^{1}$ H spectra comparing peak positions in the spectra recorded after 24 hours with saturated solution compared to the spectrum recorded for 2 minutes with pure ethanol. Recorded at 298 K, on a 400 MHz spectrometer at 12 KHz MAS rate.

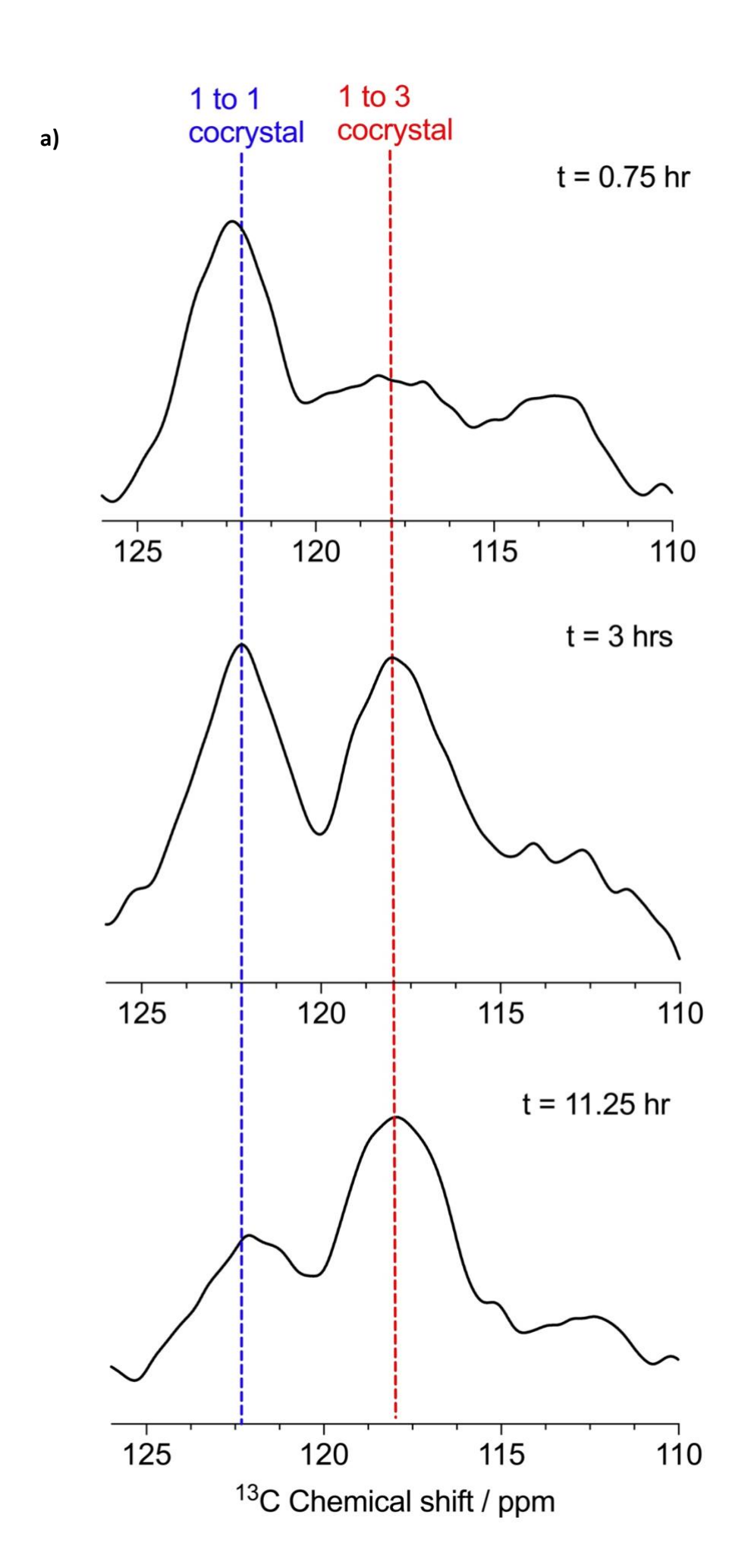
<sup>13</sup>C{<sup>1</sup>H} MAS NMR spectra recorded with a short recycle delay allowed us to observe the mobile components of the sample. Remarkably, after 20 minutes of acquisition, we observe the characteristic peak corresponding to 1:3 co-crystal around 118 ppm.

This suggests that solution-state aggregates form, displaying spectral features resembling the 1:3 cocrystal structure, indicated by its characteristic peaks. These assemblies, mirroring the solid-state arrangement, precede crystallization, accounting for the delayed appearance of corresponding signals in the <sup>13</sup>C CPMAS NMR spectrum.



**Figure 6-28** <sup>13</sup>C{<sup>1</sup>H} high polar decoupling spectra after 20 minutes of acquisition in in-situ NMR sequence. 1:3 characteristic peak starred.

From the <sup>13</sup>C CP/MAS NMR spectra, we observe a much better conversion from the 1:1 to the 1:3 form when a concentrated solution of 0.5M NA in ethanol is used, compared to pure ethanol, as seen from the peak intensity of our characteristic peak. Notably, liquid-state and solid-state spectra show strong concordance.



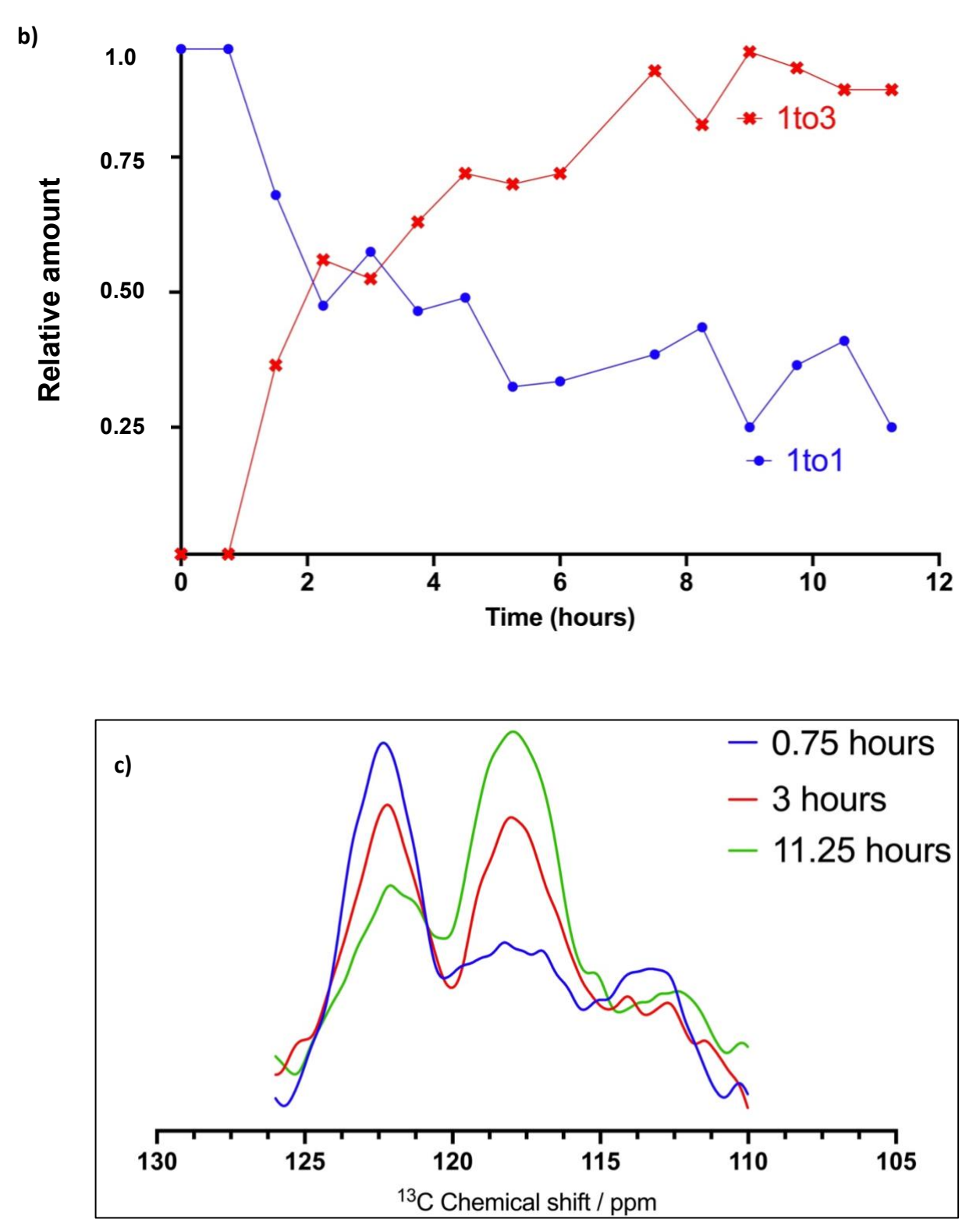


**Figure 6-29** - Results from the in-situ conversion of 3HBA<sub>1</sub>:NA<sub>3</sub> in CLASSIC NMR sequence. a) and **c)** Characteristic peak of 1:3 cocrystal (118ppm) at different time points. Peak corresponding to aromatic carbons 6a and 6b, 1:1 cocrystal at 122 ppm decreases simultaneously. **b)** Fraction of phases as a function of time, extracted from integrals of characteristic peaks.

This investigation of the 3-HBA<sub>1</sub>:NA<sub>3</sub> system revealed a gradual conversion from the 1:1 to the 1:3 cocrystal stoichiometry, observable through changes in <sup>13</sup>C CP/MAS NMR spectra. The use of a concentrated nicotinamide solution in ethanol significantly enhanced the conversion process, highlighting the importance of solution-state dynamics in cocrystal formation. The observation of spectral features resembling the 1:3 cocrystal structure in high polar decoupling spectra, prior to their appearance in solid-state spectra, suggests the formation of solution-state aggregates that precede crystallization.

#### 3-HBA<sub>1</sub>:NA<sub>3</sub> to 3-HBA<sub>1</sub>:NA<sub>1</sub>

We now consider the reversal of this transformation i.e. from the 1:3 cocrystal produced by LAG, to the 1:1 form by *in situ* NMR. CLASSIC NMR experiments demonstrate the reversibility of this transformation. The <sup>1</sup>H MAS NMR spectra initially show 3 broad peaks at 1.02, 3.55 and 6.58 ppm, corresponding to the ethanol protons and a broad peak at 8.62 ppm, which denotes the 3HBA protons. Within 1 hour, we notice a change in peak positions. After *ca*. 9 hours, the -CH<sub>3</sub> peak at 1.02 ppm shifts to 0.71 ppm. The -CH<sub>2</sub> peak at 3.55ppm shifts to 3.19 ppm. The broad peak at 6.58 ppm, splits into 4 peaks at 5.99, 6.61, 6.76, 7.09 ppm, corresponding to the 3HBA proton environments, but they also reduce in relative intensity as the experiment continues, suggesting the 3HBA is exiting the solution phase.

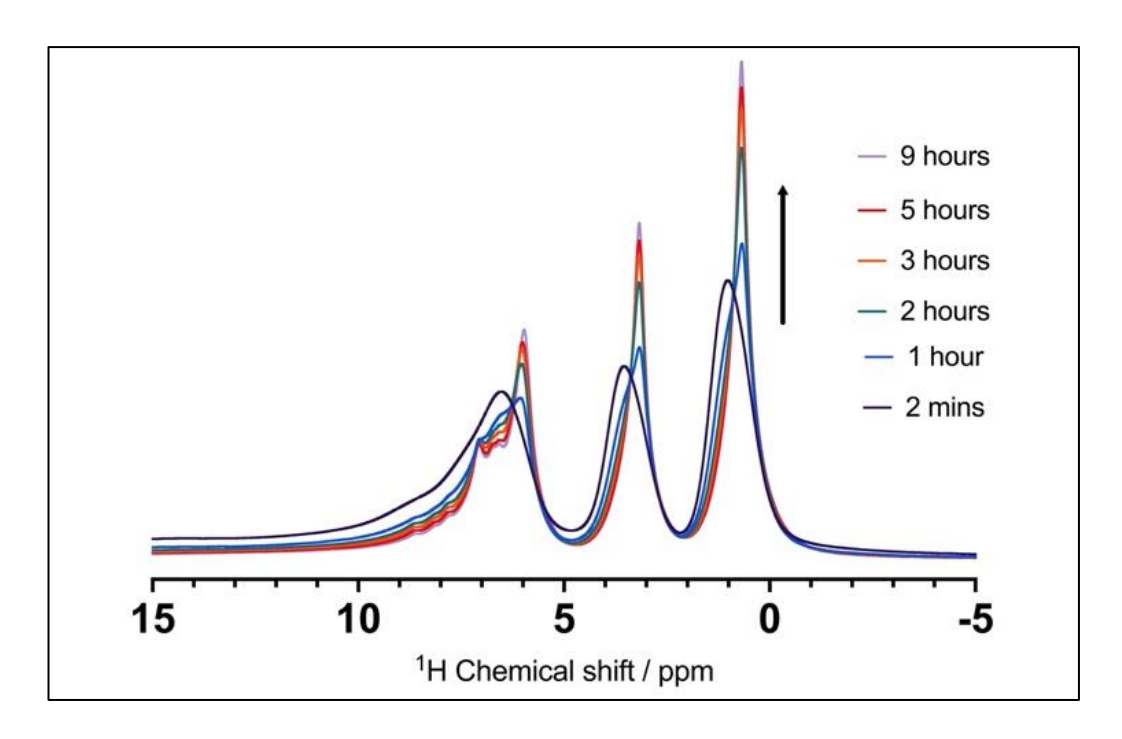


**Figure 6-30** - <sup>1</sup>H MAS NMR spectra of 3HBA<sub>1</sub>:NA<sub>3</sub> cocrystal with saturated 1M 3HBA solution for 9 hours under MAS conditions.

<sup>1</sup>H-<sup>13</sup>C CP/MAS NMR spectra show fast conversion back to the 1:1 form. After 3 hours, we notice that the relative intensity of the peaks corresponding to the 1:3 cocrystal, start to reduce, notably for the characteristic peak at 118 ppm. After 20 hours most of the 1:3 form had converted into 1:1 cocrystal. Experimental conditions are listed in Table 5-7.

**Table 6-7** . 3-HBA<sub>1</sub>:NA<sub>3</sub> In-situ NMR experimental conditions.  $^1$ H MAS (D1 = 5 s, NS = 16)  $^1$ H{ $^{13}$ C} high polar decoupling (D1= 5 s, NS=256) , and  $^1$ H- $^{13}$ C CP/MAS (D1 = 60 s, NS=40). Each cycle duration is 62 min.

STARTING MATERIALS	EXPERIMENTAL CONDITIONS	OUTCOME/OBSERVATIONS
PURE <b>3-HBA (1) + PURE NA (3)</b>	Gently <b>mix coformers</b> for 30 seconds, add <b>10µl</b> EtOH	Pure coformers – no change
PURE <b>3-HBA (1) + PURE NA (3)</b>	Grind coformers in pestle and mortar for 60 s, add 10μl EtOH	1:1 cocrystal formed from grinding. no transformation to 1:3.
PURE <b>3-HBA (1) + PURE NA (3)</b>	Grind coformers in pestle and mortar with 10μl EtOH	1:1 cocrystal formed from grinding. No transformation to 1:3.
3-HBA <sub>1</sub> :NA <sub>1</sub> [from LAG] (1) + PURE NA (3)	Gently <b>mix coformers</b> for 30 seconds, add <b>10μl</b> EtOH	Small increase in characteristic peak at 118.1ppm after 70 hours of spinning.
3-HBA <sub>1</sub> :NA <sub>1</sub> [from LAG] (1) + PURE NA (3)	Gently <b>mix coformers</b> for 30 seconds, add <b>20μl</b> of 0.5M Na in EtOH	Transformation from 1:1 to 1:3 observed, <sup>1</sup> H direct detection and <sup>13</sup> C CP/MAS both confirm
3-HBA <sub>1</sub> :NA <sub>3</sub> [from LAG ] (1) + PURE 3HBA (2)	Gently <b>mix coformers</b> for 30 seconds, add <b>30µl</b> of 1M 3HBA in EtOH	Transformation from 1:1 to 1:3 observed, <sup>1</sup> H direct detection, and <sup>13</sup> C CP/MAS both confirm

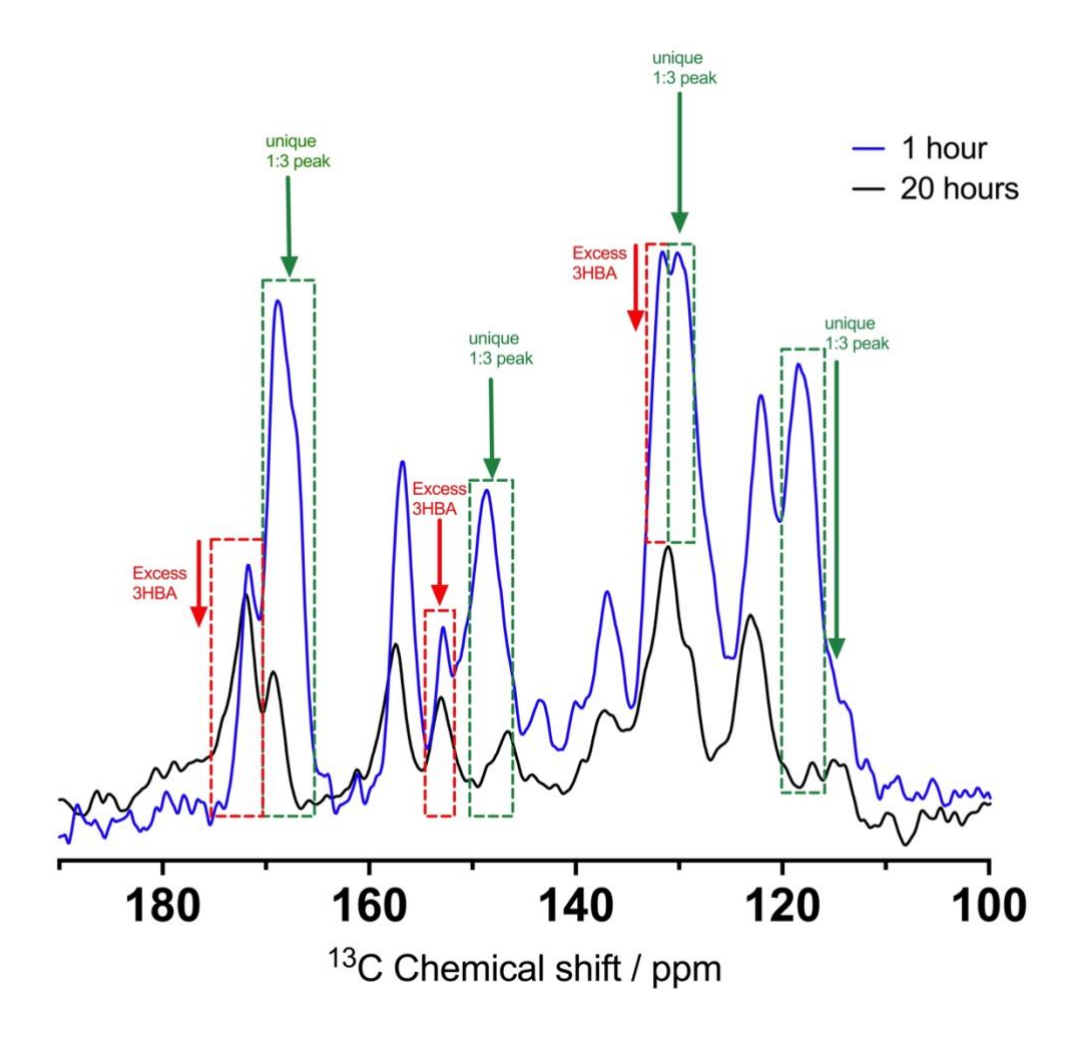


**Figure 6-31** <sup>1</sup>H-<sup>13</sup>C CP/MAS NMR spectra showing conversion of 1:3 cocrystal to 1:1. Black highlighted regions contain peaks unique to 1:3 cocrystal reducing in relative intensity. Red highlighted regions contain peaks corresponding to excess 3HBA.

#### 6.4.4 2,3-DHBA<sub>2</sub>:INA<sub>1</sub>

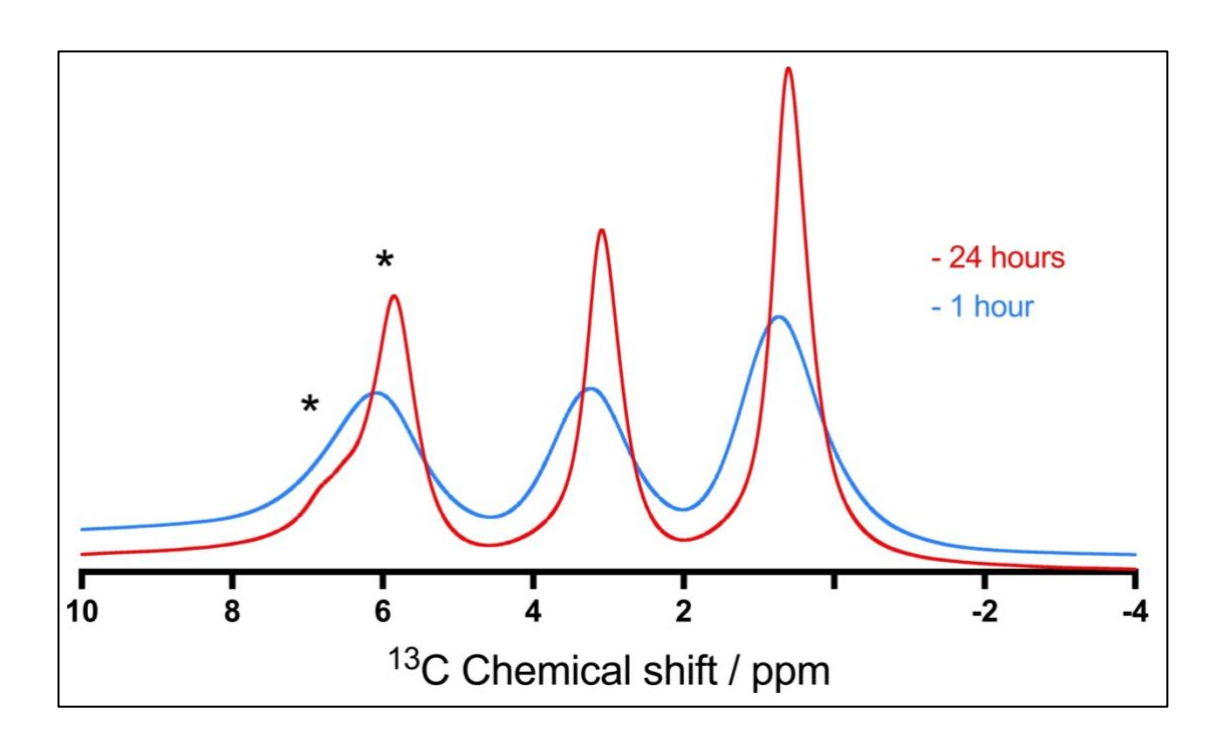
This cocrystal system is particularly interesting as during LAG, we observe an almost instantaneous conversion of coformers, marked by a distinct mustard powder when the cocrystal is formed. We adopted the same method that proved successful for 3HBA<sub>1</sub>:NA<sub>1</sub>, we started with a 1:1 cocrystal from LAG and a stoichiometric excess of 2,3-DHBA.

<sup>1</sup>H MAS NMR spectra show three broad peaks at 0.71, 3.27 and 6.13 ppm, corresponding to ethanol and 2,3-DHBA from the concentrated solution in ethanol. We observe that during acquisition, the ethanol aliphatic peaks at 0.71 and 3.27 ppm both shift 0.2ppm upfield. The

broad peak at 6.13 ppm represents overlapping signals, which split and shift during acquisition to reveal 2 distinct peaks: at 5.82 ppm corresponding to the ethanol -OH and 6.58 ppm corresponding to the 2,3-DHBA in solution. All ethanol peaks become sharper and narrower with time. Whilst the peak representing pure 2,3-DHBA reduces in intensity. This is likely a result of the fact that the 2,3-DHBA is crystallising out of solution and is being incorporated into the cocrystal unit cell, leaving the ethanol.

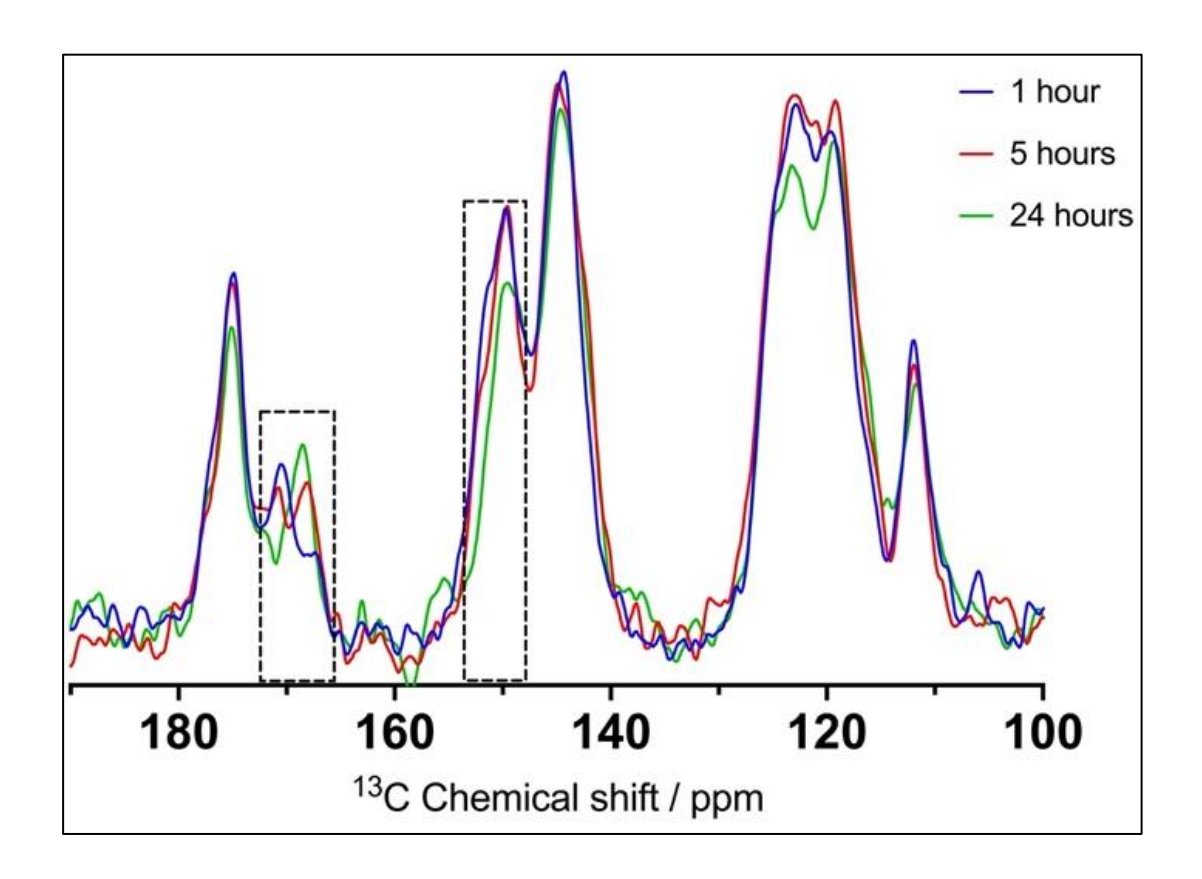
**Table 6-8** 2,3-DHBA<sub>2</sub>:INA<sub>1</sub> In-situ NMR experimental conditions.  $^{1}$ H MAS (D1 = 5 s, NS = 32) , and  $^{1}$ H- $^{13}$ C CP/MAS (D1 = 60 s, NS=40). Each cycle duration is 42 min.

STARTING MATERIALS EXPERIMENTAL CONDITIONS OUTCOME/OBSERVATIONS		
2,3-DHBA <sub>1</sub> :INA <sub>1</sub> [from LAG]	Gently mix coformers for	Transformation from 1:1 to 2:1
(1) + PURE 2,3-DHBA (2)	30 seconds, add <b>20μl</b>	observed, <sup>1</sup> H direct detection,
	0.5M 2,3-DHBA in EtOH	and <sup>13</sup> C CP/MAS both confirm



**Figure 6-32** - <sup>1</sup>H proton NMR showing chemical shifts at after 1 hour at MAS conditions vs 24 hours at MAS conditions for 2,3-DHBA<sub>1</sub>:INA<sub>1</sub> to 2,3-DHBA<sub>2</sub>:INA<sub>1</sub> conversion.

The <sup>13</sup>C CP/MAS NMR spectra show a clear shift of our characteristic peak, from 170.74 to 168.66 ppm, alongside other peaks representing this new 2:1 form. On retrieval of the sample from the rotor after acquisition, the characteristic mustard colour is also observed, as seen with LAG.



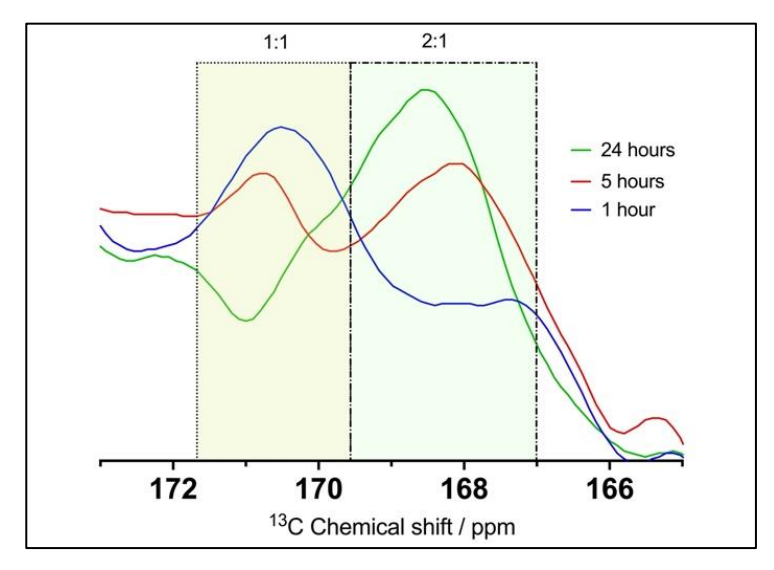


Figure 6-33 <sup>13</sup>C CP/MAS showing conversion of 2,3-DHBA<sub>1</sub>:INA<sub>1</sub> to 2,3-DHBA<sub>2</sub>:INA<sub>1</sub>. Highlighted regions contain peaks unique to 1:1 cocrystal reducing in intensity, and peaks unique to 2:1 increasing. At 5 hours, we see similar intensities, showing that is close to the midpoint.

### 6.5 Discussion and conclusions

In this study, we employed a multi-technique approach combining of Liquid-Assisted Grinding (LAG), time-resolved Powder X-ray Diffraction, and Combined Liquid- And Solid-State In-situ Crystallization (CLASSIC) NMR to investigate the stepwise conversion from pure coformers to cocrystals for three systems: 2HBA<sub>1</sub>:INA<sub>3</sub>, 3HBA<sub>1</sub>:NA<sub>3</sub>, and 2,3-DHBA<sub>2</sub>:INA<sub>1</sub>.

The array of techniques employed in this thesis was deliberately chosen to provide a holistic characterisation of complex multicomponent pharmaceutical systems. No single method can capture every aspect of these materials, but together they reveal complementary insights that build a coherent picture of structure, thermal behaviour, and molecular interactions. TGA and DSC work in tandem to define the thermal profile of a sample. DSC quantifies the heat absorbed or released during phase transitions; such as melting, crystallisation, or glass transitions while TGA tracks concurrent mass changes, pinpointing events that involve loss of water, solvent, or decomposition products. When DSC shows overlapping endothermic peaks, TGA's mass loss data clarifies whether those events reflect dehydration, de-solvation, or chemical degradation. Conversely, DSC enthalpy values validate the significance of TGA detected weight losses. By combining these two thermal techniques, one can both identify and explain each thermal event, as well as model its kinetics to extract activation energies.

Whilst thermal methods define when transformations occur, PXRD and solid-state NMR explain what those transformations entail at the molecular level. PXRD characterises long range crystalline order and quantifies polymorphic compositions, offering precise phase identification even in complex mixtures. Solid-state NMR, however, excels at probing local environments and short-range order. Its sensitivity to chemical shift anisotropy and dipolar couplings reveals structural disorder and hydrogen-bonding interactions that diffraction alone cannot resolve. Together, these methods ensure that every crystalline and amorphous component is accurately identified and quantified.

Bridging the gap between solution and solid phases, solution-state NMR and specialised insitu solid-state techniques such as CLASSIC NMR connect molecular behaviour in solution with the structures that emerge in the solid state. Solution-state NOESY and INEPT experiments reveal how co-formers associate, aggregate, and exchange in ethanol. CLASSIC NMR then captures these crystallisation events in real time within the solid-state rotor, alternating pulse sequences to monitor both dissolved and solid phases simultaneously. This dynamic view links thermally and structurally characterised solid forms back to the solution-phase interactions that drove their formation. By integrating thermal, diffraction, and spectroscopic techniques, every limitation of an individual method is mitigated by another's strengths. Thermal lag and baseline instabilities in DSC are corroborated by PXRD's structural snapshots and NMR's local probes. PXRD's preferred-orientation artefacts are cross-checked against NMR chemical shifts. This orthogonal, complementary strategy not only enhances confidence in each measurement but also aligns with regulatory expectations for robust, analytical validation in pharmaceutical development. Ultimately, the combined use of TGA, DSC, PXRD, and both NMR modalities provides a comprehensive, multi-dimensional understanding of cocrystal formation, polymorphic stability, and molecular interactions - insights that no single technique could deliver on its own.

This multi-technique approach provided comprehensive insights into the mechanisms of cocrystal formation and transformation. LAG, performed using a ball mill, induces cocrystal formation through mechanochemistry, <sup>284</sup> driven by interactions between the steel ball, coformers and solvent. In contrast, the CLASSIC NMR experiments rely on different physical factors to promote cocrystal formation within the NMR rotor. These include centrifugal pressure, <sup>285</sup> temperature changes associated with high-speed spinning, and friction between the zirconia rotor and the probe bearing gas. <sup>286, 287</sup> Despite these differences in driving forces, both techniques proved effective in facilitating cocrystal formation and transformation.

Our findings support the concept that cocrystal formation can occur in either a synchronous or asynchronous hierarchical manner, as previously observed in quadruplexes.<sup>263</sup> This principle extends to cocrystals of varying stoichiometries. Specifically, we have demonstrated that the formation of the 3HBA<sub>1</sub>:NA<sub>3</sub> cocrystal follows an asynchronous, hierarchical pathway. Initially, a 1:1 cocrystal forms, followed by a reorganization of the supramolecular synthon system, ultimately leading to the 1:3 cocrystal. This stepwise process was clearly observed in CLASSIC NMR experiments when we modified our starting point from a mixture of pure coformers to a combination of a 1:1 cocrystal (prepared by LAG) and excess pure coformer.

A particularly intriguing finding from this study is the reversibility between 3HBA:NA cocrystal forms, as evidenced by CLASSIC NMR experiments. This reversibility underscores the dynamic

nature of cocrystal systems and highlights how environmental conditions, such as solvent composition, concentration, and stoichiometric ratios, critically influence the stability and transformation pathways of different forms.<sup>54, 56, 103, 107, 108, 110, 198, 269, 284, 288-291</sup> This observation aligns with previous studies on dynamic cocrystal systems that emphasize the impact of environmental factors on phase stability.

The role of solvent in cocrystal formation and transformation was further emphasised when we varied the concentration and composition of ethanol in our experiments. We observed that in the absence of solvent, no transformation occurred, while insufficient solvent led to minimal transformation. These findings are consistent with Harris et al.'s demonstration of how solvent choice and concentration significantly impact crystallization pathways, often determining whether stable or metastable polymorphs form.<sup>127</sup>

CLASSIC NMR provided a detailed molecular-level understanding of crystallization and dissolution dynamics. Notably, we observed changes in the solution phase before detecting any alterations in solid-state spectra. While we were unable to establish favourable CLASSIC NMR conditions for the 2HBA:INA system, based on the consistent behaviour observed in isomeric hydroxybenzoic acids and the time-resolved PXRD data, we hypothesize that it likely exhibits a similar stepwise approach to cocrystal formation.

# Chapter 7 General conclusions and recommendations for future work

This investigation into cocrystal formation contributes meaningful data regarding the impact of stoichiometric variations in coformers. Statistical analysis of the cocrystals of NA and INA in the CSD revealed the dominance of -COOH····N-Pyridine synthons in prevalence and competition studies. These findings provide crucial insights for crystal engineering in pharmaceutical manufacturing, specifically in understanding and controlling cocrystal formation. There is scope for expansion of this statistical study. Further research could include statistical and structural analysis of hydrogen bonding in picolinamide cocrystals, another structural isomer of NA and INA with the pyridine in the ortho position.

A key constraint in developing accurate machine learning models for this study was the scarcity of documented unsuccessful cocrystallisation attempts published in literature. Herein is an extensive documentation of 'failed' cocrystallisation attempts and their outcomes, contributing to this body of knowledge.

The importance of exploring multiple ratios during screening has been underscored by these findings. Traditionally, cocrystal screening has focused primarily on 1:1 ratio. However, the supramolecular synthon theory suggests that multiple stoichiometric ratios should form when complementary functional groups are present. This notion is tested with multiple screening attempts in different ratios. The experimental results demonstrate that all selected cocrystal systems yielded at least one cocrystal form with a stoichiometry different from the conventional 1:1 ratio. Liquid-assisted grinding (LAG) proved to be an effective method for cocrystal synthesis, offering a favourable balance of control and efficiency compared to alternative cocrystallisation techniques.

Six new cocrystal solid forms are reported and verified three-fold by DSC, PXRD and <sup>13</sup>C CP/MAS, however single crystal structures could not be obtained. Alternative methods for obtaining crystal structure information, such as structure determination from powder X-ray diffraction were explored. However, this approach typically requires synchrotron radiation, which was not accessible to us, and the in-house diffractometer lacked the necessary capabilities. Additionally, advanced computational methods such as crystal structure

prediction and NMR-based density functional theory (DFT) calculations using software like CASTEP<sup>292</sup> could have provided further validation of our findings. Unfortunately, time constraints, and the direction of the project precluded the implementation of these sophisticated techniques.

Our systematic, comprehensive solution state <sup>1</sup>H and <sup>15</sup>N NMR studies conducted on hydroxybenzoic acid and cyclic amide systems have provided valuable insights into the solution-state behaviour and interactions of these cocrystal formers. The results offer a nuanced understanding of the molecular interactions and dynamic processes involved in cocrystal formation, highlighting the complex interplay between hydrogen bonding, concentration effects, and structural rearrangements in solution

Future work in this field should explore several key directions to further elucidate the complex solution-state behaviour of hydroxybenzoic acid and cyclic amide cocrystal systems.

A promising avenue for future research involves extending the concentration range of the titration studies. Exploring higher concentrations, such as 10:1 ratio, is expected to yield more pronounced chemical shifts. This expectation is based on previous studies with urea, where a significant 0.19 ppm<sup>241</sup> shift was observed between 1 and 8 M concentrations. To streamline this process and reduce sample preparation time, concentration gradient techniques within a single NMR tube should be implemented. <sup>293</sup> This approach would allow for a continuous range of concentrations to be studied efficiently, potentially revealing subtle concentration-dependent effects that might be missed in discrete sample preparations.

Complementary to the 'constant base-increasing acid' titration studies, the reverse, acid-base titrations could provide valuable insights. Maintaining a constant acid concentration while titrating against a base would further probe the observed phenomena, particularly the pH-dependent aspects of the coformer-coformer system. This approach could help decouple pH effects from other concentration-dependent factors, offering a clearer picture of the underlying molecular interactions.

To address the spectrometer time constraints limitation of our INEPT studies, 2D techniques such as Heteronuclear Single Quantum Coherence (HSQC) spectroscopy can be employed. HSQC not only builds upon the INEPT transfer mechanism but also offers increased sensitivity compared to direct <sup>15</sup>N detection. This enhanced sensitivity could provide additional

structural insights, particularly in identifying and characterizing key intermolecular interactions.

Finally, to complement our experimental work, conducting Molecular Dynamics (MD) simulations is proposed. These computational studies could confirm and quantify the aggregation behaviour observed experimentally, providing atomistic-level insights into the dynamic processes occurring in solution. MD simulations could also help predict and interpret the effects of changing experimental conditions, such as concentration or temperature, guiding future experimental designs.

The time resolved PXRD, and *in-situ* solid state NMR study demonstrates an effective method for monitoring the conversion between different stoichiometric ratios of cocrystals, as exemplified by the 3-HBA:NA and 2,3-DHBA:INA systems. By systematically varying experimental parameters, the direction and rate of cocrystal transformations can be influenced. The results indicate that using concentrated solutions of coformers in the CLASSIC set up significantly accelerates the conversion process.

The unique ability of CLASSIC NMR to simultaneously observe liquid and solid phases has provided unprecedented insights into the crystallization process. This dual-phase monitoring capability offers significant advantages for understanding the complex interplay between solution-state dynamics and solid-state structure formation, as evidenced by the emergence and growth of characteristic peaks in the <sup>13</sup>C CP/MAS NMR spectra.

Looking to the future, there are several promising avenues for expanding upon this research. First, applying CLASSIC NMR to a broader range of cocrystal systems could enhance the understanding of the underlying principles governing cocrystal formation. This could include investigating various combinations of coformers with diverse functional groups and hydrogen bonding capabilities. Further refinement of experimental parameters, such as solvent selection and temperature control, could lead to more efficient crystallization processes and potentially unlock new cocrystal forms. Spectrometer time was the main limitation, as some materials exhibit extremely long relaxation delays, making comprehensive studies challenging. This constraint affected our ability to conduct more extensive experiments and gather data over longer periods. Despite this limitation, we were able to observe significant transformations and gain valuable insights into the cocrystal formation processes. Future

studies could benefit from extended spectrometer access or the development of techniques to reduce acquisition times without compromising data quality. The implications of this research extend to pharmaceutical applications, where controlling cocrystal properties can significantly impact drug solubility, stability, and bioavailability. Future work should explore the practical applications of CLASSIC NMR in drug formulation development, particularly for compounds with known polymorphic behaviour.

The pharmaceutical industry continues to face mounting challenges in developing orally bioavailable drugs, with approximately 90% of new chemical entities exhibiting poor aqueous solubility. Multicomponent solid forms, particularly cocrystals, have emerged as a promising strategy to address these limitations, yet their discovery has historically remained largely serendipitous. This thesis contributes to transforming this landscape by integrating computational prediction, systematic experimentation, and mechanistic understanding to develop a rational framework for cocrystal design. The investigation of nicotinamide (NA) and isonicotinamide (INA) systems has broader implications beyond these specific molecules. As structural isomers with identical functional groups but different spatial arrangements, they serve as ideal model systems for understanding how molecular geometry influences supramolecular recognition; a fundamental question in crystal engineering with applications ranging from pharmaceuticals to agrochemicals and functional materials.

In conclusion, our comprehensive investigation has studied intermolecular interactions in multi-component pharmaceuticals using various advanced techniques and characterisation methods. The documentation of failed crystallization attempts, exploration of multiple stoichiometric ratios, and implementation of CLASSIC NMR for dual-phase monitoring have provided valuable insights into cocrystal formation mechanisms. These findings have direct industrial applications in pharmaceutical manufacturing, particularly in optimizing drug formulation processes and enhancing drug bioavailability. While technical limitations such as spectrometer availability and lack of synchrotron access presented challenges, they also highlight opportunities for future academic collaborations. Our methodologies and observations will contribute to more efficient drug development processes and improved pharmaceutical formulations.

## References

- 1. Groom, C. R.; Bruno, I. J.; Lightfoot, M. P.; Ward, S. C., The Cambridge Structural Database. *Acta Crystallogr. Sect. B-Struct. Sci. Cryst. Eng. Mat.* **2016**, *72*, 171-179.
- 2. Taylor, R.; Wood, P. A., A Million Crystal Structures: The Whole Is Greater than the Sum of Its Parts. *Chem. Rev.* **2019**, *119* (16), 9427-9477.
- 3. Ferrence, G. M.; Tovee, C. A.; Holgate, S. J. W.; Johnson, N. T.; Lightfoot, M. P.; Nowakowska-Orzechowska, K. L.; Ward, S. C., CSD Communications of the Cambridge Structural Database. *IUCrJ* **2023**, *10* (1), 6-15.
- 4. Santos, R.; Ursu, O.; Gaulton, A.; Bento, A. P.; Donadi, R. S.; Bologa, C. G.; Karlsson, A.; Al-Lazikani, B.; Hersey, A.; Oprea, T. I.; Overington, J. P., A comprehensive map of molecular drug targets. *Nat Rev Drug Discov* **2017**, *16* (1), 19-34.
- 5. Hingorani, A. D.; Kuan, V.; Finan, C.; Kruger, F. A.; Gaulton, A.; Chopade, S.; Sofat, R.; Macallister, R. J.; Overington, J. P.; Hemingway, H.; Denaxas, S.; Prieto, D.; Casas, J. P., Improving the odds of drug development success through human genomics: modelling study. *Scientific Reports* **2019**, 9 (1).
- 6. Scannell, J. W.; Blanckley, A.; Boldon, H.; Warrington, B., Diagnosing the decline in pharmaceutical R&D efficiency. *Nature Reviews Drug Discovery* **2012**, *11* (3), 191-200.
- 7. Rodrigues, M.; Baptista, B.; Lopes, J. A.; Sarraguça, M. C., Pharmaceutical cocrystallization techniques. Advances and challenges. *International Journal of Pharmaceutics* **2018**, *547* (1), 404-420.
- 8. Domingos, S.; André, V.; Quaresma, S.; Martins, I. C. B.; Minas Da Piedade, M. F.; Duarte, M. T., New forms of old drugs: improving without changing. *Journal of Pharmacy and Pharmacology* **2015**, 67 (6), 830-846.
- 9. Aitipamula, S.; Banerjee, R.; Bansal, A. K.; Biradha, K.; Cheney, M. L.; Choudhury, A. R.; Desiraju, G. R.; Dikundwar, A. G.; Dubey, R.; Duggirala, N.; Ghogale, P. P.; Ghosh, S.; Goswami, P. K.; Goud, N. R.; Jetti, R. R. K. R.; Karpinski, P.; Kaushik, P.; Kumar, D.; Kumar, V.; Moulton, B.; Mukherjee, A.; Mukherjee, G.; Myerson, A. S.; Puri, V.; Ramanan, A.; Rajamannar, T.; Reddy, C. M.; Rodriguez-Hornedo, N.; Rogers, R. D.; Row, T. N. G.; Sanphui, P.; Shan, N.; Shete, G.; Singh, A.; Sun, C. C.; Swift, J. A.; Thaimattam, R.; Thakur, T. S.; Kumar Thaper, R.; Thomas, S. P.; Tothadi, S.; Vangala, V. R.; Variankaval, N.; Vishweshwar, P.; Weyna, D. R.; Zaworotko, M. J., Polymorphs, Salts, and Cocrystals: What's in a Name? *Crystal Growth & Design* **2012**, *12* (5), 2147-2152.
- 10. Vranić, E., Amorphous pharmaceutical solids. *Bosn J Basic Med Sci* **2004,** *4* (3), 35-39.
- 11. Datta, S.; Grant, D. J. W., Crystal structures of drugs: advances in determination, prediction and engineering. *Nature Reviews Drug Discovery* **2004**, *3* (1), 42-57.
- 12. Hancock, B. C.; Zografi, G., Characteristics and significance of the amorphous state in pharmaceutical systems. *J Pharm Sci* **1997**, 86 (1), 1-12.
- 13. Vippagunta, S. R.; Brittain, H. G.; Grant, D. J. W., Crystalline solids. *Advanced Drug Delivery Reviews* **2001**, *48* (1), 3-26.
- 14. Bernstein, J., *Polymorphism*. Springer: Dordrecht, 2002; Vol. 68, p 247-260.
- 15. Hatcher, L. E.; Burgess, A. J.; Payne, P.; Wilson, C. C., From structure to crystallisation and pharmaceutical manufacturing: the CSD in CMAC workflows. *Crystengcomm* **2020**, *22* (43), 7475-7489.

- 16. McNaught, A. D. a. W., IUPAC Compendium of Chemical Terminology. *Blackwell Science Publications, Oxford* **1997,** *2nd Edition*.
- 17. Gupta, D.; Bhatia, D.; Dave, V.; Sutariya, V.; Varghese Gupta, S., Salts of Therapeutic Agents: Chemical, Physicochemical, and Biological Considerations. *Molecules* **2018**, *23* (7).
- 18. Cerreia Vioglio, P.; Chierotti, M. R.; Gobetto, R., Pharmaceutical aspects of salt and cocrystal forms of APIs and characterization challenges. *Adv Drug Deliv Rev* **2017**, *117*, 86-110.
- 19. Thakral, N. K.; Kelly, R. C., Salt disproportionation: A material science perspective. *Int J Pharm* **2017**, *520* (1-2), 228-240.
- 20. Prohotsky, D. L.; Zhao, F., A survey of Top 200 Drugs—Inconsistent Practice of Drug Strength Expression for Drugs Containing Salt Forms. *Journal of Pharmaceutical Sciences* **2012**, *101* (1), 1-6.
- 21. Serajuddin, A. T. M., Salt formation to improve drug solubility. *Advanced Drug Delivery Reviews* **2007**, 59 (7), 603-616.
- 22. Morris, K. R.; Fakes, M. G.; Thakur, A. B.; Newman, A. W.; Singh, A. K.; Venit, J. J.; Spagnuolo, C. J.; Serajuddin, A. T. M., An integrated approach to the selection of optimal salt form for a new drug candidate. *International Journal of Pharmaceutics* **1994**, *105* (3), 209-217.
- 23. Paulekuhn, G. S.; Dressman, J. B.; Saal, C., Trends in Active Pharmaceutical Ingredient Salt Selection based on Analysis of the Orange Book Database. *Journal of Medicinal Chemistry* **2007**, *50* (26), 6665-6672.
- 24. Smith, H. S., Nonsteroidal Anti-Inflammatory Drugs; Acetaminophen. In *Encyclopedia of the Neurological Sciences (Second Edition)*, Aminoff, M. J.; Daroff, R. B., Eds. Academic Press: Oxford, 2014; pp 610-613.
- 25. Tilborg, A.; Norberg, B.; Wouters, J., Pharmaceutical salts and cocrystals involving amino acids: A brief structural overview of the state-of-art. *European Journal of Medicinal Chemistry* **2014**, *74*, 411-426.
- 26. Ibuprofen. In Meyler's Side Effects of Drugs: The International Encyclopedia of Adverse Drug Reactions and Interactions (Fifteenth Edition), Aronson, J. K., Ed. Elsevier: Amsterdam, 2006; pp 1709-1713.
- 27. Vishweshwar, P.; McMahon, J. A.; Bis, J. A.; Zaworotko, M. J., Pharmaceutical cocrystal. *Journal of Pharmaceutical Sciences* **2006**, 95 (3), 499-516.
- 28. Healy, A. M.; Worku, Z. A.; Kumar, D.; Madi, A. M., Pharmaceutical solvates, hydrates and amorphous forms: A special emphasis on cocrystals. *Advanced Drug Delivery Reviews* **2017**, *117*, 25-46.
- 29. Gorbitz, C. H.; Hersleth, H. P., On the inclusion of solvent molecules in the crystal structures of organic compounds. *Acta Crystallogr. Sect. B-Struct. Sci.* **2000**, *56*, 526-534.
- 30. Stahly, G. P., Diversity in Single- and Multiple-Component Crystals. The Search for and Prevalence of Polymorphs and Cocrystals. *Crystal Growth & Design* **2007**, *7* (6), 1007-1026.
- 31. Brini, E.; Fennell, C. J.; Fernandez-Serra, M.; Hribar-Lee, B.; Lukšič, M.; Dill, K. A., How Water's Properties Are Encoded in Its Molecular Structure and Energies. *Chem. Rev.* **2017**, *117* (19), 12385-12414.
- 32. Werner, J. E.; Swift, J. A., Organic solvates in the Cambridge Structural Database. *Crystengcomm* **2021**, *23* (7), 1555-1565.

- 33. Jurczak, E.; Mazurek, A. H.; Szeleszczuk, Ł.; Pisklak, D. M.; Zielińska-Pisklak, M., Pharmaceutical Hydrates Analysis—Overview of Methods and Recent Advances. *Pharmaceutics* **2020**, *12* (10), 959.
- 34. Bhatia, A.; Chopra, S.; Nagpal, K.; Deb, P. K.; Tekade, M.; Tekade, R. K., Chapter 2 Polymorphism and its Implications in Pharmaceutical Product Development. In *Dosage Form Design Parameters*, Tekade, R. K., Ed. Academic Press: 2018; pp 31-65.
- 35. Wöhler, F., Analyse einer thierischen Concretion. *Justus Liebigs Annalen der Chemie* **1844**, *51* (3), 437-439.
- 36. Childs, S. L.; Zaworotko, M. J., The Reemergence of Cocrystals: The Crystal Clear Writing Is on the WallIntroduction to Virtual Special Issue on Pharmaceutical Cocrystals. *Crystal Growth & Design* **2009**, 9 (10), 4208-4211.
- 37. Haruo, M.; Kenji, O.; Isamu, N., Crystal Structure of Quinhydrone, C12H10O4. *Bulletin of the Chemical Society of Japan* **1958**, *31* (5), 611-620.
- 38. Desiraju, G. R., Crystal and co-crystal. Crystengcomm 2003, 5 (82), 466-467.
- 39. Dunitz, J. D., Crystal and co-crystal: a second opinion. *Crystengcomm* **2003**, *5* (91), 506-506.
- 40. Etter, M. C., Encoding and decoding hydrogen-bond patterns of organic compounds. *Accounts Chem. Res.* **1990**, *23* (4), 120-126.
- 41. Etter, M. C.; Frankenbach, G. M., Hydrogen-bond directed cocrystallization as a tool for designing acentric organic solids. *Chemistry of Materials* **1989**, *1* (1), 10-12.
- 42. Etter, M. C., Hydrogen bonds as design elements in organic chemistry. *The Journal of Physical Chemistry* **1991,** 95 (12), 4601-4610.
- 43. Desiraju, G. R., *Crystal engineering : the design of organic solids*. Elsevier: Amsterdam; New York, 1989.
- 44. Desiraju, G. R., Supramolecular Synthons in Crystal Engineering—A New Organic Synthesis. *Angewandte Chemie International Edition in English* **1995**, *34* (21), 2311-2327.
- 45. USFDA Draft Guidance for Industry on Regulatory Classification of Pharmaceutical Co-Crystals.

https://www.federalregister.gov/documents/2011/12/02/2011-31022/draft-guidance-for-industry-on-regulatory-classification-of-pharmaceutical-co-crystals-availability.

- 46. USFDA Regulatory Classification of Pharmaceutical Co-Crystals Guidance for Industry. <a href="https://www.fda.gov/media/81824/download">https://www.fda.gov/media/81824/download</a>.
- 47. Yousef, M. A. E.; Vangala, V. R., Pharmaceutical Cocrystals: Molecules, Crystals, Formulations, Medicines. *Crystal Growth & Design* **2019**, *19* (12), 7420-7438.
- 48. Thipparaboina, R.; Kumar, D.; Mittapalli, S.; Balasubramanian, S.; Nangia, A.; Shastri, N. R., Ionic, Neutral, and Hybrid Acid-Base Crystalline Adducts of Lamotrigine with Improved Pharmaceutical Performance. *Crystal Growth & Design* **2015**, *15* (12), 5816-5826.
- 49. Sanphui, P.; Devi, V. K.; Clara, D.; Malviya, N.; Ganguly, S.; Desiraju, G. R., Cocrystals of Hydrochlorothiazide: Solubility and Diffusion/Permeability Enhancements through Drug-Coformer Interactions. *Mol Pharm* **2015**, *12* (5), 1615-22.
- 50. Karimi-Jafari, M.; Padrela, L.; Walker, G. M.; Croker, D. M., Creating Cocrystals: A Review of Pharmaceutical Cocrystal Preparation Routes and Applications. *Crystal Growth & Design* **2018**, *18* (10), 6370-6387.
- 51. Patil, A. O.; Curtin, D. Y.; Paul, I. C., Interconversion by hydrogen transfer of unsymmetrically substituted quinhydrones in the solid state. Crystal structure of the 1:2

- complex of 2,5-dimethylquinone with hydroquinone. *Journal of the American Chemical Society* **1984,** *10*6 (14), 4010-4015.
- 52. Baláž, P.; Achimovičová, M.; Baláž, M.; Billik, P.; Cherkezova-Zheleva, Z.; Criado, J. M.; Delogu, F.; Dutková, E.; Gaffet, E.; Gotor, F. J.; Kumar, R.; Mitov, I.; Rojac, T.; Senna, M.; Streletskii, A.; Wieczorek-Ciurowa, K., Hallmarks of mechanochemistry: from nanoparticles to technology. *Chem. Soc. Rev.* **2013**, *42* (18), 7571-7637.
- 53. Douroumis, D.; Ross, S. A.; Nokhodchi, A., Advanced methodologies for cocrystal synthesis. *Advanced Drug Delivery Reviews* **2017**, *117*, 178-195.
- 54. Basavoju, S.; Boström, D.; Velaga, S. P., Indomethacin–Saccharin Cocrystal: Design, Synthesis and Preliminary Pharmaceutical Characterization. *Pharm. Res.* **2008**, *25*, 530.
- 55. Childs, S. L.; Hardcastle, K. I., Cocrystals of Piroxicam with Carboxylic Acids. *Crystal Growth & Design* **2007**, *7*(7), 1291-1304.
- 56. Friščić, T.; Childs, S. L.; Rizvi, S. A. A.; Jones, W., The role of solvent in mechanochemical and sonochemical cocrystal formation: a solubility-based approach for predicting cocrystallisation outcome. *Crystengcomm* **2009**, *11* (3), 418-426.
- 57. Karki, S.; Friscic, T.; Jones, W., Control and interconversion of cocrystal stoichiometry in grinding: stepwise mechanism for the formation of a hydrogen-bonded cocrystal. *Crystengcomm* **2009**, *11* (3), 470-481.
- 58. Tan, D.; Loots, L.; Friščić, T., Towards medicinal mechanochemistry: evolution of milling from pharmaceutical solid form screening to the synthesis of active pharmaceutical ingredients (APIs). *Chemical Communications* **2016**, *52* (50), 7760-7781.
- 59. Fischer, F.; Scholz, G.; Benemann, S.; Rademann, K.; Emmerling, F., Evaluation of the formation pathways of cocrystal polymorphs in liquid-assisted syntheses. *Crystengcomm* **2014**, *16*, 8272-8278.
- 60. Riaz, M. N., Chapter 19 Food Extruders. In *Handbook of Farm, Dairy and Food Machinery Engineering (Third Edition)*, Kutz, M., Ed. Academic Press: 2019; pp 483-497.
- 61. Moradiya, H. G.; Islam, M. T.; Halsey, S.; Maniruzzaman, M.; Chowdhry, B. Z.; Snowden, M. J.; Douroumis, D., Continuous cocrystallisation of carbamazepine and trans-cinnamic acid via melt extrusion processing. *Crystengcomm* **2014**, *16* (17), 3573-3583.
- 62. Dhumal, R. S.; Kelly, A. L.; York, P.; Coates, P. D.; Paradkar, A., Cocrystalization and Simultaneous Agglomeration Using Hot Melt Extrusion. *Pharmaceutical Research* **2010**, *27* (12), 2725-2733.
- 63. Medina, C.; Daurio, D.; Nagapudi, K.; Alvarez-Nunez, F., Manufacture of pharmaceutical co-crystals using twin screw extrusion: A solvent-less and scalable process. *Journal of Pharmaceutical Sciences* **2010**, 99 (4), 1693-1696.
- 64. Pawar, N.; Saha, A.; Nandan, N.; Parambil, J. V. Solution Cocrystallization: A Scalable Approach for Cocrystal Production *Crystals* [Online], 2021.
- 65. Trampuž, M.; Teslić, D.; Likozar, B., Crystal-size distribution-based dynamic process modelling, optimization, and scaling for seeded batch cooling crystallization of Active Pharmaceutical Ingredients (API). *Chemical Engineering Research and Design* **2021**, *1*65, 254-269.
- 66. Li, Z.; Matzger, A. J., Influence of Coformer Stoichiometric Ratio on Pharmaceutical Cocrystal Dissolution: Three Cocrystals of Carbamazepine/4-Aminobenzoic Acid. *Molecular Pharmaceutics* **2016**, *13* (3), 990-995.

- 67. Pantwalawalkar, J.; More, H.; Bhange, D.; Patil, U.; Jadhav, N., Novel curcumin ascorbic acid cocrystal for improved solubility. *Journal of Drug Delivery Science and Technology* **2021**, 61, 102233.
- 68. Lin, X. Q.; Li, X.; Lin, X. B., A Review on Applications of Computational Methods in Drug Screening and Design. *Molecules* **2020**, *25* (6), 17.
- 69. Issa, N.; Karamertzanis, P. G.; Welch, G. W. A.; Price, S. L., Can the Formation of Pharmaceutical Cocrystals Be Computationally Predicted? I. Comparison of Lattice Energies. *Crystal Growth & Design* **2009**, 9 (1), 442-453.
- 70. Chan, H. C. S.; Kendrick, J.; Neumann, M. A.; Leusen, F. J. J., Towards ab initio screening of co-crystal formation through lattice energy calculations and crystal structure prediction of nicotinamide, isonicotinamide, picolinamide and paracetamol multi-component crystals. *Crystengcomm* **2013**, *15* (19), 3799-3807.
- 71. Abramov, Y. A.; Iuzzolino, L.; Jin, Y.; York, G.; Chen, C.-H.; Shultz, C. S.; Yang, Z.; Chang, C.; Shi, B.; Zhou, T.; Greenwell, C.; Sekharan, S.; Lee, A. Y., Cocrystal Synthesis through Crystal Structure Prediction. *Molecular Pharmaceutics* **2023**, *20* (7), 3380-3392.
- 72. Fábián, L., Cambridge Structural Database Analysis of Molecular Complementarity in Cocrystals. *Crystal Growth & Design* **2009**, 9 (3), 1436-1443.
- 73. Fábián, L.; Friščić, T., Shape and Polarity in Co-crystal Formation: Database Analysis and Experimental Validation. In *Pharmaceutical Salts and Co-crystals*, Wouters, J.; Quéré, L., Eds. The Royal Society of Chemistry: 2011; p 0.
- 74. Khalaji, M.; Potrzebowski, M. J.; Dudek, M. K., Virtual Cocrystal Screening Methods as Tools to Understand the Formation of Pharmaceutical Cocrystals—A Case Study of Linezolid, a Wide-Range Antibacterial Drug. *Crystal Growth & Design* **2021**, *21* (4), 2301-2314.
- 75. Majumder, M.; Buckton, G.; Rawlinson-Malone, C. F.; Williams, A. C.; Spillman, M. J.; Pidcock, E.; Shankland, K., Application of hydrogen-bond propensity calculations to an indomethacin–nicotinamide (1:1) co-crystal. *Crystengcomm* **2013**, *15* (20), 4041-4044.
- 76. Sarkar, N.; Gonnella, N. C.; Krawiec, M.; Xin, D.; Aakeröy, C. B., Evaluating the Predictive Abilities of Protocols Based on Hydrogen-Bond Propensity, Molecular Complementarity, and Hydrogen-Bond Energy for Cocrystal Screening. *Crystal Growth & Design* **2020**, *20* (11), 7320-7327.
- 77. O'Sullivan, A.; Spoletti, E.; Ross, S. A.; Lusi, M.; Douroumis, D.; Ryan, K. M.; Padrela, L., Screening, Synthesis, and Characterization of a More Rapidly Dissolving Celecoxib Crystal Form. *ACS Omega* **2024**, 9 (27), 29710-29722.
- 78. Racher, F.; Petrick, T. L.; Braun, D. E., Exploring the Supramolecular Interactions and Thermal Stability of Dapsone:Bipyridine Cocrystals by Combining Computational Chemistry with Experimentation. *Crystal Growth & Design* **2023**, *23* (6), 4638-4654.
- 79. Behler, J., Constructing high-dimensional neural network potentials: A tutorial review. *Int. J. Quantum Chem.* **2015**, *115* (16), 1032-1050.
- 80. Huang, G. B., What are Extreme Learning Machines? Filling the Gap Between Frank Rosenblatt's Dream and John von Neumann's Puzzle. *Cogn. Comput.* **2015**, *7* (3), 263-278.
- 81. Devogelaer, J.-J.; Meekes, H.; Tinnemans, P.; Vlieg, E.; de Gelder, R., Co-crystal Prediction by Artificial Neural Networks. *Angewandte Chemie International Edition* **2020**, 59 (48), 21711-21718.

- 82. Devogelaer, J.-J.; Charpentier, M. D.; Tijink, A.; Dupray, V.; Coquerel, G.; Johnston, K.; Meekes, H.; Tinnemans, P.; Vlieg, E.; ter Horst, J. H.; de Gelder, R., Cocrystals of Praziquantel: Discovery by Network-Based Link Prediction. *Crystal Growth & Design* **2021**, *21* (6), 3428-3437.
- 83. Krishna, G. R.; Ukrainczyk, M.; Zeglinski, J.; Rasmuson, A. C., Prediction of Solid State Properties of Cocrystals Using Artificial Neural Network Modeling. *Crystal Growth & Design* **2018**, *18* (1), 133-144.
- 84. Gamidi, R. K.; Rasmuson, Å. C., Analysis and Artificial Neural Network Prediction of Melting Properties and Ideal Mole fraction Solubility of Cocrystals. *Crystal Growth & Design* **2020**, *20* (9), 5745-5759.
- 85. Wicker, J. G. P.; Crowley, L. M.; Robshaw, O.; Little, E. J.; Stokes, S. P.; Cooper, R. I.; Lawrence, S. E., Will they co-crystallize? *Crystengcomm* **2017**, *19* (36), 5336-5340.
- 86. Strieth-Kalthoff, F.; Sandfort, F.; Segler, M. H. S.; Glorius, F., Machine learning the ropes: principles, applications and directions in synthetic chemistry. *Chem. Soc. Rev.* **2020**, *49* (17), 6154-6168.
- 87. Wang, D.; Yang, Z.; Zhu, B.; Mei, X.; Luo, X., Machine-learning-guided cocrystal prediction based on large data base. *Crystal Growth & Design* **2020**, *20* (10), 6610-6621.
- 88. Birolo, R.; Bravetti, F.; Alladio, E.; Priola, E.; Bianchini, G.; Novelli, R.; Aramini, A.; Gobetto, R.; Chierotti, M. R., Speeding Up the Cocrystallization Process: Machine Learning-Combined Methods for the Prediction of Multicomponent Systems. *Crystal Growth & Design* **2023**, *23* (11), 7898-7911.
- 89. Heng, T.; Yang, D.; Wang, R.; Zhang, L.; Lu, Y.; Du, G., Progress in Research on Artificial Intelligence Applied to Polymorphism and Cocrystal Prediction. *ACS Omega* **2021**, 6 (24), 15543-15550.
- 90. Martínez, M. J.; Razuc, M.; Ponzoni, I., MoDeSuS: A Machine Learning Tool for Selection of Molecular Descriptors in QSAR Studies Applied to Molecular Informatics. *Biomed Res Int* **2019**, *2019*, 2905203.
- 91. Arunan, E.; Desiraju, G. R.; Klein, R. A.; Sadlej, J.; Scheiner, S.; Alkorta, I.; Clary, D. C.; Crabtree, R. H.; Dannenberg, J. J.; Hobza, P.; Kjaergaard, H. G.; Legon, A. C.; Mennucci, B.; Nesbitt, D. J., Definition of the hydrogen bond (IUPAC Recommendations 2011). *Pure Appl. Chem.* **2011**, 83 (8), 1637-1641.
- 92. Kollman, P. A.; Allen, L. C., Theory of the hydrogen bond. *Chem. Rev.* **1972,** *72* (3), 283-303.
- 93. Bernstein, J.; Davis, R. E.; Shimoni, L.; Chang, N. L., PATTERNS IN HYDROGEN BONDING FUNCTIONALITY AND GRAPH SET ANALYSIS IN CRYSTALS. *Angew. Chem.-Int. Edit.* **1995**, *34* (15), 1555-1573.
- 94. Etter, M. C.; Macdonald, J. C.; Bernstein, J., GRAPH-SET ANALYSIS OF HYDROGEN-BOND PATTERNS IN ORGANIC-CRYSTALS. *Acta Crystallogr. Sect. B-Struct. Sci. Cryst. Eng. Mat.* **1990,** *4*6, 256-262.
- 95. Hamaguchi, W.; Masuda, N.; Miyamoto, S.; Shiina, Y.; Kikuchi, S.; Mihara, T.; Moriguchi, H.; Fushiki, H.; Murakami, Y.; Amano, Y.; Honbou, K.; Hattori, K., Synthesis, SAR study, and biological evaluation of novel quinoline derivatives as phosphodiesterase 10A inhibitors with reduced CYP3A4 inhibition. *Bioorg. Med. Chem.* **2015**, *23* (2), 297-313.
- 96. Kamlet, M. J.; Taft, R. W., The solvatochromic comparison method. I. The .beta.-scale of solvent hydrogen-bond acceptor (HBA) basicities. *Journal of the American Chemical Society* **1976**, 98 (2), 377-383.

- 97. Taft, R. W.; Gurka, D.; Joris, L.; Schleyer, P. v. R.; Rakshys, J. W., Studies of hydrogen-bonded complex formation with p-fluorophenol. V. Linear free energy relationships with OH reference acids. *Journal of the American Chemical Society* **1969**, 91 (17), 4801-4808.
- 98. Abraham, M. H., Scales of solute hydrogen-bonding: their construction and application to physicochemical and biochemical processes. *Chem. Soc. Rev.* **1993**, *22* (2), 73-83.
- 99. Abraham, M. H.; Duce, P. P.; Prior, D. V.; Barratt, D. G.; Morris, J. J.; Taylor, P. J., Hydrogen bonding. Part 9. Solute proton donor and proton acceptor scales for use in drug design. *Journal of the Chemical Society, Perkin Transactions 2* **1989**, (10), 1355-1375.
- 100. Perlovich, G. L.; Raevsky, O. A., Sublimation of Molecular Crystals: Prediction of Sublimation Functions on the Basis of HYBOT Physicochemical Descriptors and Structural Clusterization. *Crystal Growth & Design* **2010**, *10* (6), 2707-2712.
- 101. Jeffrey, G. A., An Introduction to Hydrogen bonding. Oxford University Press: 1997.
- 102. Steiner, T., The hydrogen bond in the solid state. *Angew. Chem.-Int. Edit.* **2002,** *41* (1), 48-76.
- 103. Aakeroy, C. B.; Beatty, A. M.; Helfrich, B. A., A high-yielding supramolecular reaction. *Journal of the American Chemical Society* **2002**, *124* (48), 14425-14432.
- 104. Alhalaweh, A.; George, S.; Basavoju, S.; Childs, S. L.; Rizvi, S. A. A.; Velaga, S. P., Pharmaceutical cocrystals of nitrofurantoin: screening, characterization and crystal structure analysis. *Crystengcomm* **2012**, *14* (15), 5078-5088.
- 105. Alvarez-Lorenzo, C.; Castineiras, A.; Frontera, A.; Garcia-Santos, I.; Gonzalez-Perez, J. M.; Niclos-Gutierrez, J.; Rodriguez-Gonzalez, I.; Vilchez-Rodriguez, E.; Zareba, J. K., Recurrent motifs in pharmaceutical cocrystals involving glycolic acid: X-ray characterization, Hirshfeld surface analysis and DFT calculations. *Crystengcomm* **2020**, *22* (40), 6674-6689.
- 106. Gohel, S. V.; Sanphui, P.; Singh, G. P.; Bhat, K.; Prakash, M., Lower melting pharmaceutical cocrystals of metaxalone with carboxamide functionalities. *Journal of Molecular Structure* **2019**, *1178*, 479-490.
- 107. Kumar, S.; Nanda, A., Pharmaceutical Cocrystals: An Overview. *Indian J. Pharm. Sci.* **2017**, *7*9 (6), 858-871.
- 108. Lee, K.; Kim, K.-J.; Ulrich, J., N-H···O, O-H···O hydrogen bonded supramolecular formation in the cocrystal of salicylic acid with N-containing bases. *Crystal Research and Technology* **2016**, *51* (3), 197-206.
- 109. Mir, N. A.; Dubey, R.; Desiraju, G. R., Strategy and Methodology in the Synthesis of Multicomponent Molecular Solids: The Quest for Higher Cocrystals. *Accounts Chem. Res.* **2019**, *52* (8), 2210-2220.
- 110. Qiao, N.; Li, M.; Schlindwein, W.; Malek, N.; Davies, A.; Trappitt, G., Pharmaceutical cocrystals: An overview. *International Journal of Pharmaceutics* **2011**, *419* (1), 1-11.
- 111. Saha, S.; Desiraju, G. R., Acid···Amide Supramolecular Synthon in Cocrystals: From Spectroscopic Detection to Property Engineering. *Journal of the American Chemical Society* **2018**, *140* (20), 6361-6373.
- 112. Shattock, T. R.; Arora, K. K.; Vishweshwar, P.; Zaworotko, M. J., Hierarchy of Supramolecular Synthons: Persistent Carboxylic Acid center dot center dot center dot Pyridine Hydrogen Bonds in Cocrystals That also Contain a Hydroxyl Moiety. *Crystal Growth & Design* **2008**, *8* (12), 4533-4545.

- 113. Shishkin, O. V.; Zubatyuk, R. I.; Shishkina, S. V.; Dyakonenko, V. V.; Medviediev, V. V., Role of supramolecular synthons in the formation of the supramolecular architecture of molecular crystals revisited from an energetic viewpoint. *Physical Chemistry Chemical Physics* **2014**, *16* (14), 6773-6786.
- 114. Vemuri, V. D.; Lankalapalli, S., Insight into Concept and Progress on Pharmaceutical Co-Crystals: An Overview. *Indian J. Pharm. Educ. Res.* **2019**, *53* (4), S522-S538.
- 115. Vishweshwar, P.; Nangia, A.; Lynch, V. M., Recurrence of Carboxylic Acid-Pyridine Supramolecular Synthon in the Crystal Structures of Some Pyrazinecarboxylic Acids. *The Journal of Organic Chemistry* **2002**, *67* (2), 556-565.
- 116. Shan, N.; Zaworotko, M. J., The role of cocrystals in pharmaceutical science. *Drug Discovery Today* **2008**, *13* (9), 440-446.
- 117. Harner, M. J.; Mueller, L.; Robbins, K. J.; Reily, M. D., NMR in drug design. *Archives of Biochemistry and Biophysics* **2017**, *628*, 132-147.
- 118. Duer, M. J., The Basics of Solid-State NMR. In *Solid-State NMR Spectroscopy Principles and Applications*, 2001; pp 1-72.
- 119. Harris, K. D. M.; Hughes, C. E.; Williams, A.; Edwards-Gau, G. R., 'NMR Crystallization': in-situ NMR techniques for time-resolved monitoring of crystallization processes. *Acta Crystallogr. Sect. C-Struct. Chem.* **2017**, *73*, 137-148.
- 120. Mattar, S. M.; Emwas, A. H.; Calhoun, L. A., Spectroscopic Studies of the Intermediates in the Conversion of 1,4,11,12-Tetrahydro-9,10-anthraquinone to 9,10-Anthraquinone by Reaction with Oxygen under Basic Conditions. *The Journal of Physical Chemistry A* **2004**, *108* (52), 11545-11553.
- 121. Resing, H. A. In *NMR Techniques for Chemical Kinetics in Adsorption Systems*, 1980.
- 122. D'agostino, C.; Mantle, M. D.; Gladden, L. F., In situ high-pressure 13C/1H NMR reaction studies of benzyl alcohol oxidation over a Pd/Al2O3 catalyst. *Reaction Chemistry and Engineering* **2020**, *5*, 1053-1057.
- 123. Hughes, C. E.; Harris, K. D. M., A Technique for In Situ Monitoring of Crystallization from Solution by Solid-State 13C CPMAS NMR Spectroscopy. *The Journal of Physical Chemistry A* **2008**, *112* (30), 6808-6810.
- 124. Hughes, C. E.; Williams, P. A.; Harris, K. D. M., "CLASSIC NMR": An In-Situ NMR Strategy for Mapping the Time-Evolution of Crystallization Processes by Combined Liquid-State and Solid-State Measurements. *Angewandte Chemie International Edition* **2014**, *53* (34), 8939-8943.
- 125. Hughes, C. E.; Ratnasingam, N. V.; Williams, P. A.; Benhenou, E.; Patterson, R.; Harris, K. D. M., NMR crystallization: in situ NMR strategies for monitoring the evolution of crystallization processes. *Faraday Discuss.* **2025**.
- 126. Kariuki, B. M.; Bauer, C. L.; Harris, K. D. M.; Teat, S., *J. Angew. Chem. Int. Ed.* **2000**, 39, 4485.
- 127. Hughes, C. E.; Williams, P. A.; Keast, V. L.; Charalampopoulos, V. G.; Edwards-Gau, G. R.; Harris, K. D. M., New in situ solid-state NMR techniques for probing the evolution of crystallization processes: pre-nucleation, nucleation and growth. *Faraday Discuss.* **2015**, *179*, 115-140.
- 128. Harris, K. D. M.; Hughes, C. E.; Williams, P. A., Monitoring the evolution of crystallization processes by in-situ solid-state NMR spectroscopy. *Solid State Nuclear Magnetic Resonance* **2015**, 65, 107-113.

- 129. Vyazovkin, S., Thermogravimetric Analysis. In *Characterization of Materials*, pp 1-12.
- 130. Lever, T.; Haines, P.; Rouquerol, J.; Charsley, E. L.; Eckeren, P. V.; Burlett, D. J., ICTAC nomenclature of thermal analysis (IUPAC Recommendations 2014). *Pure Appl. Chem.* **2014**, *86* (4), 545-553.
- 131. Coats, A. W.; Redfern, J. P., Thermogravimetric analysis. A review. *Analyst* **1963**, 88 (1053), 906-924.
- 132. Instruments, T. In *HIGH RESOLUTION THERMOGRAVIMETRIC ANALYSIS A NEW TECHNIQUE FOR OBTAINING SUPERIOR ANALYTICAL RESULTS*, Instruments, T., Ed. 1997.
- 133. Bottom, R., Thermogravimetric Analysis. In *Principles and Applications of Thermal Analysis*, 2008; pp 87-118.
- 134. Budrugeac, P.; Cucos, A.; Miu, L., The use of thermal analysis methods for authentication and conservation state determination of historical and/or cultural objects manufactured from leather. *Journal of Thermal Analysis and Calorimetry* **2011**, *104* (2), 439-450.
- 135. Hassid, A.; Klinger, M.; Krzack, S.; Cohen, H., TGA–DSC Combined Coal Analysis as a Tool for QC (Quality Control) and Reactivity Patterns of Coals. *ACS Omega* **2022**, *7* (2), 1893-1907.
- 136. Haines, P.; Reading, M.; Wilburn, F., Handbook of Thermal Analysis and Calorimetry. *Principles and Practice* **1998**, *1*, 279.
- 137. Danley, R. L., New heat flux DSC measurement technique. *Thermochimica acta* **2002**, 395 (1-2), 201-208.
- 138. Riga, A. T.; Collins, R. In *Differential Scanning Calorimetry and Differential Thermal Analysis*, 2006.
- 139. Adams, F., X-RAY ABSORPTION AND DIFFRACTION | Overview. In *Encyclopedia of Analytical Science (Second Edition)*, Worsfold, P.; Townshend, A.; Poole, C., Eds. Elsevier: Oxford, 2005; pp 365-377.
- 140. Duer, M. J., Essential Techniques for Spin-½ Nuclei. In *Solid-State NMR Spectroscopy Principles and Applications*, 2001; pp 73-110.
- 141. Duer, M. J., Dipolar Coupling: Its Measurement and Uses. In *Solid-State NMR Spectroscopy Principles and Applications*, 2001; pp 111-178.
- 142. Hore, P. J., Nuclear Magnetic Resonance. Oxford University Press: 2015.
- 143. Claridge, T. D. W., *High-Resolution NMR Techniques in Organic Chemistry*. Elsevier Science: 2009.
- 144. Keeler, J., Understanding NMR spectroscopy. Second edition ed.; John Wiley and Sons:

  Chichester,

  U.K.,

  2010.
- https://search.ebscohost.com/login.aspx?direct=true&scope=site&db=nlebk&db=nlabk&AN=587082.
- 145. Polenova, T.; Gupta, R.; Goldbourt, A., Magic Angle Spinning NMR Spectroscopy: A Versatile Technique for Structural and Dynamic Analysis of Solid-Phase Systems. *Analytical Chemistry* **2015**, *87* (11), 5458-5469.
- 146. Klinowski, J., NMR of Solids, Theory ★. In *Encyclopedia of Spectroscopy and Spectrometry (Third Edition)*, Lindon, J. C.; Tranter, G. E.; Koppenaal, D. W., Eds. Academic Press: Oxford, 2017; pp 175-180.

- 147. Nishiyama, Y.; Hou, G.; Agarwal, V.; Su, Y.; Ramamoorthy, A., Ultrafast Magic Angle Spinning Solid-State NMR Spectroscopy: Advances in Methodology and Applications. *Chem. Rev.* **2023**, *123* (3), 918-988.
- 148. Samoson, A., H-MAS. *Journal of Magnetic Resonance* **2019**, 306, 167-172.
- 149. Liang, L.; Ji, Y.; Chen, K.; Gao, P.; Zhao, Z.; Hou, G., Solid-State NMR Dipolar and Chemical Shift Anisotropy Recoupling Techniques for Structural and Dynamical Studies in Biological Systems. *Chem. Rev.* **2022**, *122* (10), 9880-9942.
- 150. Hartmann, S. R.; Hahn, E. L., Nuclear Double Resonance in the Rotating Frame. *Physical Review* **1962**, *128* (5), 2042-2053.
- 151. Comellas, G.; Lopez, J. J.; Nieuwkoop, A. J.; Lemkau, L. R.; Rienstra, C. M., Straightforward, effective calibration of SPINAL-64 decoupling results in the enhancement of sensitivity and resolution of biomolecular solid-state NMR. *Journal of Magnetic Resonance* **2011**, *209* (2), 131-135.
- 152. Hughes, C. E.; Williams, P. A.; Peskett, T. R.; Harris, K. D., Exploiting In Situ Solid-State NMR for the Discovery of New Polymorphs during Crystallization Processes. *J Phys Chem Lett* **2012**, *3* (21), 3176-81.
- 153. Morris, G. A.; Freeman, R., Enhancement of nuclear magnetic resonance signals by polarization transfer. *Journal of the American Chemical Society* **1979**, *101* (3), 760-762.
- 154. Morris, G. A., Sensitivity enhancement in nitrogen-15 NMR: polarization transfer using the INEPT pulse sequence. *Journal of the American Chemical Society* **1980**, *102* (1), 428-429.
- 155. Kumar, A.; Christy Rani Grace, R., Nuclear Overhauser Effect. In *Encyclopedia of Spectroscopy and Spectrometry*, Lindon, J. C., Ed. Elsevier: Oxford, 1999; pp 1643-1653.
- 156. Haouas, M.; Falaise, C.; Leclerc, N.; Floquet, S.; Cadot, E., NMR spectroscopy to study cyclodextrin-based host–guest assemblies with polynuclear clusters. *Dalton Transactions* **2023**, *52* (38), 13467-13481.
- 157. Thakare, R.; Kaul, G.; Shukla, M.; Kesharwani, P.; Srinivas, N.; Dasgupta, A.; Chopra, S., Chapter 5 Repurposing nonantibiotic drugs as antibacterials. In *Drug Discovery Targeting Drug-Resistant Bacteria*, Kesharwani, P.; Chopra, S.; Dasgupta, A., Eds. Academic Press: 2020; pp 105-138.
- 158. Kansara, K.; Sen Gupta, S., Chapter Fourteen DNA Damage, Repair, and Maintenance of Telomere Length: Role of Nutritional Supplements. In *Mutagenicity: Assays and Applications*, Kumar, A.; Dobrovolsky, V. N.; Dhawan, A.; Shanker, R., Eds. Academic Press: 2018; pp 287-307.
- 159. Harrison, I. F.; Dexter, D. T., Epigenetic targeting of histone deacetylase: Therapeutic potential in Parkinson's disease? *Pharmacology & Therapeutics* **2013**, *140* (1), 34-52.
- 160. Lim, L. Y.; Go, M. L., Caffeine and nicotinamide enhances the aqueous solubility of the antimalarial agent halofantrine. *European Journal of Pharmaceutical Sciences* **2000**, *10* (1), 17-28.
- 161. Suzuki, H.; Sunada, H., Mechanistic studies on hydrotropic solubilization of nifedipine in nicotinamide solution. *Chemical & Pharmaceutical Bulletin* **1998**, *4*6 (1), 125-130.
- 162. Maheshwari, R. K.; Rathore, A.; Agrawal, A.; Gupta, M. A., New spectrophotometric estimation of indomethacin capsules with niacinamide as hydrotropic solubilizing agent. *Pharmaceutical Methods* **2011**, *2* (3), 184-188.

- 163. SCOGS, F. a. Generally Recognised As Safe. <a href="https://www.fda.gov/food/food-ingredients-packaging/generally-recognized-safe-gras">https://www.cfsanappsexternal.fda.gov/</a> (accessed 7/05/2021).
- 164. He, G.; Jacob, C.; Guo, L.; Chow, P. S.; Tan, R. B. H., Screening for Cocrystallization Tendency: The Role of Intermolecular Interactions. *The Journal of Physical Chemistry B* **2008**, *112* (32), 9890-9895.
- 165. BáThori, N. B.; Lemmerer, A.; Venter, G. A.; Bourne, S. A.; Caira, M. R., Pharmaceutical Co-crystals with Isonicotinamide—Vitamin B3, Clofibric Acid, and Diclofenac—and Two Isonicotinamide Hydrates. *Crystal Growth & Design* **2011**, *11* (1), 75-87.
- 166. Lemmerer, A.; Bernstein, J., The co-crystal of two GRAS substances: (citric acid)center dot(nicotinamide). Formation of four hydrogen bonding heterosynthons in one co-crystal. *Crystengcomm* **2010**, *12* (7), 2029-2033.
- 167. Huang, C.-M.; Leiserowitz, L.; Schmidt, G. M. J., Molecular packing modes. Part XI. Crystal structures of the 2:1 complexes of benzamide with succinic acid and furamide with oxalic acid. *Journal of the Chemical Society, Perkin Transactions 2* **1973**, (5), 503-508.
- 168. VidenovaAdrabinska, V.; Etter, M. C., Urea-glutaric acid (2:1) structural aggregates as building blocks for crystal engineering. *Journal of Chemical Crystallography* **1995**, *25* (12), 823-829.
- 169. Edwards, M. R.; Jones, W.; Motherwell, W. D. S., Cocrystal formation of 4-methyl and 4-chlorobenzamide with carboxylic acids: Chloro/methyl interchange and crystal structure. *Crystengcomm* **2006**, *8* (7), 545-551.
- 170. Chan, H. C. S.; Woollam, G. R.; Wagner, T.; Schmidt, M. U.; Lewis, R. A., Can picolinamide be a promising cocrystal former? *Crystengcomm* **2014**, *16* (21), 4365-4368.
- 171. Sarmah, K. K.; Boro, K.; Arhangelskis, M.; Thakuria, R., Crystal structure landscape of ethenzamide: a physicochemical property study. *Crystengcomm* **2017**, *19* (5), 826-833.
- 172. Steiner, T., Competition of hydrogen-bond acceptors for the strong carboxyl donor. *Acta Crystallogr. Sect. B-Struct. Sci.* **2001,** *57*, 103-106.
- 173. Kaur, R.; Guru Row, T. N., Polymorphic Anhydrous Cocrystals of Gallic Acid and Acetamide from Methanol: Pointers toward a Stable Cocrystal Form. *Crystal Growth & Design* **2012**, *12* (6), 2744-2747.
- 174. Dwyer, D. S.; Bradley, R. J., Chemical properties of alcohols and their protein binding sites. *Cell. Mol. Life Sci.* **2000**, *57* (2), 265-275.
- 175. Lemmerer, A.; Adsmond, D. A.; Esterhuysen, C.; Bernstein, J., Polymorphic Cocrystals from Polymorphic Co-crystal Formers: Competition between Carboxylic Acid···Pyridine and Phenol···Pyridine Hydrogen Bonds. *Crystal Growth & Design* **2013**, *13* (9), 3935-3952.
- 176. Jiang, Y.; Yang, Z.; Guo, J.; Li, H.; Liu, Y.; Guo, Y.; Li, M.; Pu, X., Coupling complementary strategy to flexible graph neural network for quick discovery of coformer in diverse co-crystal materials. *Nat. Commun.* **2021**, *12* (1), 5950.
- 177. Glick, M.; Klon, A. E.; Acklin, P.; Davies, J. W., Enrichment of Extremely Noisy High-Throughput Screening Data Using a Naïve Bayes Classifier. *Journal of Biomolecular Screening* **2004**, 9 (1), 32-36.

- 178. Yang, D.; Wang, L.; Yuan, P.; An, Q.; Su, B.; Yu, M.; Chen, T.; Hu, K.; Zhang, L.; Lu, Y.; Du, G., Cocrystal virtual screening based on the XGBoost machine learning model. *Chinese Chemical Letters* **2023**, *34* (8), 107964.
- 179. Delen, D.; Helfrich, S.; Silipo, R., KNIME Analytics Platform for Visual Data Science and Business Analytics Teaching. In *Proceedings of the 52nd ACM Technical Symposium on Computer Science Education*, Association for Computing Machinery: Virtual Event, USA, 2021; p 1373.
- 180. Butler, K. T.; Davies, D. W.; Cartwright, H.; Isayev, O.; Walsh, A., Machine learning for molecular and materials science. *Nature* **2018**, *559* (7715), 547-555.
- 181. Weininger, D., SMILES, a chemical language and information system. 1. Introduction to methodology and encoding rules. *Journal of Chemical Information and Computer Sciences* **1988**, *28* (1), 31-36.
- 182. <a href="https://www.rdkit.org">https://www.rdkit.org</a>.
- 183. Wicker, J. G. P.; Cooper, R. I., Will it crystallise? Predicting crystallinity of molecular materials. *Crystengcomm* **2015**, *17* (9), 1927-1934.
- 184. Mswahili, M. E.; Lee, M.-J.; Martin, G. L.; Kim, J.; Kim, P.; Choi, G. J.; Jeong, Y.-S., Cocrystal Prediction Using Machine Learning Models and Descriptors. *Applied Sciences* **2021**, *11* (3), 1323.
- 185. Tsangaratos, P.; Ilia, I., Comparison of a logistic regression and Naïve Bayes classifier in landslide susceptibility assessments: The influence of models complexity and training dataset size. *CATENA* **2016**, *145*, 164-179.
- 186. Yarava, J. R.; Potnuru, L. R.; Pahari, B.; Tothadi, S.; Ramanathan, K. V., Supramolecular Synthon Identification in Azelaic Acid Isonicotinamide. *Journal of Magnetic Resonance Open* **2022**, *10-11*, 100056.
- 187. Bojarska, J.; Remko, M.; Breza, M.; Madura, I. D.; Kaczmarek, K.; Zabrocki, J.; Wolf, W. M., A Supramolecular Approach to Structure-Based Design with A Focus on Synthons Hierarchy in Ornithine-Derived Ligands: Review, Synthesis, Experimental and in Silico Studies. *Molecules* **2020**, *25* (5).
- 188. Schultheiss, N.; Newman, A., Pharmaceutical Cocrystals and Their Physicochemical Properties. *Cryst Growth Des* **2009**, 9 (6), 2950-2967.
- 189. Vishweshwar, P.; McMahon, J. A.; Peterson, M. L.; Hickey, M. B.; Shattock, T. R.; Zaworotko, M. J., *Chem. Commun.* **2005**, 4601.
- 190. Amombo Noa, F. M.; Mehlana, G., Co-crystals and salts of vanillic acid and vanillin with amines. *Crystengcomm* **2018**, *20* (7), 896-905.
- 191. Evtushenko, D. N.; Arkhipov, S. G.; Fateev, A.; Izaak, T. I.; Egorova, L. A.; Skorik, N. A.; Vodyankina, O. V.; Boldyreva, E., A cocrystal of L-ascorbic acid with picolinic acid: the role of O-H•••O, N-H•••O and C-H•••O hydrogen bonds and L-ascorbic acid conformation in structure stabilization. *Acta Crystallogr. Sect. B-Struct. Sci. Cryst. Eng. Mat.* **2020**, *76*, 967-978.
- 192. Wang, J.-R.; Bao, J.; Fan, X.; Dai, W.; Mei, X., pH-Switchable vitamin B9 gels for stoichiometry-controlled spherical co-crystallization. *Chemical Communications* **2016**, *52* (92), 13452-13455.
- 193. Bag, P. P.; Patni, M.; Malla Reddy, C., A kinetically controlled crystallization process for identifying new co-crystal forms: fast evaporation of solvent from solutions to dryness. *Crystengcomm* **2011**, *13* (19), 5650-5652.
- 194. Stolar, T.; Lukin, S.; Tireli, M.; Sović, I.; Karadeniz, B.; Kereković, I.; Matijašić, G.; Gretić, M.; Katančić, Z.; Dejanović, I.; Michiel, M. d.; Halasz, I.; Užarević, K., Control

- of Pharmaceutical Cocrystal Polymorphism on Various Scales by Mechanochemistry: Transfer from the Laboratory Batch to the Large-Scale Extrusion Processing. *ACS Sustainable Chemistry & Engineering* **2019**, *7* (7), 7102-7110.
- 195. Sharma, N.; Tiwari, N.; Vyas, M.; Khurana, N.; Muthuraman, A.; Utreja, P., An overview of therapeutic effects of vanillic acid. *Plant Arch* **2020**, *20* (2), 3053-3059.
- 196. Taqvi, S.; Bhat, E. A.; Sajjad, N.; Sabir, J. S.; Qureshi, A.; Rather, I. A.; Rehman, S., Protective effect of vanillic acid in hydrogen peroxide-induced oxidative stress in D. Mel-2 cell line. *Saudi Journal of Biological Sciences* **2021**, *28* (3), 1795-1800.
- 197. Ingole, A.; Kadam, M. P.; Dalu, A. P.; Kute, S. M.; Mange, P. R.; Theng, V. D.; Lahane, O. R.; Nikas, A. P.; Kawal, Y. V.; Nagrik, S. U., A review of the pharmacological characteristics of vanillic acid. *Journal of Drug Delivery and Therapeutics* **2021**, *11* (2-S), 200-204.
- 198. Aitipamula, S.; Wong, A. B. H.; Chow, P. S.; Tan, R. B. H., Pharmaceutical cocrystals of ethenzamide: structural, solubility and dissolution studies. *Crystengcomm* **2012**, *14* (24), 8515-8524.
- 199. Adalder, T. K.; Sankolli, R.; Dastidar, P., Homo- or Heterosynthon? A Crystallographic Study on a Series of New Cocrystals Derived from Pyrazinecarboxamide and Various Carboxylic Acids Equipped with Additional Hydrogen Bonding Sites. *Crystal Growth & Design* **2012**, *12* (5), 2533-2542.
- 200. Fang, Z. Q.; Zeng, R. H.; Yang, M.; Liu, H.; Chen, X. L., 2-Hydr-oxy-3-methoxy-benzoic acid monohydrate. *Acta Crystallogr Sect E Struct Rep Online* **2008**, *64* (Pt 4), o691.
- 201. Excellence, N. I. f. H. a. C., BNF (2024). British National Formulary 2024.
- 202. Agafonov, M.; Garibyan, A.; Terekhova, I., Improving pharmacologically relevant properties of sulfasalazine loaded in γ-cyclodextrin-based metal organic framework. *Journal of Industrial and Engineering Chemistry* **2022**, *106*, 189-197.
- 203. Peppercorn, M. A., Sulfasalazine. Pharmacology, clinical use, toxicity, and related new drug development. *Ann Intern Med* **1984**, *101* (3), 377-86.
- 204. Collins, P.; Rhodes, J., Ulcerative colitis: diagnosis and management. *Bmj* **2006**, 333 (7563), 340-3.
- 205. Fralish, Z.; Chen, A.; Khan, S.; Zhou, P.; Reker, D., The landscape of small-molecule prodrugs. *Nature Reviews Drug Discovery* **2024**, *23* (5), 365-380.
- 206. Plosker, G. L.; Croom, K. F., Sulfasalazine. *Drugs* **2005**, 65 (13), 1825-1849.
- 207. Adsmond, D. A.; Grant, D. J. W., Hydrogen bonding in sulfonamides. *Journal of Pharmaceutical Sciences* **2001**, *90* (12), 2058-2077.
- 208. Elguero, J., Polymorphism and Desmotropy in Heterocyclic Crystal Structures. *Crystal Growth & Design* **2011**, *11* (11), 4731-4738.
- 209. Huang, S.; Cheemarla, V. K. R.; Tiana, D.; Lawrence, S. E., Exploring the Crystal Structure Landscape of Sulfasalazine through Various Multicomponent Crystals. *Crystal Growth & Design* **2023**, *23* (8), 5446-5461.
- 210. Elbakush, R. E., A crystal engineering study of selected sulfa drugs and trimethoprim. **2014**.
- 211. Tedesco, E.; Giron, D.; Pfeffer, S., Crystal structure elucidation and morphology study of pharmaceuticals in development. *Crystengcomm* **2002**, *4* (67), 393-400.
- 212. Huang, Y.; Kuminek, G.; Roy, L.; Cavanagh, K. L.; Yin, Q.; Rodríguez-Hornedo, N., Cocrystal Solubility Advantage Diagrams as a Means to Control Dissolution, Supersaturation, and Precipitation. *Molecular Pharmaceutics* **2019**, *16* (9), 3887-3895.

- 213. Pan, X.; Zheng, Y.; Chen, R.; Qiu, S.; Chen, Z.; Rao, W.; Chen, S.; You, Y.; Lü, J.; Xu, L.; Guan, X., Cocrystal of Sulfamethazine and p-Aminobenzoic Acid: Structural Establishment and Enhanced Antibacterial Properties. *Crystal Growth & Design* **2019**, *19* (4), 2455-2460.
- 214. Carney, T. J.; Collins, S. J.; Moore, J. S.; Brushett, F. R., Concentration-Dependent Dimerization of Anthraquinone Disulfonic Acid and Its Impact on Charge Storage. *Chemistry of Materials* **2017**, *29* (11), 4801-4810.
- 215. Fielding, L., NMR methods for the determination of protein-ligand dissociation constants. *Curr Top Med Chem* **2003**, *3* (1), 39-53.
- 216. Guo, M.; Wang, K.; Qiao, N.; Yardley, V.; Li, M., Investigating Permeation Behavior of Flufenamic Acid Cocrystals Using a Dissolution and Permeation System. *Molecular Pharmaceutics* **2018**, *15* (9), 4257-4272.
- 217. Evans, R.; Deng, Z.; Rogerson, A. K.; McLachlan, A. S.; Richards, J. J.; Nilsson, M.; Morris, G. A., Quantitative Interpretation of Diffusion-Ordered NMR Spectra: Can We Rationalize Small Molecule Diffusion Coefficients? *Angewandte Chemie International Edition* **2013**, *52* (11), 3199-3202.
- 218. Kuminek, G.; Cao, F.; Bahia de Oliveira da Rocha, A.; Gonçalves Cardoso, S.; Rodríguez-Hornedo, N., Cocrystals to facilitate delivery of poorly soluble compounds beyond-rule-of-5. *Advanced Drug Delivery Reviews* **2016**, *101*, 143-166.
- 219. Cogo Machado, T.; Kavanagh, O. N.; Gonçalves Cardoso, S.; Rodríguez-Hornedo, N., Synchronization of Cocrystal Dissolution and Drug Precipitation to Sustain Drug Supersaturation. *Molecular Pharmaceutics* **2022**, *19* (8), 2765-2775.
- 220. Jadrijević-Mladar Takac, M.; Vikić Topić, D., FT-IR and NMR spectroscopic studies of salicylic acid derivatives. II. Comparison of 2-hydroxy- and 2,4- and 2,5-dihydroxy derivatives. *Acta Pharm* **2004**, *54* (3), 177-91.
- 221. Singha, N. C.; Sathyanarayana, D. N., 1H and 13C NMR spectral studies of conformation of some N-(2-pyridinyl)-3-pyridinecarboxamides. *Journal of Molecular Structure* **1998**, *449* (1), 91-98.
- 222. Abraham, R. J.; Mobli, M., Modelling1H NMR Spectra of Organic Compounds. **2008**.
- 223. Madison Metabolomics Consortium Qiu Cui, I. L., Francisca Jofre, Mark E. Anderson, John L. Markley, 3-hydroxybenzoic acid (C7H6O3). **Last updated 4th December 2020**.
- 224. Charisiadis, P.; Kontogianni, V. G.; Tsiafoulis, C. G.; Tzakos, A. G.; Siskos, M.; Gerothanassis, I. P., 1H-NMR as a structural and analytical tool of intra- and intermolecular hydrogen bonds of phenol-containing natural products and model compounds. *Molecules* **2014**, *19* (9), 13643-82.
- 225. Gołdyn, M.; Larowska, D.; Nowak, W.; Bartoszak-Adamska, E., Theobromine cocrystals with monohydroxybenzoic acids synthesis, X-ray structural analysis, solubility and thermal properties. *Crystengcomm* **2019**, *21* (38), 5721-5732.
- 226. Lvov, A. G.; Kavun, A. M.; Kachala, V. V.; Nelyubina, Y. V.; Metelitsa, A. V.; Shirinian, V. Z., Structural and Spectral Properties of Photochromic Diarylethenes: Size Effect of the Ethene Bridge. *The Journal of Organic Chemistry* **2017**, *82* (3), 1477-1486.
- 227. Sutter, K.; Aucar, G. A.; Autschbach, J., Analysis of Proton NMR in Hydrogen Bonds in Terms of Lone-Pair and Bond Orbital Contributions. *Chemistry A European Journal* **2015**, *21* (50), 18138-18155.

- 228. Hansen, P. E.; Spanget-Larsen, J., NMR and IR Investigations of Strong Intramolecular Hydrogen Bonds. *Molecules* **2017**, *22* (4).
- 229. Hansen, P. E., A Spectroscopic Overview of Intramolecular Hydrogen Bonds of NH...O,S,N Type. *Molecules* **2021**, *26* (9).
- 230. Leskowitz, G. M.; Ghaderi, N.; Olsen, R. A.; Pederson, K.; Hatcher, M. E.; Mueller, L. J., The Amide Rotational Barrier in Isonicotinamide: Dynamic NMR and Ab Initio Studies. *The Journal of Physical Chemistry A* **2005**, *109* (6), 1152-1158.
- 231. Lewin, A. H.; Frucht, M.; Chen, K. V. J.; Benedetti, E.; Di Blasio, B., Restricted rotation in amides—VI: Configurations and conformations of unsymmetrical tertiary benzamides. *Tetrahedron* **1975**, *31* (3), 207-215.
- 232. Olsen, R. A.; Liu, L.; Ghaderi, N.; Johns, A.; Hatcher, M. E.; Mueller, L. J., The Amide Rotational Barriers in Picolinamide and Nicotinamide: NMR and ab Initio Studies. *Journal of the American Chemical Society* **2003**, *125* (33), 10125-10132.
- 233. Szczepura, L. F.; Eilts, K. K.; Hermetet, A. K.; Ackerman, L. J.; Swearingen, J. K.; West, D. X., Structural and spectral studies of N-(2-pyridyl)-N'-(4-substituted phenyl)thioureas. *Journal of Molecular Structure* **2002**, 607 (2), 101-110.
- 234. Charman, W. N.; Lai, C. S.; Finnin, B. C.; Reed, B. L., Self-association of nicotinamide in aqueous solution: mass transport, freezing-point depression, and partition coefficient studies. *Pharm Res* **1991**, *8* (9), 1144-50.
- 235. Lin, C.; Skufca, J.; Partch, R. E., New insights into prediction of weak  $\pi$ – $\pi$  complex association through proton-nuclear magnetic resonance analysis. *BMC Chemistry* **2020**, *14* (1), 66.
- 236. Zarycz, M. N. C.; Fonseca Guerra, C., NMR 1H-Shielding Constants of Hydrogen-Bond Donor Reflect Manifestation of the Pauli Principle. *The Journal of Physical Chemistry Letters* **2018**, 9 (13), 3720-3724.
- 237. Xu, L.; Zhang, A.; Lu, Y.; Yang, H.; Liu, Z., A phenanthroline-derived ligand and its complexation with Pd(ii): from ligand design, synthesis and Pd(ii) complexes structures to its application. *RSC Advances* **2016**, 6 (102), 99859-99866.
- 238. Fielding, L., Determination of Association Constants (Ka) from Solution NMR Data. *Tetrahedron* **2000**, *56* (34), 6151-6170.
- 239. Berry, D. J.; Seaton, C. C.; Clegg, W.; Harrington, R. W.; Coles, S. J.; Horton, P. N.; Hursthouse, M. B.; Storey, R.; Jones, W.; Friščić, T.; Blagden, N., Applying Hot-Stage Microscopy to Co-Crystal Screening: A Study of Nicotinamide with Seven Active Pharmaceutical Ingredients. *Crystal Growth & Design* **2008**, 8 (5), 1697-1712.
- 240. Lengvinaitė, D.; Aidas, K.; Kimtys, L., Molecular aggregation in liquid acetic acid: insight from molecular dynamics/quantum mechanics modelling of structural and NMR properties. *Physical Chemistry Chemical Physics* **2019**, *21* (27), 14811-14820.
- 241. Carlisle, E. A.; Holder, J. L.; Maranda, A. M.; de Alwis, A. R.; Selkie, E. L.; McKay, S. L., Effect of pH, urea, peptide length, and neighboring amino acids on alanine  $\alpha$ -proton random coil chemical shifts. *Biopolymers* **2007**, *85* (1), 72-80.
- 242. Pham, T. N.; Masiero, S.; Gottarelli, G.; Brown, S. P., Identification by 15N Refocused INADEQUATE MAS NMR of Intermolecular Hydrogen Bonding that Directs the Self-Assembly of Modified DNA Bases. *Journal of the American Chemical Society* **2005**, *127* (46), 16018-16019.
- 243. Lamm, J. H.; Niermeier, P.; Mix, A.; Chmiel, J.; Neumann, B.; Stammler, H. G.; Mitzel, N. W., Mechanism of host-guest complex formation and identification of

- intermediates through NMR titration and diffusion NMR spectroscopy. *Angew Chem Int Ed Engl* **2014**, *53* (30), 7938-42.
- 244. Marion, D.; Garbay-Jaureguiberry, C.; Roques, B. P., Use of the INEPT [Insensitive Nuclei Enhanced by Polarization Transfer] polarization transfer method for nitrogen-15 NMR relaxation study of linear peptides. *Journal of the American Chemical Society* **1982**, *104* (21), 5573-5576.
- 245. Alcicek, S.; Van Dyke, E.; Xu, J.; Pustelny, S.; Barskiy, D. A., 13C and 15N Benchtop NMR Detection of Metabolites via Relayed Hyperpolarization. *Chemistry–Methods* **2023**, *3* (7), e202200075.
- 246. Dega-Szafran, Z.; Szafran, M.; Stefaniak, L.; Brevard, C.; Bourdonneau, M., Nitrogen-15 nuclear magnetic resonance studies of hydrogen bonding and proton transfer in some pyridine trifluoroacetates in dichloromethane. *Magn. Reson. Chem.* **1986**, *24* (5), 424-427.
- 247. CRC Handbook of Chemistry and Physics, 57th Edition. *Soil Science Society of America Journal* **1977**, *41* (4), vi-vi.
- 248. Kiliç, E.; Köseogğlu, F.; Başgut, Ö., Protonation constants of some pyridine derivatives in ethanol-water mixtures. *Analytica Chimica Acta* **1994**, *294* (2), 215-220.
- 249. Catrouillet, S.; Fonteneau, C.; Bouteiller, L.; Delorme, N.; Nicol, E.; Nicolai, T.; Pensec, S.; Colombani, O., Competition Between Steric Hindrance and Hydrogen Bonding in the Formation of Supramolecular Bottle Brush Polymers. *Macromolecules* **2013**, *46* (19), 7911-7919.
- 250. Claridge, T. D. W., Chapter 9 Correlations Through Space: The Nuclear Overhauser Effect. In *High-Resolution NMR Techniques in Organic Chemistry (Third Edition)*, Claridge, T. D. W., Ed. Elsevier: Boston, 2016; pp 315-380.
- 251. Bax, A.; Grzesiek, S., Methodological advances in protein NMR. *Accounts Chem. Res.* **1993**, *26* (4), 131-138.
- 252. Denkova, P. S.; Van Lokeren, L.; Willem, R., Mixed Micelles of Triton X-100, Sodium Dodecyl Dioxyethylene Sulfate, and Synperonic L61 Investigated by NOESY and Diffusion Ordered NMR Spectroscopy. *The Journal of Physical Chemistry B* **2009**, *113* (19), 6703-6709.
- 253. Qin, X.; Liu, M.; Yang, D.; Zhang, X., Concentration-Dependent Aggregation of CHAPS Investigated by NMR Spectroscopy. *The Journal of Physical Chemistry B* **2010**, *114* (11), 3863-3868.
- 254. Gschwind, R. M.; Xie, X.; Rajamohanan, P. R., Gs-HSQC-NOESY versus gs-NOESY-HSQC experiments: signal attenuation due to diffusion; application to symmetrical molecules. *Magn. Reson. Chem.* **2004**, *42* (3), 308-312.
- 255. Krishnan, V. V.; Vazquez, S.; Maitra, K.; Maitra, S., Restricted amide rotation with steric hindrance induced multiple conformations. *Chemical Physics Letters* **2017**, 689, 148-151.
- 256. Ueda, K.; Higashi, K.; Moribe, K., Quantitative Analysis of Drug Supersaturation Region by Temperature-Variable Nuclear Magnetic Resonance Measurements, Part 2: Effects of Solubilizer. *Molecular Pharmaceutics* **2023**, *20* (4), 1872-1883.
- 257. Tomlinson, J. H.; Williamson, M. P., Amide temperature coefficients in the protein G B1 domain. *J Biomol NMR* **2012**, *52* (1), 57-64.
- 258. Trainor, K.; Palumbo, J. A.; MacKenzie, D. W. S.; Meiering, E. M., Temperature dependence of NMR chemical shifts: Tracking and statistical analysis. *Protein Sci* **2020**, *29* (1), 306-314.

- 259. Trask, A. V.; Motherwell, W. D. S.; Jones, W., Solvent-drop grinding: green polymorph control of cocrystallisation. *Chemical Communications* **2004**, (7), 890-891. 260. Good, D. J.; Rodríguez-Hornedo, N., Solubility Advantage of Pharmaceutical
- 261. Rehder, S.; Klukkert, M.; Löbmann, K. A. M.; Strachan, C. J.; Sakmann, A.; Gordon, K.; Rades, T.; Leopold, C. S. Investigation of the Formation Process of Two Piracetam Cocrystals during Grinding *Pharmaceutics* [Online], 2011, p. 706-722.

Cocrystals. Cryst. Growth Des. 2009, 9, 2252.

- 262. Trask, A. V.; Jones, W., Crystal Engineering of Organic Cocrystals by the Solid-State Grinding Approach. In *Organic Solid State Reactions: -/-*, Toda, F., Ed. Springer Berlin Heidelberg: Berlin, Heidelberg, 2005; pp 41-70.
- 263. Dudek, M. K.; Trzeciak, K.; Tajber, L.; Zając, J.; Kaźmierski, S.; Pindelska, E.; Makowski, T.; Svyntkivska, M.; Potrzebowski, M. J., A New Look at the Mechanism of Cocrystal Formation and Coformers Exchange in Processes Forced by Mechanical and/or Thermal Stimuli ex situ and in situ Studies of Low-Melting Eutectic Mixtures. *Chemistry A European Journal* **2024**, *30* (11), e202302138.
- 264. Kulla, H.; Greiser, S.; Benemann, S.; Rademann, K.; Emmerling, F., In Situ Investigation of a Self-Accelerated Cocrystal Formation by Grinding Pyrazinamide with Oxalic Acid. *Molecules* **2016**, *21* (7), 917.
- 265. Friščić, T.; Halasz, I.; Beldon, P. J.; Belenguer, A. M.; Adams, F.; Kimber, S. A. J.; Honkimäki, V.; Dinnebier, R. E., Real-time and in situ monitoring of mechanochemical milling reactions. *Nature Chemistry* **2013**, *5* (1), 66-73.
- 266. Trask, A. V.; Motherwell, W. D. S.; Jones, W., Pharmaceutical Cocrystallization: Engineering a Remedy for Caffeine Hydration. *Cryst. Growth Des.* **2005,** *5* (3), 1013.
- 267. Shan, N.; Toda, F.; Jones, W., Mechanochemistry and co-crystal formation: Effect of solvent on reaction kinetics. *Chemical Communications* **2002**, *2* (20), 2372-2373.
- 268. McMahon, J. A.; Bis, J. A.; Vishweshwar, P.; Shattock, T. R.; McLaughlin, O. L.; Zaworotko, M. J., Crystal engineering of the composition of pharmaceutical phases. 3. Primary amide supramolecular heterosynthons and their role in the design of pharmaceutical co-crystals. **2005**, *220* (4), 340-350.
- 269. Zhou, Z.; Chan, H. M.; Sung, H. H. Y.; Tong, H. H. Y.; Zheng, Y., Identification of New Cocrystal Systems with Stoichiometric Diversity of Salicylic Acid Using Thermal Methods. *Pharmaceutical Research* **2016**, *33* (4), 1030-1039.
- 270. Leiserowitz, L.; Schmidt, G. M. J., Molecular packing modes. Part III. Primary amides. *Journal of the Chemical Society A: Inorganic, Physical, Theoretical* **1969,** (0), 2372-2382.
- 271. Vishweshwar, P.; Nangia, A.; Lynch, V. M., Molecular Complexes of Homologous Alkanedicarboxylic Acids with Isonicotinamide: X-ray Crystal Structures, Hydrogen Bond Synthons, and Melting Point Alternation. *Crystal Growth & Design* **2003**, *3* (5), 783-790.
- 272. Vishweshwar, P.; Nangia, A.; Lynch, V. M., Supramolecular synthons in phenolisonicotinamide adducts. *Crystengcomm* **2003**, *5* (31), 164-168.
- 273. Darwish, S.; Zeglinski, J.; Krishna, G. R.; Shaikh, R.; Khraisheh, M.; Walker, G. M.; Croker, D. M., A New 1:1 Drug-Drug Cocrystal of Theophylline and Aspirin: Discovery, Characterization, and Construction of Ternary Phase Diagrams. *Crystal Growth & Design* **2018**, *18* (12), 7526-7532.

- 274. Setyawan, D.; Adyaksa, F. R.; Sari, H. L.; Paramita, D. P.; Sari, R., Cocrystal formation of loratadine-succinic acid and its improved solubility. *Journal of Basic and Clinical Physiology and Pharmacology* **2021**, *32* (4), 623-630.
- 275. Jessop, P. G.; Jessop, D. A.; Fu, D.; Phan, L., Solvatochromic parameters for solvents of interest in green chemistry. *Green Chemistry* **2012**, *14* (5), 1245-1259.
- 276. Friščić, T.; Jones, W., Recent Advances in Understanding the Mechanism of Cocrystal Formation via Grinding. *Crystal Growth & Design* **2009**, 9 (3), 1621-1637.
- 277. Braga, D.; Giaffreda, S. L.; Grepioni, F.; Chierotti, M. R.; Gobetto, R.; Palladino, G.; Polito, M., Solvent effect in a "solvent free" reaction. *Crystengcomm* **2007**, 9 (10), 879-881.
- 278. Mandala, V. S.; Loewus, S. J.; Mehta, M. A., Monitoring Cocrystal Formation via In Situ Solid-State NMR. *The Journal of Physical Chemistry Letters* **2014**, *5* (19), 3340-3344.
- 279. Schiffmann, J. G.; Emmerling, F.; Martins, I. C. B.; Van Wüllen, L., In-situ reaction monitoring of a mechanochemical ball mill reaction with solid state NMR. *Solid State Nuclear Magnetic Resonance* **2020**, *109*, 101687.
- 280. Hareendran, C.; Alsirawan, B.; Paradkar, A.; Ajithkumar, T. G., In Situ Monitoring of Competitive Coformer Exchange Reaction by 1H MAS Solid-State NMR. *Molecular Pharmaceutics* **2024**, *21* (3), 1479-1489.
- 281. Zhou, L.; Dodd, S.; Capacci-Daniel, C.; Garad, S.; Panicucci, R.; Sethuraman, V., Co-crystal formation based on structural matching. *European Journal of Pharmaceutical Sciences* **2016**, *88*, 191-201.
- 282. Ghanghas, R.; Jindal, A.; Vasudevan, S., Geometry of Hydrogen Bonds in Liquid Ethanol Probed by Proton NMR Experiments. *The Journal of Physical Chemistry B* **2020**, *124* (4), 662-667.
- 283. Klosek, S.; Raftery, D., Visible Light Driven V-Doped TiO2 Photocatalyst and Its Photooxidation of Ethanol. *The Journal of Physical Chemistry B* **2001**, *105* (14), 2815-2819.
- 284. Ying, P.; Yu, J.; Su, W., Liquid-Assisted Grinding Mechanochemistry in the Synthesis of Pharmaceuticals. *Advanced Synthesis & Catalysis* **2021**, *363* (5), 1246-1271.
- 285. Bartalucci, E.; Schumacher, C.; Hendrickx, L.; Puccetti, F.; d'Anciães Almeida Silva, I.; Dervişoğlu, R.; Puttreddy, R.; Bolm, C.; Wiegand, T., Disentangling the Effect of Pressure and Mixing on a Mechanochemical Bromination Reaction by Solid-State NMR Spectroscopy. *Chemistry A European Journal* **2023**, *29* (12), e202203466.
- 286. Langer, B.; Schnell, I.; Spiess, H. W.; Grimmer, A.-R., Temperature Calibration under Ultrafast MAS Conditions. *Journal of Magnetic Resonance* **1999**, *138* (1), 182-186.
- 287. Amoureux, J. P.; Pruski, M.; Lang, D. P.; Fernandez, C., The Effect of RF Power and Spinning Speed on MQMAS NMR. *Journal of Magnetic Resonance* **1998**, *131* (1), 170-175.
- 288. Shattock, T. R.; Arora, K. K.; Vishweshwar, P.; Zaworotko, M. J., Hierarchy of Supramolecular Synthons: Persistent Carboxylic Acid...Pyridine Hydrogen Bonds in Cocrystals That also Contain a Hydroxyl Moiety. *Crystal Growth & Design* **2008**, 8 (12), 4533-4545.
- 289. Schultheiss, N.; Newman, A., Pharmaceutical Cocrystals and Their Physicochemical Properties. *Cryst. Growth Des.* **2009,** 9, 2950.
- 290. Mandala, V. S.; Loewus, S. J.; Mehta, M. A., Monitoring Cocrystal Formation via in Situ Solid-State NMR. *J. Phys. Chem. Lett.* **2014,** *5* (19), 3340.

- 291. Panzade, P. S.; Shendarkar, G. R., Pharmaceutical cocrystal: a game changing approach for the administration of old drugs in new crystalline form. *Drug Dev. Ind. Pharm.* **2020**, *46* (10), 1559-1568.
- 292. Clark, S. J.; Segall, M. D.; Pickard, C. J.; Hasnip, P. J.; Probert, M. I. J.; Refson, K.; Payne, M. C., First principles methods using CASTEP. *Zeitschrift für Kristallographie Crystalline Materials* **2005**, *220* (5-6), 567-570.
- 293. Wallace, M.; Adams, D. J.; Iggo, J. A., Titrations without the Additions: The Efficient Determination of pKa Values Using NMR Imaging Techniques. *Analytical Chemistry* **2018**, 90 (6), 4160-4166.

## **Appendix**

Appendix 3.1 – Python code from Jupyter notebook used to separate the SMILES strings obtained from mercury. This enabled us to find cocrystals that had been successfully formed with both INA and NA.



```
In [216]: for line in abc:
                      cde = line.split('\t')
ref_code = cde[1]
smiles = cde[0]
efg = smiles.split('.')
ghi = []
                      for m in efg:
    if m != 'NC(=0)clccnccl':
        ghi.append(m)
s = '.'
                      print(s.join(ghi) + '\t' + ref_code + '\t' + 'iso')
                CC(Oclccc(COc2ccc(Cl)cc2)cc1)C(0)=0
                CC(=0)ClCCC1 ACOMUC iso

CC(=0)ClCCCC1 ACOMUC iso

CC(=0)ClCCCC1 ACOMUC iso
                                                                VOJKIR iso
                                                                            YUCBOQ iso
                OC(=0)CICCC1 ACOMEO ISO
OC(=0)CICCCCC1 ACOMEN ISO
OC(=0)CICCCCC1 ACONIR ISO
OC(=0)CICCCCC1 ACONIR ISO
                                                                iso
                CCCC=CC(0)=0
                                        AJAKAX iso
 In [197]: abc = isocc.split('\n')
print(abc)
                OC(=0)clccc(F)ccl
OC(=0)clccc(F)ccl
                                           ASAXUN iso
ASAXUN01
                OC(=0)clcccccl BUDWEC iso
                                                                                                     BIZTIP iso
```

Appendix 3.2 – reported coformers that form with both nicotinamide and isonicotinamide. SMILES string of coformer only

SMILES string	REF code	
CC(C)COc1ccc(cc1C#N)C1=NC(=C(S1)C(O)=O)C	HIQQIJ	Febuxostat Nicotinamide
CC(C)COc1ccc(cc1C#N)C1=NC(=C(S1)C(O)=O)C	OYADAV	Febuxostat Isonicotinamide
CC(C)Cc1ccc(cc1)C(C)C(O)=O	KIPPAD	Ibuprofen Isonicotinamide

CC(C)Cc1ccc(cc1)C(C)C(O)=O	SODDIZ	Rac-ibuprofen Nicotinamide
CC(C)Cc1ccc(cc1)C(C)C(O)=O	SODDIZ01	Rac-ibuprofen Nicotinamide
CC(C)Cc1ccc(cc1)C(C)C(O)=O	SOGLAC	(S)-ibuprofen Nicotinamide
CC(N(O)C(N)=O)C1=Cc2cccc2S1	YERYUS	Zileuton bis(nicotinamide)
CC(N(O)C(N)=O)C1=Cc2cccc2S1	YERZAZ	Zileuton Isonicotinamide
CCC(c1ccc(O)cc1)=C(CC)c1ccc(O)cc1	NOCSAC	diethylstilbestrol bis (isonicotinamide)
CCC(c1ccc(O)cc1)=C(CC)c1ccc(O)cc1	NOCSAC01	diethylstilbestrol bis (isonicotinamide)
CCC(c1ccc(O)cc1)=C(CC)c1ccc(O)cc1	NOCSOQ	diethylstilbestrol nicotinamide
CN1N=NC2=C(N=CN2C1=O)C(N)=O	KIJSUT	bis(temozolomide) nicotinamide
CN1N=NC2=C(N=CN2C1=O)C(N)=O	KIJTAA	bis(temozolomide) isonicotinamide
COc1cc(C=O)ccc1O	OBUBOE	Vanillin Nicotinamide
COc1cc(C=O)ccc1O	VESYUQ	Vanillin isonicotinamide

COc1cc(ccc1O)C(O)=O	VESZAX	Vanillic acid bis(isonicotinamide)
COc1cc(ccc1O)C(O)=O	ZOYCEX	Vanillic acid nicotinamide
COc1ccc2N(C(=C(CC(=O)OCC(O)=O)c2c1)C)C(= O)c1ccc(Cl)cc1	KARFIV	acemetacin nicotinamide
COc1ccc2N(C(=C(CC(=O)OCC(O)=O)c2c1)C)C(= O)c1ccc(Cl)cc1	WIXDOY	acemetacin isonicotinamide
COc1ccc2cc(ccc2c1)C(C)C(O)=O	HEGGAD	Naproxen nicotinamide
COc1ccc2cc(ccc2c1)C(C)C(O)=O	HEGGAD01	Naproxen nicotinamide
COc1ccc2cc(ccc2c1)C(C)C(O)=O	JULIEH	(R)-Naproxen (S)- Naproxen nicotinamide
COc1ccc2cc(ccc2c1)C(C)C(O)=O	PAMQAX	Naproxen isonicotinamide
Cc1cc(O)cc(O)c1	EWAQAV	Orcinol tetrakis nicotinamide
Cc1cc(O)cc(O)c1	EWAQID	Orcinol bis(isonicotinamide)
FC1=CN(C2CCCO2)C(=O)NC1=O	DOXDUR	Tegafur nicotinamide
FC1=CN(C2CCCO2)C(=O)NC1=O	DOXFAZ	Tegafur isonicotinamide
NC(=O)N1c2cccc2C=Cc2cccc12	LOFKIB	Carbamazepine isonicotinamide
NC(=O)N1c2cccc2C=Cc2cccc12	LOFKIB01	Carbamazepine isonicotinamide

NC(=O)N1c2cccc2C=Cc2cccc12	UNEZES	Carbamazepine nicotinamide
NC(=O)N1c2cccc2C=Cc2cccc12	UNEZES01	Carbamazepine nicotinamide
NC(=O)c1cccnc1	UMUYOR	Isonicotinamide nicotinamide
NS(=O)(=O)c1cc(C(O)=O)c(NCC2=CC=CO2)cc1C	LOFLEZ	Furosemide isonicotinamide
NS(=O)(=O)c1cc(C(O)=O)c(NCC2=CC=CO2)cc1C	LOFLID	Furosemide isonicotinamide
NS(=O)(=O)c1cc(C(O)=O)c(NCC2=CC=CO2)cc1C	YASGOQ	Furosemide nicotinamide
NS(=O)(=O)c1cc(C(O)=O)c(NCC2=CC=CO2)cc1C	YASGOQ01	Furosemide nicotinamide
NS(=O)(=O)c1cc(C(O)=O)c(NCC2=CC=CO2)cc1C	YASGOQ02	Furosemide nicotinamide
NS(=O)(=O)c1cc(C(O)=O)c(NCC2=CC=CO2)cc1C	YASGOQ03	Furosemide nicotinamide
NS(=O)(=O)c1cc(C(O)=O)c(NCC2=CC=CO2)cc1C	YASGOQ04	Furosemide nicotinamide
NS(=O)(=O)c1cc(C(O)=O)c(NCC2=CC=CO2)cc1C I.O	YASHIL	Furosemide nicotinamide
NS(=O)(=O)c1ccc(cc1)C(O)=O	FURWOG	4-sulfamoylbenzoic acid isonicotinamide
NS(=O)(=O)c1ccc(cc1)C(O)=O	FURXEX	4-sulfamolybenxoic acid nicotinamide
Nc1ccc(C(O)=O)c(O)c1	OBOVAF	bis(4-aminosalicylic) isonicotinamide

Nc1ccc(C(O)=O)c(O)c1	OFUYIZ	4-aminosalicylic acid nicotinamide
Nc1ccc(cc1)C(O)=O	SOLFUW	4-aminobenzoic acid isonicotinamide
Nc1ccc(cc1)C(O)=O.O	ABULIU	4-aminobenzoic acid nicotinamide monohydrate
Nc1cccc1C(O)=O	FEBSIR	2 aminobenzoic acid nicotinamide
Nc1cccc1C(O)=O	FEBSIR01	2-aminobenzoic acid nicotinamide
Nc1ccccc1C(O)=O	FECGAY	2-aminobenzoic acid isonicotinamide
Nc1cccc1C(O)=O	FECGAY01	2-aminobenzoic acid isonicotinamide
Nc1cccc1C(O)=O	ZIPGEN	Bis(2-aminobenzoic acid) isonicotinamide
OB(O)c1ccc(I)cc1	LOXDAF	(4-iodophenyl)boronic acid isonicotinamide
OB(O)c1ccc(I)cc1	LOXDEJ	(4-iodophenyl)boronic acid nicotinamide
OC(=O)C1=NN(Cc2ccc(Cl)cc2Cl)c2ccccc12	DAQYUS	Ionidamine Isonicotinamide
OC(=O)C1=NN(Cc2ccc(Cl)cc2Cl)c2ccccc12	DAQZUT	Ionidamine nicotinamide
OC(=O)C=CC(O)=O	EDAPOQ	Fumaric acid nicotinamide

OC(=0)C=CC(0)=0	LUNNOX	Fumaric acid bis(isonicotinamide)
OC(=O)C=Cc1ccccc1	LUNMAI	Cinnamic acid isonicotinamide
OC(=O)C=Cc1ccccc1	LUNMAI01	Cinnamic acid isonicotinamide
OC(=O)C=Cc1ccccc1	NUZTAF	Cinnamic acid nicotinamide
OC(=O)CC(O)(CC(O)=O)C(O)=O	CUYXUQ	Citric acid bis(nicotinamide)
OC(=O)CC(O)(CC(O)=O)C(O)=O	HICZIF	Citric acid bis(isonicotinamide)
OC(=O)CC(O)(CC(O)=O)C(O)=O	HICZIF01	Citric acid bis(isonicotinamide)
OC(=O)CC(O)(CC(O)=O)C(O)=O	HICZIF02	Citric acid bis(isonicotinamide)
OC(=O)CC(O)=O	NUKXUN	Malonic acid bis(nicotinamide)
OC(=O)CC(O)=O	NUKXUN01	Malonic acid bis(nicotinamide)
OC(=O)CC(O)=O	NUKXUN02	Malonic acid bis(nicotinamide)
OC(=O)CC(O)=O	ULAWEJ	Malonic acid bis(isonicotinamide)
OC(=O)CC(O)=O	ULAWEJ06	Malonic acid bis(isonicotinamide)
OC(=O)CCC(O)=O	DUZPAQ	Succinic acid bis(nicotinamide)

OC(=O)CCC(O)=O	LUNNUD	Succinic acid bis(isonicotinamide)		
OC(=0)CCC(0)=0	LUNNUD01	Succinic acid bis(isonicotinamide)		
OC(=O)CCCC(O)=O	NUKYEY	Glutaric acid nicotinamide		
OC(=O)CCCC(O)=O	ULAWOT	Glutaric acid bis(isonicotinamide)		
OC(=O)CCCC(O)=O	ULAXAG	Glutaric acid isonicotinamide		
OC(=0)CCCCC(0)=0	NUKYIC	Adipic acid Nicotinamide		
OC(=O)CCCCC(O)=O	NUKYOI	Adipic acid bis(nicotinamide)		
OC(=O)CCCCC(O)=O	ULAWUZ	Adipic acid bis(isonicotinamide)		
OC(=O)CCCC(O)=O	O)CCCC(O)=O ULAXEK			
OC(=O)CCCCC(O)=O	HOFYOT	Pimelic acid bis(isonicotinamide)		
OC(=O)CCCCC(O)=O	ISIJEA	Pimelic acid isonicotinamide		
OC(=O)CCCCC(O)=O	NUKYUO	Pimelic acid nicotinamide		
OC(=0)CCCCC(O)=O	NUKYUO01	Pimelic acid nicotinamide		
OC(=0)CCCCC(O)=O	NUKYUO02	Pimelic acid nicotinamide		
OC(=O)CCCCC(O)=O	NUKYUO03	Pimelic acid nicotinamide		

OC(=0)CCCCCC(0)=0	HOFZEK	Suberic acid bis(isonicotinamide)		
OC(=0)CCCCCC(O)=O	ISIJIE	Suberic acid isonicotinamide		
OC(=O)CCCCCC(O)=O	NUKZAV	Suberic acid nicotinamide		
OC(=O)CCCCCC(O)=O	NUKZAV01	Suberic acid nicotinamide		
OC(=O)CCCCCC(O)=O	NUKZEZ	Suberic acid bis(nicotinamide)		
OC(=O)CCCCCC(O)=O	NUKZEZ01	Suberic acid bis(nicotinamide)		
OC(=O)CCCCCCC(O)=O	HOFYUZ	Azelaic acid bis(isonicotinamide)		
OC(=O)CCCCCCC(O)=O	ISIJAW	Azelaic acid isonicotinamide		
OC(=0)CCCCCCC(0)=0	NUKZID	Azelaic acid nicotinamide		
OC(=O)CCCCCCC(O)=O	HOFZAG	Sebacic acid bis(isonicotinamide)		
OC(=O)CCCCCCC(O)=O	NUKZOJ	Sebacic acid bis(nicotinamide)		
OC(=O)Cc1ccccc1	FAKLAH	Phenylacetic acid nicotinamide		
OC(=O)Cc1ccccc1	FAKLEL	Phenylacetic acid		
OC(=O)c1cc(O)ccc1O	LAGTAR	2,5-dihydroxybenzoic acid isonicotinamide		

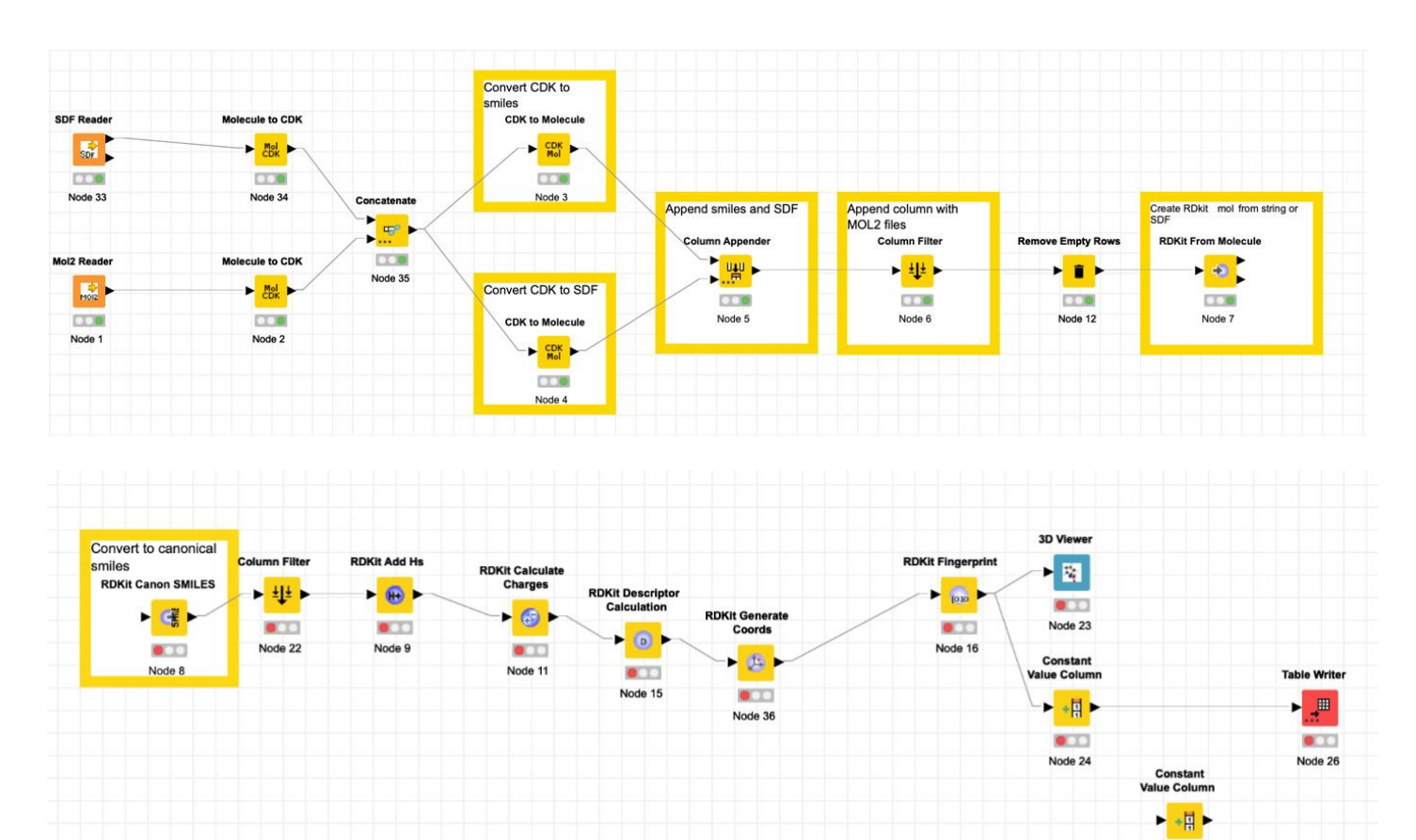
OC(=O)c1cc(O)ccc1O	PEKRUU	2,5-dihydroxybenzoic acid nicotinamide			
OC(=0)c1cc(0)ccc10	PEKRUU01	2,5-dihydroxybenzoic acid nicotinamide			
OC(=O)c1ccc(F)cc1	ASAXUN	4-fluorobenzoic acid Isonicotinamide			
OC(=O)c1ccc(F)cc1	ASAXUN01	4-fluorobenzoic acid Isonicotinamide			
OC(=O)c1ccc(F)cc1	FECFIF	4-fluorobenzoic acid Nicotinamide			
OC(=O)c1ccc(O)cc1	VAKTOR	4-hydroxybenzoic acid isonicotinamide			
OC(=O)c1ccc(O)cc1	RUYHEZ	4-hydroxybenzoic acid nicotinamide			
OC(=O)c1ccc(O)cc1O	DINRUP	2,4-dihydroxybenzoic acid nicotinamide			
OC(=O)c1ccc(O)cc1O	DINRUP01	2,4-dihydroxybenzoic acid nicotinamide			
OC(=0)c1ccc(0)cc10.0	LAGSUK	2,4-dihydroxybenzoic acid isonicotinamide monohydrate			
OC(=O)c1ccc(cc1)N(=O)=O	AJAKEB	4-nitrobenzoic acid Isonicotinamide			
OC(=0)c1ccc(cc1)N(=0)=0	FECFEB	4-nitrobenzoic acid nicotinamide			
OC(=0)c1cccc(0)c1	LUNMEM	3-hydroxybenzoic acid isonicotinamide			

OC(=O)c1cccc(O)c1	XAQQIQ	3-hydroxybenzoic acid nicotinamide			
OC(=O)c1cccc(O)c1O	LAGSOE	2,3-dihydroxybenzoic acid isonicotinamide			
OC(=O)c1cccc(O)c1O	NEFFIQ	2,3-dihydroxybenzoic acid nicotinamide			
OC(=O)c1ccccc1	BUDWEC	Benzoic acid isonicotinamide			
OC(=O)c1ccccc1	GAZCES	Benzoic acid nicotinamide			
OC(=O)c1ccccc1	GAZCES01	Benzoic acid nicotinamide			
OC(=O)c1ccccc1	МОУТОН	Bis(Benzoic acid) nicotinamide			
OC(=O)c1ccccc1	MOVTOH01	Bis(Benzoic acid) nicotinamide			
OC(=0)c1ccccc10	QAFTID	Salicylic acid bis(isonicotinamide)			
OC(=O)c1ccccc1O	SODDOF	Salicylic acid nicotinamide			
OC(=O)c1ccccc1O	SODDOF01	Salicylic acid nicotinamide			
OC(=O)c1ccccc1O	SODDOF02	Salicylic acid nicotinamide			
OC(=0)c1ccccc10	XAQQEM	Salicylic acid isonicotinamide			
OC(C(O)=O)c1ccccc1	BOBQUG	R-Mandelic acid nicotinamide			

OC(C(O)=O)c1ccccc1	BOBRAN	R-Mandelic acid nicotinamide
OC(C(O)=O)c1ccccc1	JILZOU	D-Mandelic acid nicotinamide
OC(C(O)=O)c1ccccc1	JILZOU01	D-Mandelic acid nicotinamide
OC(C(O)=O)c1ccccc1	LUNPAL	D,L-Mandelic acid isonicotinamide
OCC(O)C1OC(=O)C(=C1O)O	OXOGUF	Vitamin C isonicotinamide
OCC(O)C1OC(=O)C(=C1O)O	ОХОНАМ	Vitamin C bis(isonicotinamide)
OCC(O)C1OC(=O)C(=C1O)O	OXOHEQ	Vitamin C nicotinamide
OCC(0)C1OC(=0)C(=C10)O	ОХОНІИ	Vitamin C tris(nicotinamide)
Oc1cc(O)c2C(=O)C(=C(Oc2c1)c1ccc(O)c(O)c1)O	NAFYUR	Quercetin nicotinamide
Oc1cc(O)c2C(=O)C(=C(Oc2c1)c1ccc(O)c(O)c1)O	NUTPID	Quercetin isonicotinamide
Oc1cc2OC(=CC(=O)c2c(O)c1O)c1ccccc1	GAZWUB	Baicalein Nicotinamide
Oc1cc2OC(=CC(=O)c2c(O)c1O)c1ccccc1	KAMRAU	Baicalein bis(isonicotinamide)
Oc1ccc(CCC(=0)c2c(0)cc(0)cc2O)cc1	YUCBIK	Phloretin nicotinamide
Oc1ccc(CCC(=O)c2c(O)cc(O)cc2O)cc1	YUCBOQ	Phloretin isonicotinamide

Oc1ccc(cc1)C=CC(=O)c1ccc(O)cc1O	EYUGAI	Isoliquiritigenin
		nicotinamide
Oc1ccc(cc1)C=CC(=O)c1ccc(O)cc1O	EZAQED	Isoliquiritigenin
		isonicotinamide
Oc1ccc(cc1)C=Cc1cc(O)cc(O)c1	PEBZEE	Resveratrol
		nicotinamide
Oc1ccc(cc1)C=Cc1cc(O)cc(O)c1	PEBZII	Resveratrol
		isonicotinamide
Oc1ccc2C(=O)C(=C(Oc2c1)c1ccc(O)c(O)c1)O	JOPVAN	Fisetin nicotinamide
Oc1ccc2C(=O)C(=C(Oc2c1)c1ccc(O)c(O)c1)O	ZIKNOY	Fisetin isonicotinamide
Oc1ccc2C(=O)C(=C(Oc2c1)c1ccc(O)c(O)c1)O	ZIKNOY01	Fisetin isonicotinamide
Oc1cccc(O)c1O	HEDREP	Pyrogallol
		bis(isonicotinamide)
Oc1cccc(O)c1O	HEDRIT	Bis(pyrogallol)
		isonicotinamide
Oc1cccc(O)c1O	HEDROZ	Bis(pyrogallol)
		nicotinamide
0-1(-1)N/0)0	DIDEAN	2 mituambar al
Oc1cccc(c1)N(=O)=O	RIDFAN	3-nitrophenol isonicotinamide
		isonicomiamile
Oc1cccc(c1)N(=O)=O	RIDFER	3-nitrophenol
		nicotinamide

Appendix 3.3 Knime analytics platform pre-processing steps.



...

#### Appendix 3.4. Molecular descriptors extracted from RDkit

Number (integer)

#### 4a. D<sub>num</sub>

NumAliphaticCarbocycles

#### AMW Number (double) ExactMW Number (double) NumLipinskiHBA Number (integer) NumLipinskiHBD Number (integer) NumRotatableBonds Number (integer) NumHBD Number (integer) Number (integer) NumHBA Number (integer) Number (integer) NumAmideBonds NumHeteroAtoms NumHeavyAtoms Number (integer) NumAtoms Number (integer) NumStereocenters Number (integer) NumUnspecifiedStereocenters Number (integer) Number (integer) NumRings NumAromaticRings Number (integer) NumSaturatedRings Number (integer) NumAliphaticRings Number (integer) NumAromaticHeterocycles Number (integer) NumSaturatedHeterocycles Number (integer) NumAliphaticHeterocycles Number (integer) NumAromaticCarbocycles Number (integer) NumSaturatedCarbocycles Number (integer)

#### 4b. Dall

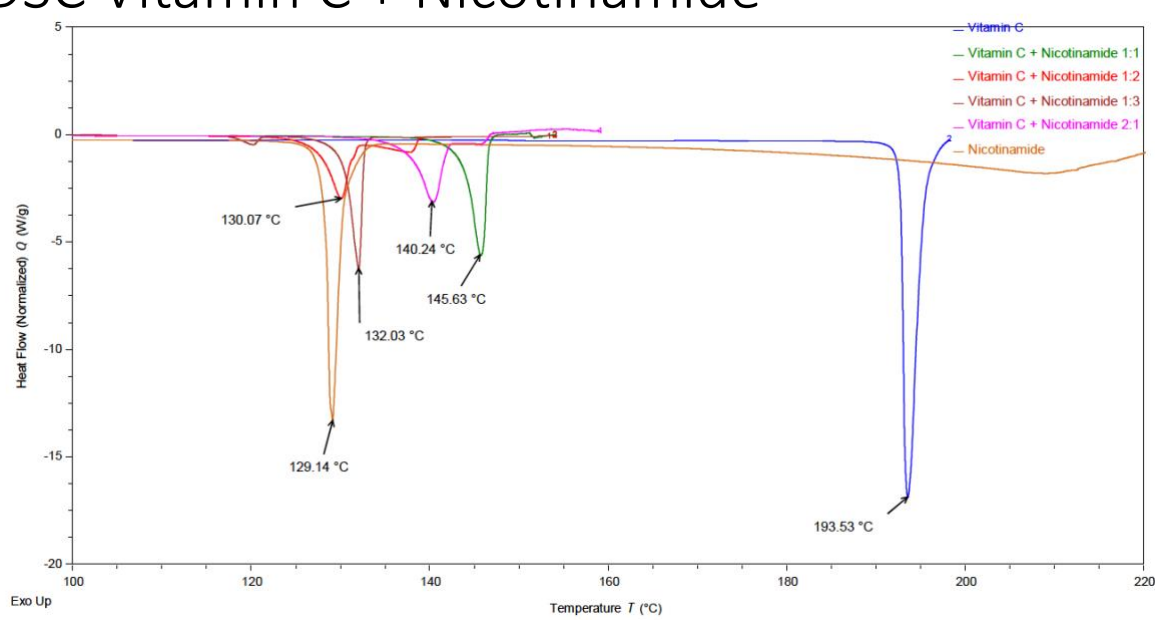
FractionCSP3	Number (double)
Chi0v	Number (double)
Chi1v	Number (double)
Chi2v	Number (double)
Chi3v	Number (double)
Chi4v	Number (double)
Chi1n	Number (double)
Chi2n	Number (double)
Chi3n	Number (double)
Chi4n	Number (double)
HallKierAlpha	Number (double)
kappa1	Number (double)
kappa2	Number (double)
kappa3	Number (double)
slogp_VSA1	Number (double)
slogp_VSA2	Number (double)
slogp_VSA3	Number (double)
slogp_VSA4	Number (double)
slogp_VSA5	Number (double)
slogp_VSA6	Number (double)
slogp_VSA7	Number (double)
slogp_VSA8	Number (double)
slogp_VSA9	Number (double)
slogp_VSA10	Number (double)
slogp_VSA11	Number (double)
slogp_VSA12	Number (double)
smr_VSA1	Number (double)
smr_VSA2	Number (double)
smr_VSA3	Number (double)
smr_VSA4	Number (double)
smr_VSA5	Number (double)
smr_VSA6	Number (double)
smr_VSA7	Number (double)
smr_VSA8	Number (double)
smr_VSA9	Number (double)
smr_VSA10	Number (double)
peoe_VSA1	Number (double)
peoe_VSA2	Number (double)
peoe_VSA3	Number (double)
peoe_VSA4	Number (double)
peoe_VSA5	Number (double)
peoe_VSA6	Number (double)
peoe_VSA7	Number (double)
peoe_VSA8	Number (double)
peoe_VSA9	Number (double)
peoe_VSA10	Number (double)
peoe_VSA11	Number (double)
peoe_VSA12	Number (double)
peoe_VSA13	Number (double)
peoe_VSA14	Number (double)
MQN1	Number (integer)
MQN2	Number (integer)
MQN3	Number (integer)
MQN4	Number (integer)

Appendix 3.5 - Stoichiometric masses used in LAG screening

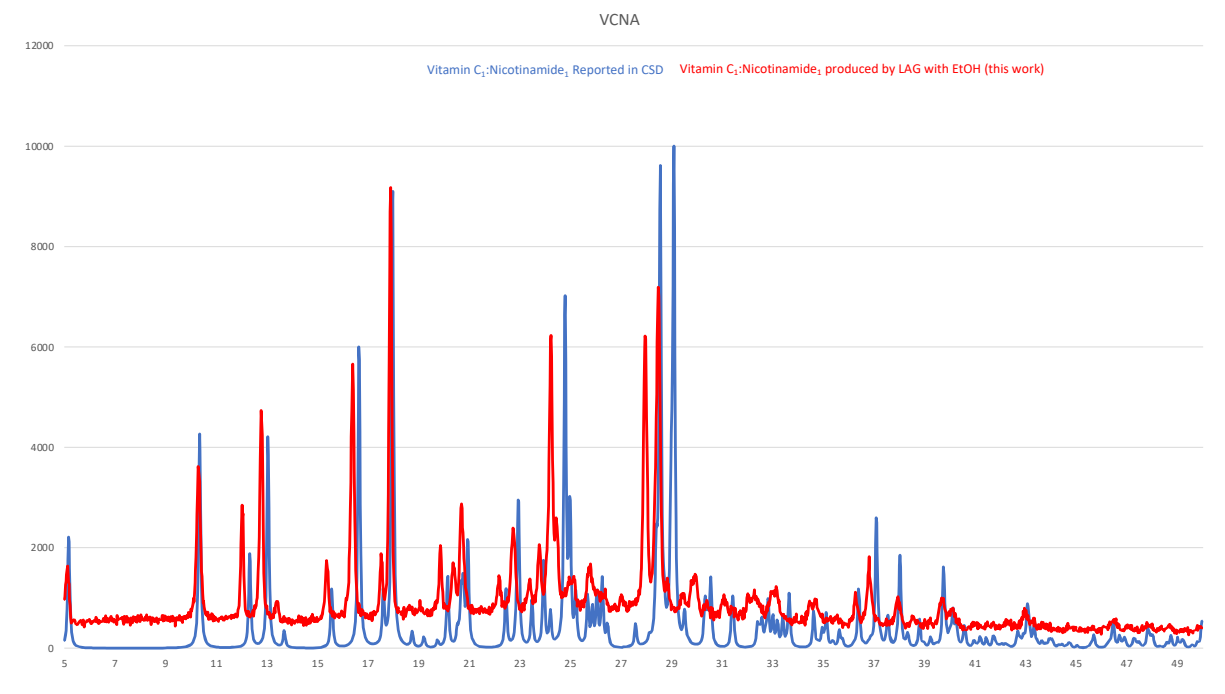
Cocrystal stoichiometry	Coformer	Mass of coformer, mg	Mass of INA/NA		
1:1	3-hydroxybenzoic Acid	138.1	122.1mg		
1:2	3-hydroxybenzoic Acid	138.1	244.2mg		
2:1	3-hydroxybenzoic Acid	276.2mg	122.1mg		
1:1	2-hydroxybenzoic Acid	138.1mg	122.1mg		
1:2	2-hydroxybenzoic Acid	138.1mg	244.2mg		
2:1	2-hydroxybenzoic Acid	276.2mg	122.1mg		
1:1	Vanillin	154.1mg	122.1mg		
1:2	Vanillin	154.1mg	244.2mg		
2:1	Vanillin	308.2mg	122.1mg		
1:1	Vanillic Acid	168.1mg	122.1mg		
1:2	Vanillic Acid	168.1mg	244.2mg		
2:1	Vanillic Acid	336.2mg	122.1mg		
1:1	Vitamin C	176.1mg	122.1mg		
1:2	Vitamin C	176.1mg	244.2mg		
2:1	Vitamin C	352.2mg	122.1mg		
1:1	Sulfasalazine	398.4mg	122.1mg		
1:2	Sulfasalazine	398.4mg	244.2mg		
2:1	Sulfasalazine	398.4mg	61.05mg		

3.6.1 DSC, PXRD, ssNMR of Vitamin C: Nicotinamide

# DSC Vitamin C + Nicotinamide

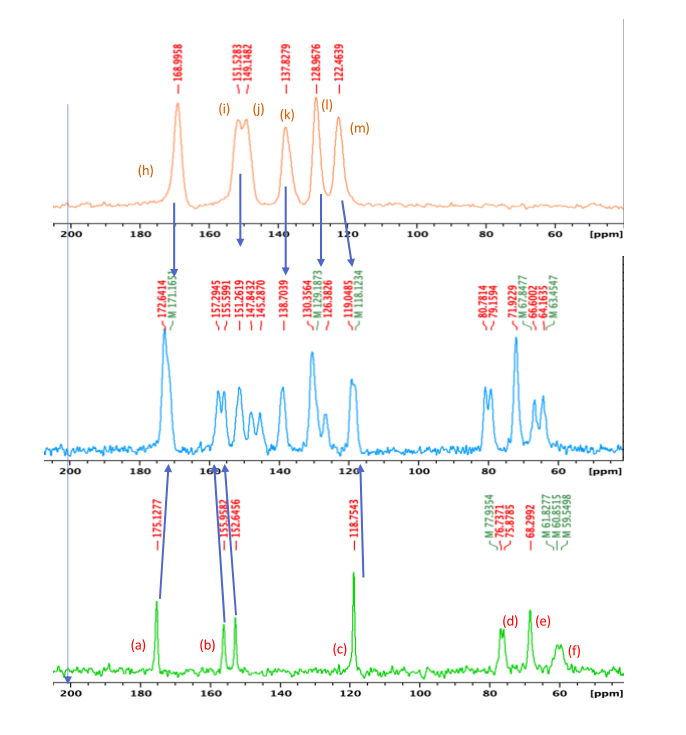


# $Vitamin C_1: Nicotinamide_1 PXRD$



## Vitamin $C_1$ : Nicotinamide<sub>1</sub> $^{13}$ C CP/MAS

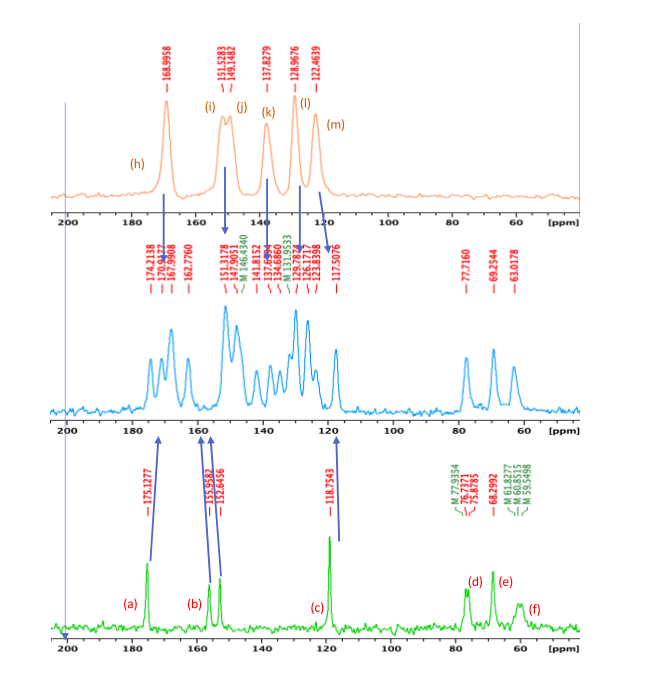




### Vitamin $C_1$ : Nicotinamide<sub>2</sub> $^{13}$ C CP/MAS







Nicotinamide

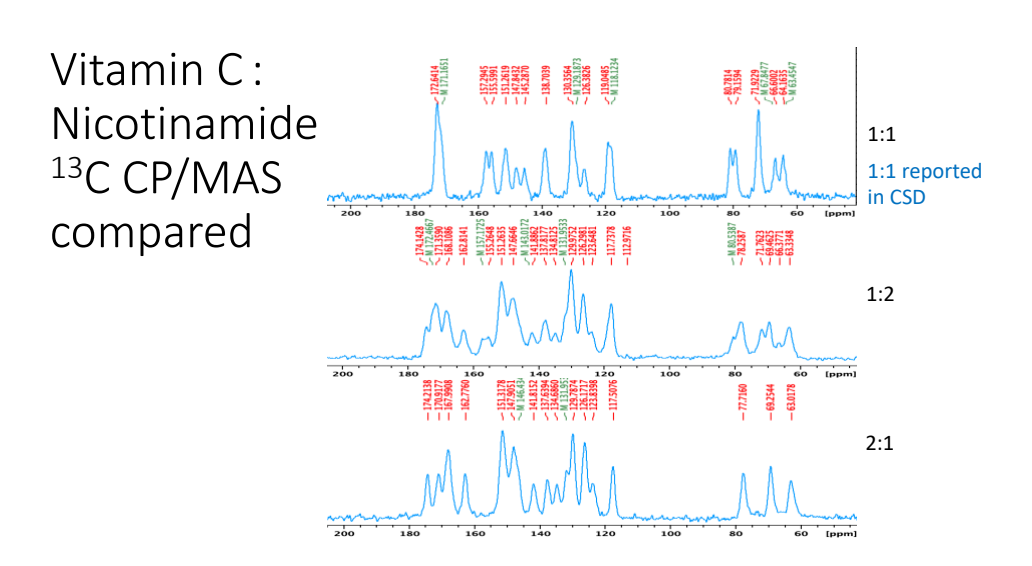
Nicotinamide

Cocrystal

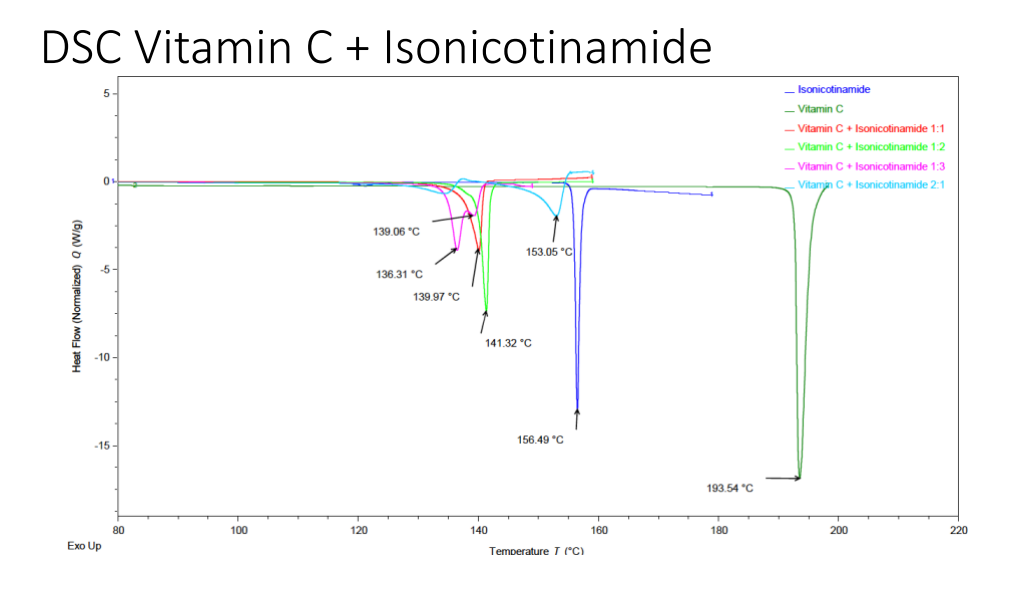
Vitamin C

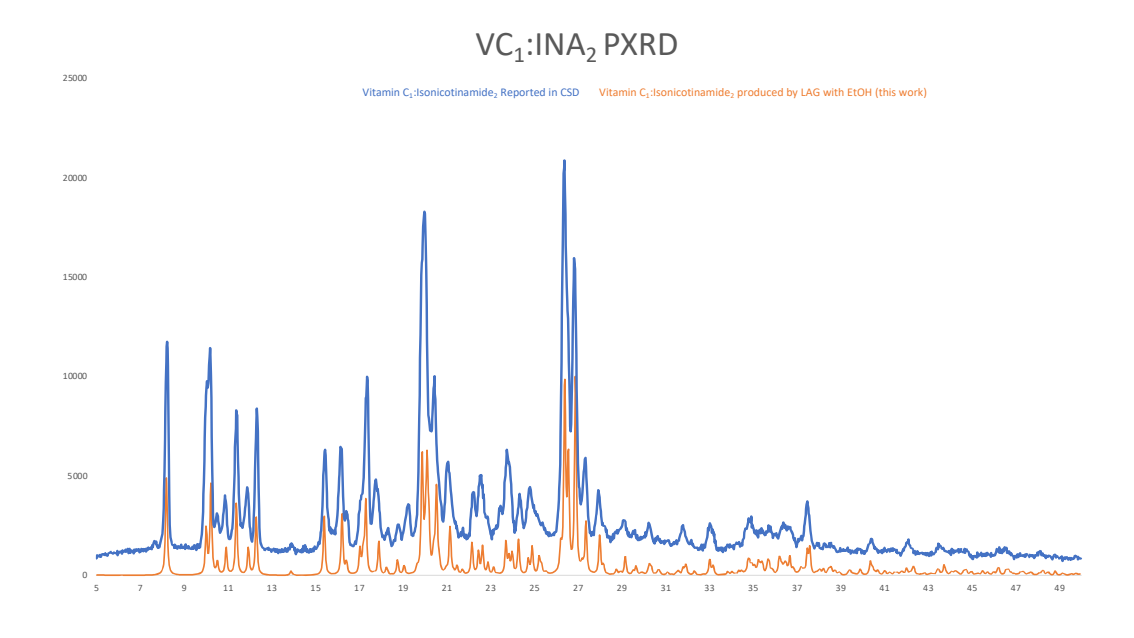
Cocrystal

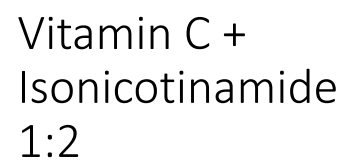
Vitamin C



### 3.6.2 Vitamin C: Isonicotinamide

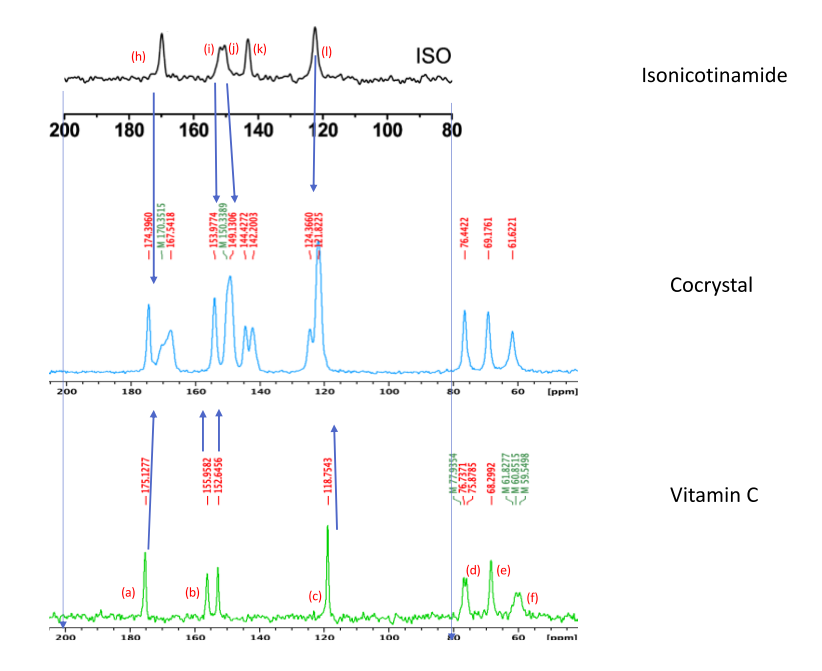






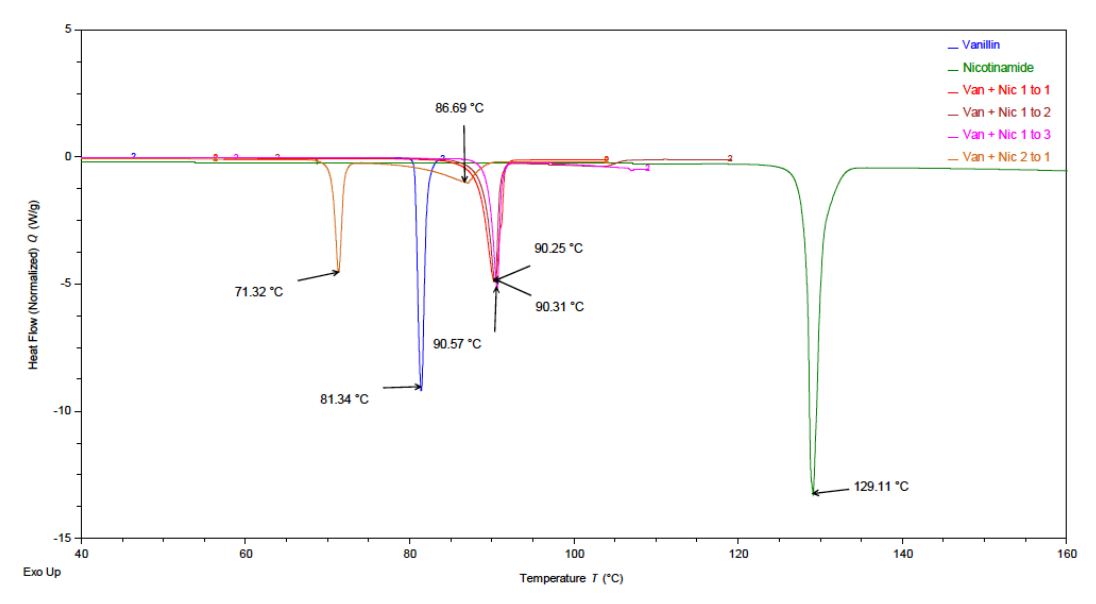


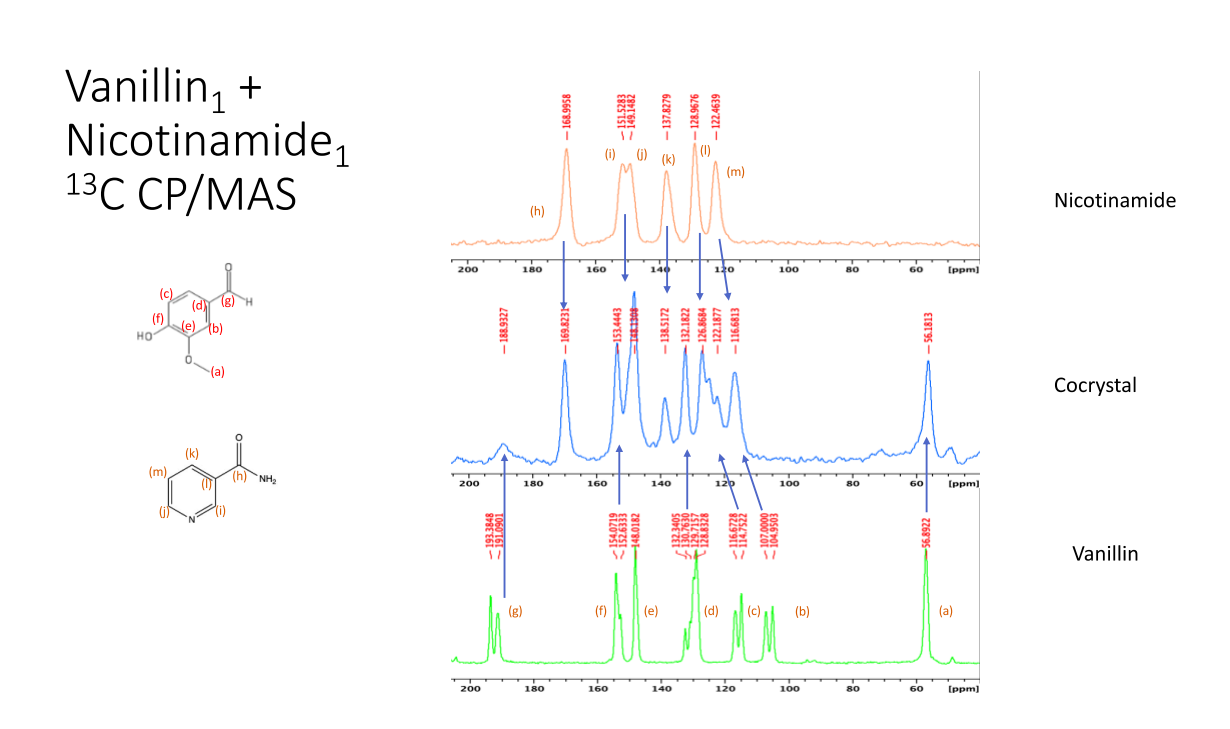


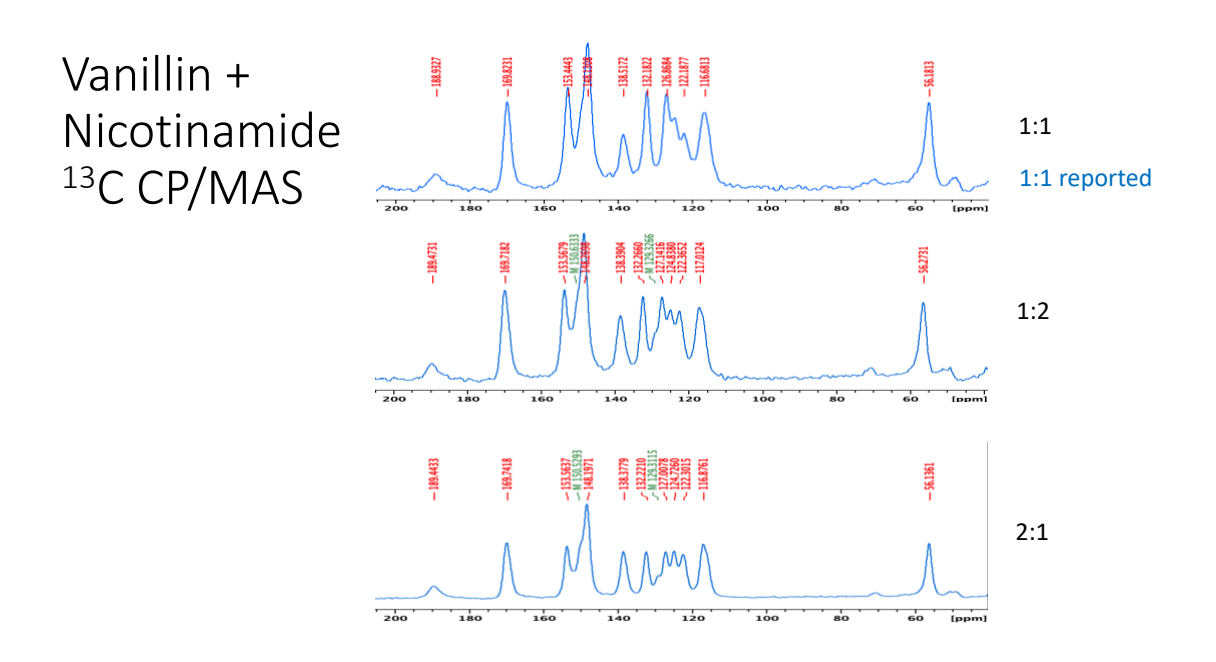


#### 3.6.3 Vanillin Nicotinamide

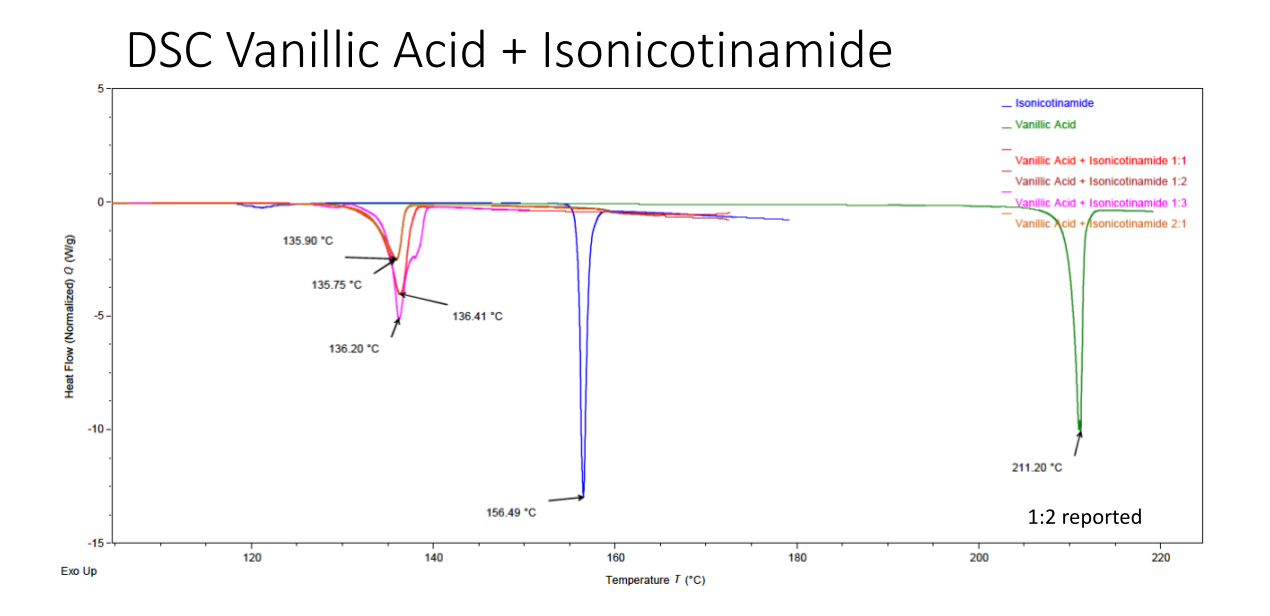
# DSC Vanillin + Nicotinamide





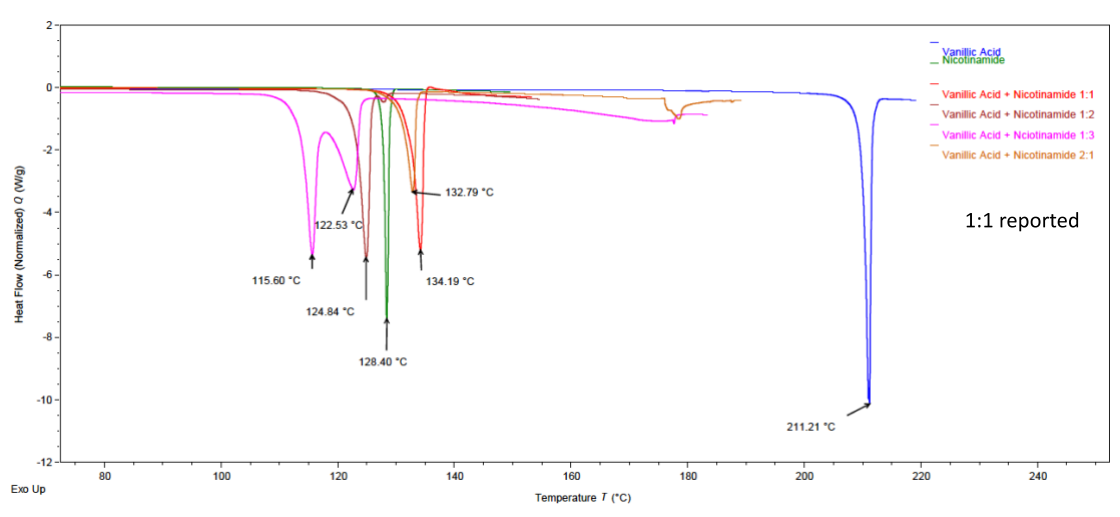


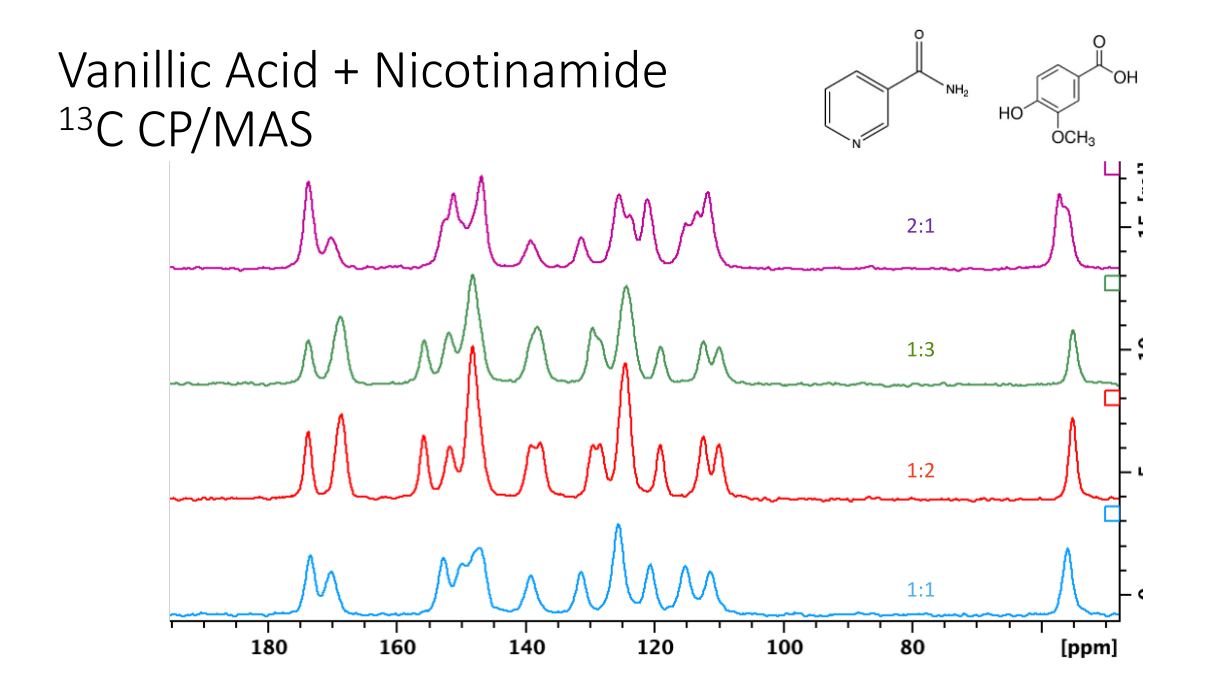
### 3.6.4 Vanillic Acid:Isonicotinamide



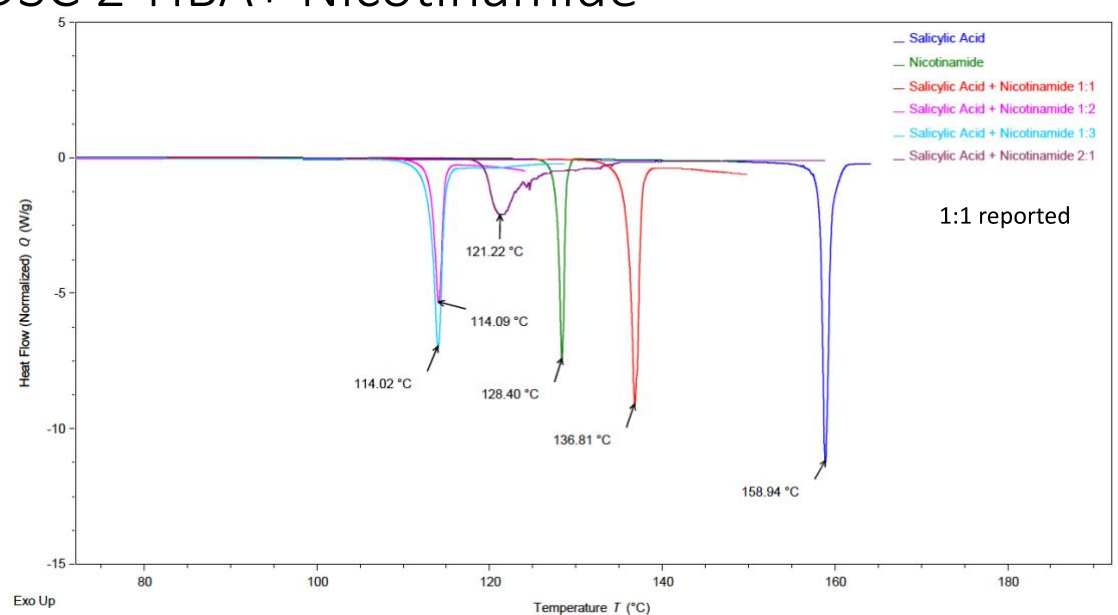
#### 3.6.5 Vanillic Acid:Nicotinamide

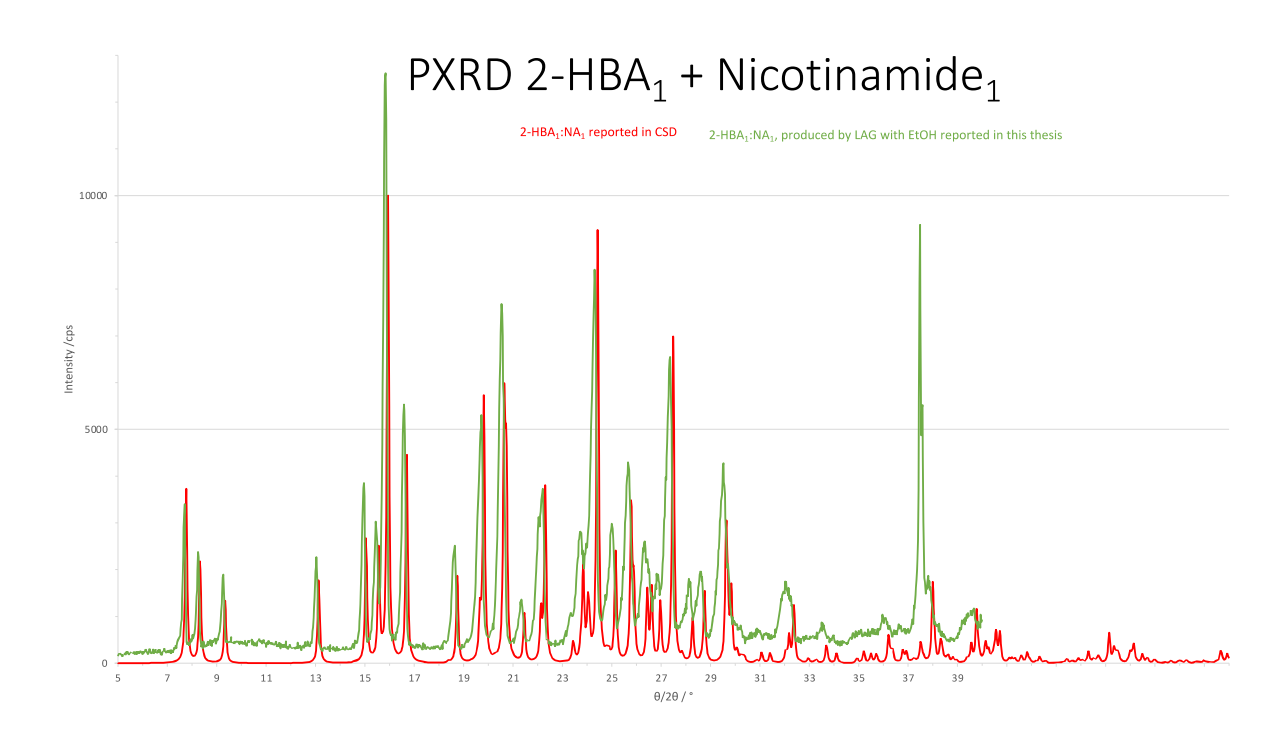
### DSC Vanillic Acid + Nicotinamide





# DSC 2-HBA+ Nicotinamide



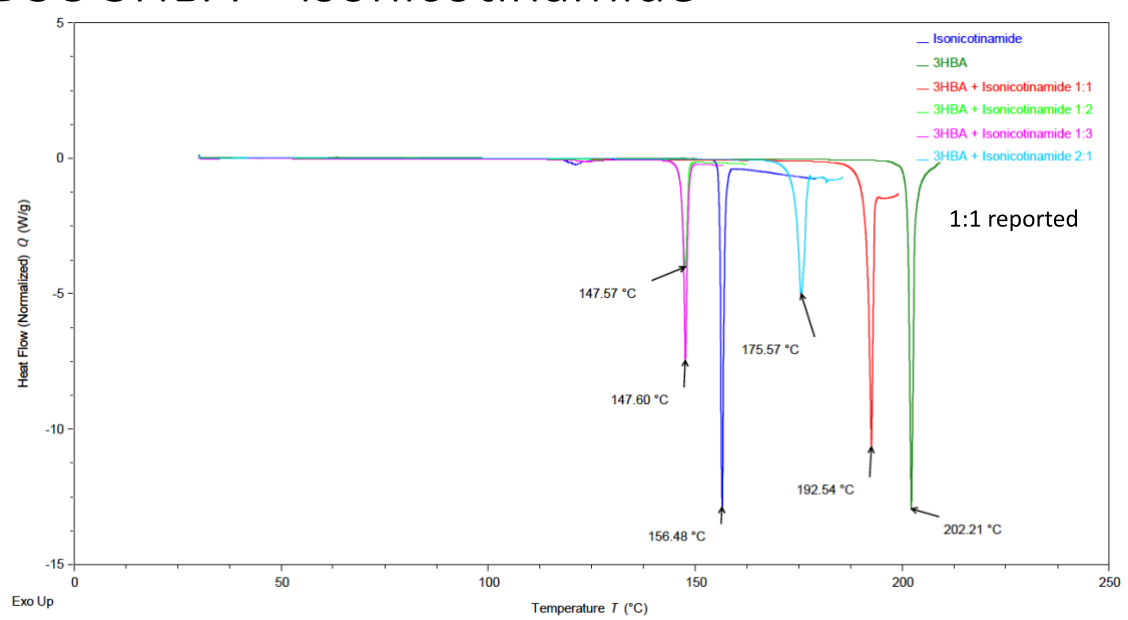


### PXRD 2-HBA: Nicotinamide

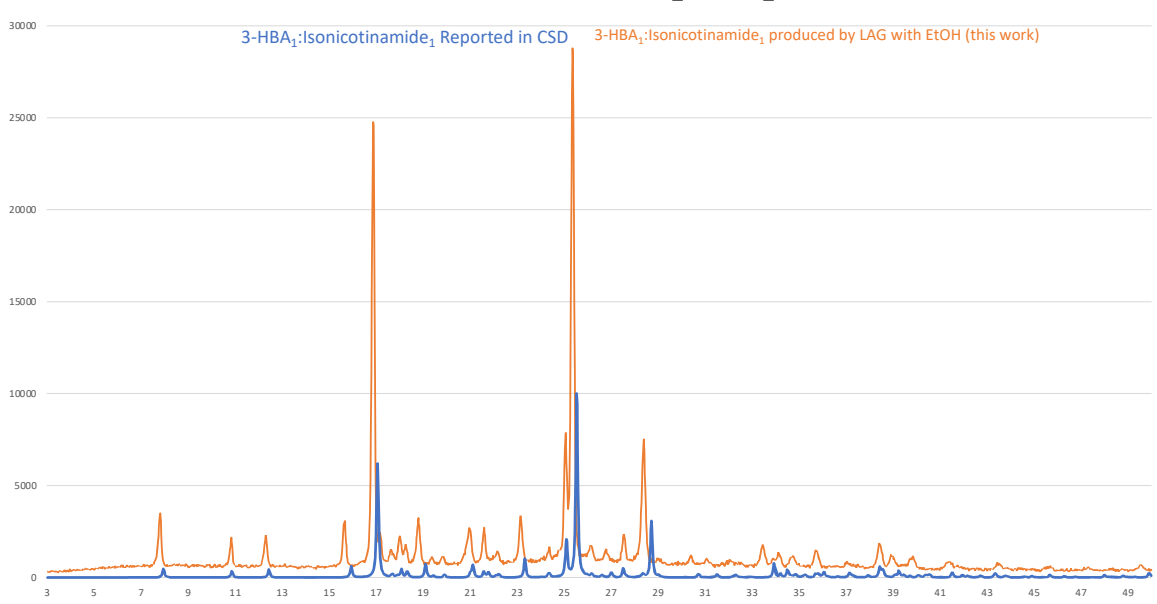


#### 3.6.7 3-HBA:Isonicotinamide

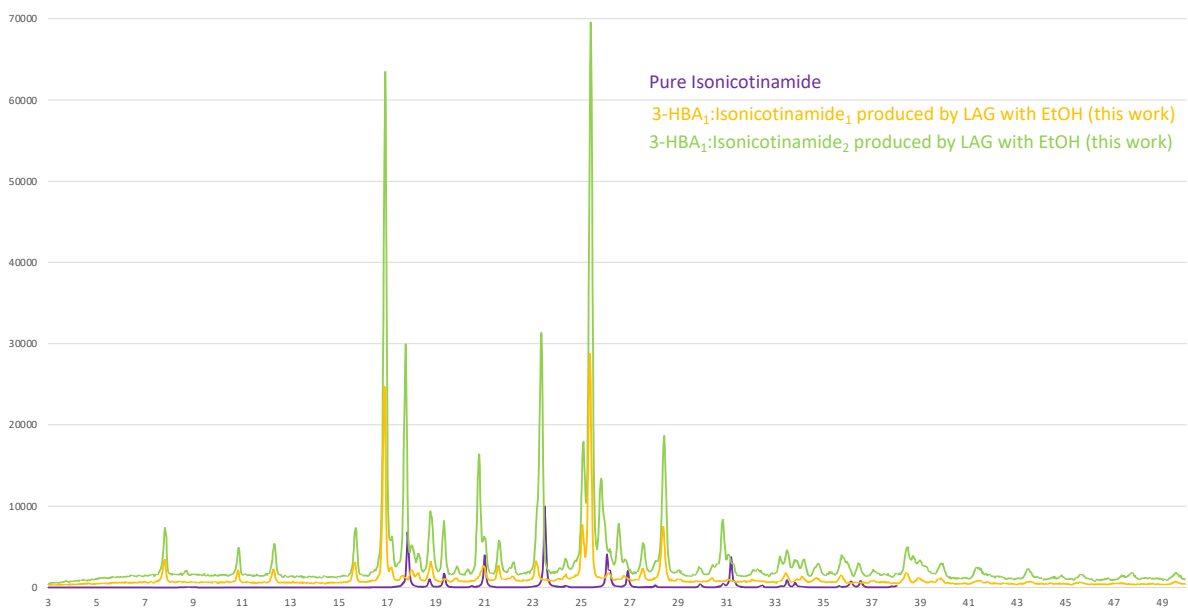
# DSC 3HBA + Isonicotinamide



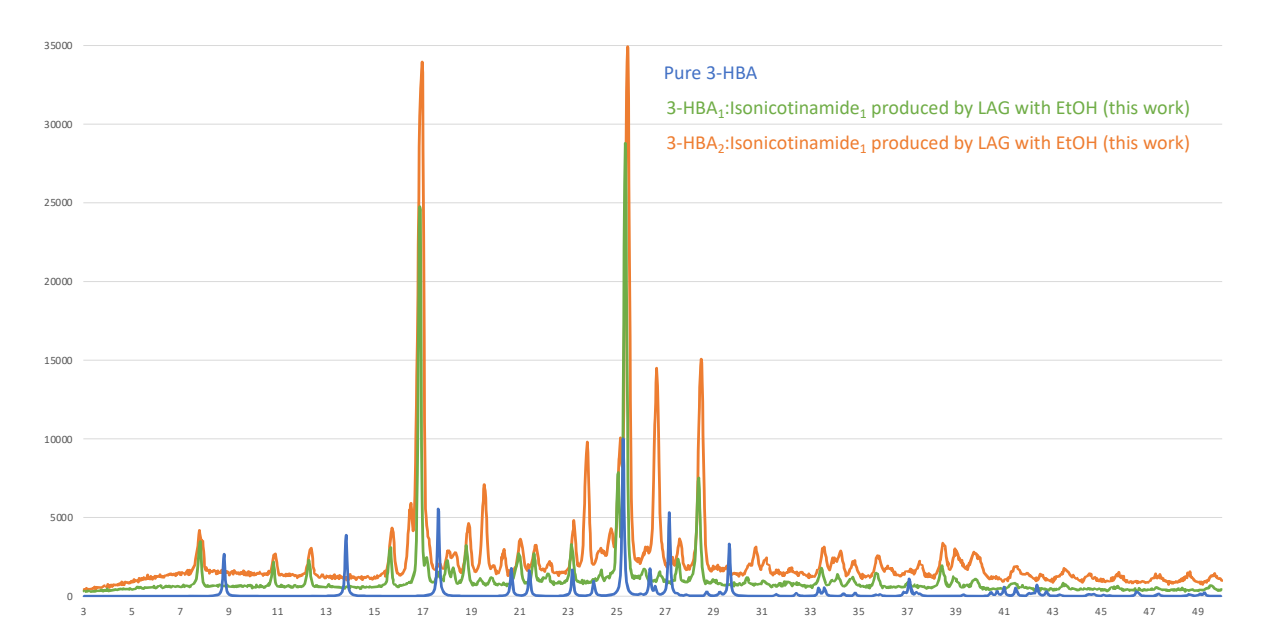
### PXRD 3HBA<sub>1</sub>:INA<sub>1</sub>



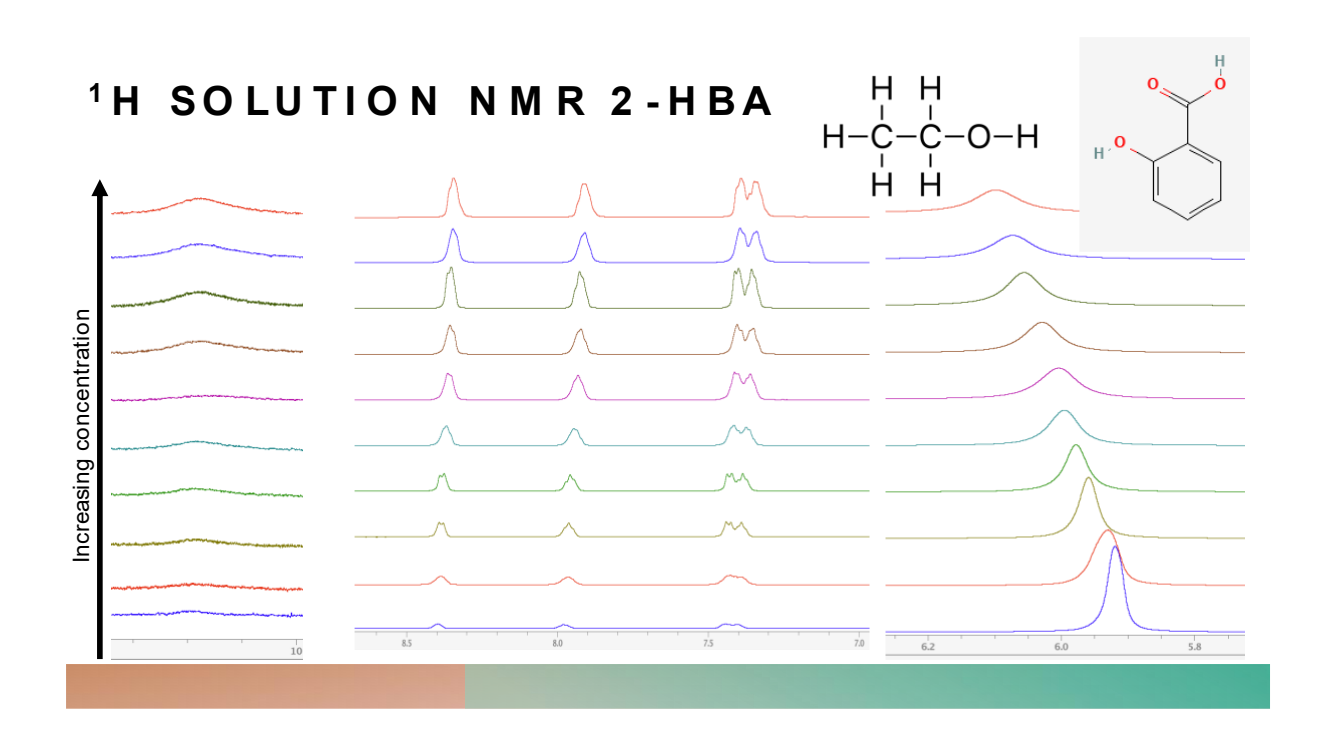
### PXRD 3HBA<sub>1</sub>:INA<sub>2</sub>

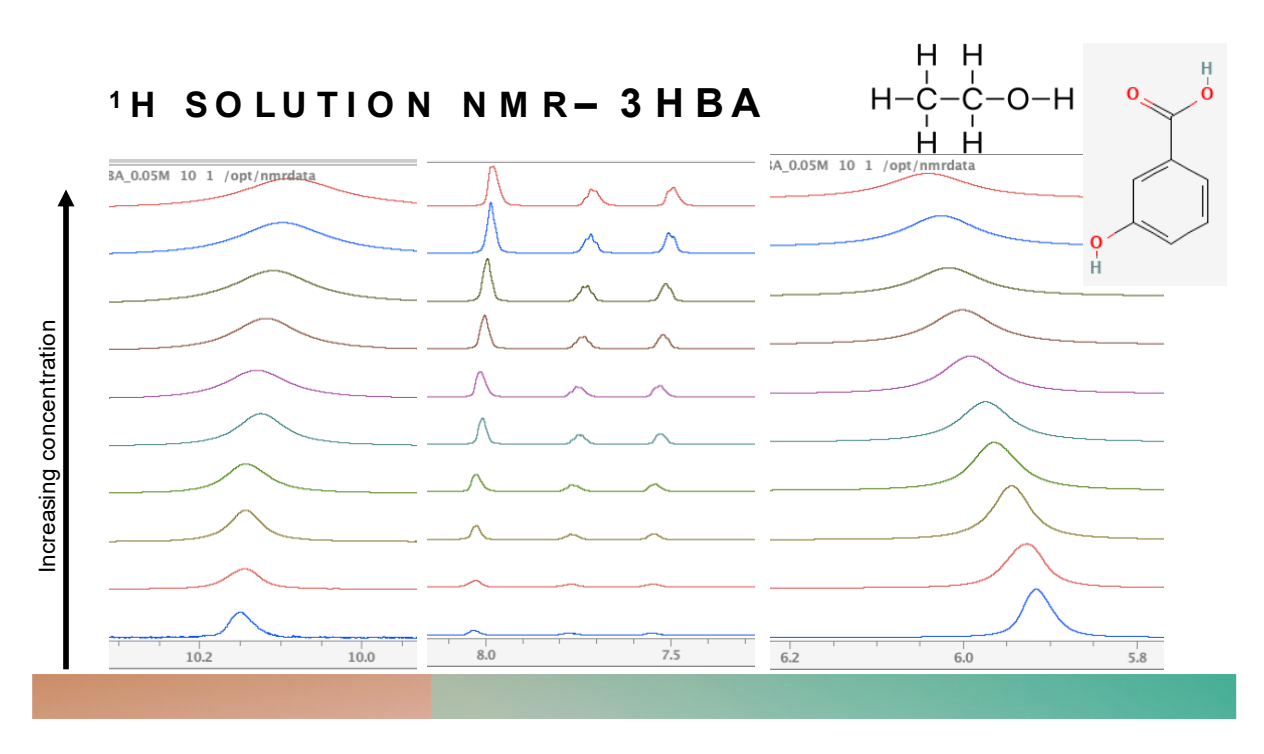


### PXRD 3HBA<sub>2</sub>:INA<sub>1</sub>



### 4.1 - <sup>1</sup>H Solution State Spectra





### **4.2** – Table showing <sup>1</sup>H NMR sample concentrations

Coformer combination	Concentration in EtOH
Pure 3-HBA	0.05M, 0.1M, 0.15M, 0.2M, 0.25M, 0.3M, 0.35M, 0.4M, 0.45M, 0.5M, 0.55M, 0.6M, 0.65M, 0.7M, 0.75M, 0.8M, 0.85M, 0.9M, 0.95M, 1M
Pure 2-HBA	0.05M, 0.1M, 0.15M, 0.2M, 0.25M, 0.3M, 0.35M, 0.4M, 0.45M, 0.5M, 0.55M, 0.6M, 0.65M, 0.7M, 0.75M, 0.8M, 0.85M, 0.9M, 0.95M, 1M
Pure INA	0.05M, 0.1M, 0.15M, 0.2M, 0.25M, 0.3M, 0.35M, 0.4M, 0.45M, 0.5M, 0.55M, 0.6M, 0.65M
Pure NA	0.05M, 0.1M, 0.15M, 0.2M, 0.25M, 0.3M, 0.35M, 0.4M, 0.45M, 0.5M

### **4.3** – NMR titrations peak list

PEAK	0.05M	0.1M	0.15M	0.2M	0.25M	0.3M	0.35M	0.4M	0.45M	0.5M
1	9.6257	9.6253	9.6240	9.6173	9.6105	9.6121	9.6050	9.6018	9.5936	9.5871
2	9.2280	9.2273	9.2228	9.2143	9.2071	9.2033	9.1952	9.1928	9.1812	9.1744
3	8.9954	8.9971	8.9993	8.9909	8.9907	8.9889	8.9843	8.9860	8.9754	8.9725
4	8.8733	8.8713	8.8696	8.8603	8.8580	8.8513	8.8444	8.8449	8.8320	8.8281
5	8.0805	8.0792	8.0764	8.0701	8.0751	8.0606	8.0637	8.0568	8.0656	8.0685
6	8.0093	8.0267	8.0402	8.0346	8.0516	8.0345	8.0302	8.0294	8.0249	8.0160
7	5.8856	5.8912	5.8876	5.8801	5.8752	5.8737	5.8635	5.8597	5.8497	5.8418